



Grain size effects on radiogenic Helium gas in the nuclear fuel UO₂

Emanuele de Bona

► To cite this version:

Emanuele de Bona. Grain size effects on radiogenic Helium gas in the nuclear fuel UO₂. Génie civil nucléaire. Université Paris Saclay (COMUE), 2019. English. NNT : 2019SACLC084 . tel-02640436

HAL Id: tel-02640436

<https://theses.hal.science/tel-02640436>

Submitted on 28 May 2020

HAL is a multi-disciplinary open access archive for the deposit and dissemination of scientific research documents, whether they are published or not. The documents may come from teaching and research institutions in France or abroad, or from public or private research centers.

L'archive ouverte pluridisciplinaire **HAL**, est destinée au dépôt et à la diffusion de documents scientifiques de niveau recherche, publiés ou non, émanant des établissements d'enseignement et de recherche français ou étrangers, des laboratoires publics ou privés.

Grain size effects on radiogenic helium gas in the nuclear fuel UO_2

Thèse de doctorat de l'Université Paris-Saclay
préparée à Centralesupélec

École doctorale n°573 Interfaces : approches interdisciplinaires,
fondements, applications et innovation (Interfaces)
Spécialité de doctorat: Physique

Thèse présentée et soutenue à Karlsruhe (Germany), le 26 Novembre 2019, par

Emanuele De Bona

Composition du Jury :

Dr. Fabienne Audubert HDR, Directeur de Recherche, CEA Cadarache	Rapporteur
Dr. Nathalie Moncoffre HDR, Directeur de Recherche, Institut de Physique des 2 Infinis de Lyon	Rapporteur, Président du jury
Dr. Lionel Thomé HDR, Directeur de Recherche Emérite, CSNSM, UPSAY	Examineur
Dr. Václav Tyrpekl Assistant Professor, Department of Inorganic Chemistry, Charles University in Prague, Czech Republic	Examineur
Dr. Damien Prieur Researcher, Helmholtz-Zentrum Dresden Rossendorf, Germany	Examineur
Dr. Gianguido Baldinozzi HDR, Directeur de Recherche, Centralesupélec, UPSAY	Directeur de thèse
Dr. Thierry Wiss HDR, Senior Expert, JRC Karlsruhe, Germany	Co-Directeur de thèse
Dr. Marco Cologna Researcher, JRC Ispra, Italy	Encadrant de thèse



Thèse préparée au sein du Joint Research Centre de
Karlsruhe (Germany)

Grain size effects on radiogenic helium gas in the nuclear fuel UO_2

Acknowledgement

Before the beginning of this manuscript, let me spend few lines to (try to) acknowledge the people who helped, supported, and guided me through this wonderful three and half years long experience.

First, my gratitude goes to the members of the jury, Dr. Fabienne Audubert, Dr. Nathalie Moncoffre, Dr. Lionel Thomé, Dr. Václav Tyrpekl, and Dr. Damien Prieur, for accepting to revise my manuscript and for their precious insight on the work performed. Despite the stress in the days before (I will not pretend I was composed), the defence has been such a nice moment of scientific discussion that I wished it could have lasted longer.

Obviously, none of what is written in the present manuscript would have been possible without my trinity of supervisors: Dr. Thierry Wiss, Dr. Marco Cologna, and Dr. Gianguido Baldinozzi. I could easily write a second, longer book about all the things I learnt from each one of them during these three years, and it still probably would not be enough. It is a pleasure, and at the same time a personal satisfaction, to know we will still have the possibility to work together in the coming years.

A large share of my appreciation goes also to the European Commission and the JRC – Karlsruhe, which funded the project, and to the director Dr. Maria Betti for granting me this fantastic opportunity. Europe has been my homeland since my childhood, then the JRC welcomed me as a master student, grew me as a PhD, and will host me as an (unpaid) visiting scientist: my gratitude to Europe and to the JRC goes well beyond the goals achieved with this work.

In particular, among all the wonderful people met during this period, I wish to thank especially the head of unit Dr. Rudy Konings, Petra Strube, and all the colleagues of the unit G.I.3 (and not only). Not a single experiment could have been performed, and not a single line of manuscript could have been written, without their huge help. A special mention is due to Daniel, Co, Herwin, Karin, Michael, Bert, Markus, Ekhard, Dragos, Oliver, Alessandro, Toto, Olaf, Jean-Yves, Luka, Sarah, Ondrej, Antony, Jean-François, Patrick, Sebastien, Andrea, Laura, Daniel B., Octavian, Jean-Cristoph, Carmen, Corinne, Francesco, Ramon, Saverio, Szolt, Guido, and all the others who found the time and motivation to help me during my work. I can just say I was really lucky to be involved in so many activities during my stay, because this meant I could work with and learn from all of these people. Last but not the least, Dr. Joseph Somers, who was the head of unit of the E.04 during my master thesis, as well as the one who interviewed (and accepted) me for the PhD position. A big thanks also to Tiankai, Lingfeng, Heike, Damien (yes, him again), Tonya, Aaron, Yuri, Elke, and Bianca for the collaborations and the support in the experiments outside JRC.

Of course, throughout these three long years, working relationships evolved and often ended up into friendships – which is actually very good, as we are supposed to spend (at least) 8 hours a day with these people. Knowing to find there Luca, Guilhem, Tommaso, Luana, Concettina, Sara, Andrea-Justin, Alberto, Luca², Luca³, Nicola (!), Pierre, Jacques, Adeline, Viktoria, Maarten, Mate, Eduard, Laura, Alexandra, JF, and Sylvain definitely made it much easier to wake up and drag myself to work every day. I wish also to acknowledge the mahlzeiters for making every KIT-casino lunch tastier, the COPAS Football Club for giving me the possibility of showing my real talent although the PhD mostly drained my energies, and Kolo and Stövchen for providing the required nutrition in solid and liquid state respectively.

Thinking back at my last three-and-half years in Karlsruhe, it is impossible not to mention Dave, Paddy, Freddy, and later on Esra and Nicholas, the people with whom I shared a flat and a living. Whenever anything was going bad during the PhD, I might have complained with family and colleagues, but, at the end of the day, the people who had to withstand me were these poor guys. Thanks for being like a family – and to Dave and Paddy also for the wonderful food and pictures taken at the defence.

A big thank you also to my crew from Belluno, FMNF and Le Prime Uve, the people I have grown up with: anytime I am with them, where the horizon is hidden behind the mountains, my problems vanish and I can only think of polenta, pastin & formai. I do not know much about my short-term future, but I owe so much to my boyhood town that I need to be back there sooner or later.

Finally, a big big big acknowledgement to my parents, Alberto and Barbara, my nonna Gina, and my family in general. They made me what I am now, they always listened to me, understood me and supported me, even when I was clearly too stubborn or just stupid, and always went that extra mile to make sure I could have everything I needed or wished for. Their confused but happy faces at the defence were maybe the best payoff for these three years of work.

The last few lines are dedicated to Isabella, my girlfriend, who accepted and understood my choice despite all the distance, the problems, and the drawbacks it would have come with. In these years, we are going through the most important challenges of our lives, and being together is what is making the impossible possible. Thanks for making me daily the luckiest and happiest person in the world.

Knowing that I surely forgot someone, a big hug and a huge thanks to everybody I shared a moment with in the last three years.

Index

Abstract.....	vii
Résumé	xi
List of figures.....	xiv
List of tables	xx
List of acronyms	xxii
1 CONTEXT OF THE STUDY	1
1.1 Nuclear energy	1
1.1.1 Nuclear energy production	1
1.1.2 Light Water Reactors (LWR)	2
1.1.3 LWR fuel	2
1.1.4 UO ₂ fuel fabrication	2
1.1.5 Spent Nuclear Fuel (SNF)	4
1.1.6 Context of the study.....	4
1.2 Sintering of UO ₂	5
1.2.1 Sintering	5
1.2.1.1 Densification	5
1.2.1.1.1 The driving force for sintering	5
1.2.1.1.2 Diffusion in crystalline solids	6
1.2.1.1.3 Defects in crystalline solids.....	7
1.2.1.1.4 Diffusion mechanisms.....	9
1.2.1.1.5 Ambipolar diffusion – atoms motion in ionic solids	9
1.2.1.1.6 Sintering mechanisms.....	10
1.2.1.1.7 Grain boundaries and porosity	10
1.2.1.1.8 Stages of sintering.....	11
1.2.1.2 Grain growth and coarsening.....	12
1.2.1.2.1 The LSW model for coarsening	13
1.2.1.2.2 The Brooke and Turnbull model for grain growth	13
1.2.1.2.3 Solute drag and pores mobility	14
1.2.1.3 Microstructure control.....	15
1.2.1.3.1 Densification and coarsening in ceramic materials	15
1.2.1.3.2 Strategies for microstructural control	15
1.2.1.4 Spark Plasma Sintering (SPS).....	17
1.2.2 Sintered UO ₂ for nuclear energy production.....	18

1.2.2.1	Requirements of NF	18
1.2.2.1.1	Density and porosity	18
1.2.2.1.2	Stoichiometry.....	19
1.2.2.1.3	Shape and roughness.....	19
1.2.2.2	Properties of NF - Thermophysical properties of stoichiometric UO_2	19
1.2.2.2.1	Crystal structure.....	19
1.2.2.2.2	Thermal expansion and melting point	20
1.2.2.2.3	Heat capacity	20
1.2.2.2.4	Thermal conductivity	20
1.2.2.3	Effect of stoichiometry.....	21
1.2.2.3.1	Crystal structure.....	21
1.2.2.3.2	Diffusion and sinterability.....	22
1.2.2.3.3	Thermal properties	23
1.2.2.4	MOX fuel	24
1.2.2.4.1	Crystal structure.....	24
1.2.2.4.2	Thermal expansion and melting point	25
1.2.2.4.3	Heat capacity	25
1.2.2.4.4	Thermal conductivity	25
1.3	In-reactor life – irradiation of Nuclear Fuel	26
1.3.1	Materials response to radiation.....	27
1.3.1.1	Stopping power	27
1.3.1.2	Nuclear energy losses – low-energy particles.....	28
1.3.1.3	Electronic energy losses – high-energy particles.....	29
1.3.2	Defects formation in UO_2 (effects of radiation damage)	30
1.3.2.1	β - and γ - decays	30
1.3.2.2	Neutrons	30
1.3.2.3	α -decays.....	30
1.3.2.4	Fission products	31
1.3.2.5	Radiations in UO_2	32
1.3.2.6	Radiation damage and defects creation	34
1.3.2.6.1	Point defects	34
1.3.2.6.2	Extended defects	34
1.3.3	Irradiated UO_2	35
1.3.3.1	Change of properties	35

1.3.3.1.1	Swelling and fission gases retention	36
1.3.3.1.2	Mechanical properties	37
1.3.3.1.3	Thermal properties	37
1.3.3.2	HBS formation	38
1.3.3.3	UO ₂ radiation resistance – polarons effect?	40
1.4	Studies on SIMFUEL and separate effect studies.....	40
1.4.1	SIMFUEL studies.....	41
1.4.1.1	Fission products inclusion	41
1.4.1.1.1	Solid fission products	41
1.4.1.1.2	Volatile fission products.....	42
1.4.1.2	HBS simulation	42
1.4.2	Separate effect studies	42
1.4.2.1	α -doped UO ₂	42
1.4.2.2	Ion-implanted UO ₂	43
1.4.2.2.1	α -damage and He migration.....	43
1.4.2.2.2	Fission gases and swift heavy ions.....	43
1.5	Chapter conclusions and thesis organisation	44
2	GENERAL EXPERIMENTAL PART	47
2.1	Standard techniques	47
2.1.1	Samples preparation – powders synthesis and sintering	47
2.1.2	Samples characterization	48
2.1.2.1	XRD – X-ray diffraction	48
	XRD devices.....	50
2.1.2.2	Scanning Electron Microscopy – SEM	50
	SEM characterization at the JRC – Karlsruhe	52
2.1.2.3	Differential Scan Calorimetry	52
	DSC characterization at the JRC – Karlsruhe	52
2.1.2.4	ThO ₂ irradiation.....	53
2.2	Innovative techniques.....	55
2.2.1	SPS.....	55
2.2.2	Transmission Electron Microscopy	56
	TEM characterization at the JRC – Karlsruhe	56
2.2.3	Raman spectroscopy	57
	Raman characterization at the JRC – Karlsruhe	58

2.2.4	LAser Flash method.....	60
	LAF characterization at the JRC – Karlsruhe	60
2.2.5	Knudsen Effusion Mass Spectrometry	62
	KEMS characterization at the JRC – Karlsruhe	62
2.2.6	Low T calorimetry.....	65
3	SAMPLES PREPARATION	67
3.1	²³⁸ Pu-doped UO ₂ samples for accelerated spent nuclear fuel ageing study through α -self-irradiation	67
3.1.1	Sample’s elaboration	67
3.1.2	Materials and methods	70
3.1.2.1	α -dopant powder.....	71
3.1.2.2	Uranium solution	71
3.1.3	Samples preparation	71
3.1.3.1	Pu dissolution and mixing	71
3.1.3.2	Precipitation and filtration.....	71
3.1.3.3	Pre-calcination and calcination.....	72
3.1.3.4	Pressing and sintering.....	72
3.1.4	Summary	73
3.2	Nanograined UO ₂ for grain size effect study on radiation resistance.....	73
3.2.1	Samples design/elaboration	73
3.2.2	Materials and methods	75
3.2.2.1	Uranyl nitrate solution	75
3.2.2.2	Uranium oxalate powder	75
3.2.2.3	Sintering of the powders.....	76
3.2.3	Samples preparation	77
3.2.3.1	Hydrolysis.....	77
3.2.3.2	Sol-gel.....	77
3.2.3.3	Oxalate thermal conversion.....	78
3.2.3.4	Oxalate hydrothermal decomposition.....	78
3.2.3.5	Overview of the synthesised powders.....	78
3.2.3.6	Spark plasma sintering.....	78
3.2.3.7	Two-step spark plasma sintering	79
3.2.3.8	High pressure spark plasma sintering	80
3.2.3.9	Calcination.....	80
3.2.4	Summary	81

3.3	Nanograined ThO ₂ for grain size effect study on radiation resistance	81
3.3.1	Interest in ThO ₂	81
3.3.2	Materials and methods	81
3.3.3	Sample preparation	82
3.3.3.1	Spark plasma sintering	82
3.3.3.2	High pressure spark plasma sintering	82
3.3.4	Summary	84
4	SAMPLES CHARACTERIZATION.....	85
4.1	Density determination	85
4.1.1	²³⁸ Pu-doped UO ₂ samples for accelerated spent nuclear fuel ageing study through α -self-irradiation.....	85
4.1.2	Nanograined UO ₂ for grain size effect study on radiation resistance	86
4.2	Microstructure – Scanning Electron Microscopy	87
4.2.1	²³⁸ Pu-doped UO ₂ samples for accelerated spent nuclear fuel ageing study through α -self-irradiation.....	87
4.2.2	Nanograined UO ₂ for grain size effect study on radiation resistance	90
4.2.2.1	UO ₂ nanopowders.....	90
4.2.2.2	UO ₂ SPS disks.....	92
4.2.2.3	Nanograined UO ₂ disks and successive annealing	93
4.3	Crystal structure – X-ray diffraction.....	95
4.3.1	²³⁸ Pu-doped UO ₂ samples for accelerated spent nuclear fuel ageing study through α -self-irradiation.....	95
4.3.2	Nanograined UO ₂ for grain size effect study on radiation resistance	96
4.3.2.1	UO ₂ nanopowders.....	97
4.3.2.2	UO ₂ disks	97
4.3.2.3	Nanograined UO ₂ disks and successive annealing.....	97
4.4	Transmission electron microscopy	99
4.4.1	²³⁸ Pu-doped UO ₂ samples for accelerated spent nuclear fuel ageing study through α -self-irradiation.....	99
4.4.2	Nanograined UO ₂ for grain size effect study on radiation resistance	100
4.5	Other fresh MOX properties	101
4.5.1	Crystal structure - Raman	101
4.5.2	Thermal diffusivity and conductivity – LAser Flash.....	102
4.6	Nanograined ThO ₂ for grain size effect study on radiation resistance	103
4.6.1	Microstructure - SEM	103
4.6.2	Crystal structure - XRD	104

4.6.3	TEM	105
4.6.4	Ion implantation at 600 °C	106
4.6.4.1	Samples before implantation.....	106
4.6.4.2	300 keV Xe.....	107
4.6.4.3	16 keV He	107
4.7	Conclusions	109
5	STORAGE – SELF IRRADIATION.....	111
5.1	Room T ageing.....	111
5.1.1	Crystal structure – XRD	111
5.1.2	Microstructure – SEM	113
5.1.3	Raman	116
5.1.4	Thermal diffusivity – LAF.....	118
5.1.5	TEM	120
5.1.6	Helium release – KEMS	123
5.1.7	Apparent specific heat – DSC.....	125
5.1.8	Summary	128
5.2	Low T C _p measurement	130
5.2.1	Results.....	130
5.2.2	Summary	131
6	CONCLUSIONS AND OUTLOOK.....	133
	References	139

Abstract

Civilian nuclear power now has more than 70 years of experience - more than 10 000 reactor-years. For a large segment of power reactors, especially in France, we are reaching the stage where choices must be made between retiring these facilities and extending their licensed lifetimes. Moreover, new advanced and innovative fuels are being studied with the aim of optimizing their safe use especially in off-normal conditions. Following the Fukushima accident, research on Accident Tolerant Fuels (ATF) has been triggered with the aim to develop fuels that can endure loss of active cooling for longer time and generally that have higher safety margins (to melt for example).

With the increase of licensed burnup, today's light water reactor (LWR) fuels develop a so-called high burnup structure (HBS) when irradiated to high burnups characterized by the formation of a rim zone where original micrometer sized grains transform into grains of around 100 nanometers associated with an increase of the local porosity. This structure is well characterized and its properties are generally better than initially thought, which would make it worth considering as an ATF.

Single effect studies would therefore require synthesizing such nanostructured fuels with the ultimate goal to irradiate these materials in a reactor, to explore the potential of the HBS in terms of radiation resistance, improved mechanical properties, thermo-physical properties, and as well as fission gases retention in a simplified system. However, such microstructures are inaccessible to the traditional production routes for nuclear fuels, which fail to suppress coarsening during powders densification. The application of innovative powders synthesis routes as well as sintering treatments (hot pressing, field assisted sintering techniques) broadened the range of the achievable final products, but more effort is needed to fully control the microstructure of the sintered UO_2 pellets to the point of obtaining a completely faithful HBS reproduction.

At the backend of the fuel cycle, the worldwide cumulative inventory of stored spent fuel is of about 2×10^8 kg of heavy metal, and it keeps increasing every year of about 10^4 tons. Most of those spent fuels consist of a mixture of U and other actinide oxides. A variety of options exist concerning spent fuel disposal. For the once-through fuel cycle approach, spent fuel is cooled and then put in corrosion resistant containers for further storage and ultimate disposal in a geological repository - although the possibility to retrieve them at a later time can also be an important factor.

A better understanding of the fundamental phenomena underpinning the physical, structural, and chemical properties of the mixed oxides of U during storage/disposal is highly desirable for the goal of a safe and sustainable management of the spent nuclear fuels. One of the main factors affecting the stability of spent fuel is linked to its alpha-activity dominating the first millenaries and generating damage and helium accumulation in the fuel lattice. The challenge in assessing the evolution of such fuels over a laboratory time scale is to accelerate the ageing and possibly to have systems easier to study than irradiated fuels. Doping UO_2 with short lived alpha emitters represents such an alternative, and it already proved to be a precious tool for understanding the effects of alpha self-irradiation in UO_2 -based compounds. Nonetheless, data are only partially complete and a comprehensive study, involving simultaneous characterization with an exhaustive set of techniques, is missing.

In a more general perspective, HBS would be the first part of LWR UO_2 fuels to interact with water in case of failure of all other barriers in disposal facilities. HBS should be studied also as first confinement system during repository, especially considering its potentially beneficial effect both in operation and during loss of coolant accidents. The ultimate goal of this work is to demonstrate the feasibility of producing SIMFUEL that could mimic the ageing of the HBS due to alpha self-irradiation during long-term storage.

Every step of UO_2 fuel production was optimised on a laboratory scale to yield final dense, nanostructured products. Optimal powder synthesis routes and sintering treatments have been designed for maximising the microstructure control during the densification process, resulting in identical final products with different grain sizes spanning over two orders of magnitude, covering the range observed in the HBS.

In parallel, periodic multi-technique characterization on a broad set of identical alpha-doped UO_2 samples was conducted, resulting in a solid and reliable benchmark dataset of (U,Pu) O_2 properties evolution under prolonged alpha-irradiation. The lattice swelling and thermal conductivity decrease already reported in literature were confirmed and re-assessed with improved accuracy. Defects evolution and clustering in extended defects was followed by means of transmission electron microscopy and calorimetry measurements, and thermal effusion mass spectrometry assessed the full retention of the radiogenic Helium. Raman scattering was acquired for the first time on (U,Pu) O_2 samples as a function of the dose, and scanning electron microscopy was used to assess the sample integrities. This accelerated ageing approach allowed estimating the situation equivalent to a LWR SNF after about 300 years of storage, as well as re-assessing the independence of macroscopical effects on the sample activities, i.e. the kinetic of damage generation, within certain compositional limits.

The role of interfaces was highlighted in several aspects of the radiation response of the material, from damage recombination to gas migration. Moreover, the preliminary results obtained by ion implantation on samples of very different grain sizes showed extremely different behaviours. This work underlines the need, and at the same time represents the starting point of systematic studies based on SIMFUEL for understanding the impact of interfaces on SNF ageing. Eventually, this would help assessing the feasibility of the HBS as a kind of ATF in determinate conditions, its impact in SNF repository strategies, as well as providing basic information for the modelling of NF in operation, and potentially guide the design of innovative ATF microstructures in the future.

The manuscript is structured as follows. After introducing general considerations on the nuclear energy, chapter one is devoted to a state-of-the-art survey on the knowledge around LWR fuels and their behaviour under irradiation. The production process is described, highlighting the critical aspects towards microstructure control during sintering, and the most important properties of LWR fuels are listed. The mechanisms of radiation damage creation are presented in relation to nuclear fuels and their beforehand described thermophysical properties, including the HBS formation and its consequences. Finally, an overview on the different techniques and strategies used in separate effect and accelerated ageing studies was provided.

Chapter two presents the materials and the devices used in the study, with extensive descriptions of the nuclearisation of the experimental setups available at the Joint Research Centre in Karlsruhe (JRC-KA), where most of the work has been performed.

In chapter three the sample preparations are described, and two main portions can be distinguished which differ by the problem that they tackle. The first one reports about the production of the alpha-doped UO_2 with particular attention to the design phase, given the importance of the dopant concentration for the accelerated ageing study. The second part illustrates how UO_2 with tailored microstructures was produced, through the application of different synthesis routes, sintering treatments, and the constant interaction with the characterization phase.

Chapter four presents the sample characterizations after production, including the intermediate steps which led to finally lower the grain size of the sintered UO_2 down to the one of the HBS. Considering their more conventional production processes, more characterization data were reported about the final sintered alpha-doped UO_2 rather than during their production.

In chapter five, the results of the accelerated ageing study are presented. The evolution of the properties characterized in chapter four was reported, especially for the safety relevant ones already mentioned in the first chapter. For some phenomena, a correlation between the evolution kinetics observed by means of different techniques was attempted.

Chapter six finally summarises the work performed and draws the conclusions of the study, giving some perspectives for future works.

Résumé

L'exploitation de l'énergie nucléaire civile compte désormais plus de 70 ans d'expérience - plus de 10 000 équivalent années-réacteurs. Pour un grand nombre de réacteurs de puissance, notamment en France, nous arrivons au stade où des choix doivent être faits entre la mise hors service de ces installations et la prolongation de leur durée de vie autorisée. De plus, de nouveaux combustibles avancés et innovants sont à l'étude dans le but d'optimiser leur utilisation en toute sécurité notamment dans des conditions opérationnelles hors normes. À la suite de l'accident de Fukushima, des recherches sur les combustibles tolérants aux accidents (ATF) ont été lancées dans le but de développer des combustibles capables de supporter un Accident de Perte de Refrigérant Primaire (APRP) pendant une certaine durée et généralement ayant des marges opérationnelles de sécurité plus élevées (écart à la fusion par exemple).

Avec l'augmentation du taux de combustion autorisé, les combustibles des réacteurs à eau légère (LWR) actuels développent une structure dite à haut taux de combustion (HBS) caractérisés par la formation d'une zone périphérique où les grains originaux de taille micrométrique se transforment en grains d'environ 100 nanomètres associés à une augmentation de la porosité locale. Cette structure est bien caractérisée et ses propriétés sont généralement meilleures que ce que l'on pensait initialement, ce qui mériterait de considérer cette microstructure comme un ATF potentiel.

Les études à effet séparés nécessiteraient donc de synthétiser de tels combustibles nanostructurés dans le but ultime d'irradier ces matériaux dans un réacteur, d'explorer le potentiel du HBS en termes de, résistance à l'irradiation, amélioration des propriétés mécaniques et des propriétés thermo-physiques ainsi que rétention des gaz de fission et cela dans un système simplifié. Cependant, ces microstructures sont inaccessibles par voies de synthèse conventionnelles des combustibles nucléaires, qui ne parviennent pas à supprimer la croissance de grain lors de la densification des poudres. L'utilisation de voies de synthèse de poudres innovantes ainsi que de traitements de frittage (pressage à chaud, frittage flash ou SPS) a élargi la gamme des produits finaux réalisables, mais plus de recherches sont nécessaires pour contrôler pleinement la microstructure des pastilles d' UO_2 frittées en vue d'obtenir une reproduction HBS totalement fidèle.

À l'aval du cycle du combustible, le stock cumulé mondial de combustible usé et stocké est d'environ 2×10^8 kg de métal lourd, et il continue d'augmenter chaque année d'environ 10^4 tonnes. La plupart de ces combustibles usés sont constitués d'un mélange d'U et d'autres oxydes d'actinides. Il existe diverses options couvrant l'élimination du combustible usé. Pour l'approche du cycle du combustible à cycle ouvert, le combustible usé est refroidi puis placé dans des conteneurs résistants à la corrosion pour un entreposage supplémentaire suivi d'un stockage final dans un dépôt géologique - bien que la possibilité de les récupérer ultérieurement peut également être un facteur important.

Une meilleure compréhension des phénomènes fondamentaux qui sous-tendent les propriétés physiques, structurelles et chimiques des oxydes mixtes d'U durant l'entreposage / stockage est hautement souhaitable pour garantir une gestion sûre et durable des combustibles nucléaires usés. L'un des principaux facteurs affectant la stabilité du combustible usé est lié à son activité alpha qui domine les premiers millénaires et génère des dommages et une accumulation d'hélium radiogénique dans le réseau cristallin du combustible. Le défi pour évaluer l'évolution de ces combustibles sur une échelle de temps en laboratoire est d'accélérer le vieillissement et éventuellement d'avoir des systèmes plus faciles à étudier que les combustibles irradiés. Le dopage

d' UO_2 avec des émetteurs alpha à courte durée de vie représente une telle alternative, et il s'est déjà révélé être un outil précieux pour comprendre les effets de l'auto-irradiation alpha dans les composés à base d' UO_2 . Néanmoins, les données sont incomplètes et une étude approfondie, impliquant une caractérisation simultanée avec un ensemble exhaustif de techniques, fait défaut.

Dans une perspective plus générale, le HBS serait la première partie des combustibles LWR UO_2 à interagir avec l'eau en cas de défaillance de toutes les autres barrières dans les installations de stockage. La HBS doit également être étudiée en tant que premier système de confinement pendant le stockage, compte tenu en particulier de son effet potentiellement bénéfique à la fois en fonctionnement et lors des accidents de perte de liquide de refroidissement. Le but ultime de ce travail est de démontrer la faisabilité de produire du SIMFUEL qui pourrait reproduire le vieillissement du HBS dû à l'auto-irradiation alpha pendant le stockage à long terme.

Chaque étape de la production de combustible UO_2 a été optimisée à l'échelle du laboratoire pour produire des produits finaux denses et nanostructurés. Des voies de synthèse de poudre et des traitements de frittage optimaux ont été conçus pour maximiser le contrôle de la microstructure pendant le processus de densification, résultant en des produits finaux identiques avec des tailles de grains différentes s'étendant sur deux ordres de grandeur et couvrant la gamme observée dans la HBS.

En parallèle, une caractérisation périodique multi-technique sur un large ensemble d'échantillons d' UO_2 dopés alpha a été réalisée, résultant en un ensemble de données de référence robuste de l'évolution des propriétés $(\text{U}, \text{Pu})\text{O}_2$ sous irradiation alpha prolongée. L'accroissement du paramètre de maille ainsi que la diminution de la conductivité thermique déjà signalés dans la littérature ont été confirmés et réévalués avec une précision améliorée. L'évolution des défauts et le regroupement en défauts étendus ont été suivis au moyen de microscopie électronique à transmission et de mesures de calorimétrie, et la spectrométrie de masse à effusion thermique a permis de déterminer la rétention complète de l'hélium radiogénique. La diffusion Raman a été acquise pour la première fois sur des échantillons $(\text{U}, \text{Pu})\text{O}_2$ en fonction de la dose, et la microscopie électronique à balayage a été utilisée pour évaluer l'intégrité des échantillons. Cette approche de vieillissement accéléré a permis d'estimer l'état équivalent à un combustible LWR utilisé après environ 300 ans de stockage, ainsi que de réévaluer l'indépendance des effets macroscopiques sur les activités de l'échantillon, c'est-à-dire la cinétique de formation des dommages et ce dans certaines limites de composition.

Le rôle des interfaces a été mis en évidence dans plusieurs aspects de la réponse aux rayonnements du matériau, de la recombinaison des dégâts d'irradiation à la migration des gaz. De plus, les résultats préliminaires obtenus par implantation ionique sur des échantillons de grains de tailles très différentes ont montré des comportements extrêmement différents. Ce travail souligne la nécessité et représente en même temps le point de départ d'études systématiques basées sur SIMFUEL pour comprendre l'impact des interfaces sur le vieillissement du combustible utilisé. Finalement, cela aiderait à évaluer la faisabilité de la HBS comme une sorte d'ATF dans des conditions déterminées, son impact dans les stratégies de stockage du combustible, ainsi qu'à fournir des informations de base pour la modélisation du combustible nucléaire en fonctionnement, et pourrait guider à la conception de microstructures ATF innovantes.

Le manuscrit est structuré comme suit. Après avoir introduit des considérations générales sur l'énergie nucléaire, le premier chapitre est consacré à une étude sur l'état de l'art sur les

combustibles à eau légère et leur comportement sous irradiation. Le processus de synthèse est décrit, mettant en évidence les aspects critiques du contrôle de la microstructure pendant le frittage, et les propriétés les plus importantes des combustibles LWR sont répertoriées. Les mécanismes de création de défauts par rayonnement sont présentés en relation avec les combustibles nucléaires et leurs propriétés thermophysiques décrites précédemment, y compris la formation de la HBS et ses conséquences. Enfin, un aperçu des différentes techniques et stratégies utilisées dans des études à effets séparées et le vieillissement accéléré sera présenté.

Le chapitre deux présente les matériaux et les dispositifs utilisés dans l'étude, avec des descriptions détaillées de la nucléarisation des montages expérimentaux disponibles au Centre Commun de Recherche de Karlsruhe (JRC-Ka), où la plupart des travaux ont été effectués.

Dans le chapitre trois, les préparations d'échantillons sont décrites, et deux parties principales seront distinguées qui diffèrent par le problème qu'elles abordent. Le premier rend compte de la production d' UO_2 dopé alpha avec une attention particulière à la phase de conception, étant donné l'importance de la concentration de dopants pour l'étude du vieillissement accéléré. La deuxième partie illustre comment UO_2 avec des microstructures adaptées a été produit, grâce à l'application de différentes voies de synthèse, des traitements de frittage et l'interaction constante avec la phase de caractérisation.

Le chapitre quatre présente les caractéristiques de l'échantillon après la synthèse, y compris les étapes intermédiaires qui ont finalement permis de réduire la taille des grains de l' UO_2 fritté jusqu'à celle de la HBS. Compte tenu de leurs processus de production plus conventionnels, davantage de données de caractérisation ont été rapportées sur l' UO_2 dopé alpha fritté final plutôt que pendant leur production.

Dans le chapitre cinq, les résultats de l'étude sur le vieillissement accéléré sont présentés. L'évolution des propriétés caractérisées au chapitre quatre a été rapportée, en particulier pour les propriétés relevant de l'aspect sécurité des combustibles déjà mentionnées dans le premier chapitre. Pour certains phénomènes, une corrélation entre la cinétique d'évolution observée au moyen des différentes techniques a été tentée.

Enfin, le chapitre six résume le travail effectué et tire les conclusions de l'étude, donnant quelques perspectives pour les travaux futurs.

List of figures

Figure 1: scheme of a BWR (left) and PWR (right). While in the BWR the water used to cool down the core is directly used for steam generation, in PWR instead the heat is transferred to a secondary loop. (5).....	2
Figure 2: Scheme of the UO_2 fuel fabrication process from the enriched UF_6 . (7)	3
Figure 3: typical commercial fuel pellet. (6)	3
Figure 4: left: long-term dominance of α -activity in SNF.(8) right: cumulated α -dose over time for different types of SNF (for dpa definition see 1.3.1; for burnup definition see 1.3.3).....	4
Figure 5: Defects in crystalline solids: a) interstitial impurity; b) edge dislocation; c) self-interstitial; d) vacancy; e) precipitate; f) vacancy dislocation loop; g) interstitial dislocation loop; h) substitutional impurity. (18)	7
Figure 6: Schottky and Frenkel types of defects. In both cases, the charge neutrality of the solid is preserved: in the first case, one ion vacancy is compensated by a vacancy of the opposite ion; in the second case, by a self-interstitial.	8
Figure 7: edge (left) and screw (right) dislocations. The upper plane is shifted of a vector b , the <i>Burger vector</i> . (19)	8
Figure 8: sintering mechanisms: 1) surface diffusion; 2) lattice diffusion from the surface; 3) vapour transport; 4) grain boundary diffusion; 5) lattice diffusion from the grain boundary; 6) plastic flow. Only mechanisms 4, 5 and 6 lead to densification, while 1, 2 and 3 lead to neck growth. (13)	10
Figure 9: A) scheme of the forces balance around an ideal pore. B) Schematic densification of a powder system, with the initial particles surfaces collapsing into grain boundaries. (13)	10
Figure 10: powder particles (a) and the three stages of sintering theorized by Coble: b) initial stage; c) intermediate stage; d) final stage. (21).....	11
Figure 11: diffusion mechanisms responsible for pore mobility. (13)	14
Figure 12: density and grain size as a function of increasing T during sintering of TiO_2 powders.(31).....	15
Figure 13: advantage of fast firing and external pressure. A) at high temperatures, the densification rate can overtake the coarsening rate; B) grain size as a function of the relative density during sintering of MgO -doped Al_2O_3 , showing the effect of fast firing and external pressure. (13)	16
Figure 14: SPS functioning scheme.(32) The graphite die serves also as heating element, as pulsed current is fluxed through it resulting in Joule heating.	17
Figure 15: scheme of a typical SPS thermal treatment. I) chamber evacuation; II) pressure application; III) heating; IV) cooling.(32).....	18
Figure 16: UO_2 fluorite (CaF_2) structure. The U lattice (black spheres) is face centred cubic, while the O lattice (grey spheres) is primitive cubic.....	19
Figure 17: stoichiometric 95 % TD dense UO_2 thermal conductivity. The graph has been taken from the work of Fink et al, the references cited in the table can be found in the original publication. (51).....	20
Figure 18: U-O phase diagram as proposed by Higgs et al (56) in the range $\text{O/M} = 1.9 - 2.4$. The references for the experimental points can be found in the related publication.	22
Figure 19: U and O self-diffusion coefficients in UO_{2+x} as a function of the deviation from stoichiometry. (58) The references can be found in the original publication.	23
Figure 20: variation of the coefficients A and B of equation 18 as function of the variation from stoichiometry in UO_{2+x} . (59)	23
Figure 21: pseudo-binary phase diagram of the UO_2 - PuO_2 system. (43) The full lines represent the solidus and liquidus lines recommended by Adamson (49,50), while the dotted ones the new	

estimation based on the more recent melting temperature values for PuO ₂ . (66,67) The other references can be found in (43).	24
Figure 22: fission reaction of a ²³⁵ U atom. The capture of a neutron brings the nucleus into an excited state, and the unstable ²³⁶ U fissions soon after producing a γ particle, two to three neutrons and two fission product, releasing in total about 200 MeV. (73)	26
Figure 23: Energy loss of a 5.5 MeV particle in air (or stopping power of air for α-particles of 5.5 MeV).	27
Figure 24: SRIM simulation of the displacement cascade generated by a recoil nucleus produced during an α-decay (100 keV). (73).	28
Figure 25: A) ion tracks generated by 310 MeV Au ²⁺ ions passing through UO ₂ . (76) B) calculation of the lattice temperature around the trajectory of a 11.4 MeV U ion in UO ₂ . (79)	29
Figure 26: α-decay of a ²³⁸ U nucleus, resulting in a 5.5 MeV He ion and a 100 keV ²³⁴ Th recoil nucleus. (73)	31
Figure 27: fission products fractional cumulative fission yield for ²³⁵ U and ²³⁹ Pu. (85).	32
Figure 28: comparison between the energy losses regimes of an α-particle and a fission product in UO ₂ . (73).	32
Figure 29: total losses of a ⁹⁵ Zr nucleus travelling into UO ₂ as function of the ion energy. (73).	33
Figure 30: upper part: calculated displacement cascades for a light and a heavy fission product, and for an α-particle in UO ₂ ; lower part: energy losses and deposition range for the same particles. (86)	34
Figure 31: relative lattice swelling as function of the cumulated dose (dpa) in a UO ₂ single crystal irradiated with 5.5 MeV α-particles. [66]	36
Figure 32: hardness increase as function of the fuel burnup, as measured on real and simulated spent fuel. (94).	37
Figure 33: thermal conductivity of SNF for increasing burnup at fuel discharge, or End Of Life (EOL) burnup (bu). (95).	38
Figure 34: High Burnup Structure (HBS) observed in a spent UO ₂ fuel with local burnup of 200 Gwd / tU.	39
Figure 35: left) EPMA and SIMS Xe radial profile. In the HBS, significant amount of Xe is trapped in the pores instead of in the lattice(108); right) thermal diffusivity as function of the burnup, showing an increase due to the occurrence of the HBS for high burnup(95).	40
Figure 36: example of single crystal (a) and polycrystalline/powder (b) X-ray diffraction. While in (a) the beam is diffracted only for points corresponding to a reciprocal lattice vector, in (b) this effect is averaged over a large amount of crystals resulting in circles. (c) Bragg peaks obtained by measuring a polycrystalline sample in a Bragg-Brentano diffractometer. (240)	49
Figure 37: scheme of the two possible Bragg - Brentano configurations. In the θ-θ configuration, the sample is stationary and the X-ray source is rotating, while in the θ-2θ it is the reverse. θ-θ configuration is preferred in case of loose samples, such as powders. (241)	49
Figure 38: scheme of the volume of sample interacting with the electron beam, and corresponding depths probed by SE, BSE and EDS characterizations. (193)	51
Figure 39: SRIM (75) simulation of the implanted He profile and ballistic damage introduced in the matrix.	54
Figure 40: (A) - nuclearized small scale SPS at the JRC-KA; (B) - SPS water-cooled chamber; (C) - SPS graphite die and punch. (195).	55
Figure 41: TEM available at the JRC-KA. The picture on the right shows a detail of the glovebox attached to the compustage of the microscope.	57

Figure 42: scheme (left) and picture (right) of the Plexiglas sample holder designed at the JRC-KA for Raman characterization of nuclear materials. (196)	58
Figure 43: sample holder connected to the bag (left) and bag-out operation of a loaded sample holder from a glovebox at JRC-KA. (196)	59
Figure 44: Raman acquisition from a highly active sample confined inside the Plexiglas sample holder through the quartz window.	59
Figure 45: detailed scheme of the LAF system developed at the JRC-KA. (200)	61
Figure 46: Knudsen Effusion Mass Spectrometry (KEMS) and Quantitative Gas Measurement Setup (Q-GAMES) schematic setup.	62
Figure 47: Scheme of the KEMS and furnace. 1: Knudsen cell, 2: heating coil, 3: chopper, 4: lift, 5: LN2 cold trap, 6: camera, 7: mass spectrometer, 8: thermal shields, 9: revolving windows, 10: gas inlet, 11: pyrometer, 12: thermocouple. (203).....	63
Figure 48: scheme of the Q-GAMES developed at JRC-KA. All components mentioned in the text are labelled in the picture. (204).....	64
Figure 49: Example of the use of the dpa scale to compare the relative variation (from their initial value to the saturation) of different properties. The data shown in this picture are only the fit curves, and not the experimental data, proposed by the three authors respectively (Staicu et al. (96) for thermal diffusivity, Rondinella et al. (144) for the hardness and Wiss et al. (88) for the lattice parameter). These were however not the only data taken into account during the dpa range assessment.....	68
Figure 50: pre-calcination (left) and calcination (right) treatments. Apart from the 2 h under simulated air, the rest of the treatments were performed respectively under inert (Ar) and reducing (Ar-4%H ₂) atmospheres.	72
Figure 51: comparison among the sintering behaviour of the four UO ₂ powders tested. In Figure 51-A the piston displacement is plotted, but the sintering range might be better identified in Figure 51-B where the speed is plotted.	79
Figure 52: SPS behaviour of the ThO ₂ powder. The small displacement ongoing during the dwell time at 1600°C indicates that full densification has not yet been achieved at this temperature.	82
Figure 53: HP – SPS treatment applied to the ThO ₂ powders for the realization of the nanograined pellet. The load/unload cycles helped breaking the powder agglomerates. The treatment was stopped as soon as the piston displacement was exhausted at 915°C.	83
Figure 54: HP – SPS treatment applied to the ThO ₂ powders for the realization of the micrograined pellet. In this case, no load/unload cycle was foreseen. On the contrary, more attention was put on the release of the pressure, which was done at 1200°C in an attempt to improve the mechanical stability of the final disk. Notably, the sintering is exhausted around 900°C also in this case, followed by a long part of thermal expansion.	84
Figure 55: SE overview on the fracture surface of the 10 wt % Pu sample.	87
Figure 56: SE overview on the fracture surface of the 2.5 wt % Pu sample	88
Figure 57: EDX in four different points of the fracture surface of the 10 wt % Pu sample observed at the SEM	88
Figure 58: detail of the regions of interest of the EDX scanning in the 10 wt % Pu-doped sample.	89
Figure 59: higher magnification images of three different zones of the fracture surface of the 2.5 wt % Pu-doped sample. The different zones are the same as marked A, B and C in Figure 56.	89
Figure 60: comparison of the four powders tested for the production of nanograined UO ₂ pellets. A-B hydrolysis; C-D sol-gel; E-F oxalate thermal conversion; G-H oxalate hydrothermal conversion. The	

last row of pictures defines what has been labelled as agglomerate and primary/secondary particle in the text.....	91
Figure 61: SE images of the fracture surfaces of the four disks obtained by sintering the powders shown in 4.2.2.1 under the same conditions (70 MPa, vacuum, 200°C/min) and interrupting the treatment as soon as densification was achieved.....	92
Figure 62: SE images of the fracture surfaces of the UO ₂ samples sintered with different SPS treatments. A-B high temperature (70 MPa - 1600°C) SPS, C-D low temperature (70 MPa - 700°C) SPS, E-F two-step (70 MPa - 650-550°C) SPS, G-H high pressure (500 MPa - 700°C) SPS.....	94
Figure 63: SE images of the fracture surfaces of the HP – SPS sample before (A) and after (B) annealing at 600 °C under Ar-H ₂ for 2h.	95
Figure 64: XRD patterns of the 2.5 and 10 wt % Pu samples.....	95
Figure 65: Vegard law for the lattice parameter of solid solutions (such as UO ₂ -PuO ₂) and experimental points from this work, Elorrieta et al (223) and Lyon and Baily (224).....	96
Figure 66: effect of the annealing treatment on the HP – SPS sample (A), and on the HT – SPS sample (B) for comparison. The HP – SPS sample undergoes significant reduction (peak shift) and microstrain relaxation (peak breadth decrease).....	99
Figure 67: TEM image (A) and diffraction pattern (B) of a freshly annealed 10 wt % Pu-doped UO ₂ sample. The annealing of the sample resulted in a damage-free sample.	99
Figure 68: nanograined UO ₂ FIB lamella STEM overview (A), microstructure as seen from TEM (B – C) and diffraction pattern (D).....	100
Figure 69: T _{2g} and defect bands of the two different compositions.....	101
Figure 70: linear dependence of the ω^2 of the T _{2g} mode on the Pu content. Considering the harmonic oscillator approximation, the oxygen oscillation frequency is related to the M-O bond stiffness as $\omega^2 = K/M$. The elastic constant K, i.e. the bond stiffness, increases linearly with the Pu content. Data from Elorrieta et al (223) and Talip et al (227) are shown for comparison.	102
Figure 71: SEM images of the ThO ₂ powders derived by hydroxide hydrothermal decomposition.	103
Figure 72: SE images of the fracture surfaces of the two HP – SPS ThO ₂ samples produced at 915 °C (A) and 1600 °C (B).....	104
Figure 73: SE higher magnification images of the fracture surface of the ThO ₂ HP – SPS samples sintered at 915 °C.....	104
Figure 74: comparison of the XRD patterns of the two HP – SPS ThO ₂ samples produced at 915 °C and 1600 °C for low (A) and high (B) angles.	105
Figure 75: TEM images of the ThO ₂ nanopowders produced by hydroxide hydrothermal decomposition	105
Figure 76: TEM images of the of the two HP – SPS ThO ₂ samples produced at 1600 °C (A) and 915 °C (B).....	106
Figure 77: TEM images of lamellas produced from nanograined (left) and micrograined (right) ThO ₂ samples.	106
Figure 78: micrograined ThO ₂ irradiated at 600 °C with 300 keV Xe ions at increasing fluences. Bubbles start being visible at 10 ¹⁶ Xe/cm ²	107
Figure 79: same regions of the He-implanted nanograined ThO ₂ sample shown in Figure 80, with part of the lined-up He bubbles highlighted in red, while in blue and yellow some of the more isolated ones.....	108
Figure 80: over and under focused TEM images of micrograined (above) and nanograined (below) ThO ₂ samples implanted with 16 keV He, 600 °C to the fluence of 10 ¹⁶ cm ⁻²	108

Figure 81: first XRD peak of both compositions. As a consequence of the radiation-induced cell swelling, the peaks shift to lower angles as the damage accumulation proceeds until about 0.4-0.6 dpa.	111
Figure 82: lattice parameter relative increase, as calculated from XRD data, as function of the dpa. The different activities, and hence the radiation damage kinetics, do not seem to have an impact on the lattice parameter swelling, which appears to depend only on the cumulated dose.	112
Figure 83: comparison of the data found in the present work with some samples previously measured at the JRC – Karlsruhe (red dots). In blue the fit curve proposed for the data derived in this work, which aims to represent a reassessment of what done in (144).	112
Figure 84: microstrain calculated with the Williamson-Hall approach for the samples of both compositions, plotted as function of the dpa.	113
Figure 85: SE images of the same point on the fracture surface of a 10 wt % sample over 550 days of storage, resulting in 0.4 dpa. No significant change in the microstructure can be detected.	114
Figure 86: SE images of the same point on the fracture surface of a 2.5 wt % sample over 550 days of storage, resulting in 0.1 dpa. No significant change in the microstructure can be detected.	115
Figure 87: SE images of the "fresh" fracture surface created after 550 days of storage, and 0.4 dpa of accumulated damage, in the 10 wt % samples. No differences with the fracture surface of the as-sintered material can be detected.	116
Figure 88: evolution of the Raman spectra for the 2.5 and 10 wt % samples over 583 days of ageing, resulting in 0.077 and 0.307 dpa respectively. As the damage accumulation proceeds, the T_{2g} peak becomes asymmetric and the defects triple band increases in intensity and broadens.	116
Figure 89: A: T_{2g} apparent relative shift as function of the dpa for both compositions. B: ratio between the intensity of the low-wavenumber dispersed component and T_{2g} . Both trends seem so show dependence on the dpa and not on the activity of the samples.	117
Figure 90: T_{2g} integrated area increase as function of dpa (A) and days (B)	117
Figure 91: thermal conductivity of the 2.5 wt % Pu-doped UO_2 and phonon mean free path over dpa and time (days). The thermal conductivity was measured at 550 K and corrected for 95 % TD, for sake of consistency with the literature.	118
Figure 92: thermal conductivity (at 550 K and corrected for 95 % TD) degradation and microstrain evolution as function of the dose. Both trend decrease more steeply before about 0.0025 dpa, and successively they proceed more slowly towards the final saturation. The days scale reported on the top x axis is referred to the 2.5 % composition.	119
Figure 93: TEM picture of a 2.5 wt % sample aged 170 days (0.031 dpa). This ageing time corresponds roughly to the saturation time for the thermal conductivity decrease.	120
Figure 94: TEM picture of a 10 wt % sample aged 100 days (0.073 dpa).	120
Figure 95: the same sample pictured in Figure 94, observed again after additional 50 and 150 days of storage (150 and 250 days in total), having cumulated a dose of 0.109 and 0.182 dpa.	121
Figure 96: dislocation loops families visible on the 10 wt % doped sample after 100 days (0.73 dpa) for different tilting angles.	121
Figure 97: dislocation loop annealing under the TEM beam, observed in a 10 wt % sample aged 100 days (0.073 dpa).	122
Figure 98: 10 wt % sample crashed after 450 days of ageing, and 0.328 dpa accumulated.	122
Figure 99: Over and under focused images of the 10 wt % sample stored 450 days (0.328 dpa) showing He bubbles.	123

Figure 100: He release while heating a 10 wt % sample up to 2300 K as measured by KEMS (left) and Q-GAMES (right).....	123
Figure 101: He release obtained in this work compared with the KEMS curves of infused polycrystalline UO ₂ (149,235), ²³⁸ Pu-doped UO ₂ (150) and irradiated MOX fuel (238) previously measured at JRC-KA. The MS signal on the y axis is only relative to the present work data, the others had to be rescaled in order to be all presented in the same plot.	124
Figure 102: A) and B) post-treatment TEM; C) annealed 10 wt % from Section 4.4.1.	125
Figure 103: DSC plot of the 2.5 and 10 wt % samples after 450 days of ageing, having cumulated respectively 0.082 and 0.328 dpa. The curve presented is the difference of the descending and ascending curves, obtained at a 15 K/min rate, which (taken into account self-heating of the sample) have the same slope.	126
Figure 104: DSC data of the 10 wt % sample used in this work together with the data collected over the years from similar samples at the JRC-Karlsruhe (partially included in (96)).	127
Figure 105: low temperature heat capacity of (U,Pu)O ₂ 2.5 wt %, together with the curve for PuO ₂ obtained by Flotow <i>et al.</i> (242) and UO ₂ measured at JRC.....	130
Figure 106: variations of peak height (a), position (hence Neel temperature – b) and excess entropy of the peak (c) as a function of time and accumulated dose.....	131

List of tables

Table 1: sintering equations as summarised by Rahaman (13) from the work of different authors.(21–24) In the initial stage equations, * denotes nondensifying mechanism, i.e., shrinkage $\Delta L/L_0 = 0$. The terms in the equations are: D_s , D_l , D_{gb} , diffusion coefficients for surface, lattice, and grain boundary diffusion; δ_s , δ_{gb} , thickness for surface and grain boundary diffusion; γ_{sv} , specific surface energy; p_0 , vapor pressure over a flat surface; m , mass of atom; k , Boltzmann constant; T , absolute temperature; η , viscosity; a , particle radius; X , neck radius. For the intermediate and final stage(21): p_a , the hydrostatic component of the applied stress; ϕ , geometrical factor (stress intensification factor, for round pores $\phi = 1 / \rho$); A , constant depending on the geometrical model; G , grain size; m , exponent depending on the mechanism of diffusion; α , constant depending on the geometry of the pore.....	12
Table 2: mobility of grain boundary and pores. (30) D_s , D_l and D_g are the surface, lattice and vapour transport diffusion coefficients respectively; r is the pore size; f is a correlation factor; k is the Boltzmann constant; d_s and d_g are the densities in the solid or gas phase of the rate-controlling species and Ω is their atomic volume.	15
Table 3: irradiation conditions of the Xe and He ion implantations on UO_2 and ThO_2	53
Table 4: batches of samples produced for each composition.	72
Table 5: summary of the powders produced and their key features: crystallite size and deviation from stoichiometry. The shape and size of the agglomerates will be discussed in chapter 4. ^(w) and ^(e) in the hydrolysis powder line indicate the powder washed respectively with water and acetone-ethanol.....	78
Table 6: sintering conditions applied to each powder. 250-300 mg of powder were placed in a 6 mm diameter die and pre-pressed with 0.5 kN (17 MPa). Before the start of the thermal treatment, the force was raised to 2 kN (70 MPa) and held until the end of the cooling. Every treatment was done entirely under vacuum and with a 200 °C/min rate for heating and cooling.	79
Table 7: 2S – SPS temperatures tested. Each sintering was done under vacuum, in 6 mm diameter dies with an applied pressure of 70 MPa, with a dwell time of 3 s at T_1 and 100 min at T_2 . Heating and cooling were done at 200 °C/min, and the pressure was loaded and unloaded at room temperature.	80
Table 8: HP – SPS temperatures, heating rates and dwell times tried. Each treatment was performed under vacuum and with an applied pressure of 500 MPa, loaded and unloaded during a 4 min dwell at 250 °C.....	80
Table 9: calcination conditions tried on the UO_{2+x} samples resulting from incomplete reduction of the powders during 2S – SPS and HP – SPS treatments.	80
Table 10: sintering conditions of the ThO_2 samples produced in HP – SPS.....	83
Table 11: examples of geometrical densities of some of the produced samples. Geometrical density was measured on the samples which exhibited a regular geometry. Average = 94.7 ± 0.7 % TD.	86
Table 12: sintering conditions for having dense (≥ 95 %TD) UO_2 disks while minimising the grain growth. HP – SPS at 650 °C with 50 °C/min heating rate is also effective but does not reduce further the final grain size. All treatments were performed under vacuum.	87
Table 13: main characteristics of the powders tested in SPS. Before sintering the powders were pre-pressed at 17 MPa and thermal treatments were performed in vacuum, with an applied pressure of 70 MPa and heating and cooling rate of 200 °C/min.....	92

Table 14: sintering conditions applied to produce the four microstructures shown in Figure 62. Before sintering the powder was pre-pressed at 17 MPa and every treatment was performed under vacuum. LT – SPS are the same sintering conditions used during the powders	93
Table 15: refined lattice parameters, values predicted by the Vegard, and microstrain of the samples.	96
Table 16: O/M of the powders sintered in SPS, sintering temperature and O/M of the resulting final pellet. In every treatment the powder was pre-pressed at 17 MPa and sintered with an applied pressure of 70 MPa, under vacuum. The treatments were all stopped as soon as densification was completed, to avoid grain growth.	97
Table 17: initial O/M of the powders, sintering conditions, and final O/M and microstrain of the sintered material. All the samples were sintered in vacuum. The powders were pre-pressed with 17 MPa and then sintered under 70 MPa in HT, LT and 2s – SPS, and 500 MPa in HP – SPS.....	98
Table 18: O/M of the sintered samples, annealing conditions, and final O/M and microstrain of the annealed samples.	98
Table 19: measured values of the thermal diffusivity α at the reported temperatures and with the calculated values for specific heat capacity, real measured density corrected for 550 K, and thermal conductivity corrected for 5 % porosity.....	103
Table 20: main sintering parameters of the ThO ₂ HP – SPS samples and resulting disks lattice parameter, micrstrain and grain size. Powder data are also shown for comparison.....	105
Table 21: 6 main peaks were identified on the apparent C_p^* curve and attributed to different defects recombination, based on the interpretation given by Staicu et al. (96).....	127

List of acronyms

2S – SPS	2-Step Spark Plasma Sintering
BWR	Boiling Water Reactor
CANDU	CANadian Deuterium Uranium
dpa	displacement per atom
DSC	Differential Scanning Calorimetry
EDX	Energy Dispersive X-Ray (analysis)
EPMA	Electron Probe MicroAnalyzer
FG	Fission Gas
FIB	Focused Ion Beam
FP	Fission Product
GCR	Gas Cooled Reactor
GEN-IV	Generation Four Reactors
HBRP	High Burnup Rim Project
HBS	High Burnup Structure
HWR	Heavy Water Reactor
HP – SPS	High-Pressure Spark Plasma Sintering
JRC	Joint Research Centre
KA	Karlsruhe
KEMS	Knudsen Effusion Mass Spectrometry
LAF	LAser Flash (analysis)
LWR	Light Water Reactor
MA	Minor Actinide
MOX	Mixed OXide (fuel)
NF	Nuclear Fuel
NR	Nuclear Reactor
PHWR	Pressurised Heavy Water Reactor
PWR	Pressurised (light) Water Reactor
SEM	Scanning Electron Microscopy
SIMFUEL	SIMulated (high-burnup nuclear) FUEL
SIMS	Secondary Ion Mass Spectrometry
SNEEL	Synergy between Nuclear and Electronic Energy Losses
SNF	Spent Nuclear Fuel
SPS	Spark Plasma Sintering
TD	Theoretical Density
TEM	Transmission Electron Microscopy
XRD	X-Ray Diffraction

1 CONTEXT OF THE STUDY

In this chapter, an overview about the context of the study is given. Section 1.1 provides a brief description of the nuclear fuel cycle, contextualising the topics of the manuscript within the field of nuclear energy production.

Section 1.2 focuses on the production of fresh nuclear fuel, describing the sintering process (Sub-section 1.2.1), which constitutes a major step in the fabrication route for nuclear fuel and also the one used in the present work. The phenomena driving this process are illustrated, with particular attention to microstructural control, one of the challenges tackled in this study. Finally, a summary on the properties of the most common nuclear fuels, UO_2 and MOX, is presented (Sub-section 1.2.2).

A supplementary effect in the fuel cycle is described in Section 1.3, where the irradiation environment experienced by the nuclear fuel is outlined. The effects of radiation on matter, and in particular on UO_2 , are overviewed together with the resulting modifications of the microstructure and macroscopical properties of the material. The hazards and complexity of studying complicated systems like spent nuclear fuels are pointed out.

Section 1.4 briefly describes some possible solutions for the study of material radiations response and spent fuel characterization. The possibilities offered by SIMFUEL, α -doping and ion implantation were reviewed through a list of recent experiments.

Finally, section 1.5 summarises the content of the chapter and delineates the outline of the work.

1.1 Nuclear energy

32 countries worldwide rely on a total of 448 reactors to partially power up their economies. (1) Consistently with the world energetic demands, these numbers, although subject to many factors, are foreseen to steadily increase in the coming years. (2) Nuclear waste, which was already amounting to about 3676000 tons as of December 2013 (3), will hence constitute an increasing issue in the long term future. Nuclear energy production represents a very articulated topic, touching different fields from nuclear physics to material science, as well as addressing increasingly advanced engineering challenges.

1.1.1 Nuclear energy production

Nuclear reactors are based on several different designs and concepts, although they all share a common and relatively simple working principle. The heat produced by nuclear fission is removed by means of a fluid in a heat exchanger and (more or less directly) used to produce steam and drive turbines for electricity generation. In order to result in energy production, the nuclear fission reactions occurring in a reactor have to self-sustain.

The differences in the types of reactors lie in the fuel composition, the material used to moderate the fission chain-reaction and the types of fluids used for heat removal from the fissioning fuel. In Europe, the most popular concept (87 % of the installed reactors) is the Light Water Reactor (LWR) where enriched uranium dioxide is used as fuel and normal water provides the functions of both moderator and coolant.(4) Other concepts are the Heavy Water Reactors (HWR), Gas Cooled

Reactors (GCR), and Light Water Graphite Moderated Reactors (LWGR). Some reactors, like the Pressurised Heavy Water Reactors (PHWR) CANDU, can operate using natural or low enriched UO_2 .

1.1.2 Light Water Reactors (LWR)

LWRs are divided into two types: Boiling Water Reactors (BWRs) and Pressurised Water Reactors (PWRs). These two concepts share fuel type, moderator and heat conversion into electricity, but differ in the design of the heat exchanger circuit. In BWRs, the water moderating the fission chain reaction is the same that boils to steam and is conveyed to drive the turbines; in PWRs instead, an intermediate circuit is foreseen, so that the water used as a moderator transfers its heat to a secondary water cycle, which is the one that becomes steam and leads the turbines to generate power. A scheme of BWR and PWR is shown in Figure 1. (5)

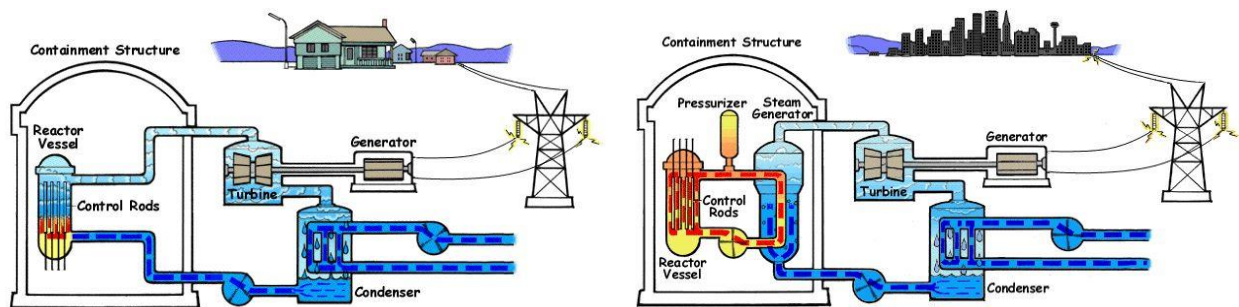


Figure 1: scheme of a BWR (left) and PWR (right). While in the BWR the water used to cool down the core is directly used for steam generation, in PWR the heat is transferred to a secondary loop. (5)

1.1.3 LWR fuel

As mentioned in the previous two sub-sections, the type of fuel used in BWRs and PWRs is the same. Small cylinders (*pellets*, with 8.19 or 10.57 mm of diameter for PWR and BWR respectively) of UO_2 , enriched up to 5 % of the fissile ^{235}U isotope, are piled up in metal rods which are then bundled together in fuel rods assemblies. These assemblies altogether are the fuel elements which are placed in the reactor pool/core. The enrichment from the natural value of 0.7 % ^{235}U to 5 % is needed to make the chain reaction self-sustaining with the use of light water as moderator.

1.1.4 UO_2 fuel fabrication

The way to go from the rough material to the final enriched UO_2 fuel pellet is quite long and complex. Uranium is mainly present in nature as Pitchblende ($\text{U}_2\text{O}_5 \cdot \text{UO}_3$ or U_3O_8) or Uraninite (UO_2) minerals, and can be extracted by different routes: mining (in open pit or underground) and *in-situ* leaching (also called solution mining). Around the world, the largest producers of U are Kazakhstan, Canada, Australia and Namibia.(6) The product of mining and milling (a leaching step devoted to separating the uranium from the rest of the ore) is a yellow powder commonly called "yellowcake".

In order to be enriched, uranium is converted to a gaseous form, such as UF_6 which is gaseous at relatively low temperatures (but still solid at room temperature). The yellowcake is then first converted into UO_2 , and then into UF_6 in dedicated conversion plants. Enrichment can be performed in several ways, but the two generic commercial methods are gas diffusion and by gas centrifuges. Enriched UF_6 is then stored in solid form inside steel cylinders and shipped to the fuel fabrication facilities. The successive steps towards the final UO_2 product are schematised in Figure 2. (7)

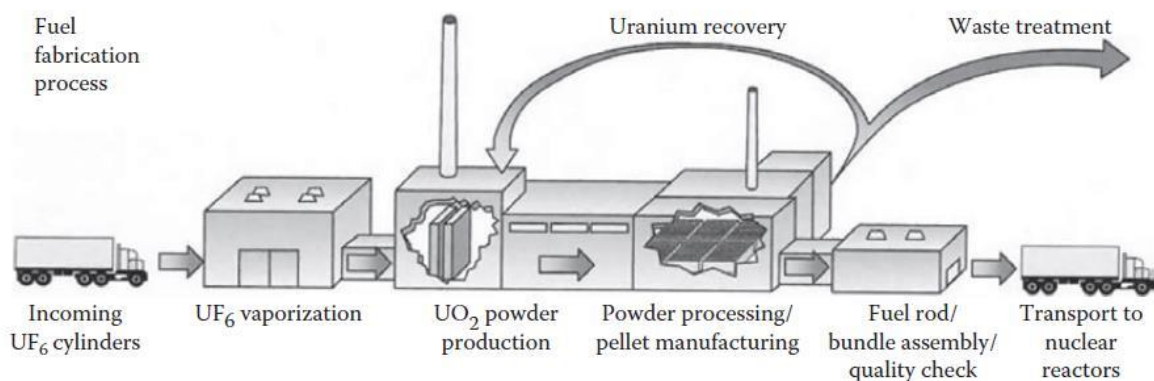


Figure 2: Scheme of the UO_2 fuel fabrication process from the enriched UF_6 . (7)

In order to be processed, uranium is converted from UF_6 back to UO_2 , in a process which involves two main steps. First, UF_6 is vaporised and hydrolysed with steam to form UO_2F_2 powder. Then, this powder gets defluorinated with additional steam and reduced to UO_2 by using H_2 in a rotary kiln.

Before being used to press and sinter pellets, the powder undergoes a series of treatments to make the process easier and grant a better final product, such as homogenization, blending, precompaction and granulation, and spheroidization and lubrication. The optimised UO_2 powder is pressed into green pellets and sintered in reducing atmosphere at temperatures around 1750°C to achieve high density. The sintered pellets (Figure 3 (7)) are then ground to match very precise dimensional requirements, and carefully inspected before being moved to storage facilities.

Finally, pellets are placed inside fuel rods, which are filled up with 10 atm of He before being sealed by welding. Fuel rods are then bundled together to form fuel rod assemblies, where every single rod is traceable by means of a unique code permanently printed during fabrication, which allows traceability even after reactor operations.



Figure 3: typical commercial fuel pellet. (6)

1.1.5 Spent Nuclear Fuel (SNF)

After reactor use, the spent fuel has very different composition and properties with respect to fresh fuel. Although the majority of the Spent Nuclear Fuel (SNF) is still constituted of unfissioned U, a significant quantity of fission products (FP) are embedded in the matrix, together with a smaller quantity of transuranic elements (*minor actinides*, MA) produced by neutron capture and subsequent β decay from U. The high activity of these FP and MA, together with the biological compatibility of some, makes them represent the biggest hazard to life forms.

At the moment of writing, the most popular solution for the disposal of SNF foresees an interim storage after reactor discharge followed by deep geological disposal. In the long term, due to the long half-life of the α -emitting MA, the activity of SNF will be dominated by α -radiation (Figure 4 (8)), which strongly affects the thermal and mechanical properties of the material. A deep and complete understanding of the magnitude of these changes is crucial to predict the long term behaviour of the SNF, and to license the proposed disposal options.

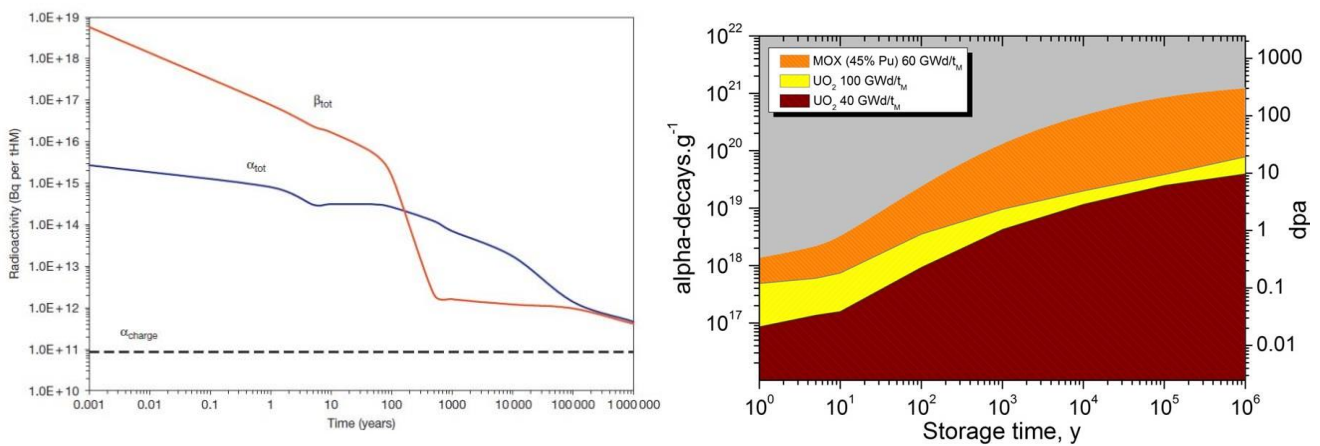


Figure 4: left: long-term dominance of α -activity in SNF.(8) right: cumulated α -dose over time for different types of SNF (for dpa definition see 1.3.1; for burnup definition see 1.3.3).

Another approach to lower the long-term impact of SNF is to reprocess the MA present in the UO_2 matrix to produce new Mixed Oxide Fuel (MOX) to be used in the so-called Generation IV Fast Reactors (Gen-IV FR). These reactors, which are still in the design phase, would be able to produce energy and at the same time reduce the amount of nuclear waste, representing a big step towards a closed nuclear fuel cycle. This strategy is currently the one adopted by most of the states with the largest nuclear programmes, such as France, China, Japan, the Russian Federation and the United Kingdom (3). Again, a comprehensive understanding of the behaviour of MOX fuel before, during, and after irradiation is crucial for the licensing process of these new reactor designs.

1.1.6 Context of the study

The study of real SNF is hence very challenging, due to its hazardous nature and its complexity, as microstructural, chemical and radiation-related effects overlap and compete. For these reasons, separate-effect studies have been set up to decrease the complexity of the problem and decouple these effects from each other. In the present work, the impact of internal interfaces on radiation damage resistance and fission gases accumulation was investigated in a double approach. As it will be shown in the following parts of the chapter, grain boundaries play a fundamental role in several aspects of radiation resistance and fission gas retention in the NF matrix. This has important

practical implications, since during operation, at the rim of the NF, a structure characterised by sub-micrometric grains develops (which will be explained more in detail in Section 1.3.3).

The modifications on the SNF behaviour were studied by accelerated ageing of natural UO_2 doped with α -emitting ^{238}Pu . In this way, we expect to be able to carry on a detailed study the effect of α -radiation on the microstructure and the thermophysical properties of SNF matrix without the complication of chemical composition (given by FP and MA), porosity and grain size.

In a second stage, we aimed to introduce the second variable in the system, by studying the grain-size effect on the above-mentioned behaviour. Due to technical limitations, it was not possible to synthesise ^{238}Pu -doped UO_2 with very small grain sizes, so the α -damage was also induced by means of He-implantation using ion beams on UO_2 samples of different microstructures.

Finally, a wrap-up and comparison of the observed phenomena provides valuable data for the modelling of long-term behaviour of spent nuclear fuel. In some areas of common interest, results were also contributing to the H2020 INSPYRE project for licensing of Gen-IV MOX fuel. (9,10)

1.2 Sintering of UO_2

The fabrication of UO_2 pellets starting from powders is a process that has been developed and optimised over several decades. Nowadays, the requirements for NF used in nuclear reactors are very precise and tolerances are very strict. The industrial process has been optimised and is now extremely reliable (less than 1 failure per 10000 fuel assemblies produced).(11) However, when trying to synthesise innovative or out-of-ordinary UO_2 compounds, a deep knowledge of the sintering mechanisms in general, and more in detail of UO_2 sintering behaviour, must be achieved prior to the treatment execution.

1.2.1 Sintering

Sintering is a thermal treatment that has been used for thousands of years (12) to transform powders of different nature, already formed at the required shape, into a useful dense body. In more recent times, sintering has become an increasingly controlled process, resulting into the development of theory and practice of sintering of metals and ceramics. Processing conditions can now be tuned, based on experimental evidences and/or theoretical models, to achieve the desired final microstructure of the densified material.

Given the nature of UO_2 , the focus in this chapter will be centred on the specific sintering behaviour of ceramics, although most of the principles can be extended to metals.

1.2.1.1 Densification

The main effect taking place during sintering is densification. Thanks to this process, a porous pressed powder compact (the *green body*) gradually transforms into a dense bulk solid. *Theoretical density* (TD) is the density of the ideal compacted material without residual porosity, and the densification degree of a sintering powder is commonly given in terms of *relative density* (% TD).

1.2.1.1.1 The driving force for sintering

Just like every other irreversible process, sintering is related with lowering of the Gibbs free energy of the system. The Gibbs free energy of a powder system can be decreased by elimination of the internal surfaces. That constitutes the *driving force for sintering*, and it can be achieved mainly

through three processes: the decrease of the particle surface curvature, the application of an external pressure, and a chemical reaction. This last process is however very rarely used, as it does not allow a good control on the microstructure of the final product.

In a very simple approach, considering only non-porous particles and no grain boundaries in the densified material (such as in the case of glass), the energy E_s of a fixed amount (1 mole) of material as a function of the size of its constituent particles can be derived as: (13)

$$E_s = 3 \frac{\gamma_{sv} V_m}{a} \quad (1)$$

Where γ_{sv} is the specific surface energy of the particles (at the solid vapour interface), V_m is the molar volume of the material and a is the particles radius. Increasing the size of the particles (and therefore decreasing their number) in the system leads to a decrease of the free energy. It is also worth noting that a system constituted of smaller initial particles has a higher driving force for sintering.

If an external pressure is applied during a considerable part of the heat treatment, it will provide extra driving force for densification, that may be significantly higher than the one provided by the reduction surface curvature. (14)

1.2.1.1.2 Diffusion in crystalline solids

The transition from powder to dense material is intrinsically related to the transport of atoms within the material. (15) Diffusion is the process by which matter flows from one place to another as a result of atomic motion in solids, driven by the gradient of chemical potential. (16)

A simple model for diffusion in a system without accounting for defects and crystal structure is the one described by the first and the second Fick equations:

$$J = -D \frac{\partial C}{\partial x} \quad (2)$$

$$\frac{\partial C}{\partial t} = D \frac{\partial^2 C}{\partial x^2} \quad (3)$$

Where J is the atoms flux [$1 / m^2 s$], C is the concentration [mol / m^3], x the space coordinate [m] and D is the diffusivity (or diffusion coefficient) [m^2 / s], which depends on temperature and on chemical composition. In the cases where D does not depend on x , analytic solutions of these equations can be derived for simple geometries and boundary conditions.

At an atomic level, diffusion can be imagined as the random hopping of an atom from one position to the next one. This process involves the overcoming of a higher energy barrier separating the two more energetically favourable atomic sites. The diffusion coefficient can then be expressed as:

$$D = D_0 e^{(-\frac{Q}{RT})} \quad (4)$$

Where Q is the activation energy per mole [J / mol], R is the gas constant ($N_a \cdot k$, in $J / K mol$) and T is the temperature [K]. This formulation evidences the exponential temperature-dependence of the

diffusivity, with $D_0 \approx v \cdot l^2$ (v is the vibration frequency of the atoms constituting the lattice, and l is the lattice interplanar distance).

In real solids however, the diffusion process is favoured by the presence of defects, resulting in values of D_0 several orders of magnitude higher than in an ideal lattice. (17) Two factors enhancing the diffusion in solids, and therefore favouring the sintering process, are then the temperature and the concentration of defects in the lattice (which can be a function of the temperature, but also of the surrounding atmosphere, and of the material composition).

1.2.1.1.3 Defects in crystalline solids

Defects are intrinsically present in crystals because of the non-ideal stacking of atoms in the lattice.

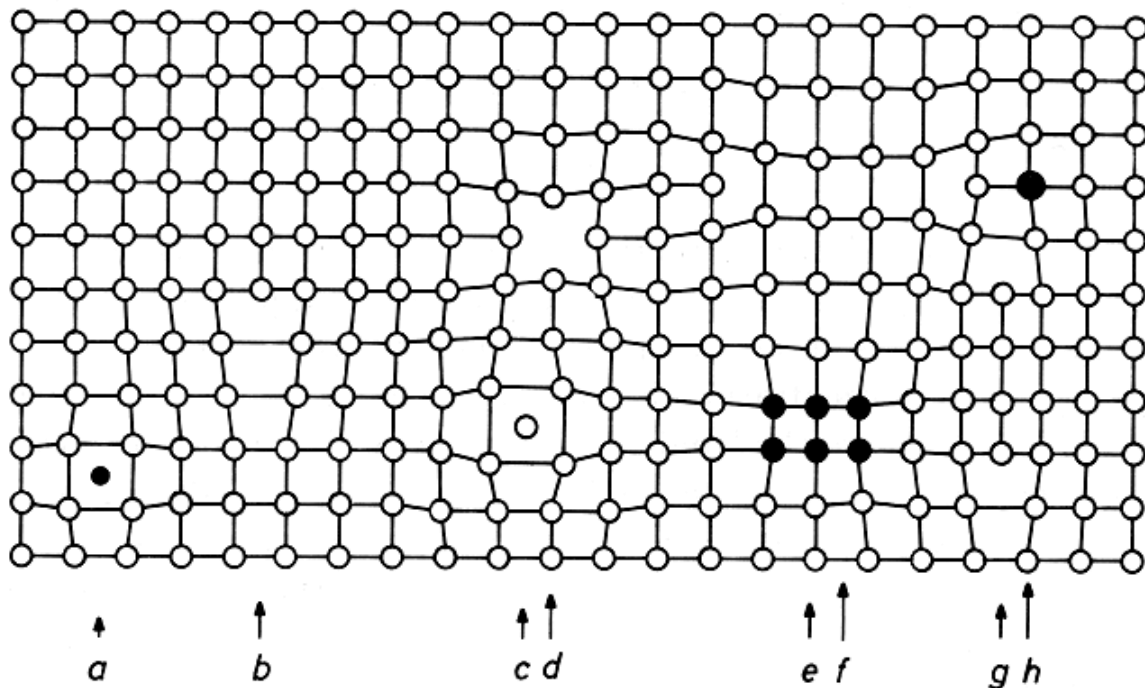


Figure 5: Defects in crystalline solids: a) interstitial impurity; b) edge dislocation; c) self-interstitial; d) vacancy; e) precipitate; f) vacancy dislocation loop; g) interstitial dislocation loop; h) substitutional impurity. (18)

Figure 5 (18) shows a 2D representation of possible crystallographic defects.

Defects can be classified according to their dimension:

- Point defects (0 dimensions): they involve one lattice position and influence its immediate vicinities. A missing atom from a lattice position is called vacancy, while an atom standing outside lattice positions is called interstitial. These two types of point defects are called *intrinsic*, and a small concentration of them is actually thermodynamically favoured in the crystals at temperatures other than 0 K.

Foreign atoms can also be included in the lattice, constituting an *extrinsic* defect in the matrix crystal. These impurities (or dopants, if introduced voluntarily) can be substitutional, if they replace an atom of the original lattice, or interstitial, if they occupy intermediate lattice spaces.

In ionic solids, point defects cannot be generated independently one from another. Mass, electroneutrality and stoichiometry of the material are indeed conserved during defects generation. For these reasons, vacancies and interstitials are organised in Frenkel or Schottky defects, exemplified in Figure 6. Essentially, when a vacancy is compensated by an analogue interstitial atom, the combination of the two defects is called a Frenkel pair; while when the vacancy is balanced by one or more vacancies of the oppositely charged ion, the assembly is labelled as Schottky defect. More complicated arrangements and interactions of defects result into extended defects.

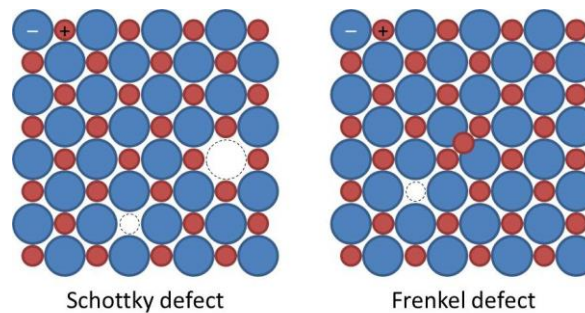


Figure 6: Schottky and Frenkel types of defects. In both cases, the charge neutrality of the solid is preserved: in the first case, one ion vacancy is compensated by a vacancy of the opposite ion; in the second case, by a self-interstitial.

- Line defects (1 dimension): they are also called dislocations, and are displacement in the periodic structure of the lattice in one direction, indicated by the *Burger vector* (Figure 7 (19)). Their movement plays a major role in plastic deformation of materials. Depending on the relative orientation of the Burger vector and the dislocation, they can be edge dislocations if they are perpendicular, or screw dislocations when they lie in the same direction.

In real solids, the Burger vector of a dislocation is usually lying in an intermediate direction, and the dislocation has hence a *mixed* character. Furthermore, these dislocations are generally curved due to the interactions with the rest of the matrix, up to the formation of dislocation loops. The clustering of interstitials or vacancies into loops is thermodynamically more stable than the same amount of defects individually dispersed in the matrix.

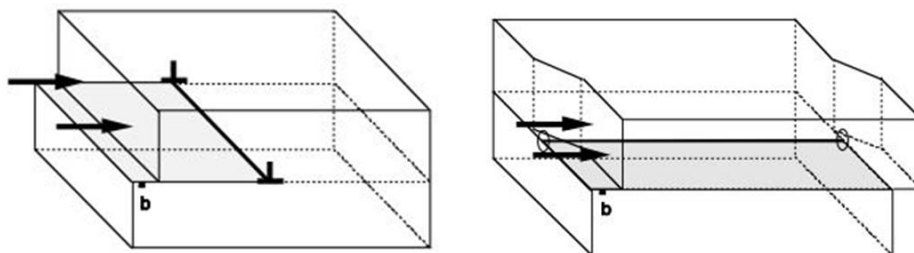


Figure 7: edge (left) and screw (right) dislocations. The upper plane is shifted of a vector b , the *Burger vector*. (19)

- Planar defects (2 dimensions): they include the crystals free surfaces, stacking faults, shear planes and the interfaces between different grains or different phases. Due to the different interactions that atoms have on grain boundaries (such as on free surfaces), these disordered regions have higher energy than the bulk of the material. As it will be shown in the next sections, this has an impact on sintering, as grain boundaries constitute another source of excess energy that the system tries to minimize.

- 3-dimensional defects: they are constituted of 3-D clusters of defects, and take their name based on whether they are made of impurities or a vacancies. A second phase within a crystal is not considered as a defect, regardless its size, but its interface with the main phase constitutes indeed a planar defect.

1.2.1.1.4 Diffusion mechanisms

According to the different types of defects involved in the diffusion process, different diffusion paths can be identified. The main diffusion path active in the system defines the preferential diffusion mechanism taking place: lattice diffusion, grain boundary diffusion, or surface diffusion. (13,17)

- Lattice diffusion is the movement of atoms through the bulk of the sample. It can be fostered by several types of defects, but vacancy mechanism and interstitial mechanism are often the dominating two; other mechanisms are interstitialcy, ring, and charge mechanisms.
- Grain boundary diffusion is due to the fact that grain boundaries are highly defective regions in polycrystalline solids. Assuming that the grain boundary width is constant, the grain boundary contribution to the total diffusion, over a certain volume of solid, increases by decreasing the grain size (hence increasing the density of grain boundaries in the given volume).
- Surface diffusion takes place within a sub-surface layer of 0.5 – 1 nm of thickness below the free surface of the material, thanks to the (facile) movement of adatoms and the migration of vacancies (which are also present at the surface).

Due to the fewer mutual interactions of surface atoms, the activation energy for their diffusion is the lowest, while the barrier for lattice diffusion is the highest. From this, the diffusion coefficients for the three diffusion mechanisms increase, generally, in the following order: $D_s > D_{gb} > D_l$. (13)

1.2.1.1.5 Ambipolar diffusion – atoms motion in ionic solids

Most of real solids differ from the model proposed earlier for several reasons, first of all because atoms are not neutral particles. The migration of the ions in the lattice has then to fulfil both the conditions of stoichiometry and electroneutrality locally. In addition to that, the application of an external electric field, such as in Field Assisted Sintering Techniques (FAST), may also influence ion migration, interfering with the concentration effect.

It can be easily demonstrated that the resulting rate of atomic transport is determined by the slowest diffusing species. However, the faster motion of one of the two species (in oxides, generally the oxygen anion) will generate a force in the same direction of the concentration gradient, which will enhance the diffusion of the slower ion. Ambipolar diffusion is the name given to the coupled diffusion of charged species.

Combining the two concepts that were just exposed, it results that the rate-limiting process is the diffusion of the slowest species along the fastest diffusion path.

1.2.1.1.6 Sintering mechanisms

During the sintering of polycrystalline solids, atoms move along several types of paths, that define the sintering mechanisms. Six main mechanisms (13) were identified as contributing to the sintering process, although only three of them lead to densification. A summary of the six generally considered sintering mechanisms is presented in Figure 8.

Mechanisms which do not lead to densification but to neck growth, reduction of the curvature

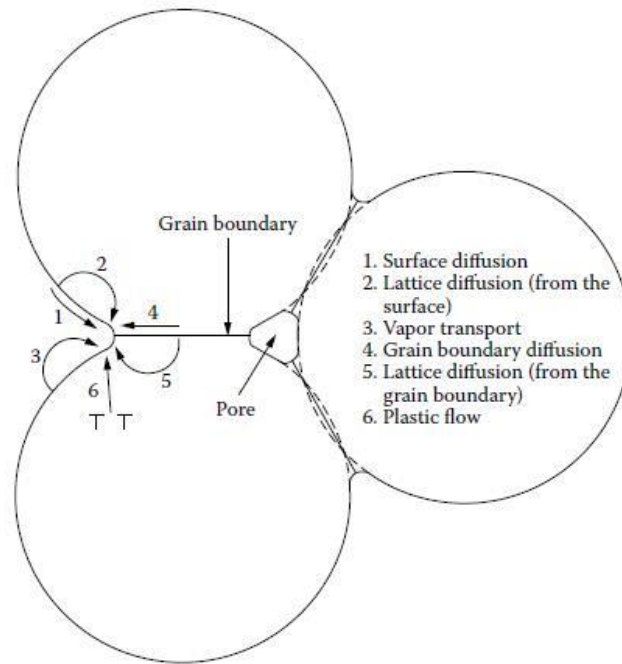


Figure 8: sintering mechanisms: 1) surface diffusion; 2) lattice diffusion from the surface; 3) vapour transport; 4) grain boundary diffusion; 5) lattice diffusion from the grain boundary; 6) plastic flow. Only mechanisms 4, 5 and 6 lead to densification, while 1, 2 and 3 lead to neck growth. (13)

radius, and specific surface energy are surface diffusion, lattice diffusion from the particle surfaces to the neck, and vapour transport (1, 2 and 3 in Figure 8). They are generally referred to as *nondensifying mechanisms*. Grain boundary diffusion and lattice diffusion from grain boundary to the pore (4 and 5 in Figure 8) are the two main densifying mechanisms in ceramics, with the latter contributing to both neck growth and densification, while plastic flow by dislocation motion is a mechanism more characteristic of metals sintering. As mentioned earlier in Section 1.2.1.1.1, the particle curvatures decrease is one of the driving forces of sintering, and since nondensifying mechanisms reduce the curvature of the neck surface without contributing to densification, they are substantially harmful for sintering.

1.2.1.1.7 Grain boundaries and porosity

Contrarily to the ideal case presented in Section 1.2.1.1.1, real solids are mostly polycrystalline, and they contain grain boundaries and pores within the densified solid. A scheme of the balance of

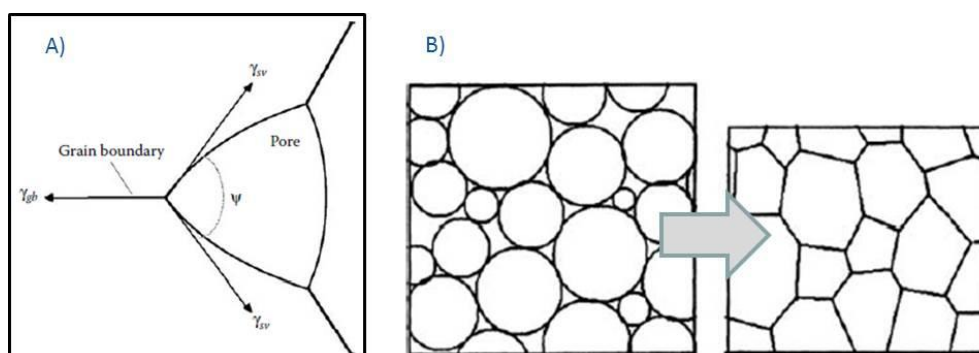


Figure 9: A) scheme of the forces balance around an ideal pore. B) Schematic densification of a powder system, with the initial particles surfaces collapsing into grain boundaries. (13)

forces around an ideal pore is shown in Figure 9-A. Each one of these forces acts tangentially to the related interface and arises from the energy increase that would be generated by an increase of the surface area.

At the equilibrium, these forces are balanced as follows:

$$\gamma_{gb} = 2\gamma_{sv} \cos\left(\frac{\psi}{2}\right) \quad (5)$$

Where γ_{sv} is the surface tension in the solid-vapour interface at the pores, and γ_{gb} is the one at the grain boundary.

While polycrystalline materials densify, part of the free energy decrease achieved by the elimination of free surfaces is taken over for the generation of grain boundaries. This makes the driving force for sintering by decrease of particles curvature somewhat lower than theoretically predicted. In a schematic case where two particle surfaces collapse into a single grain boundary, such as in the example in Figure 9-B, the energy decrease coming from densification is:

$$\Delta E_D = -A_s \left(\gamma_{sv} - \frac{\gamma_{gb}}{2} \right) \quad (6)$$

Where A_s is the total surface area of the powder. The unavailable energy:

$$\Delta E_G = -A_s \frac{\gamma_{gb}}{2} \quad (7)$$

is indeed driving the growth of the grains during densification and it represents another way by which the powder system can decrease its free energy, competing with sintering. In general, grain growth is accompanied by pore growth in a process called *coarsening*.

Due to the complexity of the whole evolution, a model which rigorously accounts for sintering, grain growth, interactions among particles and their three-dimensional arrangement does not exist yet; coarsening and sintering are therefore normally treated separately, with their interactions being analysed only in a second moment.

1.2.1.1.8 Stages of sintering

Given the complexity of the evolution of the microstructure during sintering, the use of a geometrical model for modelling the whole process allowing to relatively simply solve the mass equations is impossible (13,20). In order to try to simplify the problem, three stages of sintering are distinguished. Each one of them spans an interval of time or density where the geometry of the powder particles can be assumed to be reasonably well defined and constant. An example of the three stages, with their related geometries proposed by Coble (21), is shown in Figure 10.

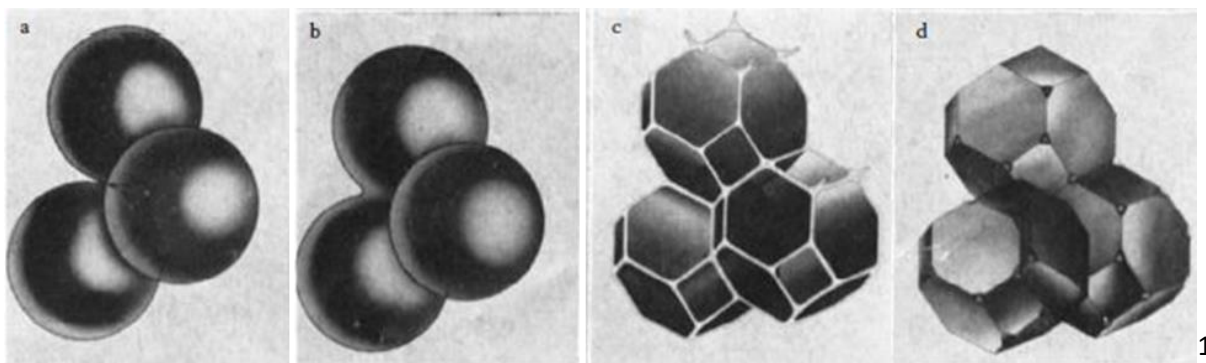


Figure 10: powder particles (a) and the three stages of sintering theorized by Coble: b) initial stage; c) intermediate stage; d) final stage. (21)

- Initial stage: density up to 65 % of the material theoretical density (TD). Neck growth is quite rapid, reaching values up to 0.4-0.5 the particles size.
- Intermediate stage: density up to 90 % TD. Pores have now reached their equilibrium shape and still constitute a continuous array around the grains, but some of them can eventually pinch off from the grain boundary and end up as isolated porosity.
- Final stage: density above 90 % TD. Progressive removal of the isolated porosity, which can be more or less successful depending on the sintered material. During this stage, microstructures may develop in a variety of different ways, so their influence on grain growth has to be taken into account (see Section 1.2.1.2).

For each one of these stages, under certain assumptions (uniform shape, size, and packing of the powders), a portion of the system can be isolated and analysed. Considering the whole powders assembly as a continuum of these elemental units, mass transport equations can be written and solved after setting the appropriate boundary conditions. However, due to the extreme simplifications needed, all the derived sintering models fail to provide an accurate quantitative description of the phenomenon; they can be used only to gain a qualitative overview of the process.

A summary of the mass transport equations reported in literature (13) for each stage is listed in Table 1. The derivation of these equations can be found in the referenced publications.

Initial stage (22–24)				
Equations	Diffusion mechanism	m	n	H
Neck growth $\left(\frac{X}{a}\right)^m = \frac{H}{a^n} t$	Surface diffusion *	7	4	$56D_s\delta_s\gamma_{sv}\Omega / kT$
	Lattice diffusion from the surface *	4	3	$20D_l\gamma_{sv}\Omega / kT$
	Vapor transport *	3	2	$3p_o\gamma_{sv}\Omega / (2\pi mkT)^{1/2}kT$
Shrinkage $\left(\frac{\Delta L}{L_0}\right)^{m/2} = -\frac{H}{2^m a^n} t$	Grain boundary diffusion	6	4	$96D_{gb}\delta_{gb}\gamma_{sv}\Omega / kT$
	Lattice diffusion from the grain boundary	5	3	$80\pi D_l\gamma_{sv}\Omega / kT$
	Viscous flow	2	1	$3\gamma_{sv} / 2\eta$
Intermediate and final stage (21)				
No external pressure $\frac{1}{\rho} \frac{d\rho}{dt} \approx A \left(\frac{D\Omega}{G^m kT} \right) \left(\frac{\alpha\gamma_{sv}}{r} \right)$		With external pressure $\frac{1}{\rho} \frac{d\rho}{dt} \approx A \left(\frac{D\Omega}{G^m kT} \right) \left(\frac{\alpha\gamma_{sv}}{r} + p_a\phi \right)$		
Mechanism	Diffusion coeff.	Intermediate stage		Final stage
Lattice diffusion	$D = D_l$	$A = 40/3; m = 2; \alpha = 1$		$A = 40/3; m = 2; \alpha = 2$
Grain boundary diffusion	$D = D_{gb}\delta_{gb}$	$A = 95/2; m = 3; \alpha = 1$		$A = 15/2; m = 3; \alpha = 2$

Table 1: sintering equations as summarised by Rahaman (13) from the work of different authors.(21–24) In the initial stage equations, * denotes nondensifying mechanism, i.e., shrinkage $\Delta L/L_o = 0$. The terms in the equations are: D_s , D_l , D_{gb} , diffusion coefficients for surface, lattice, and grain boundary diffusion; δ_s , δ_{gb} , thickness for surface and grain boundary diffusion; γ_{sv} , specific surface energy; p_o , vapor pressure over a flat surface; m , mass of atom; k , Boltzmann constant; T , absolute temperature; η , viscosity; a , particle radius; X , neck radius. For the intermediate and final stage(21): p_a , the hydrostatic component of the applied stress; ϕ , geometrical factor (stress intensification factor, for round pores $\phi = 1 / \rho$); A , constant depending on the geometrical model; G , grain size; m , exponent depending on the mechanism of diffusion; α , constant depending on the geometry of the pore.

1.2.1.2 Grain growth and coarsening

Coarsening, as mentioned earlier, is the term given to the process of grain growth coupled with pores growth. With the name grain growth instead it is usually described the increase in the grain

size of a single-phase solid, or in the matrix grain size of a solid containing a second phase (such as indeed porosity can be). It takes place in dense and non-dense solids at high temperatures, and by conservation of matter it occurs concomitantly with a decrease of the number of grains. (25)

It is worth noting that, densification is negatively affected by coarsening, as it is a second way by which the system can lower its energy by decreasing the inner interfaces. Furthermore, a coarse microstructure with larger grains and pores implies longer diffusion paths, and less sinks, for the species migrating during densifying mechanisms. Limiting coarsening is hence a key point for achieving densification with controlled microstructure.

1.2.1.2.1 The LSW model for coarsening

The coarsening of precipitated particles in a liquid or a solid is governed by the process called Ostwald ripening. Due to the higher energy resulting by their higher curvature, smaller particles tend to consume by transferring matter to the larger particles, which in turn grow bigger. Grain growth and pore growth share many features with the Ostwald ripening process, which can then be used to efficiently describe them, at least in a simplified model. Greenwood (26), Wagner (27), and Lifshitz and Slyozov (28) developed independently their theories for coarsening from the work of Ostwald, leading to the so-called LSW model. Under some assumptions, notably that the total volume (mass) of the precipitates does not change, due to mass conservation, the model provides two equations for particle coarsening based on the rate-limiting mechanism in place:

- Ostwald ripening controlled by interface reaction: when the slowest process in the mass transport from the smaller to the bigger particles is matter dissolution from the precipitate to the matrix, or matter deposition from the matrix onto the precipitate.

$$(a)^2 - (a_0)^2 = \left(\frac{\alpha_T C_0 \gamma \Omega^2}{kT} \right) t \quad (8)$$

- Ostwald ripening controlled by diffusion: when the slowest process is the diffusion of the precipitate atoms through the lattice.

$$(a)^3 - (a_0)^3 = \left(\frac{8D C_0 \gamma \Omega^2}{9kT} \right) t \quad (9)$$

Where a is the precipitate radius at time t , a_0 is the initial average precipitate radius, γ is the interface energy between precipitate and matrix, Ω is the atomic volume, C_0 is the precipitate concentration in equilibrium with a flat surface (i.e. the solubility), k is the gas constant and T is the temperature. α_T , a transfer constant of the solute to/from the matrix, and D , the diffusion coefficient of the solute in the matrix, are both strongly temperature-dependent.

1.2.1.2.2 The Brooke and Turnbull model for grain growth

A model for grain growth under the driving force of the pressure gradient across the grain boundary was derived by Brooke and Turnbull. (29) In their assumptions, the grain boundary width δ_{GB} was considered constant and the grain boundary energy isotropic and independent from the crystallographic orientation. The resulting grain size as a function of time was:

$$G^2 - G_0^2 = Kt \quad (10)$$

Where G_0 is the initial grain size, and K is a temperature-dependent factor given by:

$$K = 2\alpha\gamma_{GB}M_b \quad (11)$$

The temperature dependence is included in the factor M_b , the boundary mobility, which also depends on the diffusion coefficient D_a (for T-dependence, see Section 1.2.1.1.2) of the atoms across the grain boundary following the relation:

$$M_b = \frac{D_a}{kT} \left(\frac{\Omega}{\delta_{GB}} \right) \quad (12)$$

Where Ω is the atomic volume of the material and k the Boltzmann constant.

A more general form based on experimental observations is:

$$G^m - G_0^m = Kt \quad (13)$$

With the exponent m ranging between 2 and 4 and also depending on the temperature. The most typical value for ceramics is about 3, and its deviation from the theoretically predicted 2 was explained by the dragging effect of solutes and impurities at the grain boundary. However, also the measurements on extremely pure zone-refined metals show a deviation from this value. (13)

1.2.1.2.3 Solute drag and pores mobility

The presence of second phases in the matrix of the densifying solid has the effect of pinning the grain boundaries during their migration. The boundary mobility in these cases is reduced by a contribution depending on the solute mobility M_s :

$$M_b = \left(\frac{1}{M_b} + \frac{1}{M_s} \right)^{-1} \quad (14)$$

In the possible applications of this work, solution pinning is not a viable possibility, so we will consider only the case of pore pinning of the grain boundaries. The presence of pores at the grain boundary affects the grain mobility in a similar way to the solute drag:

$$M_{eff} = \frac{M_p M_b}{N_p M_b + M_p} \quad (15)$$

Where N_p is the number of pores along the grain surface, and M_p the pore mobility, which can be calculated based on the assumed predominant diffusion mechanisms (Figure 11), resulting in the equations proposed in Table 2. (30)

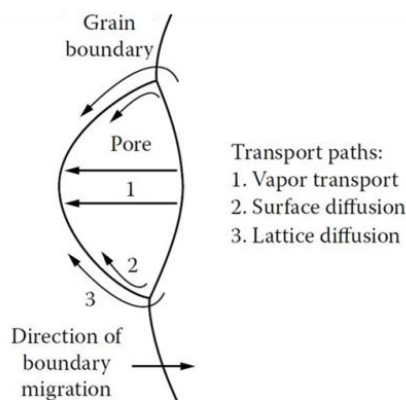


Figure 11: diffusion mechanisms responsible for pore mobility. (13)

Equations	Migration mechanism	M_p
$M_b = \frac{D_a}{kT} \left(\frac{\Omega}{\delta_{gb}} \right)$	Surface diffusion	$D_s \delta_s \Omega / kT \pi r^4$
	Lattice diffusion	$D_l \Omega / f kT \pi r^3$
	Vapor transport	$D_g d_g \Omega / 2kT d_s \pi r^3$

Table 2: mobility of grain boundary and pores. (30) D_s , D_l and D_g are the surface, lattice and vapour transport diffusion coefficients respectively; r is the pore size; f is a correlation factor; k is the Boltzmann constant; d_s and d_g are the densities in the solid or gas phase of the rate-controlling species and Ω is their atomic volume.

1.2.1.3 Microstructure control

As seen up to now, both densification and microstructural evolution of a sintering ceramic are strongly dependent on temperature, mostly through the diffusion coefficients of the different species involved. The choice of an appropriate thermal treatment, together with a correct use of the grain boundary pinning possibilities, can lead to very different final microstructures in equally dense final products.

1.2.1.3.1 Densification and coarsening in ceramic materials

A typical trend of density and grain size for ceramic materials is the one shown in Figure 12 for sintering of TiO_2 (31). During the early stages of sintering, grain growth is relatively limited. Some coarsening can however take place, through processes such as surface diffusion or vapour transport, which would in case affect the successive sintering stages. As the sintering body densifies, grain growth slowly increases, but does not become pronounced until the final stage of sintering. In general, a first region characterized by important densification with limited grain growth is followed by a second region of reduced densification and significant grain growth.

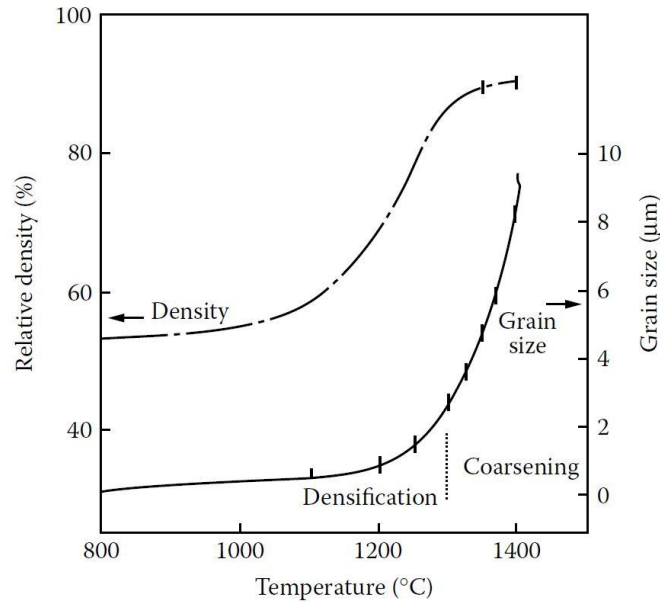


Figure 12: density and grain size as a function of increasing T during sintering of TiO_2 powders.(31)

1.2.1.3.2 Strategies for microstructural control

In the present work as in many other applications, the requirement is to achieve a high-density final product while limiting as much as possible the grain size. Some solutions can be adopted to enhance densification over grain growth during the sintering process: (13,25,31)

- Fast firing: in case of powders having significantly greater activation energy for densification rather than grain growth, a quick heating to high temperatures can improve significantly the final microstructure. An example is shown in Figure 13-A.
- Applied pressure: an alternative strategy is to lower the activation energy for densification. As discussed in Section 1.2.1.1.1, the driving force for sintering under an applied pressure is much higher than the intrinsic one due to the particle curvature. However, the application of an external pressure does not affect the grain boundary mobility. A sufficiently high applied pressure during sintering can then allow reaching very high density without suffering from excessive grain growth.

An example of the beneficial effect of fast firing and external pressure on MgO-doped Al_2O_3 sintering is shown in Figure 13-B. (13)

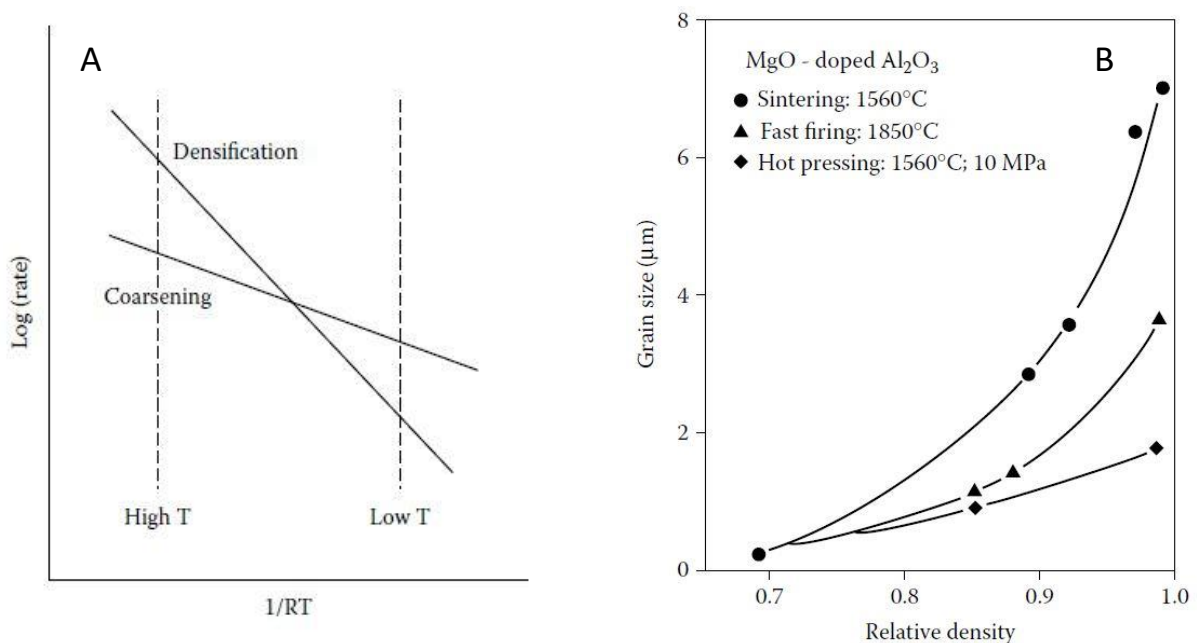


Figure 13: advantage of fast firing and external pressure. A) at high temperatures, the densification rate can overtake the coarsening rate; B) grain size as a function of the relative density during sintering of MgO-doped Al_2O_3 , showing the effect of fast firing and external pressure. (13)

Other possible strategies for enhancing densification over grain growth during sintering involve the use of dopants, fine inclusions, uniformly packed fine powders, and liquid-phase sintering. Nevertheless, for the specificities of the present work, the use of dopants or second phases cannot be taken into consideration. As it will be detailed in chapter 3, significant effort was put into lowering the size of the starting powders to improve their intrinsic sintering potential, but the optimisation of the packing factor was not tried.

In order to take advantage of fast firing and externally applied pressure, Spark Plasma Sintering was used in the present work for the densification of UO_2 with limited grain growth. As it will be discussed in the following Section, this technique involves other intrinsic advantages for the sintering of UO_2 and grain growth control.

1.2.1.4 Spark Plasma Sintering (SPS)

Spark Plasma Sintering (SPS) is a Field Assisted Sintering Technique (FAST) which involves electric field, pressure and typically high heating rates, resulting into quick and early sintering of powders. In this Section, a general description of the SPS functioning is provided, highlighting the advantages of its use for the present work, while the description of the specific device used is reported in chapter 2.

A scheme of a standard SPS setup is shown in Figure 14.(32) The powder to be sintered is loaded and pressed inside electrically conductive dies and pistons, generally made of graphite. Other materials,

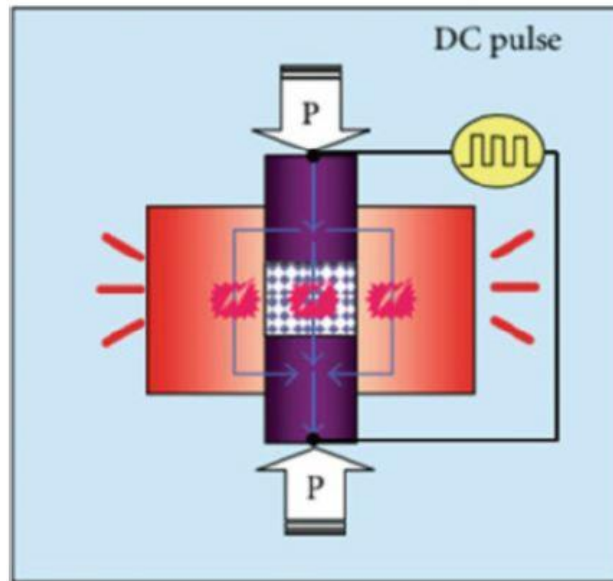


Figure 14: SPS functioning scheme.(32) The graphite die serves also as heating element, as pulsed current is fluxed through it resulting in Joule heating.

such as SiC or WC may be chosen, if the desired pressure to be applied exceeds the strength of graphite of about 100 MPa. An electric field is then applied, and heating is obtained by Joule effect of the direct pulsed current through the die-sample assembly. Electrically conductive samples will then possibly heat up also internally, but this happens only marginally in the case of semi conducting UO_2 .

In a typical SPS treatment, four stages can be identified:

- Chamber evacuation
- Pressure application
- Heating
- Cooling

The four stages are schematized in Figure 15. During the pressing stage, powders packing and porosity distribution are improved, and the constant application of pressure throughout the whole treatment activates sintering mechanisms such as plastic deformation and grain boundary sliding (33). The exact effects of the electric on the sintering process depend on the material to be sintered and are still under investigation. As already mentioned in Section 1.2.1.1.1, the external pressure plays a fundamental role in enhancing densification over grain growth during sintering.

In SPS, the advantages of externally applied pressure are combined to those of fast firing, thanks to the extremely high heating rates allowed by joule heating. The successful densification with limited grain growth by SPS has been reported for several ceramic materials, such as ZrO_2 and CeO_2 (34), Al_2O_3 (35), Y_2O_3 (36), MgO (37) and also more recently UO_2 (38–41).

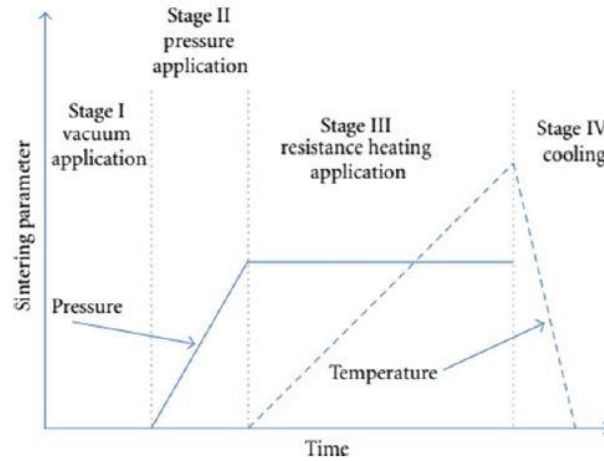


Figure 15: scheme of a typical SPS thermal treatment. I) chamber evacuation; II) pressure application; III) heating; IV) cooling.(32)

1.2.2 Sintered UO_2 for nuclear energy production

The sintered UO_2 pellets resulting from the fabrication process are carefully inspected to make sure these pellets fit strict geometry and composition requirements. Indeed, some of the relevant properties for reactor use of UO_2 strongly depend on a series of microstructural features. The fulfilment of the geometry and composition requirements is fundamental to guarantee the good performances of NF during irradiation, and therefore the safety of the reactor operation. (42,43)

The heat removal from the fuel assembly is crucial, both for power generation and for safety issues, in order to avoid core meltdown. For this reason, particular attention is put on the fuel features that affect the thermal conductivity properties of the fuel itself and of the fuel assembly in general.

1.2.2.1 Requirements of NF

1.2.2.1.1 Density and porosity

Density and porosity are key parameters controlling many materials properties. In the case of UO_2 pellets for power generation, complete densification to 100 % TD of the powders during sintering is not desired. Some residual porosity is fundamental for fission gas retention. A high density is also not ideal for radiation-induced swelling accommodation (explained more in detail in Section 1.3). (11)

However, insufficient density negatively affects the thermal and mechanical properties of the fuel, in particular the thermal conductivity, that is of crucial importance for the safety of the reactor. In general, a density of 95 % TD is targeted, with the remaining 5 % of porosity being as homogeneously distributed as possible. The use of pore-formers can be needed to achieve the desired porosity fraction and size distribution after sintering.

1.2.2.1.2 Stoichiometry

The O/M ratio of the UO_2 fuel also strongly affects the materials physicochemical properties. Again, the focus is put on the thermal conductivity, which is heavily affected by even small deviations from stoichiometry (as it will be more detailed in Section 1.2.2.3). Moreover, chemical interaction with the cladding material is also strongly enhanced for hyperstoichiometric fuel.

Sintering of UO_2 is generally conducted under reducing Ar-H_2 atmosphere, yielding stoichiometric $\text{UO}_{2.00}$ final products. One of the intrinsic advantages of SPS in UO_2 processing is the natural reductive environment at temperatures above 600°C , because of the graphite components. (44) An appropriately designed SPS treatment therefore results in full reduction of hyperstoichiometric powders to $\text{UO}_{2.00}$ during densification. (45)

1.2.2.1.3 Shape and roughness

Fuel pellets presenting evident damage, such as chip or cracks, cannot be used for fuel rods fabrication. However, also the tolerances for the geometry and roughness of the pellets are very strict, to avoid undesired and potentially harmful interactions with the cladding that could lead to failure (shape) or hinder the heat transfer (roughness).

After sintering, centreless grinding is performed on the pellets, since the as-sintered material generally does not fulfil the requirements. (7)

1.2.2.2 Properties of NF - Thermophysical properties of stoichiometric UO_2

All the controls and inspections listed in the previous Section are needed to ensure the optimal state of the sintered product, resulting in a safe and predictable behaviour during irradiation. A summary of the most relevant properties of UO_2 is presented in this Section, followed by a quick discussion on the harmful effects of porosity and stoichiometry in Section 1.2.2.3.

1.2.2.2.1 Crystal structure

As shown in Figure 16 UO_2 has a cubic crystal structure, with the uranium atoms in a face centred array and the oxygen atoms occupying the tetrahedral holes. Each cation is surrounded by eight anions, that in turn are shared among four equivalent cations. Such a structure is called "fluorite", by analogy with the one of CaF_2 .

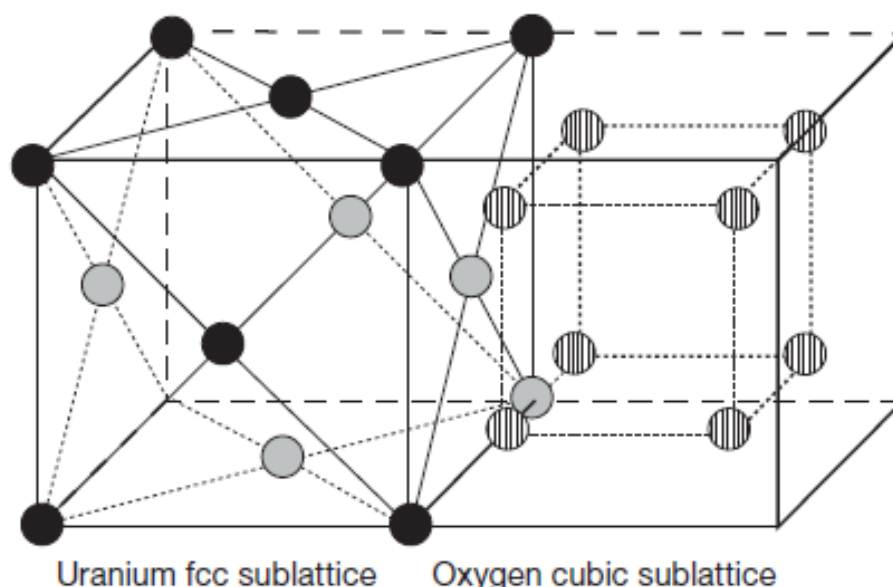


Figure 16: UO_2 fluorite (CaF_2) structure. The U lattice (black spheres) is face centred cubic, while the O lattice (grey spheres) is primitive cubic.

The lattice constant of stoichiometric UO_2 at room temperature (293 K) is 547.07 ± 0.08 pm, resulting in a theoretical density of 10.9511 ± 0.0005 g / cm^3 . (46)

1.2.2.2.2 Thermal expansion and melting point

For thermal expansion, IAEA (47) recommends the equations derived by Martin et al (48):

- For temperatures ranging from 273 to 923 K:

$$\frac{L}{L_{273}} = 0.9973 + 9.082 \cdot 10^{-6}T - 2.705 \cdot 10^{-10}T^2 + 4.391 \cdot 10^{-13}T^3 \quad (16)$$

- For temperatures going from 923 up to the melting point:

$$\frac{L}{L_{273}} = 0.99672 + 1.179 \cdot 10^{-5}T - 2.429 \cdot 10^{-9}T^2 + 1.219 \cdot 10^{-12}T^3 \quad (17)$$

The melting point was measured by Adamson et al (49) to be 3120 ± 20 K. This value was confirmed by more modern measurements and it is also the one recommended by the most recent reviews (50,51) and IAEA (47).

1.2.2.2.3 Heat capacity

The heat capacity of UO_2 presents an anomalous behaviour at high temperatures (above 2000 K) due to the formation of Frenkel-pairs in the anion sublattice, culminating in a lambda order-disorder transition at a temperature around 2670 ± 30 K. (52) Measurements of the heat capacity above this transition were performed by Ronchi et al (53) and were found to follow with relative good agreement the trend traced between room temperature and the transition temperature. The most recent formulation was provided by Konings (54) and it is valid below and above the lambda transition at 2670 ± 30 K:

$$C_p = 66.7437 + 43.1393 \cdot 10^{-3}T - 35.640 \cdot 10^{-6}T^2 + 11.655 \cdot 10^{-9}T^3 - 1.16863 \cdot 10^6 T^{-2} \quad (18)$$

Where T is the temperature in K and the resulting C_p is expressed in [J/K·mol].

1.2.2.2.4 Thermal conductivity

As already mentioned earlier, thermal conductivity has a crucial importance in the efficiency and, most importantly, the safety of a NR. Among the uranium compounds, UO_2 has a relatively poor thermal conductivity, dominated at low temperatures by phonon transport. As shown in Figure 17(51), it decreases with temperature down to a minimum around 2000 K, above which the

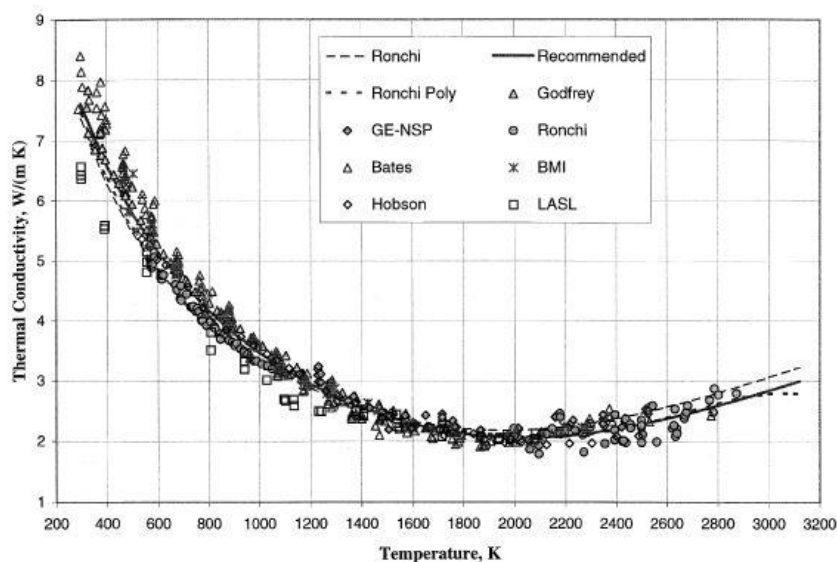


Figure 17: stoichiometric 95 % TD dense UO_2 thermal conductivity. The graph has been taken from the work of Fink et al, the references cited in the table can be found in the original publication. (51)

electronic contribution becomes significant.

The two different contributions in $\lambda = \lambda_{ph} + \lambda_{el}$ were quantified schematically by the two following equations:

$$\lambda_{ph} = \frac{1}{A + BT} \quad (19)$$

For the phonons contribution, where A is a factor representing the phonon scattering due to imperfections (stoichiometry, burnup, impurities, pores, bubbles, defects...) and B is instead responsible of the phonon-phonon interactions (Umklapp process), which are temperature-dependent.

$$\lambda_{el} = \frac{C}{T^n} e^{\left(-\frac{W}{kT}\right)} \quad (20)$$

For the electrons contribution, where k is the Boltzmann constant ($8.6144 \cdot 10^{-5}$ eV/K), n is a constant ranging between 2 and 3, and C and W are respectively $4.715 \cdot 10^9$ and 1.41, as found by Harding and Martin (55).

These two formulations are helpful to discern the different temperature dependences of the phonon and electronic contributions.

As already mentioned, pores negatively affect thermal conductivity, as they are generally filled with gas that poorly conducts heat and therefore act as thermal barriers. The value of the intrinsic thermal conductivity λ_0 of the 100 % dense material can be correct for fractional porosity P using the Schultz formula:

$$\lambda = \lambda_0 \frac{1 - P}{1 + \beta P} \quad (21)$$

The value of the constant β being unity in case of spherical porosity, such as is generally the case in UO_2 . In general, to rule out the porosity effect, in literature the thermal conductivity values are reported already corrected for a porosity of 5 % (95 % TD).

The following general formula for the thermal conductivity of 95 % dense stoichiometric UO_2 was calculated by Fink (51), based on experimental data and previous models:

$$\lambda = \frac{100}{7.5408 + 17.692t + 3.6142t^2} + \frac{6400}{t^{2/5}} e^{\frac{-16.35}{t}} \quad (22)$$

Where t is T/1000, with the temperature expressed in K.

1.2.2.3 Effect of stoichiometry

1.2.2.3.1 Crystal structure

Thanks to the wide range of oxidation states of uranium (+4, +5 and +6) and the capacity of the fluorite structure to accommodate interstitial atoms, the phase UO_{2+x} can exist over an interval of O/M ratios at room temperature (see phase diagram (56) in Figure 18). However, the introduction of oxygen atoms affects the regularity of the structure and with it the material properties.

A direct effect of the inclusion of extra atoms is the modification of the atomic structure. As the O/M increases, more and more cations are passing to the valence state +5 and +6, shrinking the reference fluorite cell following the relation proposed by Teske et al (57):

$$a = 5.4705 - 0.132x \quad (23)$$

Where x is the deviation from stoichiometry of $O/M = 2+x$ ($x \leq 0.22$).

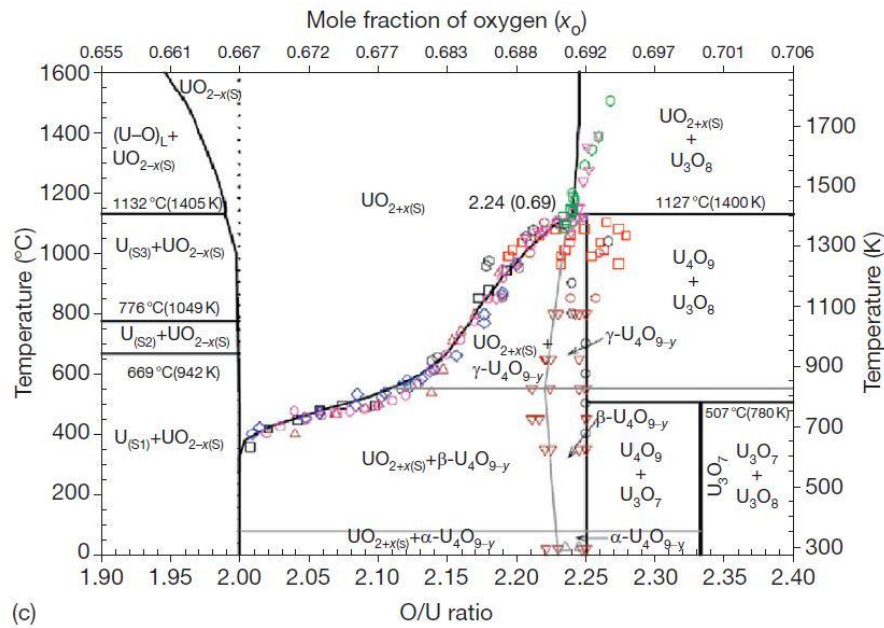


Figure 18: U-O phase diagram as proposed by Higgs et al (56) in the range O/M = 1.9 - 2.4. The references for the experimental points can be found in the related publication.

1.2.2.3.2 Diffusion and sinterability

As mentioned in Section 1.2.1.1.2, the diffusion coefficients depend on the defects in the structure. The presence of vacancies and interstitials enhances the number of atoms migrating, resulting in a significant increase of the self-diffusion coefficients already for small deviations from stoichiometry.

The plot in Figure 19, derived by Matzke (58), shows the magnitude of the self-diffusion coefficients variation in the range between UO_2 and $UO_{2.2}$. Recalling the importance of diffusion coefficients in sintering (section 1.2.1.1.8), it is straightforward to understand the much higher sinterability of hyperstoichiometric UO_2 powders. The figure suggests a massive failure of the point defect model. The discrepancy between predictions and experimental values is 3 orders of magnitude, suggesting a problem of entropy of the Schottky defects and the activation energy of the barriers. On the other hand, the x dependence is correct.

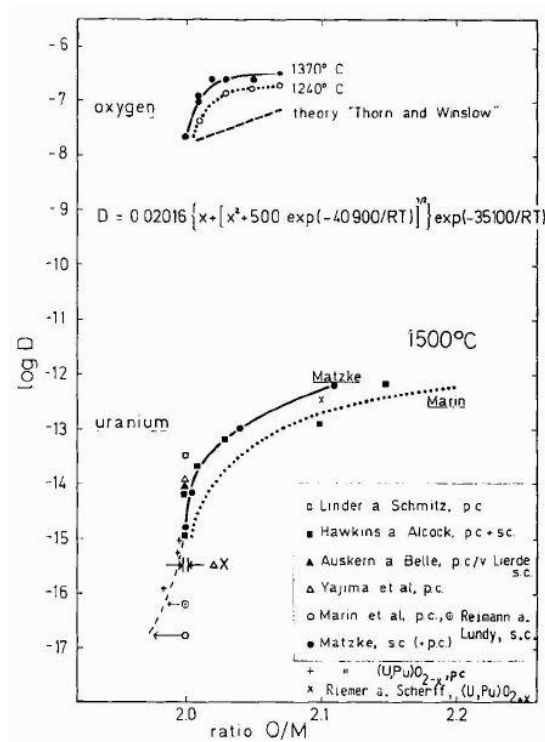


Figure 19: U and O self-diffusion coefficients in UO_{2+x} as a function of the deviation from stoichiometry. (58) The references can be found in the original publication.

1.2.2.3.3 Thermal properties

As discussed in Section 1.2.2.2.4, thermal conductivity is heavily dependent on defectivity of the lattice. Indeed, the factor A (and to a minor extent B) in equation 18 indeed is representative of the discontinuities in the lattice that hinder phonons transmission. Lucuta et al (59) found a linear dependence of this parameter with the deviation from stoichiometry x , as shown in Figure 20.

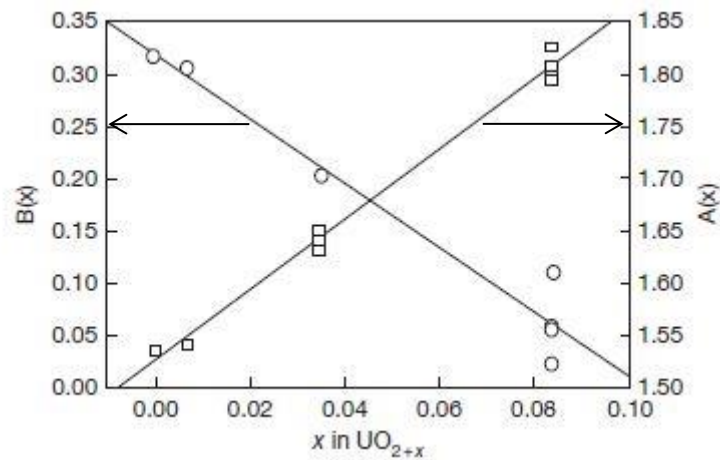


Figure 20: variation of the coefficients A and B of equation 18 as function of the variation from stoichiometry in UO_{2+x} . (59)

1.2.2.4 MOX fuel

Mixed Oxide (MOX) fuel is starting to be used in NR in some countries, both to foster a more efficient use of the uranium resources and to decrease the plutonium stock. Although not being the central point of the present work, which is focused on the UO_2 system, MOX has several contact points with this study. In the first place, the strategy adopted for the investigation of self-irradiation in the SNF UO_2 matrix practically foresees the preparation of low-Pu MOX samples (see Section 1.5). For this reason, the behaviour of the UO_2 - PuO_2 system has to be known, at least for low Pu concentrations. Secondly, since self-irradiation is present in MOX fuels also prior to irradiation, the results coming from this work can be used to increase the knowledge on post-fabrication behaviour of fresh MOX fuel.

1.2.2.4.1 Crystal structure

Unlike U, which exists as U^{4+} , U^{5+} and U^{6+} , Pu can have oxidation states from +3 to +7(60–62), meaning that the U-O-Pu ternary phase diagram is even more complex. Indeed, also due to the lack of experimental data, some regions of the phase diagram are still not completely assessed. However, for our practical case, the analysis can be limited to the mixture of the two isostructural dioxides UO_2 and PuO_2 . Stoichiometric PuO_2 has a lattice parameter of 539.54 ± 0.04 at 298 K (63), and a theoretical density of 11.46 g / cm^3 .

As it can be seen in the pseudo-binary phase diagram in Figure 21 (43), UO_2 and PuO_2 form a continuous solid solution in the hyperstoichiometric range. The lattice parameter of the $(\text{U}_{1-y}\text{Pu}_y)\text{O}_2$ mixture follows the ideal Vegard law.

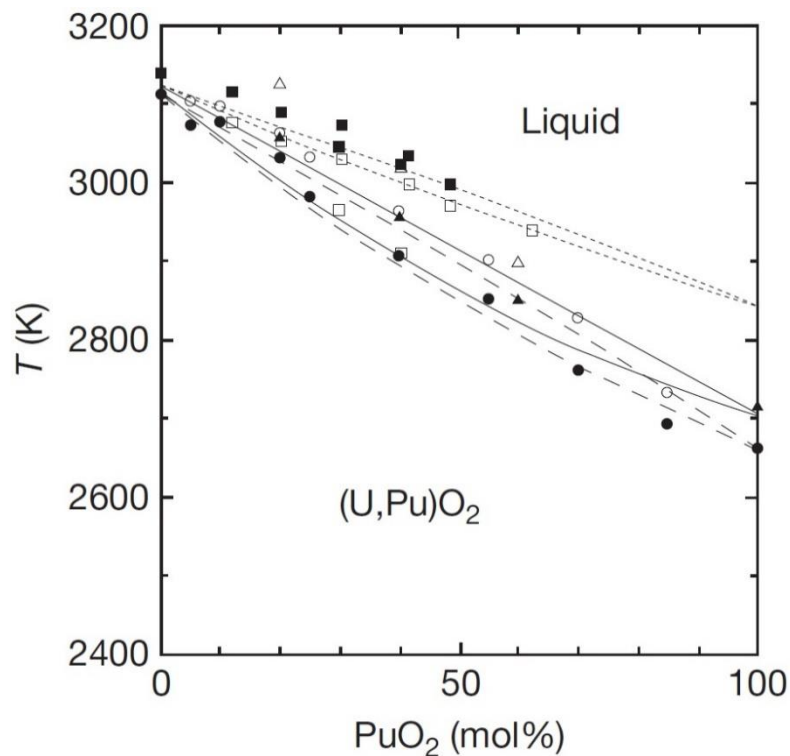


Figure 21: pseudo-binary phase diagram of the UO_2 - PuO_2 system. (43) The full lines represent the solidus and liquidus lines recommended by Adamson (49,50), while the dotted ones the new estimation based on the more recent melting temperature values for PuO_2 . (66,67) The other references can be found in (43).

1.2.2.4.2 Thermal expansion and melting point

The thermal expansion of PuO₂ is very similar to the one of UO₂ (64) and, within the solid solution range with UO₂, the same equations proposed in Section 1.2.2.2.2 can be used for (U,Pu)O₂.(50,65)

As shown in Figure 21, the liquidus and solidus temperatures of the solid solution follow a nearly ideal behaviour, leading to a decrease in the melting point with the increasing of the Pu content. The recommended equations are those proposed initially by Adamson et al:(49,50)

$$T_{(solidus)} = 3120 - 655.3y + 336.4y^2 - 99.9y^3 \quad (24)$$

$$T_{(liquidus)} = 3120 - 388.1y - 30.4y^2 \quad (25)$$

However, uncertainty is present around the melting temperature of PuO₂, as recent measurements (66,67) found higher values than in the previous literature (2701 ± 35 K is the value considered by Adamson et al(49)), pointing out the need for further investigation and a potential reassessment of the above mentioned equations.

1.2.2.4.3 Heat capacity

PuO₂ heat capacity measurements were performed by several authors (68,69) up to 2715 K and an equation was derived by Flotow et al (70):

$$C_p = 35.2952 + 0.15225 T - 127.255 \cdot 10^{-6}T^2 + 36.289 \cdot 10^{-9}T^3 - 3.47593 \cdot 10^5T^{-2} \quad (26)$$

However, PuO₂ exhibits a rapid C_p increase above 2370 K, similarly to what observed in UO₂, and this equation fails to accurately reproduce this trend in the 2470-2640 K range. (54)

Again, based on the ideal character of the solid solution, and on experimental data, Carbajo (50)proposed that the heat capacity of (U_{1-y},Pu_y)O₂ can be described by the Neumann-Kopp rule:

$$C_p = (1 - y)C_p(T, UO_2) + yC_p(T, PuO_2) \quad (27)$$

This equation proved to be accurate to predict with a good agreement (2 – 3 %) experimental results on MOX containing up to 40 % Pu. (71,72)

1.2.2.4.4 Thermal conductivity

Unlike the other properties listed up to now, thermal conductivity does not follow the law of mixtures between the two end members UO₂ and PuO₂. In fact, each substitutional atom in the solid solution acts as phonon-scattering centre and affects the thermal conductivity; the result is that the mixed oxides conduct heat more poorly than the end members. The addition of a small amount of PuO₂ lowers the thermal conductivity of UO₂, but this effect is composition-independent for PuO₂ contents between 3 and 15 %. (50,71)

An expression for the calculation of the thermal conductivity of a 95 % TD (U_{1-y}Pu_y)O_{2±x}, valid for y≤0.15, x≤0.05 and T between 700 and 3100 K, was proposed by Carbajo(50) based on the works of Duriez (71)and Ronchi (53):

$$\lambda = \frac{1}{A(x) + B(x)t} + \frac{6400}{t^{2/5}} e^{\frac{-16.35}{t}} \quad (28)$$

With $A(x) = 2.85x + 0.035$ [mK / W], $B(x) = - (0.715x + 0.286)$ [m / W], and $t = T / 1000$ (and T expressed in K).

1.3 In-reactor life – irradiation of Nuclear Fuel

As mentioned in Section 1.1.5, after irradiation and discharge from the reactor the nuclear fuel is significantly different from the fresh unirradiated UO_2 . Inside the reactor, NF undergoes nuclear fission reactions which release the heat that is used for energy production. In order for the reactor to actually produce energy, the fission reaction has to self-sustain (*i.e.* chain reaction). The isotopes that can sustain a nuclear fission chain reaction are called *fissile*. A scheme of the nuclear fission reaction taking place in an LWR is shown in Figure 22. (73)

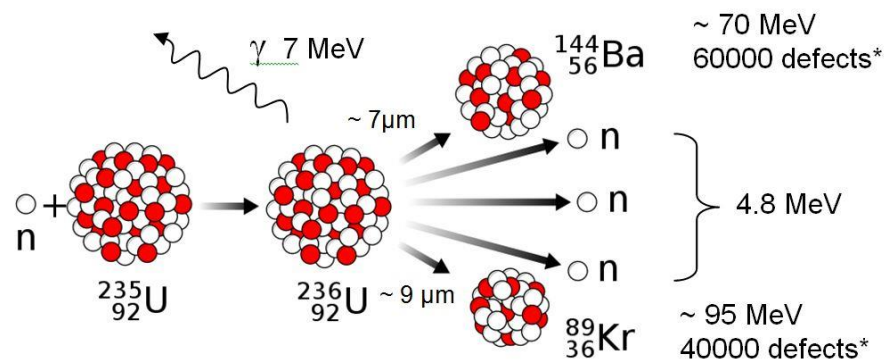


Figure 22: fission reaction of a ^{235}U atom. The capture of a neutron brings the nucleus into an excited state, and the unstable ^{236}U fissions soon after producing a γ particle, two to three neutrons and two fission product, releasing in total about 200 MeV. (73)

To start the fission reaction, a fissile isotope has to get hit by a low energy neutron (also called a *thermal* neutron). This neutron compounds with the fissile nucleus, resulting in an excited state, such as the excited ^{236}U . Figure 22 shows the result of neutron absorption by the fissile ^{235}U nucleus. After a short time, the excited ^{236}U nucleus fissions, splitting itself into two high energy lighter isotopes and two or three free neutrons, with an overall released energy of about 200 MeV.

The fission reaction becomes self-sustaining when the two/three neutrons emitted from a fission event serve as initiators for further fission reactions. This is possible when:

1. There is a sufficient density of fissile material surrounding the fission event (*i.e.* natural uranium has to be enriched)

and

2. The very fast emitted neutrons are *moderated* (*i.e.* their energy is lowered) to be slow enough to be captured by the surrounding fissile material. In BWR, the moderator is the same water that is used for steam, while in PWR an intermediate circuit is foreseen.

The ratio between the neutrons produced and consumed by the chain reaction can be adjusted by changing the configuration of the fuel and by using neutron absorbers (control bars and neutron poisons, *e.g.* cadmium). When the population of neutrons is constant generation after generation of fission events, the system is *critical*. Delayed neutrons produced during the beta process allow controlling the chain reaction; since Pu fission results into more prompt neutrons than in the case of U, MOX chain reactions are more delicate to control.

1.3.1 Materials response to radiation

In the extreme environment of a nuclear reactor core, UO_2 is subject to very severe conditions that modify significantly its composition and microstructure. The extremely high energy released by the fission reaction is mainly transferred as kinetic energy to the emitted particles. These particles slow down by transferring their energy to the fuel matrix that results into heat production but also into significant damage to the crystal lattice.

Moreover, more radiation (and more heat) is emitted by the radioactive decays of the fission products that are generated during the chain reaction. Most of these atoms originated from the splitting of the ^{235}U nuclei are unstable, and undergo several other decays before transforming into a stable isotope. In the course of their decay, fission products can form metallic phases, gas elements, but also ceramic phases. Some are soluble in the UO_2 crystal, like the lanthanides; insoluble elements precipitate as gas bubbles (Xe, Kr) or as metallic inclusions (Mo, Tc, Ru, Rh, Pd).

Minor Actinides (MA), such as Np, Am, and Cm, are also formed during irradiation by successive neutron captures and contribute to the fuel damage by their intense α -emission.

Finally, the intense neutron flux needed for the self-sustainment of the chain reaction also induce radiation damage in the nuclear fuel.

Depending on the nature and on the energy of the impinging particle, different interactions with the matrix can take place. Collisions with the atoms can be either elastic or inelastic, and involve the nucleus and the electrons of the target atoms.

1.3.1.1 Stopping power

The stopping power is defined as the energy loss of a particle as a function of the depth of penetration in a material:

$$S(E) = -\frac{dE}{dx} \quad (29)$$

and its plot is called Bragg curve. Figure 23 shows the Bragg curve for an α -particle of 5.5 MeV travelling in air.

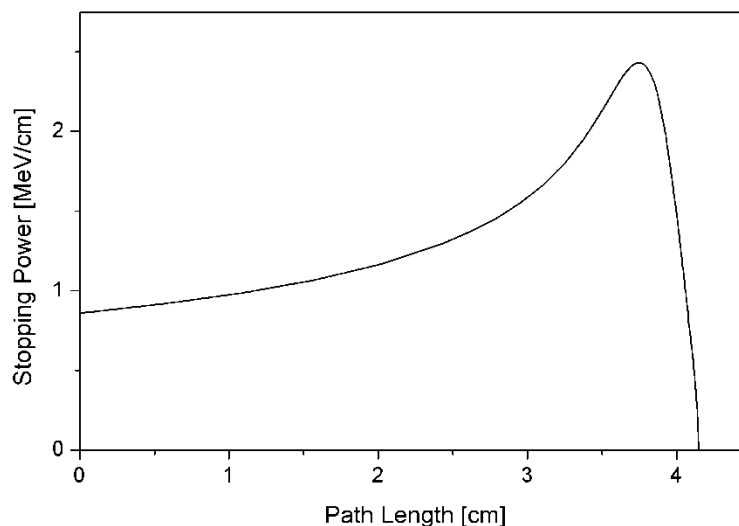


Figure 23: Energy loss of a 5.5 MeV particle in air (or stopping power of air for α -particles of 5.5 MeV).

By losing energy, most of the particles increase their cross section, and hence the interactions with the matrix. For this reason, the stopping power raises (Bragg peak in Figure 23) right before the particle comes to rest.

1.3.1.2 Nuclear energy losses – low-energy particles

When the incoming particle has a sufficiently low energy, elastic scattering with the matrix atoms nuclei can take place. Kinetic energy is transferred during the collision to the target atom which is then knocked out of its original lattice position, if the transferred energy is high enough. The energy needed to displace U and O atoms in UO_2 is 40 and 20 eV respectively (74). If the displaced atom has sufficient energy, its collision with the other matrix atoms will generate further displacements, resulting in collision cascades and sub cascades (see Figure 24).

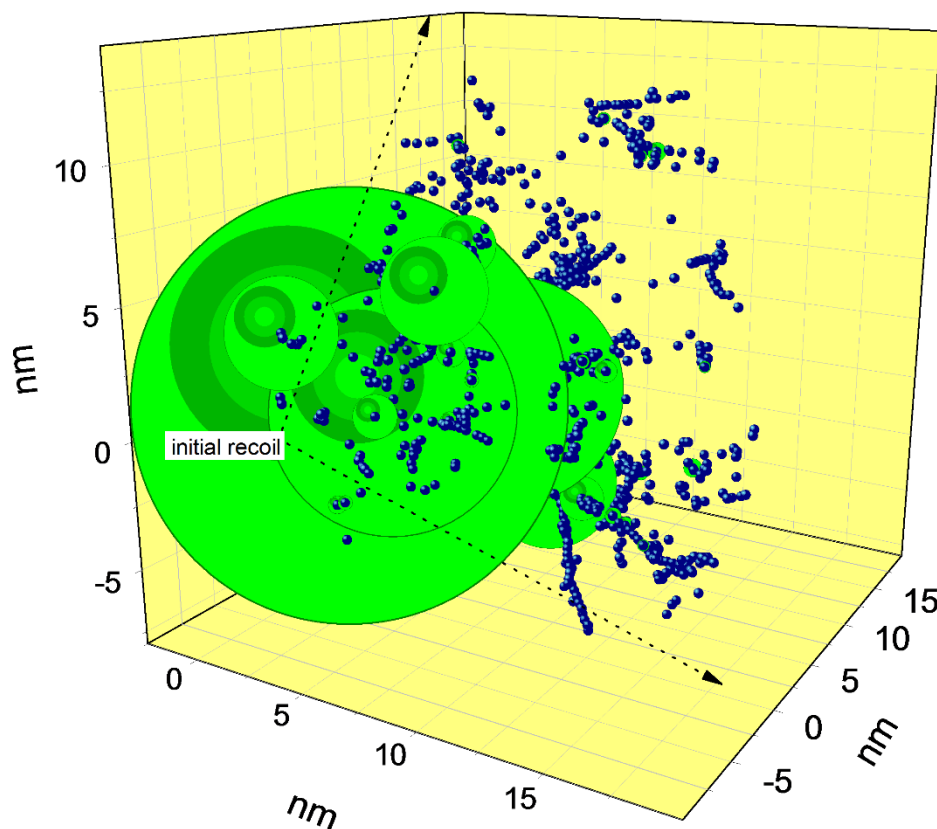


Figure 24: SRIM simulation of the displacement cascade generated by a recoil nucleus produced during an α -decay (100 keV). (73)

The displacement cascade in Figure 24 was calculated using SRIM (75) for a recoil nucleus generated from an α -decay, whose typical energy is a 100keV. The energy transferred to each knock-out atom can range from 50 eV to several keV, generating the sub cascades. This is represented by the blue circles (oxygen atoms) and green circles (uranium atoms) whose diameter is equivalent to their energy (after collision). The (heavy) uranium atoms evidently can absorb energy from the primary knock-on atom (pka) generating further sub-cascades. As a result, a number of defects is generated in the lattice (vacancies and interstitials), that can partially recombine shortly afterwards. A common way to quantify the dose of radiation received in the nuclear energy loss regime is the number of displacements per atom (dpa), by taking into account the average amount of displacements per decay calculated using software like SRIM.

$$dpa = \frac{\text{displacements}}{\text{atoms}} = \frac{\frac{\text{displacements}}{\alpha\text{-decay}} \cdot a \cdot t \cdot m_{\alpha}}{3 \cdot N_{\alpha} \cdot \text{mol}_{\text{UO}_2}} \quad (30)$$

Where a is the specific activity of the α -emitter, m_{α} is its mass, t is the time, N_{α} is the Avogadro number and mol_{UO_2} are the total moles of the material for which the dpa are calculated.

The recombination of the generated defects depends on several factors, such as the properties of the material and the temperature, but also the interactions (overlap) among different cascades (and hence the activity), and it is not taken into account in the quantification of the dpa. This last aspect in particular constitutes a possible weak point of the usage of dpa as a measure of the damage introduced in the material, as it disregards the influence of the dose rate. It must be always kept in mind that dpa is a measure that allows comparing equal amounts of damage injected by different sources, but depending on the rate of this damage deposition it might not be reflected in the damage actually remaining/surviving.

1.3.1.3 Electronic energy losses – high-energy particles

In the case of highly energetic particles, interactions with the nuclei of the matrix atoms become very unlikely. Rather, the particle will be slowed down by inelastic collisions with the bound electrons, depositing energy and ionizing the atoms along its path (*ionizing radiation*). The response to such a radiation depends on the electronic structure of the material, with insulators being much more sensitive due to the lack of conduction electrons. In the case of UO_2 the result is the creation of *ion tracks*, such as those shown in Figure 25-A. (76) Seitz and Koehler (77) proposed a thermal-spike model for the creation of ion tracks, based on the assumption of the formation of a high temperature region around the trajectory of the high energy particle. Depending on the thermal conductivity of the material, the temperature in this region can exceed the melting point, such as in the case of UO_2 . Toulemonde (78) later revisited this model to include thermodynamical parameters and was used by Wiss et al (79) calculate the observed radius of ion tracks in UO_2 . Figure 25-B shows the lattice temperature as a function of time and radial distance from the ion path for a U ion of 11.4 MeV u^{-1} in UO_2 .

This result adds up to the previous evidences of some thermal-spike effects caused by FP passage in

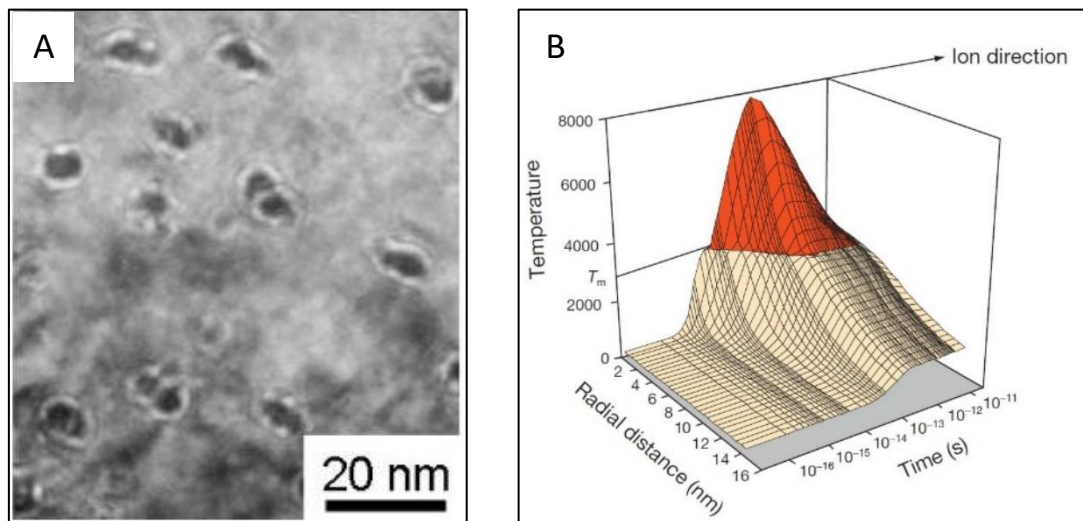


Figure 25: A) ion tracks generated by 310 MeV Au^{2+} ions passing through UO_2 . (76) B) calculation of the lattice temperature around the trajectory of a 11.4 MeV U ion in UO_2 . (79)

UO₂, which could be explained with the temperature and pressure conditions predicted by the model:

- Phase change from UO_{2+x} to U₄O₉ needles, which occurs normally at 1150 °C (80)
- Enhanced U diffusion in UO₂ (81)
- Fission gases bubbles destruction and resolution (82)

1.3.2 Defects formation in UO₂ (effects of radiation damage)

As mentioned in 1.3.1, UO₂ is targeted by many different types of radiation inside the reactor, which are slowed down due to both electronic and nuclear interactions depending on the nature and energy of the radiation.

1.3.2.1 β - and γ - decays

The energy distribution for β -decays of the FPs in NF covers the range between 2.6 keV and 10.4 MeV, with the emitted e^- and e^+ ionizing the matrix. These particles have also a large cross section for Rutherford scattering. However, the energy transferred to the target atom depends also on the ratio between its mass and the one of the impinging particle, and therefore very few point defects are generated from β -decays.

The displacement damage by photons, X and γ rays can be neglected in comparison to the effects of the other radiation damage sources present during irradiation conditions.

1.3.2.2 Neutrons

In the reactor core, the neutron energy spectrum can be broad, and they can be divided in three groups: *thermal* ($E < 1\text{eV}$), *epithermal* ($1\text{ eV} < E < 10\text{ keV}$) and *fast* neutrons ($E > 10\text{ keV}$). Thermalisation of a sufficient number of neutrons is of course a necessary condition for the self-sustainment of the fission chain reaction, to which also epithermal neutrons contribute. Fast neutrons instead generate almost only damage in the fuel matrix. In this range of energies, capture can take place and only nuclear losses should be considered. The maximum energy transferred by a neutron of mass m and energy E_n to the material atoms of mass M can be written as:

$$E_{max} = \frac{4mM}{(m + M)^2} E_n \quad (31)$$

Which becomes $E_{max} \approx 4E_n/M$ for $M \gg m$, such as in the case of UO₂. Again considering 20 and 40 eV as displacement energies for O and U atoms respectively in UO₂ (74), it results that neutrons with energies lower than $E_n \approx 0.1\text{ keV}$ cannot produce direct displacements.

1.3.2.3 α -decays

Each α -decay process, such as the one shown in Figure 26 for a ²³⁸U atom, produces two very different damage sources:

- the emitted α -particle (i.e. a He ion) at about 5.5 MeV, undergoes mainly electronic energy losses in around 200 collisions along its penetration depth (typically between 10 and 20 μm)

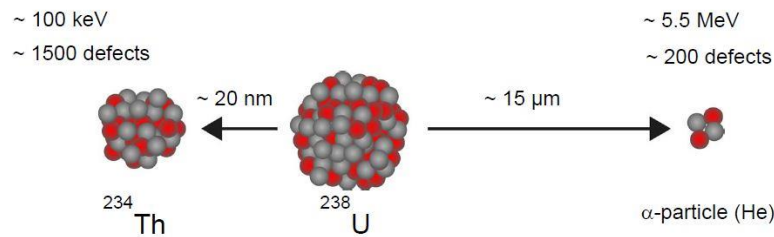


Figure 26: α -decay of a ^{238}U nucleus, resulting in a 5.5 MeV He ion and a 100 keV ^{234}Th recoil nucleus. (73)

- the heavy recoil nucleus (^{234}Th in the case of a ^{238}U α -decay) with $E \approx 100$ keV (by conservation of the momentum $E_N M = E_\alpha m$) undergoes binary nuclear collisions, generating a dense cascade of about 1500 displacements within a radius of 20 nm. As discussed previously, these defects can partially recombine, or form clusters.

Therefore, in the case of α -self-irradiation damage is simultaneously introduced in the structure by both electronic (α -particle) and nuclear (recoil nucleus) stopping power. The interaction between the two energy losses regimes, especially when simultaneous, is not yet fully understood and still under investigation. As it will be detailed in Section 1.4.2.2, ion implantations are typically used for single effect studies to assess the behaviour of UO_2 against damage formation. In multiple irradiation, depending on the sequence between different ions with different properties e.g. energy loss) or even simultaneity of irradiations the effects can vary substantially. The synergetic effect of irradiation in two energy loss regimes (nuclear, electronic) has been named SNEEL as described for example for SiC Thomé et al.(83) More recently Gutierrez et al (84) performed a study on the synergetic effect on the irradiation response of UO_2 . It could be shown that strain and stress levels in a UO_2 polycrystal irradiated in the $S_n \& S_e$ regime (i.e. simultaneously with two ion beams) were lower when compared to irradiation performed by S_n alone. This result is a direct evidence of an interactive effect of nuclear and electronic energy depositions in UO_2 . It proves that ionization can modify the structure and density of the defects generated by nuclear collisions.

1.3.2.4 Fission products

As already introduced, in each fission event the ^{235}U nucleus splits into two fission products, and two or three neutrons. The generated fission products fall into two groups, as shown in Figure 27(85), with the heavier atoms (mostly Ba or I) having around 70 MeV, and the lighter ones (mainly Mo or Kr) with about 100 MeV of kinetic energy.

Fission products interact with UO_2 mainly by electronic stopping, with very high energy deposition rates of 20 – 30 keV / nm generating fission spikes. Other effects of the passage of a FP are the formation of defects and the rearrangement of pre-existing ones thanks to the high temperature reached, and the destruction of fission gas bubbles. In reactor operation, the production of FP is very homogeneous, generating high levels of damage already within the first hours of presence in the reactor and leading to significant fission-enhanced diffusion, creep and gas bubbles resolution.

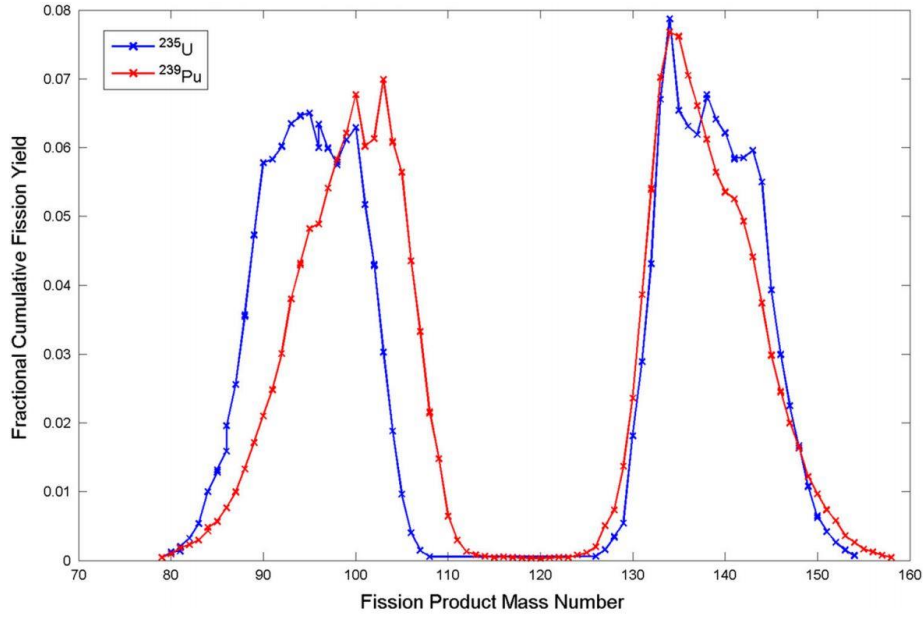


Figure 27: fission products fractional cumulative fission yield for ^{235}U and ^{239}Pu . (85)

1.3.2.5 Radiations in UO_2

Figure 28 show the comparison between the nuclear and electronic losses of an α -particle and a median heavy FP in UO_2 . Both graphs show a much stronger electronic component, with the nuclear losses becoming significant only where implantation occurs

It is worth noting that the example shown in Figure 28 only takes into account the α -particle but not the recoil nucleus generated during an α -decay. The recoil nucleus has a very short range (10 – 20 nm), which makes it hard to represent by using the same scale.

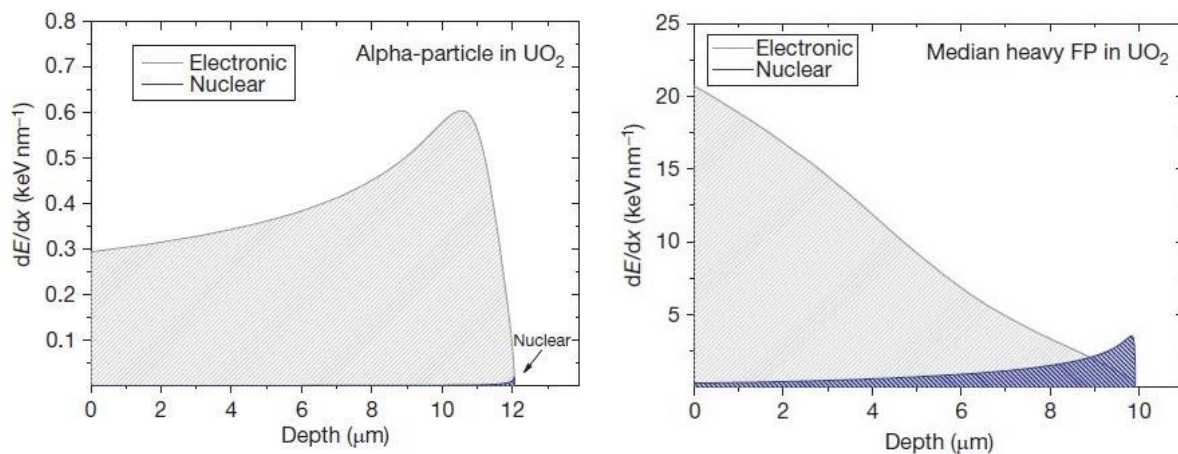


Figure 28: comparison between the energy losses regimes of an α -particle and a fission product in UO_2 . (73)

Another way of visualising the interactions of a particle with the medium through which it is projected is shown in Figure 29. It plots the energy loss as a function of the ion energy, showing that different type of stopping mechanisms can occur at different energies of the same particle. The description of the displacements generated by the nuclear stopping is relatively straightforward (although the quantification of the recombining defects is not), while the consequences of electronic energy losses are generally less quantifiable. Remarkably, at very high ion energy (above the fission energy) the electronic losses decrease again, due to the extremely high ion speed that reduces the energy deposited per unit distance.

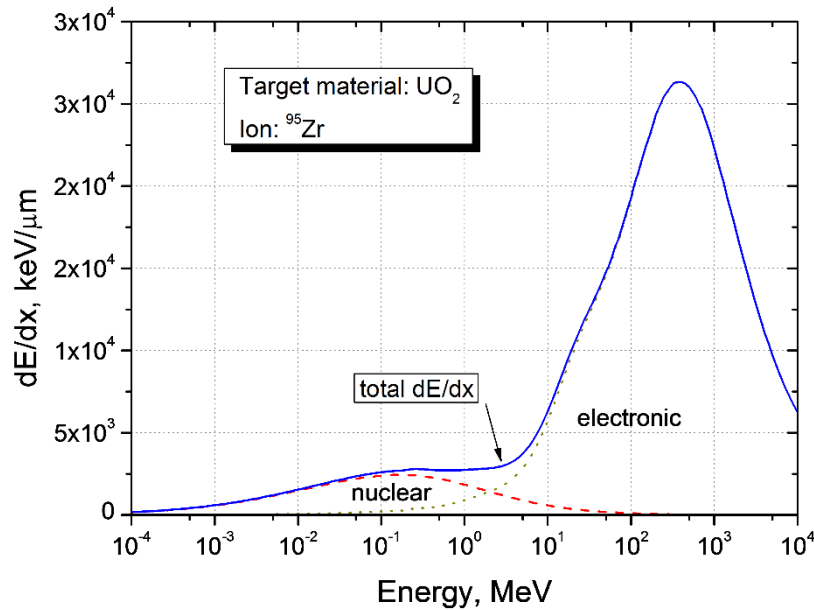


Figure 29: total losses of a ^{95}Zr nucleus travelling into UO_2 as function of the ion energy. (73)

Based on their energy, particles will have more or less interactions with the medium per unit distance. The travelled distance and the trajectory depend on the collision that the particle experiences while being slowed down. Highly energetic particles incur into very few scattering events, having mainly electronic losses along their path, thus almost do not deviate from their initial direction and have very long penetration. Only at the end of their penetration these particles will finally experience some high-angle scattering events, which instead are characteristic of the trajectory of a low energy particle. Figure 30 (86) shows the almost straight paths of an α -particle and two FP in UO_2 , in contrast with the broad but short cascades generated by the recoil atom presented in earlier in Figure 24. The lower part of Figure 30 plots the energy losses of the particles in the medium and the corresponding deposition range, i.e. the depth at which the penetrating particles implants.

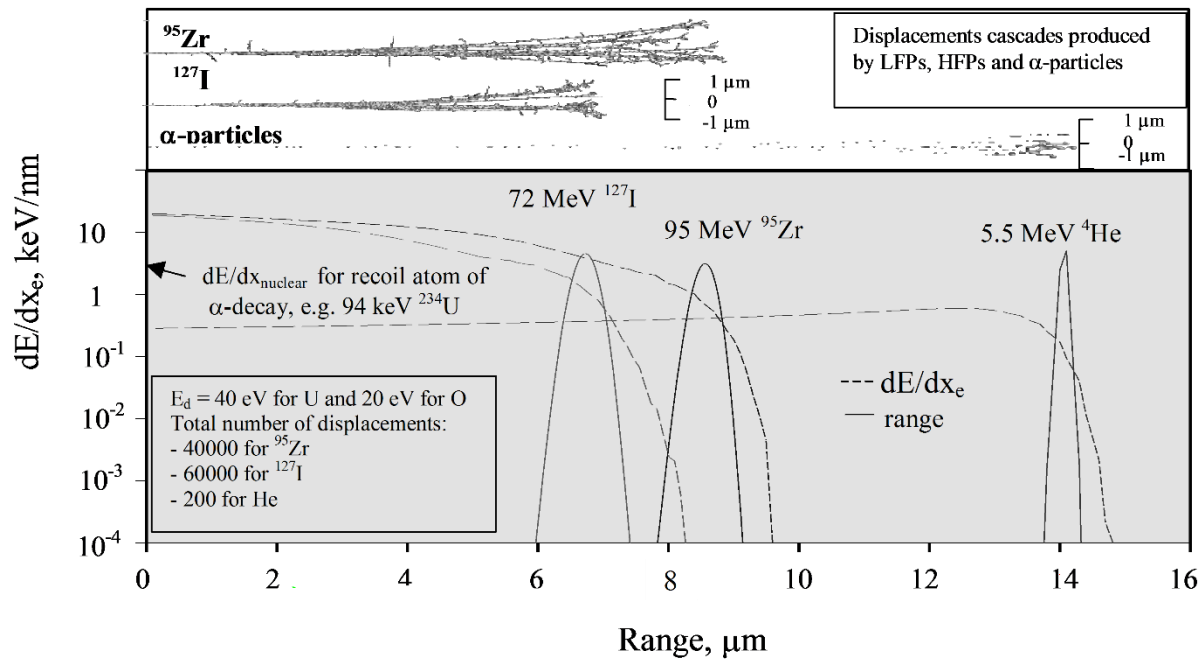


Figure 30: upper part: calculated displacement cascades for a light and a heavy fission product, and for an α -particle in UO_2 ; lower part: energy losses and deposition range for the same particles. (86)

1.3.2.6 Radiation damage and defects creation

By recalling the defects classification presented in Section 1.2.1.1.3, a summary of the consequences of the passing of low energy particles in UO_2 is attempted.

1.3.2.6.1 Point defects

Whenever a recoil nucleus or a neutron passes through UO_2 , atoms are knocked out from their original sites and possibly start colliding with other matrix atoms giving rise to displacement cascades. Each displacement involves the formation of two point defects, a vacancy and a self-interstitial. Some of these defects recombine shortly after, while the others might remain in the lattice or cluster with other defects thanks to favourable temperature conditions, minimising their overall energy. In addition to that, the recoil nucleus will come to rest as an extrinsic defect in the matrix. This is valid also for the highly energetic α -particles or FPs ending up as interstitials.

1.3.2.6.2 Extended defects

As defects diffuse through the solid, they can combine to form larger clusters that lower the overall energy. The two main types of extended defects caused by radiation damage in UO_2 are dislocation loops and voids.

- Dislocation loops can be of two types: single loops or prismatic loops. Single loops include those described in Section 1.2.1.1.3 and are formed by plastic deformation of the lattice, hence are not a direct consequence of irradiation. Prismatic loops instead are the result of the diffusion and clustering of self-interstitials or vacancies, stacked as platelets between two lattice planes. These loops grow by absorbing defect of the same type, and shrink by emitting them or absorbing defects of the opposite type. Vacancy prismatic loops are actually intrinsically unstable at all temperatures.

- Voids are three dimensional clusters, which are indeed the most favourable extended defects configuration for vacancies.

For both extended defects, two different and subsequent steps are generally identified: nucleation and growth. During nucleation, loops/voids increase in number without increasing significantly their average size, and their formation can occur by clustering of randomly-diffusing interstitials or vacancies in the matrix (*homogeneous* nucleation), or on some specific discontinuities of the lattice (*heterogeneous* nucleation) such as pre-existing bubbles, incoherent precipitates or even dislocations or collision cascades depleted zones. In the growth phase, diffusion of defects results in the increase of the size of the existing voids and loops. Overlapping of growing dislocation loops results in dislocation lines and tangles.

Voids themselves can then serve as heterogeneous nucleation sites for gas bubbles, by trapping the diffusing gas atoms, in a process that in turn stabilises the void against collapse.

1.3.3 Irradiated UO₂

During reactor operation, UO₂ is subject to all the radiation and damage sources listed up to now, for a period of about 5 years (87). As a result, the microstructure is dramatically changed, which leads to changes in the macroscopical properties. Moreover, the chemical composition is constantly changing during irradiation as a result of the inclusion of FPs and α -decays recoil nuclei, as well as the new elements generated by β -decays. This also leads to changes in the chemical and physical properties of the fuel.

Burnup is the measure of the energy extracted from the nuclear fuel during irradiation, expressed in GWd per tons of fissile material (GWd / tU). It is a very useful quantity which allows to scale the changes of the fuel properties based on how much of the fuel was used, as the radiation dose absorbed by the fuel and its effects, but also the amount of MA and FP included in the matrix, are in general proportional to the fuel burnup. Due to the different temperature and radiation conditions at the different radial positions of the NF, SNF is a very heterogeneous system, and its properties changes must be evaluated as a function of the burnup but also of the radial position within the fuel matrix.

After discharge, SNF is still subject to high radiation fluxes due to the extremely active MA products present in the matrix. The long half-life of these elements results in α -damage accumulation that can last up to some million years after discharge, depending on the burnup of the fuel. Figure 4 in Section 1.1.5 shows the α -dose accumulated by some fuels with different burnup as a function of the storage time. This, together with the chemical changes concurrently ongoing, results into microstructural and properties evolution for long time after discharge of NF from the reactor.

1.3.3.1 Change of properties

All of the above-mentioned phenomena lead to macroscopical changes in the thermal and physical properties of NF, which are extremely different in the case of SNF with respect to fresh fuel. Some of these properties are crucial for modelling of fuel performance during operation, while other ones are more significant for SNF treatment. Also, different types and sizes of defects affect in different way the change of the different properties of the NF.

In many cases, the analysis of real SNF is too hazardous (due to the radiotoxicity of the material) and complicated (due to the complexity of the system, involving many concurrent effects). As it will be detailed in the following Section (1.4), a good strategy to understand radiation damage is to study its effects on simpler and less dangerous systems such as UO_2 doped with α -emitters or implanted in ion-beams.

1.3.3.1.1 Swelling and fission gases retention

Volume change in NF during and after irradiation is dictated by several factors. Point defect accumulation leads to a lattice parameter increase up to a saturation value when defect creation and recombination rates compensate, as was also assessed using α -doped (88,89) or He-implanted (90) UO_2 .

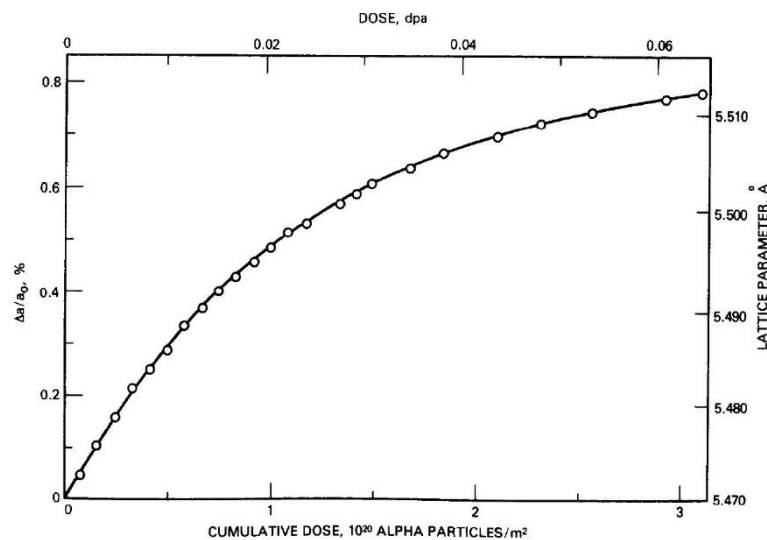


Figure 31: relative lattice swelling as function of the cumulated dose (dpa) in a UO_2 single crystal irradiated with 5.5 MeV α -particles. [66]

However, Fission Gases (FG) contributes the most to macroscopic swelling of the fuel. Each fission produces on average 0.3 Xe and Kr atoms, that are insoluble in the fuel matrix and can either remain in the fuel pellet contributing to the swelling or be released in the rod, after bubble formation, resolution and atom diffusion through the lattice. In both cases, the integrity and thermal properties of the fuel rod are affected, so the understanding of the FG behaviour is crucial for the safety of the reactor.

FG diffusion through the matrix is enhanced by the lattice defects and deviation from stoichiometry, but also by the generation of fission tracks (Section 1.3.1.3). Fission-enhanced diffusion is indeed an athermal process and dominates for temperatures below 1000 °C, hence in the outer rim of the NF. The migrating FG atoms can then be trapped on crystalline imperfections (impurities, pores, voids, precipitates, bubbles...) or at grain boundaries producing bubbles. Grain boundaries start acting as traps rather than fast diffusion paths at rather low burnups. (91) These bubbles cannot be thermally resolved, but instead can be dissolved by interaction with a FP, in a process called *irradiation-induced resolution* that keeps the average bubble size relatively small.(92) For specific burnup and temperature conditions, the bubbles population along grain boundary can be sufficient to have bubbles interconnection, which leads to burst FG release but also potentially to cracking of the fuel pellet.

1.3.3.1.2 Mechanical properties

SNF mechanical properties change can be related to the microstructure in terms of porosity/density changes as well as grain polygonization. Some properties are affected by the radiation environment, such as fission-enhanced in-pile creep (or self-diffusion), leading to very different behaviour in and outside operating conditions. Some other properties instead suffer from the damage cumulation, and remain altered even after the radiation source has ceased.

An example is the change in the hardness or elastic modulus of nuclear fuel. Cappia et al (93) and Spino et al (94) analysed SNF as a function of the burnup and radial position, finding a general hardness increase for increasing fuel burnup. Figure 32 shows the evolution of the hardness of the centre of the pellet as a function of the burnup.(94) As it will be shown in Section 1.3.3.2, the development of a particularly porous microstructure at the rim of the fuel under irradiation affects mechanical properties in that region. Hardness increase has also been reported by Wiss et al (88) as a consequence of α -decay in SNF UO_2 surrogates (see Section 1.4.2.1).

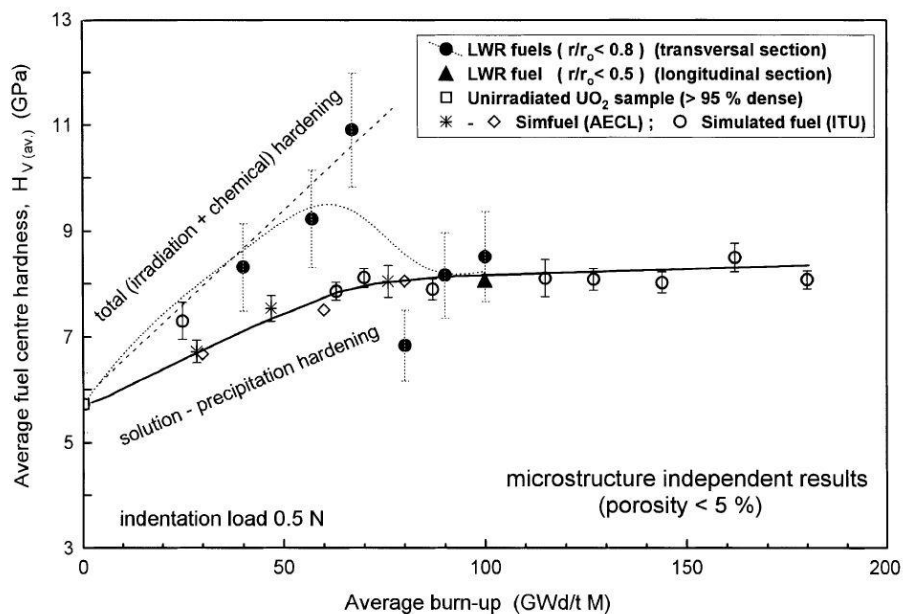


Figure 32: hardness increase as function of the fuel burnup, as measured on real and simulated spent fuel. (94)

1.3.3.1.3 Thermal properties

Thermal conductivity is probably the most important parameter in fuel performance codes for the prediction of fuel behaviour in reactor operations. It depends on many parameters, such as composition, atomic structure, and microstructure, all of which are constantly changing during irradiation. An example of the thermal conductivity variation in SNF for increasing burnup levels is shown in Figure 33 by Ronchi et al (95).

As discussed already in Section 1.2.2.3.3, thermal conductivity is strongly affected by point defects. In SNF, where the α -activity is still very high but the temperature conditions for defects recombination and annealing are basically absent, thermal conductivity is also decreasing as a function of the dose. Thermal property degradation was already reported by several authors in UO_2 doped with α -emitters as SNF simulant. (88,96)

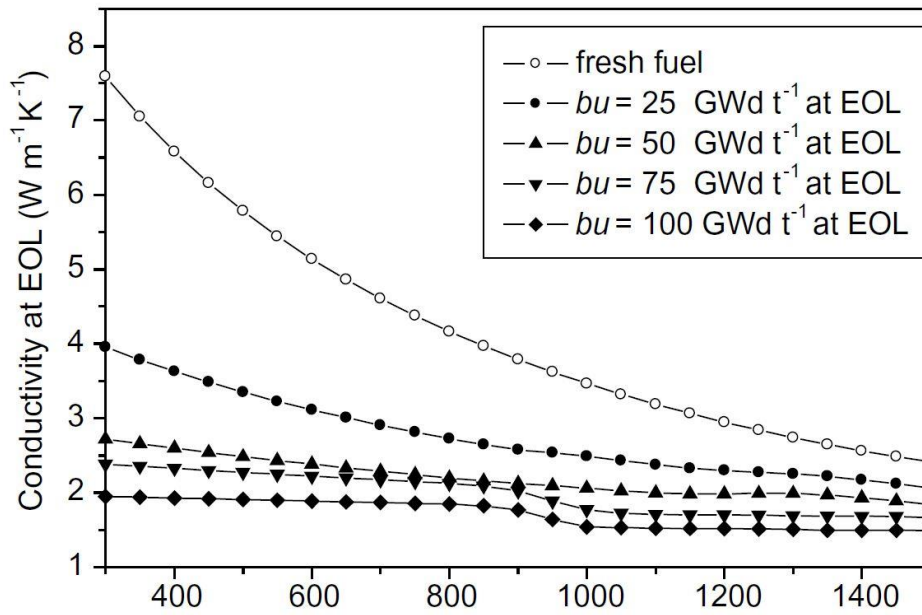


Figure 33: thermal conductivity of SNF for increasing burnup at fuel discharge, or End Of Life (EOL) burnup (bu). (95)

1.3.3.2 HBS formation

Another effect of radiation on the microstructure is the restructuring of the initial microstructure into a pattern of smaller grain called *polygonization*. This term describes the rearrangement of those dislocations formed in the earlier stage of irradiation that do not annihilate one another into walls of dislocations, forming low-energy sub-boundaries and perfect but slightly misaligned sub-grains.

In its periphery, NF experiences higher neutron fluxes than in the bulk, resulting in an increased capture rate by ^{238}U in the resonance range, with the consequent production of ^{239}Np and ^{239}Pu .(97) This leads to a rim region of about 200 μm of thickness (around 8 % of the total fuel volume) of higher fissile material density, and therefore higher local burnup. In this region, the original 10 – 15 μm grains are subdivided into 100 – 300 nm grains (meaning roughly 10^4 new grains per initial grain), and increased porosity is also observed. This very peculiar microstructure is shown in Figure 34 and it is labelled *High Burnup Structure* (HBS).

In the case of heterogeneous MOX fuels, HBS develops also locally around Pu-rich zones throughout the whole pellet diameter, and the same is true for UO_2 fuels with heterogeneous ^{235}U distributions. (98,99)

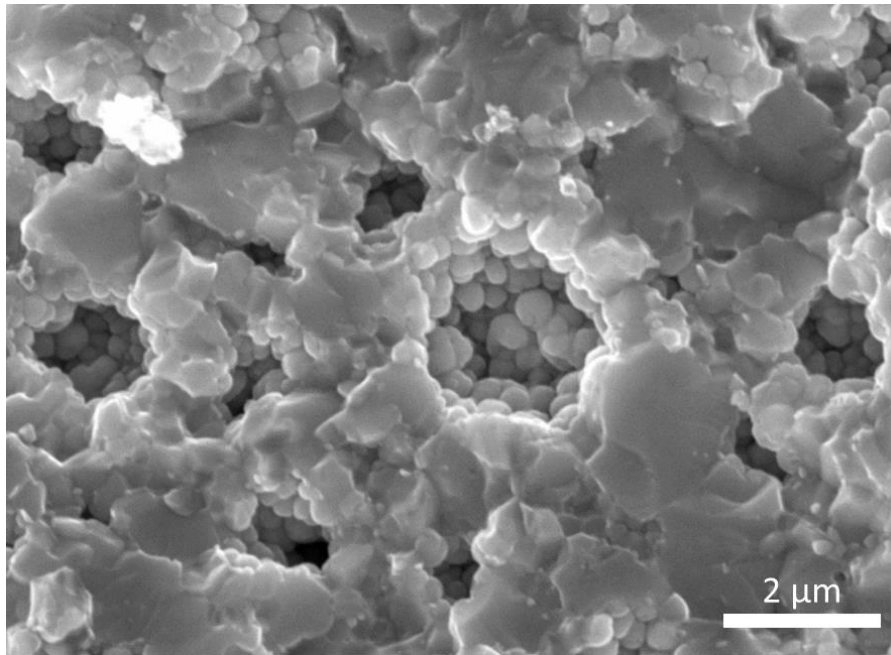


Figure 34: High Burnup Structure (HBS) observed in a spent UO_2 fuel with local burnup of 200 Gwd / tU.

The mechanisms leading to the HBS formation are still under investigation, but increasing evidence seems to relate it to the polygonization process. In a dedicated investigation campaign denominated Rim High Burnup Project (100), TEM observations performed by Sonoda et al (101) showed that in the HBS the initial grains are subdivided rather than recrystallized, a phenomenon that seems to proceed further with increasing fuel burnup (102). More recent investigations performed by Gerczak (103) on the cross section of high-burnup commercial UO_2 fuel showed Low Angle Grain Boundaries (LAGBs) in the rim zone at the onset of HBS, typical of polygonization. Only after complete restructuring of the microstructure, high angle GB can be found. This interpretations are backed up by evidence of ongoing polygonization in 84 MeV Xe irradiated UO_2 as observed by Miao et al.(104) Grain subdivision was recently found to take place also in intermediate radial positions, and it was explained as a possible extension of the rim HBS (105) or as local domain around lattice imperfections due to rare earths or transuranic elements in solid solution (98), but more investigation is needed to reach an univocal interpretation.

Whatever the formation mechanism, it is instead quite commonly accepted that the HBS structure has remarkable gas retention properties (106,107) as it does not evolve into open porosity up to very high levels (35 %).(98) Moreover, due to some partial matrix recovery and gas trapping in the pores, a slight beneficial effect of the HBS was found also on the thermal conductivity (100), leading to enhanced fission gas retention. Figure 35 shows the beneficial HBS effects: on the left plot, the Xe radial profile comparison by EPMA and SIMS highlights the trapping effect of the HBS porosity(108); on the right graph, thermal conductivity increase for high burnup (occurrence of the HBS) and moderate irradiation temperatures.(95) Better HBS oxidation resistance was proved by Raman (109) and attributed to the stabilising effect on the fluorite structure given by the presence of Pu and FPs.

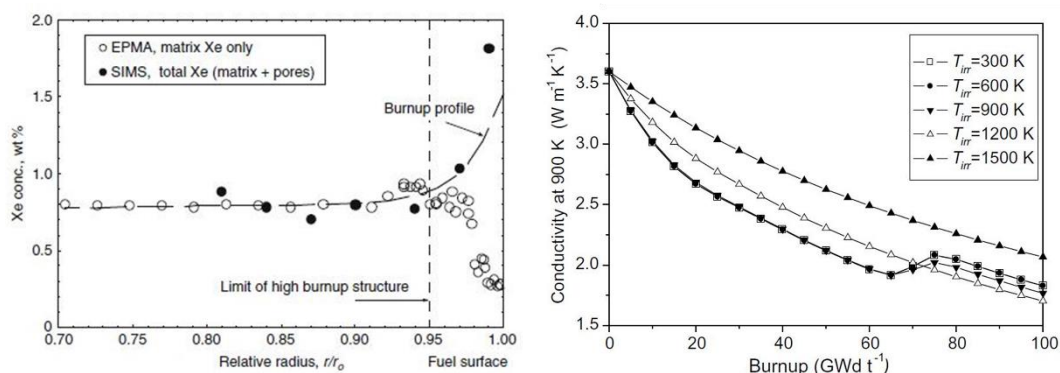


Figure 35: left) EPMA and SIMS Xe radial profile. In the HBS, significant amount of Xe is trapped in the pores instead of in the lattice(108); right) thermal diffusivity as function of the burnup, showing an increase due to the occurrence of the HBS for high burnup(95).

The study of the properties of HBS as a potentially helpful microstructure is currently ongoing, and part of the work in this study is aimed at understanding grain size effects on radiation damage resistance.

1.3.3.3 *UO₂ radiation resistance – polarons effect?*

Taking into account all the effects mentioned until now, UO₂ still results as a fairly radiation tolerant material. Its fluorite structure is conserved over a broad range of deviation from stoichiometry and it allows the inclusion of high amounts of foreign atoms as interstitials. Even more important, UO₂ does not amorphize under ionising radiations even for energies exceeding the calculated energy losses threshold for amorphization. (79,110,111)

Recent studies focused their attention on the existence and behaviour of polarons in UO₂.(112) Polarons are quasiparticles composed by an electronic carrier (holes in UO₂) together with the strain field they generate on the lattice. The passage of an electron in an ionic solid such as UO₂ in fact results in some attractive and repulsive forces on the surrounding atoms, which themselves counter act on the electron and increase its effective mass. Remarkably, UO₂ presents a high concentration of polarons at high temperatures.

A reassessment of the thermodynamic properties of UO₂ taking into account the polaron effect was performed and the inclusion of these quasi-particles in the models allowed reproducing some anomalies with better accuracy. (113) In particular, the higher values of the heat capacity with respect to the previous models were explained by the presence of polarons.

Recalling the thermal-spike model presented in Section 1.3.1.3, the importance of the material thermal properties on its ionising radiation resistance is quite clear. Both the experimental evidences and the theoretical calculations hint for a reformulation of the thermal-spike model that takes into account the occurrence of polarons. This model would explain in a more consistent way the non-amorphization of UO₂ for energy loss values above its amorphization threshold, as well as provide a criterion for the identification of other highly radiation resistant materials. (114,115)

1.4 Studies on SIMFUEL and separate effect studies

As already mentioned, the study of SNF necessitates stringent radioprotection measures, due to its high radioactivity and radiotoxicity. Furthermore, SNF represents a very complex system in which several effects coexist and interact among each other: radiation damage, chemical composition changes, porosity build up, microstructural reorganisation... In order to better understand the

influence of each one of these parameters, and to lower the risks connected with working with such a hazardous material, separate effect studies have been set up. In these studies, simple materials such as natural UO_2 are employed, and the effect of one single phenomenon is studied at each time. This led to the application of several innovative techniques to UO_2 production, aimed at reproducing very specific features that have been observed in SNF. Thin films have been also widely employed thanks to the ease of preparation of very exotic structures while at the same time probing extremely low amount of material, hence minimising any radiological hazard. (116)

SIMFUEL is the name used to define UO_2 -based materials produced with the inclusion of fission products (such as Cs, Mo, Ba...) in accurately calculated concentrations to reproduce the chemical composition of SNF (excluding the MA). UO_2 or other materials synthesised with a controlled microstructure mimicking the HBS are also labelled as SIMFUELS.

In the frame of separate effect studies, but not strictly falling into the SIMFUEL group, are natural UO_2 samples doped with α -emitters, or implanted with He ions by ion beams, which are used for the study of α -damage. Ion beams indeed allow introducing high amount of damage in a limited time and without activation of the sample. Other ions (Xe, Kr...) are implanted to study FGs behaviour and interaction with radiation damage, which can be generated from the same ion or by concurrent or sequential implantation by other ions, especially in the case of chemical compatibility between the elements.

Some examples were already introduced in this chapter to illustrate some specific features of radiation damage or irradiated UO_2 . In the following Sections, a brief overview of some of the latest innovations introduced in the fabrication of SIMFUEL or UO_2 for separate effect studies are presented, together with some of their applications and the respective findings.

1.4.1 SIMFUEL studies

Besides a more conventional production route (powders milling/mixing followed by conventional sintering as described in Section 1.1.4) and fostered by the need of producing completely new microstructures, the synthesis of UO_2 for SIMFUEL had been exploring several techniques that do not have necessarily direct industrial applications, but allow to tune some microstructural features otherwise inaccessible. Powders preparation was optimised to produce nanograined fuels(117,118) or to include in the material other elements that would be otherwise insoluble.(119) The application of different sintering techniques such as hot pressing and FAST helped the densification of these materials allowing a broader range of final microstructures(120), as well as the inclusion of volatile species.

1.4.1.1 Fission products inclusion

1.4.1.1.1 Solid fission products

Although the chemical composition and microstructure of real SNF is not homogeneous, big effort was put since the beginning in optimising the homogeneity of SIMFUEL. The removal of gradients in the structure allows analysing a simpler system in a more proficient way, decoupling the different effects of burnup (density/porosity and microstructure), chemical composition or stoichiometry. Dry mixing, high-energy wet milling and conventional sintering guaranteed homogeneous final products reproducing SNF (121,122), that were used to study thermal conductivity (123), specific heat (124,125), gas release (126), and mechanical properties (127,128). SIMFUEL were also broadly

employed in the study of leaching behaviour of SNF in repository conditions (129,130), also in combination with radiation effects (131), and these data were validated against real SNF benchmarks (132,133). In general, despite their differences with the real SNF, SIMFUEL studies have contributed to the advancement of the understanding of SNF properties and behaviour. (133–135)

1.4.1.1.2 Volatile fission products

Some fission products, such as Cs, are volatile at the temperatures required for conventional sintering (1650 °C or more), making impossible to efficiently include them in a sintered UO₂ matrix. (136) Ion beams were used extensively to overtake this issue (see Section 1.4.2.2.2) but the result is localised and very far from homogeneous. The use of FAST, and SPS in particular, helped significantly reduce time and most importantly temperature needed for densification. This paved the way for the inclusion of Cs and CsI (137) and to study its interaction with other FP (138).

1.4.1.2 HBS simulation

Besides the efforts in mimicking the chemical composition of SNF, the microstructure of the HBS represents an even more complicated challenge. The peculiar configuration of micrometric pores surrounded by sub-micrometric grains is particularly difficult to be obtained via sintering of powders. The use of pore formers in the sintering of Y-PSZ (yttria-partially-stabilised zirconia) resulted in excellent final products in terms of grains and pores size, but involved a long and troublesome powder processing step which prevented scaling-up of the procedure. (106,139) Other attempts have been made by combining SIMFUEL and ion implantation to induce polygonization similarly to what happens in operation, which were only partially successful but provided further evidence of the correlation between grains subdivision and heavy ions irradiation. (140)

Recent works show the capability of FAST, in particular SPS, to reduce significantly the grain size in the densified material down to approximately the one observed in HBS (40,41) although so far no optimisation of the process has been done to include controlled porosity.

1.4.2 Separate effect studies

1.4.2.1 α -doped UO₂

The study of UO₂ systems doped with α -emitters proved to be extremely helpful for the understanding of SNF evolution. A clear advantage of this strategy is the complete uniformity of the radiation damage within the matrix, proven that the α -emitter is homogeneously distributed, which is not a difficult achievement when using affine elements such as ²³⁸Pu or even better ²³³U(141). Novel synthesis techniques were developed in the last decades to improve the homogeneity of the dopant distribution in the final product. (119,142)

Extensive study of the long-term behaviour of SNF was performed using ²³⁸Pu doped UO₂ by Rondinella (143,144), Wiss (88), Staicu (96), Jonnet (145), Roudil (89,146) by monitoring with several techniques the evolution of the material as a function of the cumulated dose, up to values representative of several millennia of storage. In particular, the works by Rodinella et al (144) and Wiss et al (88), investigated also the effect of dose rate by using different dopant concentrations, and found independence of the macroscopic effects measured, at least for low ²³⁸Pu contents (up to 10 wt %). This aspect is particularly relevant for the present work, and will be discussed further in Section 4.1.1.

The migration of radiogenic He atoms resulting from α -self-irradiation was studied on similar samples by Ronchi (147), Nakajima (148), Maugeri (149) and Talip (150), who also observed grain boundary opening and significant He accumulation after prolonged storage (more than 30 years on 10 wt % doped samples) as also seen by Ferry (151). The effect of α -damage on oxidation and/or dissolution kinetics of UO_2 in different conditions was also subject of study from several authors. (152–156)

1.4.2.2 Ion-implanted UO_2

Ion irradiations played a major role in understanding radiation effects in UO_2 (and in materials in general). The main advantage of this approach is the possibility to reach extremely high doses in a short time without activating the sample. Moreover, several ion beam facilities allow the simultaneous or sequential implantation of different ions, also in combination with *in-situ* characterization techniques that allow following the response of the irradiated material during the experiments.

An evident drawback is the complete loss of homogeneity of the damage deposition, which results in a modified shallow portion of the material and the related analyses must be limited to those regions. Damage and implantation profiles can be calculated using software programs like SRIM. (75)

1.4.2.2.1 α -damage and He migration

In a complementary way to what seen in Section 1.4.2.1, α -damage and He-migration were studied by irradiating natural UO_2 in ion beam facilities.

Lattice swelling due to α -particles was found to be larger than the one produced by α -self-irradiation both on single crystal (90,157) and polycrystalline (158,159) samples. Moreover, higher lattice expansion saturation values as well as different thermal annealing mechanisms were found for UO_2 single crystal samples.

Raman characterization was proficiently used both *in-situ*(160) and *ex-situ*(161) experiments and highlighted very precise features (162,163) indicating an increase of strain and defect concentrations as a consequence of increasing fluence. Annealing studies and benchmarks with literature data helped identifying the (Magneli type) nature of the defects which affect Raman spectra in radiation damaged UO_2 . (164,165)

TEM post-mortem observations were conducted to investigate the fluence effect on the introduced damage, showing no variation in the damaged plateau zone before the implantation depth, where the higher damage level induced blistering initiation. (166)

In parallel, other studies were devoted to the investigation of He bubbles formation and thermal migration in implanted samples. (167–173) Temperatures for intergranular precipitation and thermal resolution of He bubbles found on α -irradiated samples were in good agreement with analogue studies on α -doped materials. (170,174) In μNRA analysis before and after annealing, grain boundaries were found to play a key role in He migration and release. (168,169,173–175)

1.4.2.2.2 Fission gases and swift heavy ions

As mentioned already in Section 1.4.1.1.2, ion beams were used to introduce in SIMFUEL volatile fission products (Cs, Te...) as well as fission gases (Xe, Kr...) and to study their precipitation and thermal migration; Swift Heavy Ions (SHI) allowed the study of ion tracks formation. Kr-implanted

UO₂ experiments shed light on the bubbles nucleation mechanism already visible at room temperature (176), and proved to be a suitable technique to reproduce microstructural damage (dislocation loops and lines) as obtained in in-pile irradiation. (177) Xe implantations were used to understand the fission gas behaviour and its thermal migration (178–181), highlighting the importance of the fission-induced resolution on otherwise thermally stable bubbles. (182) Xe implanted atoms in the lattice were also found to delay the microstructural damage evolution in a comparison study with Au implanted UO₂ without exogenous Xe incorporated. (183–185) The behaviour of Xe was compared to the one of He under similar implantation and annealing conditions, showing very different macroscopic damage of the sample (186), as well as different bubble sizes and nucleation temperatures.(187)

The defects formation(185), microstructural evolution(188) and amorphisation (189) of UO₂ under different irradiation conditions was followed by in-situ characterisation techniques combined with the ion beam. As already anticipated in 1.3.2.3, simultaneous multi beam implantations followed by XRD characterization highlighted the synergetic effects of nuclear and electronic losses (S_e & S_n regime) which result in lower stress and strain than in the sole S_n experiment. This finding is particularly interesting for the present study as interaction between electronic and nuclear losses is also present in α -self-irradiation, especially when overlapping of decay events takes place.

1.5 Chapter conclusions and thesis organisation

In this chapter, the background of the study was described, stressing the principal challenges that were faced during the experimental parts. The goal of the work is to contribute pushing the limits of our knowledge about SNF to help predicting its long-term behaviour and thus choosing the best repository option, as well as improving the databases for NF modelling.

A first brief general introduction on nuclear reactors and nuclear fuel was given, and the strategy of the study is outlined. The present work focuses on the interaction between microstructural interfaces and radiation effects in UO₂: grain boundaries play a key role as sources and sinks of defects, as well as recombination sites, dopant and gas traps and fast diffusion paths. However, studying this effect on real SNF is hardly viable, both because of the extreme hazard of handling such a highly radiotoxic material, and because of the high complexity of the system, in which several effects coexist and compete. In this work, the effect of the grain size was studied by producing samples with controlled microstructures and studying their response to the same irradiation conditions. In parallel, the influence of α -self-irradiation in SNF was reproduced in a separate effect study using natural UO₂ (which constitutes still about 95 % of the SNF matrix) doped with α -emitters (²³⁸Pu).

Considering the importance of the synthesis aspects in the present study, the phenomena related to the synthesis of such materials are then described. UO₂ is produced by powder sintering, so the process is described first in its basic principles and later with more attention to microstructural control. The temperature sequence is crucial, as it controls both densification and coarsening of the powder, the two competing processes that lower the free energy of a powder system and are essentially based on diffusion.

More insight was given on the sintering of UO₂, explaining especially the very strict dimensional and chemical requirements that the final product has to match. Many properties indeed strongly depend

on the stoichiometry of the material, while geometrical parameters are more crucial for safety related matters. Given the importance it has in the work, MOX is also briefly described.

In the second part of the chapter, the effects of radiations on matter, and more in detail on UO_2 , were described. Defects of increasing complexity are generated within the matrix, and their formation mechanisms are not completely clear yet for each one of them. The interconnection between the generated defects and the macroscopical properties changes are also not fully understood yet. An overview on the state of the art on the knowledge about radiation damage was given.

Finally, an overview of some of the similar experiments conducted in the past was attempted. Significant advancements in understanding radiation damage and SNF behaviour was reached thanks to SIMFUEL, α -doped and ion-implanted UO_2 . In particular, the flexibility given by ion beam facilities allows the study the effect of different damage sources, also in combination with each other both sequentially or simultaneously.

In an attempt of shedding light on the influence of grain boundaries on radiation-induced effects, the thesis work described in this dissertation was carried on along two main research axes:

- Ion-implantation study of UO_2 with controlled microstructure, where the effect of the grain size is studied on the radiation resistance towards He (and Xe) irradiations, but also on the retention/release mechanisms of the implanted gases atoms.
- Self-irradiation study of ^{238}Pu -doped UO_2 , where the samples are monitored periodically by different characterization techniques to assess the microstructural as well as the macroscopic property evolutions due to α -self-irradiation and radiogenic He accumulation. Finally, annealing studies are performed to quantify the defects concentration and identify the He release mechanisms.

Considerable effort was devoted to the synthesis of the starting materials, as each facet of the study presents specific requirements. The homogeneity of the $(\text{U,Pu})\text{O}_2$ samples was crucial in order to constitute an acceptable SNF surrogate for the study of α -self-irradiation. The study of the impact of interfaces implied the synthesis of materials with a desired and well-characterized density of grain boundaries. Microstructural control in the UO_2 samples for ion irradiation was therefore absolutely vital, and also constituted a big innovation introduced by this study. The preparation of the samples is exhaustively described in the corresponding section (chapter 3). Chapter 2 provides an overview on the materials and devices used throughout the whole work, with particular attention to the nuclearized experimental setups which allowed studying hazardous materials such as Pu-doped UO_2 .

Careful characterization was performed on the as sintered material, since that constitutes the main starting reference material for characterizing the radiation effects. During the production of UO_2 for ion irradiation, close interaction between production and characterization was needed to select the best processing parameters, both in the powders synthesis and sintering parts. The characterization of the samples used in this work is presented in chapter 4.

The self-irradiating $(\text{U,Pu})\text{O}_2$ samples were monitored over almost two years of damage accumulation by several characterization techniques, among which SEM, XRD, Raman, TEM, LAF and DSC. The effect of the grain size on irradiation damage and gas precipitation/release was

investigated by means of TEM on sample lamellas prepared by FIB. Each characterization technique provided insight on different aspects of α -damage. A summary and comparison among the gathered data was made in order to relate the accumulated dose, its microscopical effects in terms of defects creation inside the lattice, and the macroscopical consequences on the thermophysical properties of SNF. Results and final conclusions are reported in chapters 5 and 6 respectively.

2 GENERAL EXPERIMENTAL PART

In this chapter, the devices used throughout the whole work are described. The first section (2.1) briefly presents the more standard machines and procedures, which do not differ significantly from their applications in other works or in non-nuclear fields. The second section (2.2) instead includes some deeper insights on the site-specific devices, which were partially modified, or in some cases entirely developed, at the institute to perform otherwise impossible experiments on actinide materials.

The work described in the manuscript was entirely carried out at the JRC-Karlsruhe, except for the ion implantation on UO_2 and ThO_2 (Section 2.1.2.4). In order to perform experiments on radioactive and radiotoxic materials, the research centre is equipped with gloveboxes which are shielded differently according to the activity of the materials they contain. Thorium and natural or depleted Uranium are handled in gloveboxes mainly to rule out any possible risk of incorporation, while the gloveboxes hosting also transuranic elements or enriched uranium have additional dedicated lead shieldings to protect the operators against gamma radiations.

Small amounts of sintered UO_2 or ThO_2 are allowed to be handled in fume hoods, yielding a much lower incorporation risk than powders. For this reason, the characterization of these materials was often significantly quicker than in the case of $(\text{U,Pu})\text{O}_2$.

All the gloveboxes involved in the work are under N_2 atmosphere, whose purity is kept at few ppm of O_2 by purification systems. However, due to the unavoidable failures and/or maintenance periods of the institute N_2 plant over such a long time span (about 3 years), the O_2 level in the gloveboxes was occasionally found to be higher.

2.1 Standard techniques

The machines listed in this section did not undergo any special design step or modification, but they are in most cases completely included in a glovebox. Besides the nuclearisation of the devices, they do not present any major difference from the analogue machines employed in other fields.

2.1.1 Samples preparation – powders synthesis and sintering

All the devices used in the samples preparation were standard devices, with the exception of the SPS used to sinter the UO_2 powders which will be treated in section 2.2.1. All of the furnaces listed in the present section are connected to high-purity gas bottles and can be operated with oxidising, inert and reducing atmospheres.

Pre-calcination of $(\text{U,Pu})\text{O}_2$ powders was performed in a Pilz tubular furnace, while for calcination they were moved to a tubular Linn FR0-H-2-120/250.

Calcination of UO_2 powders was performed also in a Linn FR0-H-2-120/250 alumina tubular furnace dedicated solely to Uranium and Thorium bearing compounds. This same furnace was also used for the final annealing of the HP – SPS samples described in 4.2.3.9.

$(\text{U,Pu})\text{O}_2$ powders were pressed using a Laufer VIUG16 press and then successively sintered in a Degussa VSL 10/18 cold wall furnace.

2.1.2 Samples characterization

2.1.2.1 XRD – X-ray diffraction

Important information about the structure of a crystalline solid are extracted from its interaction with an incoming monochromatic X-ray. Max von Laue was the first to theorize that crystalline lattice could act as 3-D diffraction gratings for X-ray wavelengths similar to the spacing of planes, and was awarded the Nobel Prize in Physics in 1914 for his finding. X-rays Diffraction (XRD) is based on the constructive interferences of the monochromatic X-ray diffracted by the crystal.

Before describing the principles of XRD, it might be useful to recall the concept of *reciprocal lattice*, which is the Fourier transform of the *direct lattice*. In crystallography, the direct lattice is the Bravais lattice, and its Fourier transform is composed by the Miller indexes associated to the families of parallel planes in the direct space. In other words, each family of planes hkl of the direct lattice is represented by a point of coordinates (h,k,l) in the reciprocal lattice.

When a crystalline material is illuminated by an X-ray beam, its atoms act as scattering centres and diffract the radiation in every direction. Only for very specific angles (configurations), however, the interference among the diffracted beams will be constructive, and hence the signal clearly detectable. The condition to have constructive interference was formulated by von Laue considering a crystal of identical microscopic objects positioned at Bravais lattice sites specified by the vector $\mathbf{R} = n_1\mathbf{a}_1 + n_2\mathbf{a}_2 + n_3\mathbf{a}_3$. Constructive interference occurs only when the scalar product of the scattering vector \mathbf{Q} (i.e. the difference between incoming and outgoing wave vectors) and the crystal lattice \mathbf{R} fulfils the condition:

$$\mathbf{Q} \cdot \mathbf{R} = 2\pi \times \text{integer} \quad (32)$$

Which is fulfilled by vectors like $\mathbf{G} = h\mathbf{a}_1^* + k\mathbf{a}_2^* + l\mathbf{a}_3^*$, the vector specifying the reciprocal lattice positions, hence for $\mathbf{Q} = \mathbf{G}$, all the scattering vectors that are vectors of the reciprocal lattice. This condition can be demonstrated to be equivalent to the more popular Bragg Law, which was formulated taking into account reflections on a 2-D stack of crystalline planes.

The practical outcome is presented in Figure 36-a: when an X-ray beam impinges a crystal with the correct angle, it will be diffracted in the so-called *Laue spots*, each one corresponding to a particular reciprocal lattice vector of the crystal. Information about the size and symmetry of the unit cell can be extracted by the spots positions, while nature and lattice positions of the atoms can be derived from the spots intensities.

In most practical cases however materials are polycrystalline, which means that the impinging X-ray beam is diffracted by every crystal constituting the sample in a different direction according to its relative orientation. As a result, the recorded pattern is not constituted by the Laue spots but by smooth diffraction rings around the beam axis (*Debye-Scherrer rings* – Figure 36-b). Moreover, for every family of planes there will be some crystals correctly oriented to diffract, hence the rings of all the families will be visible.

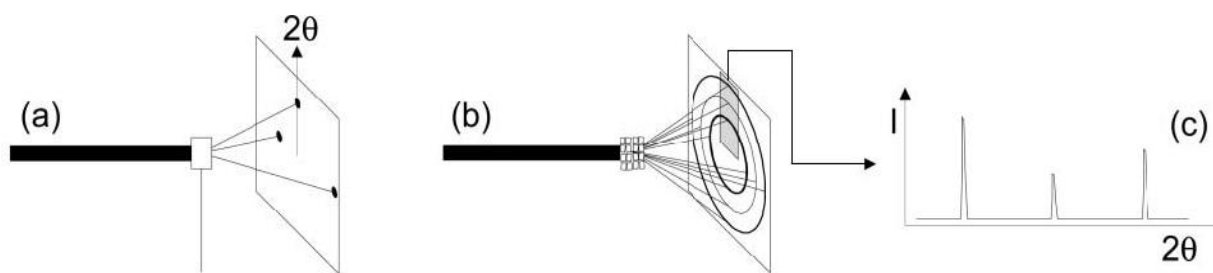


Figure 36: example of single crystal (a) and polycrystalline/powder (b) X-ray diffraction. While in (a) the beam is diffracted only for points corresponding to a reciprocal lattice vector, in (b) this effect is averaged over a large amount of crystals resulting in circles. (c) Bragg peaks obtained by measuring a polycrystalline sample in a Bragg-Brentano diffractometer. (240)

These diffracted patterns can be recorded either on a film detector (Debye-Scherrer film chamber) or using a scintillator detector mounted on a goniometer (Bragg-Brentano diffractometer). In diffractometers, the detector is rotating around the sample, while also the angle between the impinging X-ray and the sample is varied. The output diffraction pattern is then given by the signal intensity as a function of the detection angle, with peaks at the angles resulting in constructing diffraction interferences (*Bragg peaks* – Figure 36-c). Depending whether the X-ray source or the sample is moving (in addition to the detector), the configuration of the diffractometer is labelled as θ - θ or θ - 2θ respectively (Figure 37).

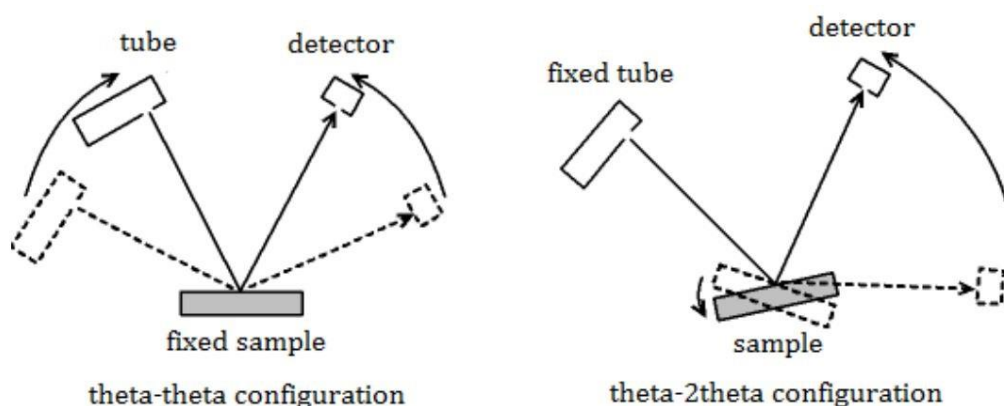


Figure 37: scheme of the two possible Bragg - Brentano configurations. In the θ - θ configuration, the sample is stationary and the X-ray source is rotating, while in the θ - 2θ it is the reverse. θ - θ configuration is preferred in case of loose samples, such as powders. (241)

XRD patterns can then be analysed to extract important information about the crystal structure. Detailed analyses are generally performed using the so-called Rietveld refinement, from the name of its theorizer (190). This technique calculates the theoretical diffractogram of the expected structure based on data libraries, and then uses it to fit the experimental by least-square optimisation. Data such as the size and symmetry of the cell (hence the peak indexes h,k,l), have to be inserted by the operator and are then refined during the fit.

The breadth of the Bragg peaks also carries some information about the microstructure, since both reduced crystallite size and local variations in the lattice cell (*microstrain*) decrease the coherence of the diffracting domains, resulting into diffused peaks rather than sharp lines. After subtracting the possible device contribution (*instrumental broadening*) to the peaks breadth, the contribution of

crystalline domain size and microstrain can be decoupled, based on their different dependence on the Bragg angle, as first demonstrated by Williamson and Hall.(191)

XRD devices

(U,Pu)O₂ powders and disks were analysed using a Bruker D8 diffractometer mounted in a $\Theta - 2\Theta$ Bragg–Brentano geometry with a curved Ge (1,1,1) monochromator and a ceramic copper tube (40 kV, 40 mA), and supplied with a LinxEye position sensitive detector. Samples were dispersed in isopropanol and mechanical ground, then poured onto flat Si(911) specimen holders which provide a very low background. Data were acquired in the 20 – 120 ° range with steps of 0.0132 ° and a counting time of 2 s.

UO₂ and ThO₂ samples were probed using a Rigaku Miniflex 600 also in Bragg – Brentano configuration, with a ceramic copper source (40 kV, 15 mA) but without monochromator ($K\alpha_1 = 1.5406 \text{ \AA}$, $K\alpha_2 = 1.5444 \text{ \AA}$), supplied with a Hy-Pix 400MF 2D HPAD detector. Just like for (U,Pu)O₂, samples were prepared by mechanical grinding but dispersed in paraffin to be poured onto the Si holders. This device is installed in a fume hood at the JRC-KA, which was fundamental to have quick feedback on the effectiveness of the production routes adopted, but required additional care while handling and crashing the material. For sake of quickness, analyses were sometimes performed on smaller 2Θ ranges and with lower acquisition times.

Both devices were calibrated using LaB₆ as reference material.

Analysis of the diffraction patterns were performed using the software Jana2006 (192) using Pseudo – Voigt functions for fitting the peaks shape. Rietveld refinement was performed for lattice parameter evaluation, while microstrain and crystallite size were estimated by applying the Williamson – Hall approach. (191)

2.1.2.2 Scanning Electron Microscopy – SEM

Microstructural characterization of UO₂, ThO₂ and (U,Pu)O₂ samples was performed by means of electron microscopy. This non-destructive technique employs electrons instead of light to image the surface of the sample to be analysed, and furthermore allows gathering information about the chemical composition through the emitted X-rays. The principle behind electron microscopy relies on the acceleration of electrons to high energy, thus having much shorter wavelengths than the visible light, providing hence a better resolution, as described by the Rayleigh equation:

$$R = \frac{0.61 \lambda_e}{\eta \sin \alpha} \quad (33)$$

Where η is the refraction index of the medium through which radiation passes, α is half of the maximum solid angle captured by the electron lens and λ_e is the wavelength of the e⁻, given by:

$$\lambda_e = \frac{h}{m_e v_e} \quad (34)$$

In which h is the Planck constant and m_e and v_e are the mass and the velocity of the e⁻, respectively, which can be accelerated by increasing its momentum through the application of an acceleration potential V as follows:

$$v_e = \sqrt{2Vem_e} \quad (35)$$

With e being the charge of the electron.

Depending on the type of interaction (reflexion, emission, diffraction, transmission), different analyses can be performed. In Scanning Electron Microscopy (SEM), Secondary Electrons (SE) and Back Scattered Electrons (BSE) are collected for imaging. SE are the excited electrons coming from the atoms down to several nanometers under the sample surface, providing high resolution images of its topology. BSE instead are primary e^- from the beam that undergo high angle scattering, which is an event strongly dependent on the atomic number Z of the hit atom. BSE provide very good elemental contrast, with the disadvantage of carrying lower energy and hence yielding a worse resolution.

The e^- beam also knocks out a small fraction of e^- from the inner shells of the sample atoms (inner shell ionization), which are quickly replaced by outer shell e^- with the emission of a characteristic X-ray. The energy needed for the inner shell ionization to take place depends on the atomic number, making the emitted X-ray a very useful fingerprint for elemental mapping of the sample surface, although with low resolution ($0.5 \mu\text{m}$) due to the large volume of material probed. This phenomenon is exploited in Energy-dispersive X-ray spectroscopy (EDX, EDS).

When the sample to be characterized on a SEM is non-conductive, the region being studied gets charged with the electrons from the beam that cannot escape the material, leading to a large brightness spot which impedes the production of good images; this is the so-called charging-effect. In order to avoid such problem samples need to be coated with some conducting element, typically Carbon or Gold.

Figure 38 (193) shows the volume of sample interacting with the e^- beam and the depth of origin of the different detectable signals.

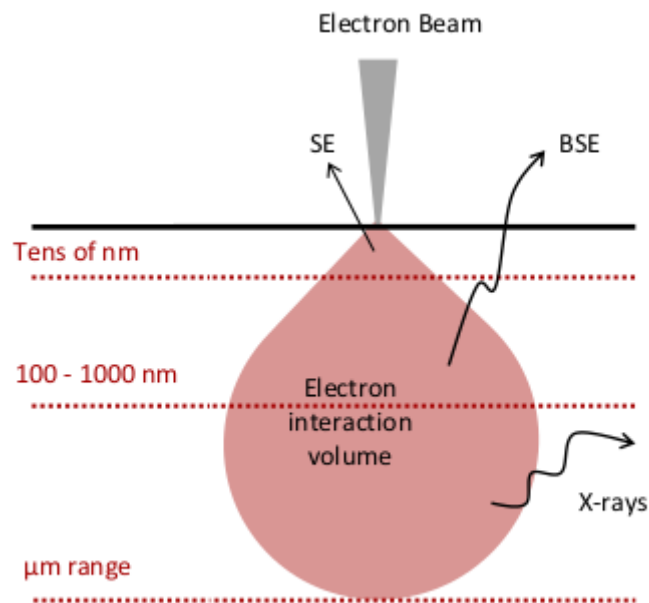


Figure 38: scheme of the volume of sample interacting with the electron beam, and corresponding depths probed by SE, BSE and EDS characterizations. (193)

SEM characterization at the JRC – Karlsruhe

Images of (U,Pu)O₂ samples were obtained in a Philips/FEI™ XL40 SEM operated at 25 kV, equipped with a SAMx Energy Dispersive X-ray analysis system (EDX). This microscope (high-voltage unit, column, chamber, and turbomolecular pump) is placed inside a glovebox, while the components which are not getting in contact with the active materials (primary vacuum system, the water-cooling circuit, and the acquisition electronic) are outside.

UO₂ and ThO₂ samples were observed using a dual-beam Focused Ion Beam (FIB) ThermoFisher Scientific (ex FEI™) Versa 3D SEM with Field Emission Gun (FEG) operated at 30 KeV, and also equipped with an XFLASH Detector 410M EDX. The grain size was evaluated with the intercept method according to the standard ASTM E112 – 12. (194)

This last microscope is capable of operating as Environmental SEM (ESEM), reducing the charging-effect on the samples and therefore no coating was required.

Initially, the FEG-SEM was not available yet, so during the development of the process for the achievement of nanograined dense samples, characterization was performed on a Vega Tescan TS5130LSH operated at 20 kV. This microscope was also equipped with an Oxford EDX for the elemental analysis. In this case gold coating was necessary to obtain good quality images.

These last two devices are not inside a glovebox, and the vacuum pumps are provided with filters to purify the exhaust gas of the chamber from any particle coming from the samples.

2.1.2.3 Differential Scan Calorimetry

Important data about a material can be extracted from calorimetry measurements, such as phase equilibria, enthalpy of formation or mixing, melting point or heat capacity. In this work, Differential Scanning Calorimetry (DSC) was used to measure the changes induced by self-irradiation on the apparent heat capacity C_p^* of the α -doped (U,Pu)O₂ samples.

DSC is based on measuring the heat flow needed to impose a certain temperature schedule to two crucibles, one containing a reference and the other the sample to be measured. Both heat flows are evaluated by difference with a previously performed *blank* run with the empty crucible. The heating schedule can be constant (continuous method), or proceed stepwise (step method). When performing the DSC measurement with the continuous method, the heat capacity can be calculated for each point using this relation:

$$C_p(sample) = C_p(ref.) \cdot \frac{m_{ref.} \cdot (\Phi_{sample} - \Phi_{blank})}{m_{sample} \cdot (\Phi_{ref.} - \Phi_{blank})} \quad (36)$$

Where m_{ref} and m_{sample} are the masses of the reference and sample respectively, and Φ are the heat fluxes of the corresponding runs. In the step method, the integral flow over each temperature step is compared, providing hence an average value assigned to the mean temperature of the incremental step.

DSC characterization at the JRC – Karlsruhe

The apparent heat capacity C_p^* of the (U,Pu)O₂ samples was measured using a NETZSCH Thermal Analyser STA 409 C. All the measurements were performed on samples of minimum 100 mg in the range 400 – 1500 K with a 15 K/min heating and cooling rate, under an Ar flow of 100 mL/min as

cover gas. In the present work, each measurement constituted of 5 heating-cooling cycles: a first run with empty crucibles to create the baseline, then a second run with a known calibration material (sapphire disk), successively two runs with the sample to be analysed (the need of repeating the experiment is soon explained) and finally another calibration run with the same material as before.

In our case, due to the isotopic composition of the samples to be analysed, self-heating effect had to be considered. The heat produced by the ^{238}Pu present in the samples is indeed non-negligible, and if not taken into account can lead to misinterpretation of the acquired data.

In order to discern and isolate the self-heating contribution to the measurement, a second cycle is repeated after the first measurement (which is, by definition, perturbed by the presence of defects). While heating up the annealed sample, the ascending curve results shifted downwards by effect of the radiogenic heat, meanwhile in the cooling the descending curve is symmetrically shifted upwards for the same reason. The average of the two ascending and descending curves gives indeed exactly the theoretic $(\text{U,Pu})\text{O}_2$ C_p . (71)

Moreover, the ascending curve of the second cycle serves as baseline for the quantification of the defects effect on the ascending curve of the first cycle (as the subtraction from the first cycle descending curve would be hugely perturbed by the self-heating effect).

Finally, the self-heating effect can be exploited as calibration method to estimate the recovery of the latent heat of the lattice defects during thermal healing. The difference in the first and second ascending curves is indeed the net contribution to C_p^* of defects healing during the annealing of the sample. Once this effect on the C_p^* has been quantified, it can be converted into released heat by using the self-heating effect on C_p^* as a reference, since the heat generated by the sample can be indeed easily calculated from its chemical and isotopic composition.

2.1.2.4 *ThO₂ irradiation*

As mentioned in section 1.4.2.2, He implantation has been widely used to simulate α -damage on UO_2 (158,163) as well as to understand its atomic and gaseous behaviour in the matrix (172,173,175); similar studies were performed on Xe.(182,187) In the present work, a first experiment was performed through a Rapid Turnaround Experiment (RTE) proposal to the Nuclear Science User Facilities (NSUF) network, in the framework of the collaboration between Idaho National Lab (INL) and JRC in the International Nuclear Energy Research Initiative (INERI). The main focus of the project was the investigation of the effect of the grain size on the rare gases retention/release, by implanting He and Xe in UO_2 and ThO_2 of different microstructures. The energy of the ions was kept low to assess also the ballistic damage induced as a function of the grain boundaries density, but at the time of writing characterization has been performed only to investigate bubbles precipitation. The irradiation conditions are summarised in Table 3.

Ions	Energy (keV)	Dose [ions/cm ²]	T [°C]	Duration [min]
He	16	10^{16}	RT – 300 – 600	30 min
Xe	300	10^{16}	300 – 600	30 min

Table 3: irradiation conditions of the Xe and He ion implantations on UO_2 and ThO_2 .

The ion implantations were performed on FIB lamellas of 100 nm of thickness. Fragments of pellets of different grain sizes (already extensively characterized at the JRC) were shipped to INL for FIB

preparation. The UO_2 and ThO_2 lamellas were then transported to Argonne National Lab (ANL) to be implanted and in-situ characterized by TEM at the Intermediate Voltage Electron Microscopy (IVEM) – Tandem facility. The TEM available at IVEM – Tandem is a Hitachi-9000 with LaB_6 filament, equipped with a GATAN OneView digital camera (4k x 4k pixels, 16-bit dynamic range) and GATAN double-tilt heating stage. The microscope was operated at 300 keV while used for microstructure characterization, and the electron beam was turned off during irradiation experiment.

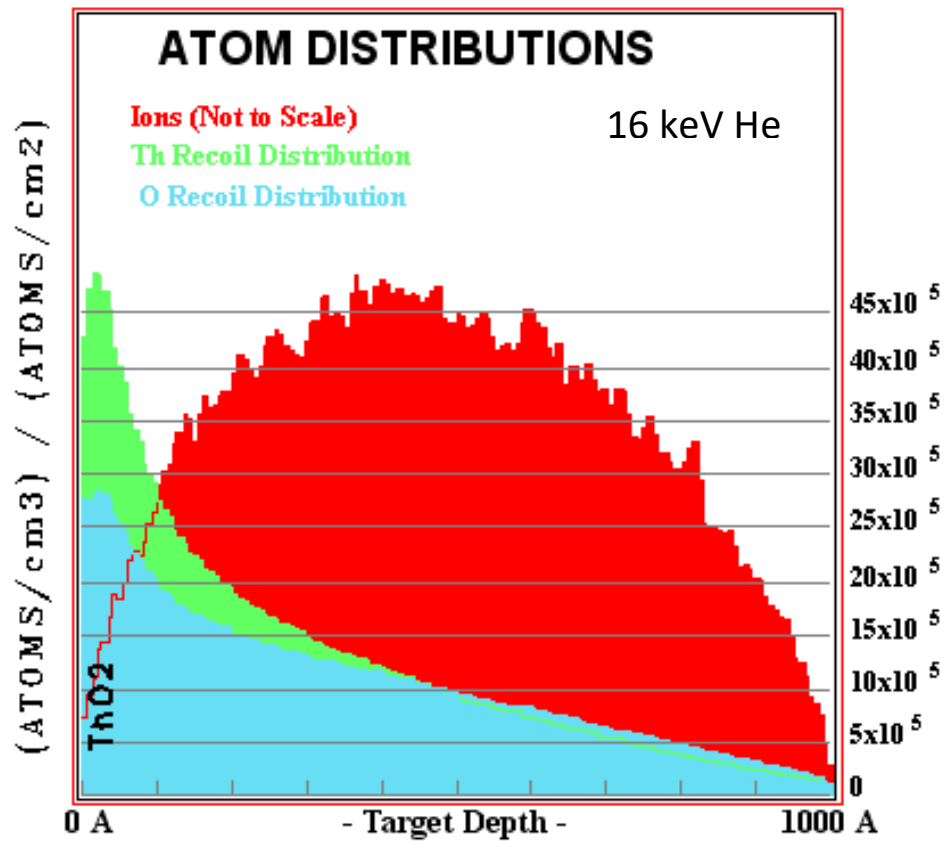


Figure 39: SRIM (75) simulation of the implanted He profile and ballistic damage introduced in the matrix.

The implantations were performed with an incidence angle of 15° with respect to the normal direction of the lamellas, resulting from the imposed 30° angle due to the TEM and ion beam configuration and appropriate tilting of the sample stage. Figure 39 shows that the calculated SRIM (75) He deposition profile, for such an incidence angle and ion energy (16 keV), entirely falls within the thickness of the lamella, allowing ideal observation of bubble formation. The ballistic damage introduced in the matrix is also plotted.

It is worth noting that SRIM does not include the temperature as a parameter in the simulation. For this reason, the graph presented Figure 39 does not take into account flattening of the deposited ions profile (169) nor damage healing.

2.2 Innovative techniques

Contrarily to the devices described in section 2.1, those that will be described here present significant modifications with respect to commercially available machines. In some cases (SPS, TEM) the modified machines were adapted according to the requirements of the institute by the supplying company, and then were entirely or partially included in a glovebox. Other devices instead represent a complete innovation as the setup was entirely developed at the JRC. The Raman spectrometer instead was not nuclearized at all, but the innovative JRC-developed encapsulation system allows the analyses of highly active samples.

2.2.1 SPS

UO₂ and ThO₂ powders were sintered into dense disks using an FCT Systeme GmbH SPS modified for inclusion in a 1 x 1 x 1.5 m glovebox. At the time of writing, the glovebox has not been contaminated with transuranic elements yet, hindering the possibility to produce nanostructured (U,Pu)O₂ samples. Some pictures of the SPS device and its components are shown in Figure 40 A-C.

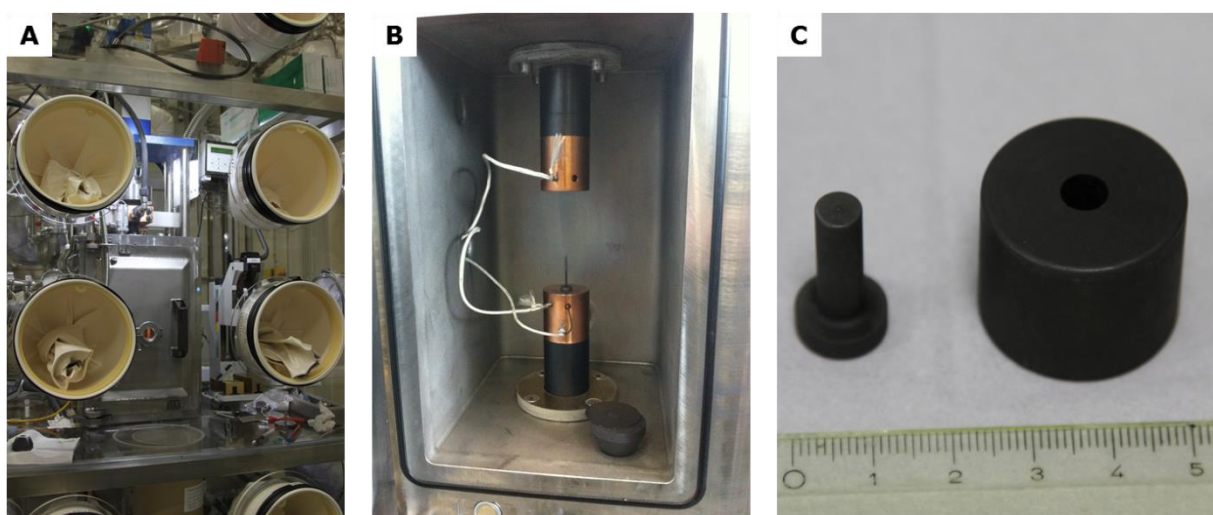


Figure 40: (A) - nuclearized small scale SPS at the JRC-KA; (B) - SPS water-cooled chamber; (C) - SPS graphite die and punch. (195)

In order to fit the machine into a glovebox, the main modification to be done was a significant dimensional downscaling of a standard FCT Systeme GmbH SPS. This downscaling did also make sense for the fact that the dimensions of conventional nuclear fuels are smaller than the size of the pieces commonly pressed by SPS. The small scale SPS inside the glovebox is shown in Figure 40-A.

Thanks to the reduced diameter of the samples to be pressed, high pressures could be reached with the use of an electromechanical spindle instead of a hydraulic pump, reducing enormously the components to be included in the glovebox. Cables could replace the oil lines, resulting in a much more compact system, with fewer components that would eventually become contaminated (including the organic waste constituted by the oil itself).

Directly linked to the smaller dimensions of samples and dies (Figure 40-C), is the reduced size of the water-cooled chamber (Figure 40-B), which was kept anyways relatively large in order not to make the sample loading-unloading procedures too troublesome. As a drawback, the accurate measurement of the temperature via pyrometer on such small samples was very complicated, making it extremely more suitable and accurate to use instead a thermocouple located in the fixed

lower punch of the compaction unit. The complete nuclearization of the machine, together with the first applications of the newly nuclearized device, was described by Tyrpekl et al. (195)

2.2.2 Transmission Electron Microscopy

Very important information about the microstructure of the materials can be extracted by Transmission Electron Microscopy (TEM), which takes advantage of the same principles described in 2.1.2.2 but exploiting different interactions of the e^- with the sample. In TEM, a collimated e^- beam is passing through the sample and electrons are collected afterwards, either to obtain images or diffraction patterns depending on the focal length of the camera.

Electron diffractions are obtained by recording the e^- scattered by the atoms of a small region in the sample (Selected Area Electrons Diffraction – SAED), setting the focal length of the electronic lenses exactly on the camera CCD, obtaining the diffraction pattern of the crystal. This tool is very useful for identifying crystalline phases and orientations.

Imaging instead can be performed either by looking at the transmitted (Bright Field – BF) or scattered e^- (Dark Field – DF). In BF images, only the unscattered e^- are collected, and hence the sample parts which are thicker, denser or include heavier atoms are pictured in dark due to the greater e^- scattering in the region. DF images instead are acquired by focusing on the scattered e^- , hence the contrast is opposite, and the sample appears light on a dark background (where there is no matter to scatter e^-). The most interesting feature of DF imaging is that intensity of the collected signal changes with the relative orientation of the sample crystals with the beam. With this tool, either one selected crystal can be imaged by focusing on the corresponding diffracted point, or the combination of different diffractions can be imaged altogether resulting in different contrast for the different crystal orientations.

Scanning Electron Transmission Microscopy (STEM) is another imaging capability of a TEM, in which the e^- beam is focused and then rastered along the material. The image is then reconstructed from the information recorded point-by-point. Also STEM can be performed in BF or DF or DF depending of the type of detector used for the collection of e^- .

Elemental analysis can be performed by EDX in TEM in the same way as for SEM (2.1.2.2), but Electron Energy Loss Spectroscopy (EELS) offers a broader range of capabilities. It relies on studying the amount of electrons reaching the camera as function of the energy they lost on the interaction with the electrons from the sample. The energy that can be shared between beam electrons and core shell electrons is element-specific, and thus can be used for identifying the composition of the sample, as peaks will appear for those energies. Moreover, the shape of these peaks is sensitive to the oxidation state and chemical environment of the atoms in the sample, yielding then more information with respect to EDX. The thickness of the sample can also be probed by means of EELS provided the mean free path on the material can be known or estimated for electrons.

TEM characterization at the JRC – Karlsruhe

TEM analyses of all samples were performed using a FEI™ Tecnai G2, equipped with a field emission gun, a GATAN Tridiem GIF camera for EELS analyses, an Oxford EDX system, and a high-angle annular dark field (HAADF) detector for the scanning transmission electron microscopy (STEM) imaging.

This device was not included entirely in a glovebox, but rather modified during its fabrication in order to allow the use of highly active or irradiated materials. As shown in Figure 41, a small glovebox was attached to the microscope by means of a flange. This flange has been inserted in the octagon hosting the objective lenses, and allowed the mounting of the glovebox around the compustage. The insertion of materials in the microscope glovebox is done thanks to a double door allowing confinement of contamination (La Calhène DPTE transfer system, Getinge, Rush City, MN).

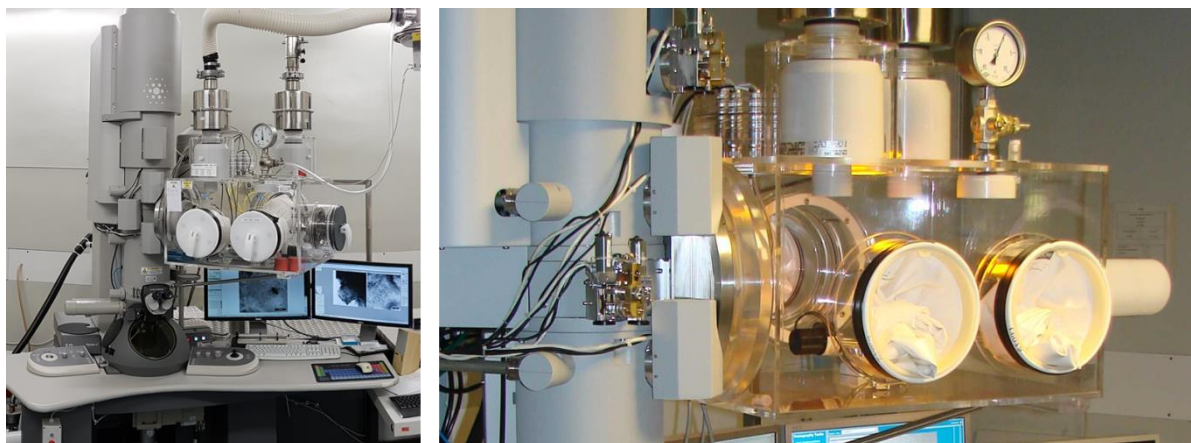


Figure 41: TEM available at the JRC-KA. The picture on the right shows a detail of the glovebox attached to the compustage of the microscope.

Samples were indeed prepared in a separated glovebox (equipped with dimpler, ultrasonic disk cutter, ion-milling, electrochemical etching devices and plasma cleaner) and subsequently moved to the microscope. The samples preparation was done by crushing few milligrams of material in methanol in an agate mortar and then, after decanting, dripped over a 400 mesh copper grid coated with carbon.

2.2.3 Raman spectroscopy

Insight about atomic bonds and microstructural disorder can be acquired using Raman, a very useful non-destructive technique which exploits the interaction of the samples with incoming monochromatic electromagnetic radiation, and requires no sample preparation.

Raman spectroscopy is based on the inelastic scattering of photons from a crystal, an effect which was first observed by V. C. Raman, who was awarded the Nobel Prize for his findings and gave the name both to the phenomenon (*Raman effect/scattering*) and the technique.

Raman scattering takes place when visible light photons impinging a crystal are emitted at different optical frequencies. Due to the polarizability of the molecules constituting the crystal, an oscillating polarisation is induced by the incoming photons. If this oscillating polarisation can couple with one allowed vibrational mode of the crystal, the molecule will be excited to another vibrational state. As a result, a phonon is created in the lattice, and the photon is scattered at lower frequencies, the difference (*Stokes shift*) in energy being the one needed for the change in the vibrational energy. A similar but opposite effect (*anti-Stokes shift*) can also take place, when the final state of the molecule has a lower energy than the starting one, and a more energetic photon is emitted by annihilation of a phonon in the crystal. However, Stokes mechanism is much stronger than anti-Stokes at room T. Raman spectroscopy measures the Stokes shift of the emitted photons, hence

provides information about the crystal bonds by exploring the allowed vibrational modes in the lattice.

Recalling the notion of reciprocal space quickly illustrated in Section 2.1.2.1, it is now time to introduce the *Brillouin zone*, i.e. the primitive cell of the reciprocal lattice, or, in other words, a representation of the allowed energetic regions in the crystal. In an ideal lattice, Raman scattering takes place at the centre of the Brillouin zone, which is the zone of most symmetry.

It can be demonstrated that to be active in Raman spectroscopy, a vibrational mode has to produce a change in the polarizability of the molecule, while it is going to be active in infrared (IR) spectroscopy when it produces a change in the dipole moment. This is called the *selection rule*, and it implies that no mode can be active in both Raman and IR spectroscopies in a symmetric molecule.

Fluorite structures with MO_2 formula unit have 3 triple-degenerate frequencies of vibration at the centre of the Brillouin zone. One is the acoustic mode of the T_{1u} representation and it is measured in Brillouin scattering. The other two are the triple-degenerate optical modes of the T_{1u} and T_{2g} , and are active in IR and Raman respectively. T_{1u} (*ungerade*) is related to the oscillation of the metal and O atoms in antiphase with each other, and it splits into a longitudinal and a transversal optical component (LO and TO respectively). The Raman-active T_{2g} (*gerade*) instead arises from the antiphase oscillation of the O atoms around the metal atom which is at rest.

Raman characterization at the JRC – Karlsruhe

Raman spectra of the $(\text{U,Pu})\text{O}_2$ samples were acquired using a Horiba Jobin-Yvon T 64000 spectrometer equipped with a 1800 grooves/mm grating, a low noise LN_2 cooled CCD detector and an edge filter blocking the laser elastic scattering coming from the sample. On the device is mounted a long working distance (10.6 mm) objective which offers a 0.5 numerical aperture with a X50 magnification. Acquisitions were performed from 200 to 1300 cm^{-1} using a 647 nm Kr^+ excitation laser. The spectrograph is calibrated with the T_{2g} excitation of a Si single crystal (520.5 cm^{-1}).

Contrarily to the other devices described in this section, this machine is never in direct contact with the active sample and hence it is completely outside of a glovebox and non-contaminated. This is possible thanks to an innovative setup designed at the JRC-KA, which limits the confinement to the active sample.

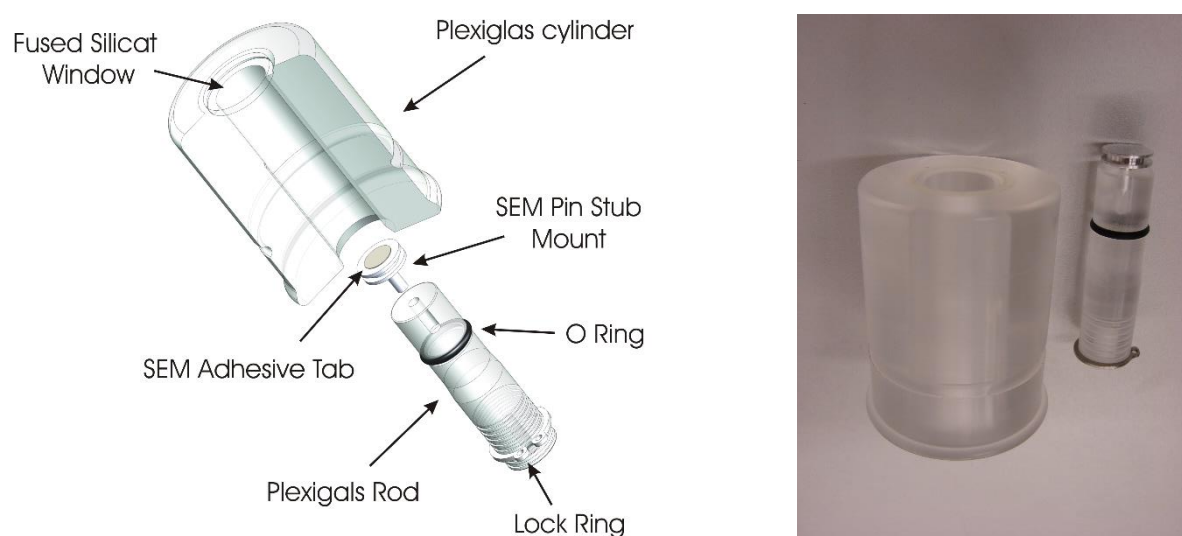


Figure 42: scheme (left) and picture (right) of the Plexiglas sample holder designed at the JRC-KA for Raman characterization of nuclear materials. (196)

A scheme of the sample holder is shown in Figure 42 (left) and some of its components are pictured in Figure 42 (right). The sample holder assembly is constituted of a Plexiglas hollow cylinder closed on one side by a one wave optically polished fused silicate window, which is tested for tightness after gluing. From the other side, the sample, mounted on a standard aluminium pin stub, is placed right below the quartz window by means of a Plexiglas rod. On the rod, an O-ring preserves the tightness of the assembly while a lock ring prevents the contact between the sample and the silica. A screw is fixed at the end of the rod to allow controlling the distance between the window and the



Figure 43: sample holder connected to the bag (left) and bag-out operation of a loaded sample holder from a glovebox at JRC-KA. (196)

sample.

This sample holder is then hermetically fixed onto a bag of those used for the transfer of materials between gloveboxes, as shown in Figure 43 (left), and then tested again for tightness. Such a bag can then be attached to a glovebox, where the sample is prepared and placed in the cylinder, and then detached after welding as in a regular bag-out operation (Figure 43 – right).

Raman analyses are then performed through the quartz window as shown in Figure 44. A more detailed description of the design and applications of the setup can be found in the work of Naji et al. (196)

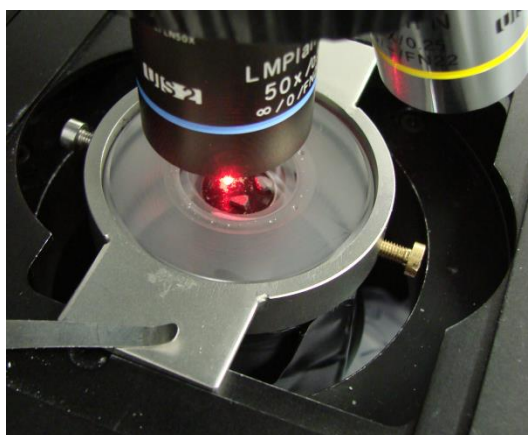


Figure 44: Raman acquisition from a highly active sample confined inside the Plexiglas sample holder through the quartz window.

2.2.4 LAser Flash method

The thermal conductivity degradation of the (U,Pu)O₂ samples was followed by measuring the thermal diffusivity by LAser Flash method. (197) Thermal conductivity k [W/m·K] and thermal diffusivity α [m²/s] are related by the following law:

$$k = \alpha \rho c_p \quad (37)$$

Where ρ and c_p are the density [kg/m³] and the specific heat capacity [J/kg·K] of the measured sample.

In LAF, thermal diffusivity is evaluated by recording the temperature perturbation profile on one face of a sample of well-defined geometry after a laser heat pulse is deposited on the opposite face. The temperature of the sample before the application of the pulse has to be steady and very accurately controlled. Generally, the sample is heated up externally by a furnace, and is held in place by thermally insulating holders to minimize the heat losses.

The output thermogram is then analysed using realistic heat transfer models, which calculates thermal diffusivity and the various possible heat losses. The geometry of the sample and the temperature of the experiment have extreme importance in the model, and hence have to be quantified as accurately as possible.

LAF characterization at the JRC – Karlsruhe

Thermal diffusivity measurements were performed in a machine developed in the past at the JRC-KA. (198) This unique setup allows the simultaneous measurement of thermal diffusivity and heat capacity of the sample, and can be used also to detect phase transitions. In the present work however, only the thermal diffusivity was measured, and for the calculation of the thermal conductivity the heat capacity predicted by Duriez et al (71,199) was used. A scheme of the apparatus is shown in Figure 45.

In the setup available at JRC – KA, the sample is positioned on a sapphire glass inside a graphite tube, which is heated up by high frequency induction coils under vacuum ($10^{-4} - 10^{-7}$ mbar). The vacuum chamber is water cooled and, thanks to this setup, measurements can be performed from 500 to 1600 K. This part of the LAF device is placed inside a shielded glovebox, allowing to measure highly contaminated samples.

Once a steady temperature is reached, a Nd:YAG laser applies a pulse on the lower side of the sample (front face). The thermal radiation emitted from the upper side of the sample (rear face) is focused with lenses and conveyed through glass fibres to an InGaAs or Si photodetector, for low or high T respectively. A fast-transient recorder acquires the amplified signal and converts it into a temperature profile, and the same signal is also used to determine the absolute reference temperature of the sample.

The resulting thermogram is fitted with the axial temperature equation derived from the analytical solution of the heat flow equation in the sample. A combination of Newton-Raphson, Levenberg-Marquardt and Steepest Descent methods (200) is used and the thermal diffusivity is extracted.

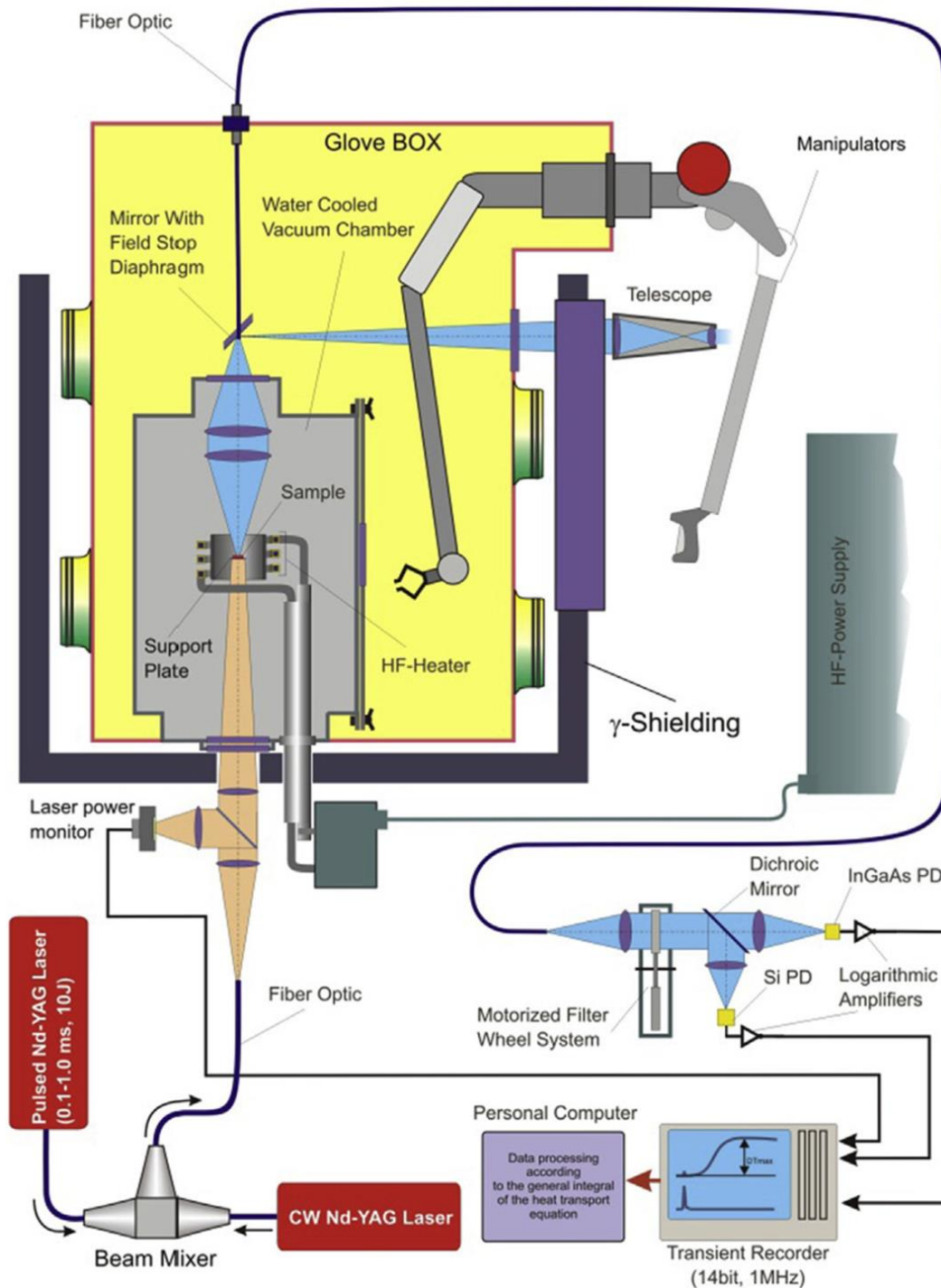


Figure 45: detailed scheme of the LAF system developed at the JRC-KA. (200)

Given the complexity of the model, sample-related parameters, as well as experimental conditions (laser pulse parameters), have to be determined as accurately as possible. For this reason, a sample with a very regular geometry is normally required, and thus specimens for LAF analyses were prepared on purpose with different specifications from the rest. In general, a disk thickness of at least 1 mm is targeted to have relatively low uncertainties, and the faces of the sample have to be parallel. More details on the LAF history and theoretical background, equations solution and data

fitting strategy can be found in the work of Sheindlin et al (198), which describes the design and setup of the machine at the JRC-KA.

2.2.5 Knudsen Effusion Mass Spectrometry

Quantification of the radiogenic He accumulated in the (U,Pu)O₂ samples due to α -decays was done by means of Knudsen Effusion Mass Spectrometry (KEMS). Mass Spectrometry (MS) is an analytical technique in which ionised species are sorted according to their mass/charge ratio, allowing quantification of the chemical species composing the sample. Generally, the sample is ionised by e⁻ bombardment, and its charged fragments are accelerated and then deflected thanks to an electric or magnetic field onto the detector. Different mass/charge ratio result in different deflections, so ions can be identified and counted as a function of their mass/charge ratio.

KEMS combines the MS with a Knudsen Cell, an effusion cell whose orifice is dimensioned in order to fulfil the Knudsen condition, hence having diameter lower than the mean free path of the gas molecules developed inside the cell. The flux of molecules escaping the cell is thus proportional to the partial pressure of the said molecules inside the cell. (201) This allows also the measurement of other thermodynamic properties such as sublimation enthalpies, ionisation energies of gaseous species, enthalpies of formation and activity coefficients.

However, in the present work, this device was used only to study the kinetics of gas release, by quantifying the He released from the samples as a function of the annealing temperature. Since the KEMS allows quantitative determination only of condensable vapours, it was operated in combination with a second device entirely developed at the JRC – Karlsruhe (while the KEMS can be considered as a nuclearized version of a more standard machine) called Quantitative Gas Measurement Setup (Q-GAMES).

KEMS characterization at the JRC – Karlsruhe

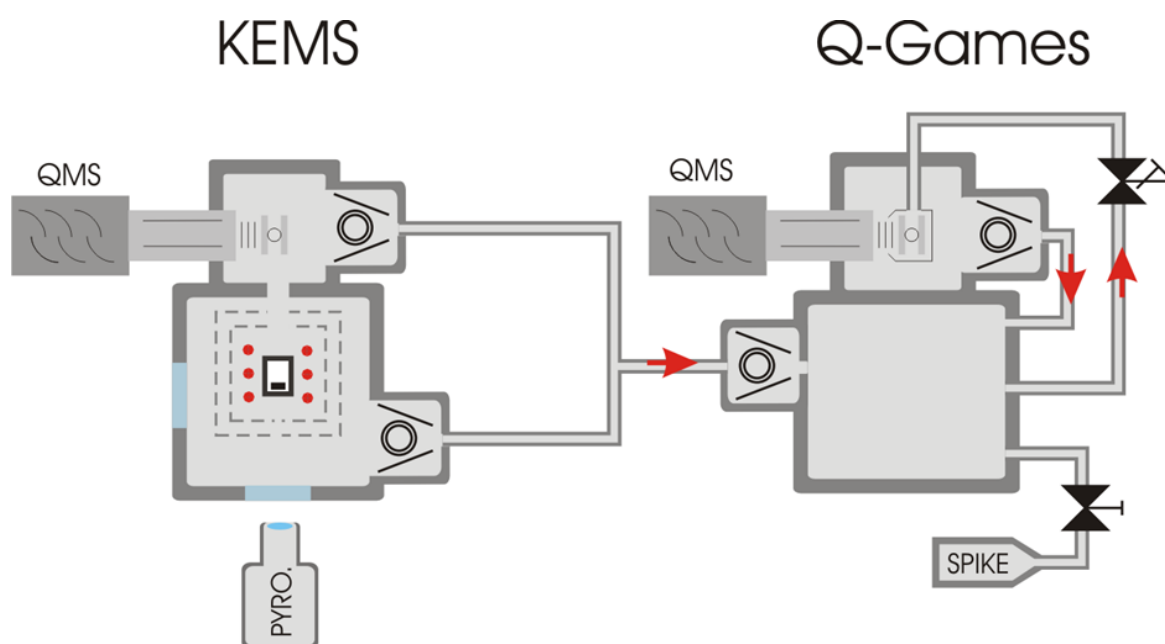


Figure 46: Knudsen Effusion Mass Spectrometry (KEMS) and Quantitative Gas Measurement Setup (Q-GAMES) schematic setup.

The setup used for Helium desorption from (U,Pu)O₂ samples consisting of a high temperature KEMS and the Q-GAMES was developed at JRC-KA to allow measurements at temperatures up to 2800 K on highly active materials. A sketch of the two devices connected to each other is presented in Figure 46.

Figure 47 shows a scheme of the KEMS instrument, whose design and setup were explained in detail by Hiernaut et al (202) and Colle et al (203). The cell (number 1 the figure) is made of a refractory material (BN, W, ZrO₂ or Al₂O₃) and has an inside diameter of 7 mm and an effusion hole of around 0.5 mm. The temperature is measured with a pyrometer through a horizontal blackbody hole. A gas inlet at the bottom of the cell allows a small quantity of gas to be introduced into the cell during the measurement. The mass spectrometer (a Pfeiffer Vacuum QMG422 quadrupole mass spectrometer equipped with a crossbeam electron bombardment ionization source and 90° secondary electron multiplier) is placed in a chamber above the furnace. The cell is heated in a vacuum by a tungsten coil surrounded by seven thermal shields ensuring temperature homogeneity in the cell. Our measurements were performed with a heating rate of 10 K/min in a W cell.

The Q-GAMES is pictured in Figure 48 and described more extensively in the works of Maugeri et al (149) and Colle et al (204). As shown in Figure 46, the machine is connected to the KEMS, from which it collects the gas coming from the annealed sample into a high-pressure chamber. Here, the gas is purified from gaseous species (such as N₂, O₂, CO₂, CO, H₂O, C_nH_m, H₂, DH, DD...) which can perturb the measurement by a combination of a liquid nitrogen (LN₂) cold trap, a getter pump (SAES Getters GP50) and/or a plasma discharge. After purification, the gas is sampled through an inlet and microvalve to a low pressure chamber, and the system quantifies the gas with its own independent

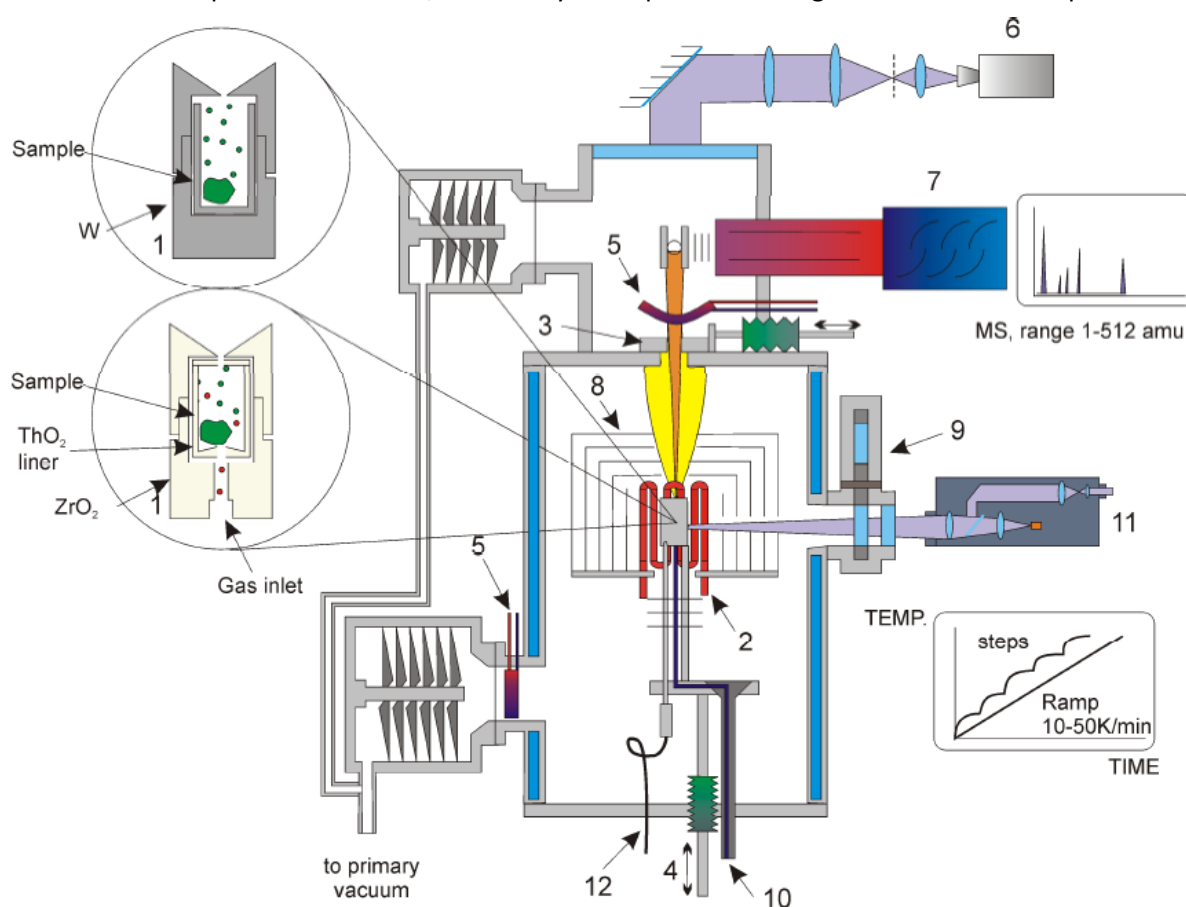


Figure 47: Scheme of the KEMS and furnace. 1: Knudsen cell, 2: heating coil, 3: chopper, 4: lift, 5: LN₂ cold trap, 6: camera, 7: mass spectrometer, 8: thermal shields, 9: revolving windows, 10: gas inlet, 11: pyrometer, 12: thermocouple. (203)

MS (Pfeiffer-vacuum QMG 422 quadrupole) by comparison with a spike of the same element. The spike is generated with temperature controlled calibrated volumes. The measurement possibilities range between 10^{-12} and 10^{-5} mol with a relative error below 2%. (150)

The pumping system works in closed circuit for the whole duration of the experiment, meaning that the gas is pumped back through the feedback to the HP sample chamber. This yields several

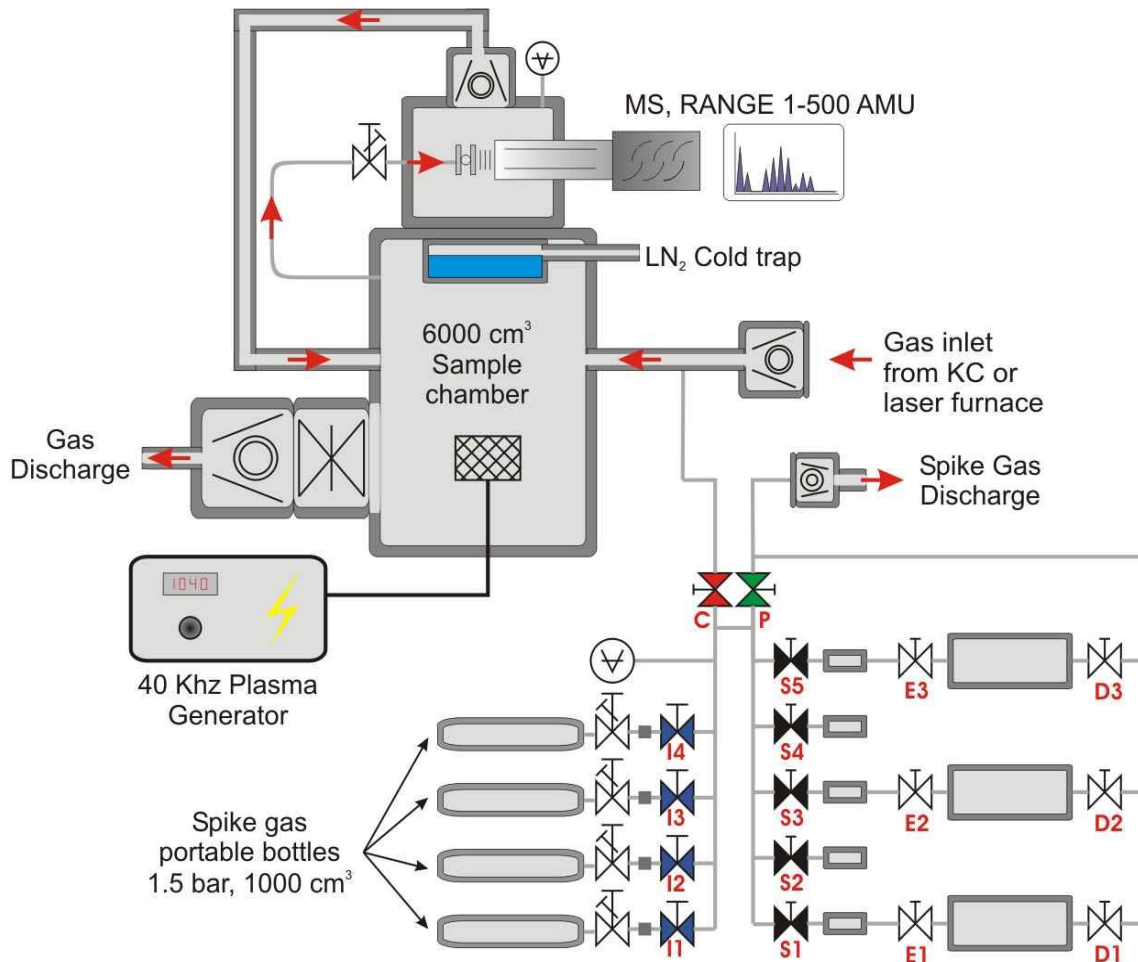


Figure 48: scheme of the Q-GAMES developed at JRC-KA. All components mentioned in the text are labelled in the picture. (204)

advantages:

- Increases the sensitivity of the measurement (allows sampling a big amount of gas without depleting the total quantity)
- Allows kinetic and long measurements (the measurement can be done continuously during the release cycle since the gas is never depleted)
- Results in the integral of the gas released
- Retains the total inventory of the released gas for further analyses

Quantification of the measured gas by comparison with the spike is done using the following formula:

$$\frac{N_s}{N_{sp}} = \frac{S_1 - BG}{S_2 - S_1} \quad (38)$$

Where N_s and N_{sp} are the number of atoms in the measured sample and in the spike respectively, BG is the background signal, S_1 is the mass spectrometer signal to be analysed before the introduction of the spike, and S_2 the signal intensity after the spike. (204)

2.2.6 Low T calorimetry

Heat capacity measurements at low T were performed using a PPMS-9 (Physical Property Measurement System, Quantum Design) and its determination was done by a relaxation method, which allows to measure relatively small samples with a mass of a few mg. (205) This device can be used to measure electric resistivity and heat capacity the temperature range between 0.4 K and 380 K. However, due to ^{238}Pu self-heating, the minimum T probed in this work was 5 K.

The device is not included in a glovebox, so samples containing transuranic elements have to be encapsulated before the measurement. Encapsulation was done in a clean glovebox and was followed by decontamination. The samples were also tested for contamination after the measurement. Stycast 2580 FT glue was used in this work to embed the samples, and its contribution on heat capacity was first measured on inactive standards and then subtracted from the real measurement. The encapsulation increased the uncertainty of the measurement up to 5 %. The setup of the machine as well as the encapsulation of the samples and its effects on the measurement accuracy have been published in detail by Javorský et al. (205,206)

3 SAMPLES PREPARATION

In this chapter, the preparation of the samples used during the whole PhD work is described. The chapter is structured in two main blocks describing the production of the UO_2 -based pellets and a third smaller section on the production of nanograined ThO_2 . In each part, the design of the concerned samples is discussed, the starting materials are described and the samples preparation is reported.

The preparation of the Pu-doped samples is treated separately than the other UO_2 -based samples as the involvement of such a highly radioactive element implied in most cases the use of different devices and techniques.

3.1 ^{238}Pu -doped UO_2 samples for accelerated spent nuclear fuel ageing study through α -self-irradiation

As described in Section 1.3.1, the degradation of the spent nuclear fuel during repository time is driven by a combination of several factors of different nature, mostly interconnected among each other. Since it will be the dominating activity in spent nuclear fuel in the long term, the focus of this work is to study the α -radiation effect, to be later extended to its interaction with the spent fuel microstructure (as will be described in section 3.2).

In order for the study to successfully decouple the effect of α -radiation from all the other phenomena ongoing in spent nuclear fuel, few key points were selected as prerequisites for the good outcome of the work, in particular the homogeneity of:

- 1) the chemical composition
- 2) the microstructure
- 3) the damage distribution within the matrix

To match these requirements, a material with tailored characteristics has to be designed and synthesised. A good preliminary insight on the ageing effect and a careful samples design were fundamental requirements for the success of the study. The preparation of a material with uniform microstructure and chemical composition would allow to separate and study only the specific effects of the homogeneous α -radiation onto the crystalline matrix.

In the present chapter, the production of UO_2 doped with ^{238}Pu as α -emitter is described. The procedure involved intensive bibliographic research and samples design phases, in order to be able to later study a significant extent of damage accumulation with the most appropriate techniques and over a short time. The powder synthesis, pressing and sintering are described. The systematic study of the degradation of the samples thermophysical, microstructural and thermodynamic properties as a function of the damage accumulation will be discussed instead in a dedicated section.

3.1.1 Sample's elaboration

Different properties of the spent nuclear fuel evolve following very different kinetics. This behaviour is due to the different sensitivity of each thermo-physical property to different type/order of defects. As the damage builds up in the lattice, defects of increasing complexity are formed, from point defects towards extended defects (which can be linear, planar or three-dimensional).

Imperfections in the lattice such as interstitials or vacancies might dramatically affect some properties which are particularly sensitive to the regularity of the crystal, but might result almost completely neutral to some other material characteristic.

As already discussed in section 1.3.3.1.3, the thermal diffusivity (and conductivity) is one of the properties that shows the quickest degradation as a function of the cumulated damage. A small irregularity of the periodic lattice, such as a vacancy or a substitutional atom, introduces a strain in the crystal lattice, that increases phonon scattering processes detrimental to the thermal diffusivity especially at lower temperatures.(96)

On the other hand, the lattice constant keeps increasing on a very long damage scale (88,89) since it is affected not only by point defects but also by the incorporation of He atoms in the lattice.

Lattice parameter swelling and thermal diffusivity (or conductivity) degradation are two examples of very important properties that are both closely related to the lattice, but then show different degradation kinetics as function of the damage build-up. By comparing their evolution as a function of a measure of the damage injected in the matrix, such as dpa (as introduced in chapter 1), it is immediately clear that they differ by orders of magnitude in reaching the saturation values (Figure 49). Transposing this onto a laboratory timescale, and considering that dpa increases linearly with time, a crucial issue is self-evident: how to accurately follow the evolution of thermo-physical properties that differ by orders of magnitude in their time dependence?

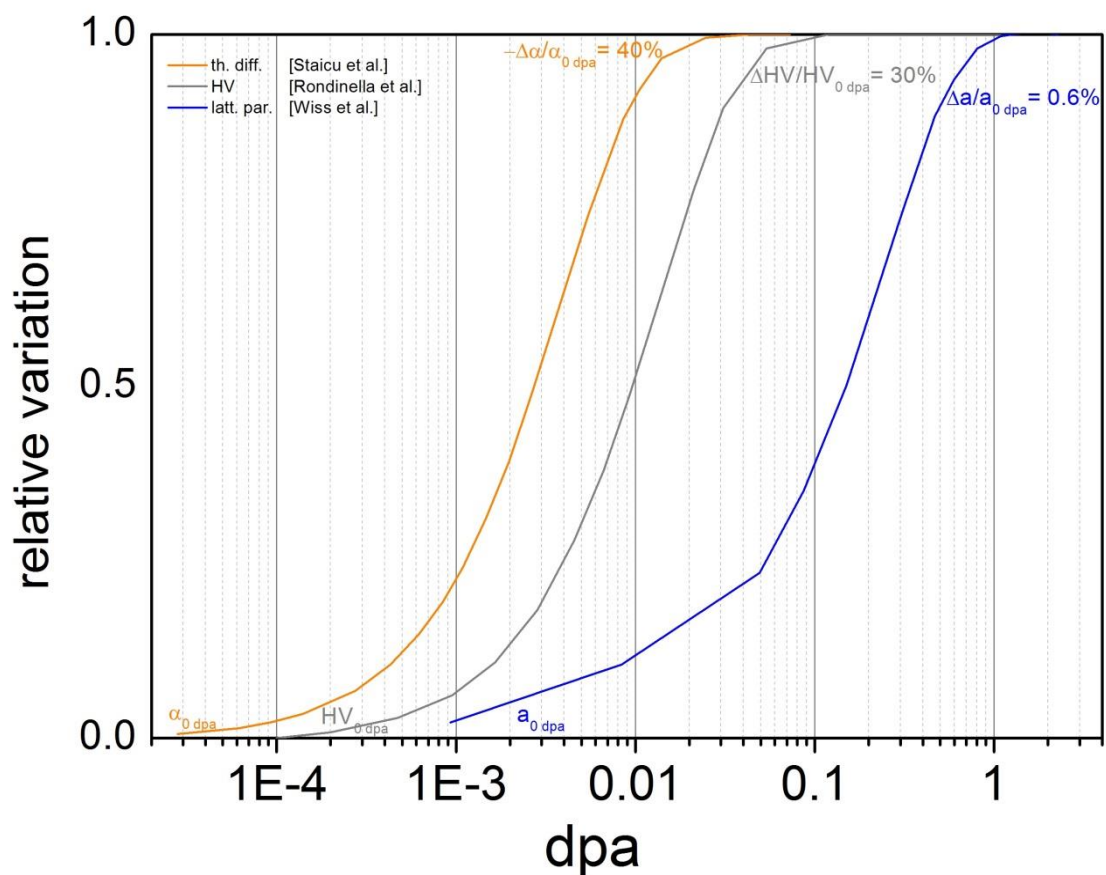


Figure 49: Example of the use of the dpa scale to compare the relative variation (from their initial value to the saturation) of different properties. The data shown in this picture are only the fit curves, and not the experimental data, proposed by the three authors respectively (Staicu et al. (96) for thermal diffusivity, Rondinella et al. (144) for the hardness and Wiss et al. (88) for the lattice parameter). These were however not the only data taken into account during the dpa range assessment.

On the other hand, past studies on α -doped fuels (88,144) report the independence of the properties evolution on the kinetics of the damaging of the matrix, even in the case of two orders of magnitude of difference in the activities of the samples involved. In these studies, properties such as Vickers hardness and lattice parameter swelling were monitored on α -doped UO_2 samples, and showed no dependence on the samples activity nor composition. The conclusion of the authors is that, within limited ranges of dopant concentrations (i.e. up to 10 wt % Pu in UO_2 , the evolution of microstructural defect populations and macroscopic properties is not affected by the rate at which the corresponding levels of damage are injected.

Based on these very promising results, in this study it was chosen to produce samples with two different activities, tuned in such a way to have a relatively smooth evolution of the concerned properties over the timeframe of the PhD project. Moreover, this approach allows us to monitor more accurately the initial part of the ageing of the samples, which is when the change is more abrupt in any case. In fact, most of the properties age tracing a sigmoid curve on the logarithmic time scale. Finally, this study proposes a more accurate re-assessment of the non-dependence of the ageing from the kinetic of damage generation, by comparing the two different compositions evolutions in several techniques with an improved accuracy with respect to past works.

To adapt the samples activities, a plot grouping the relative variation of the different measurable parameters as a function of the dpa was created. The literature data and the activities of our samples were converted to dpa with the following formula (already introduced in chapter 1):

$$dpa = \frac{\text{displacements}}{\text{atoms}} = \frac{1650 \cdot a \cdot t \cdot m_{Pu}}{3 \cdot N_a \cdot \frac{m_{UO_2}}{mm_{UO_2}}} = \frac{1650 \cdot a \cdot t \cdot mm_{UO_2}}{3 \cdot N_a} \cdot (Pu\%) \quad (39)$$

Where a is the specific activity [$1/s \cdot g$], t is time [s], mm_{UO_2} is the molar mass of our samples [g/mol], N_a is the Avogadro number [$1/mol$] and the factor 1650 is the number of displacement per decay event, as calculated using SRIM code (75) and assuming 40 eV displacement energy for U and Pu atoms and 20 eV for O atoms. Note that dpa is a dimensionless unit and depends linearly on the dopant fraction (Pu%).

The use of dpa allows representing on the same scale the data coming from samples of very different activities, although it must be kept in mind that samples with very different compositions might respond differently to the same amount of damage. The values of dpa to be targeted in the PhD timeframe were around 0.5 and 0.12 dpa, meaning to have a dopant concentration four times higher in the samples intended for the monitoring of the slowly-evolving properties.

These two values were selected to cover, with reasonably slow kinetics, the whole evolution of the properties measurable with the instrumentation available at the institute. The only exception was the lattice parameter swelling, which is the most reported in literature and whose dpa saturation values appear to be very spread. In particular, the lattice constant relative increase seems to proceed in very different ways depending on the different actinide compounds, and much higher dpa saturation values are reported for mixed U-Pu oxides than for pure compounds or Am-containing solid solutions (158,207–209). The value of 0.5 dpa should be sufficient to cover the main part of the lattice parameter relative increase, especially considering that most of the variation takes place in the initial part of the damage accumulation. Moreover, since the data collection of this work

has been more exhaustive than those available in the literature, it potentially paves the way for a re-assessment of the saturation value and dpa for the lattice constant expansion, at least in UO_2 -based compounds, as well as to provide a precise kinetic evolution model.

Microstrain data are instead less abundant in literature, and it is reported to reach a plateau already for low values of dpa (207), although in this case data on UO_2 or UO_2 - PuO_2 solid solutions are almost completely unavailable. An accurate monitoring of the microstrain evolution in our samples was an additional reason to analyse by means of XRD both the samples compositions throughout the whole PhD timeframe.

Once chosen the desired compositions tuned on the desired damage accumulation during a fixed time, the next issue was the determination of the target chemical composition based on the compounds available at the institute. For this reason, there could be a significant difference in the nominal and actual compositions of the samples, while the final overall samples activities are the targeted ones.

In addition to this, the number of samples for each composition had to be carefully evaluated in order to have enough material to perform all the characterizations foreseen until the end of the study. Some techniques in fact are destructive, while others perturb the sample in such a way that its ageing would be different after the characterization (for example while grinding the sample) or completely anneal all the accumulated damage (DSC, KEMS). Furthermore, some characterization techniques have some size limitations, implying that the geometry for at least some of the samples was fixed in terms of minimum diameter (LAF, for modelling reasons) or height (indentation, for guaranteeing the integrity of the samples even after polishing).

It is worth mentioning that the Pu content affects some of the thermophysical properties that were studied in this work. While for some properties, as it will be discussed more in detail in the appropriate sections of chapter 4, the low Pu content does not alter significantly the UO_2 matrix behaviour, for some others the change is more marked. Moreover, the difference between the two compositions involved also yields some differences in the response of the materials. (50)

However, the present study puts its focus on the degradation of the properties as a function of the damage build up. The relative change of the properties was monitored, more than their absolute variations, in order to study the response of a UO_2 -based material to the self-irradiation effect. As the UO_2 radiation resistance is not reported to be affected by the Pu doping, the goal of the study was preserved.

3.1.2 Materials and methods

Due to the high radiotoxicity of Pu, all of the experiments and procedures described in this section were performed in shielded gloveboxes at the JRC-KA. All of the materials and devices (described in chapter 2) used in the work were already available at the institute at the beginning of the project.

The goal of the samples preparation was to achieve a homogeneous PuO_2 - UO_2 solid solution in the final pellets, so to have uniform α -damage within the matrix. The Pu-dopant was provided in form of powder, while the U was available as uranyl nitrate solution. Solution mixing and co-hydrolysis had already proven to be a reliable method for the synthesis of mixed oxide precursor powders with a high degree of homogeneity(119), suitable for densification in conventional sintering.(142) Following

this procedure, the Pu powder was dissolved, the solutions were mixed in stoichiometric amounts and co-precipitated, and the resulting precipitates were washed, dried, calcined, pressed and sintered.

3.1.2.1 *α -dopant powder*

The powder used as α -emitter dopant in this study was already present at JRC-KA and was purchased several decades ago. The powder was composed of 13 wt% U isotopes and 73.6 wt% Pu isotopes, with the first being mainly oxidized to U_3O_8 and the latter to PuO_2 . Initially it was constituted of mostly ^{238}Pu , whose half-life is 87.75 years, with the result that the ^{238}Pu concentration was 54 % at the time of the synthesis of the samples.

The availability, for this study, was limited to 250 mg of Pu, equivalent to a total amount of dioxide dopant powder of 348 mg.

As mentioned earlier in the introduction to this chapter, the discriminant of this study was the target activity of the samples. This reason, combined with the high amount of U and Pu isotopes present in the powder in addition to ^{238}Pu , makes the nominal and actual compositions of the α -dopant very different.

Throughout the rest of the thesis the samples will be referred at by using their nominal composition, which is related to the weight fraction of the overall dopant material. The actual composition of the ^{238}Pu doping is roughly half this value, while the actual overall Pu dopant concentration is between these two values.

Considering the specific activity of the dopant powder, which was 342 GBq/g, the desired dpa level after two years could be achieved with 2.5 and 10 wt% dopant material in the UO_2 .

3.1.2.2 *Uranium solution*

The uranium used in this work was also belonging to the JRC-KA stock. All the uranium involved is natural and is available at the facility as uranyl nitrate solution, in our specific case the concentration was 494.19 g/L.

3.1.3 Samples preparation

3.1.3.1 *Pu dissolution and mixing*

The dopant powder was dissolved using HNO_3 and a dropwise addition of HF during 24 hours. The solution was then diluted with H_2O to bring the overall volume to 20 mL, resulting in a solution of concentration 15.35 g/L.

The dopant solution was then divided into two solutions of 8 and 12 mL, and each one was added to a separate volume of U solution in the appropriate ratio (respectively, 9.65 and 3.35 mL).

3.1.3.2 *Precipitation and filtration*

The solutions were then added with 70 mL of ammonia solution (10 vol%) to achieve the precipitation. The precipitates were collected by filtering the solution with paper filters, and were then washed with distilled water.

The material obtained was an U,Pu hydroxide as characterized by means of XRD.

3.1.3.3 Pre-calcination and calcination

To limit the material losses, the precipitates were pre-calcined together with the paper filters under air, in order to burn the filters away. A successive calcination step was performed to obtain the final powder.

The pre-calcination treatment is summarized in Figure 50-(left) and consisted in a dwell at 400°C during which the atmosphere was switched from inert (Ar) to simulated air (N₂ with 20% O₂) for two hours and then back to inert.

After the treatment it appeared clear that the paper filters were not completely removed. Part of the original filter shape could be seen in a crumbly black layer underneath the powder. For this reason, the calcination process was modified with the addition of another step under simulated air. The profile of the calcination treatment can be found in Figure 50-(right). The dwell temperature was 700°C, with the first 2 h under simulated air and the remaining 2 under Ar-4%H₂.

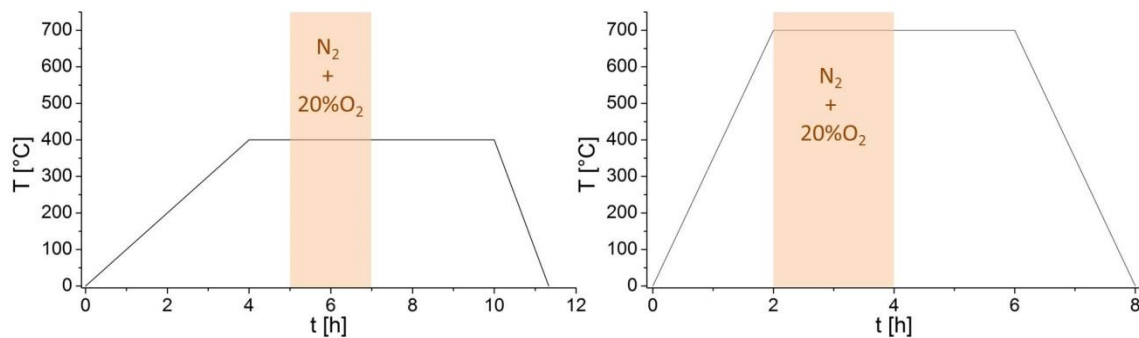


Figure 50: pre-calcination (left) and calcination (right) treatments. Apart from the 2 h under simulated air, the rest of the treatments were performed respectively under inert (Ar) and reducing (Ar-4%H₂) atmospheres.

The resulting powder consisted of a mixture of a cubic Pu-rich phase and a more oxidized U-rich U₃O₈ phase due to the local composition variations. This inhomogeneity is usual when performing a calcination under air for burning away the organic impurities inherited from the powder synthesis. In our case, the final part of the treatment in reducing atmosphere was obviously too short, and thus the reduction to a dioxide solid solution was incomplete.

3.1.3.4 Pressing and sintering

The powder was pressed in disks of 5 mm of diameter using 14.5 kN of force, resulting in a pressure of 738 MPa. Samples of different masses were produced, in order to achieve the geometrical requirements foreseen by the different characterization techniques. Table 4 summarizes the different batches of samples that were produced.

Samples amount	Mass [mg]	Targeted height [mm]	Nominal Pu [wt%]
3	170	1	2.5
10	130	0.8	2.5
36	100	0.6	2.5
24	90	0.55	10

Table 4: batches of samples produced for each composition.

The samples were sintered following the standard sintering treatment for MOX fuel with a dwell time of 6 h at the nominal temperature of 1650 °C under Ar-4%H₂.

3.1.4 Summary

In this section, the production of α -emitting ^{238}Pu -doped UO_2 samples for self-irradiation studies was described. The process involved an extensive literature review and design phase for carefully tuning the final samples compositions. Two different compositions were selected that would allow a complete and systematic study of the samples ageing under α -self-irradiation within a PhD timeframe. Solution mixing and co-hydrolysis resulted in intimately mixed U-Pu powders that were densified in highly homogeneous $(\text{U,Pu})\text{O}_2$ disks via conventional sintering for 6 h at 1650 °C under Ar- H_2 atmosphere.

3.2 Nanograined UO_2 for grain size effect study on radiation resistance

As described in section 1.2.1.3, the application of FAST to ceramic powders allows to strongly decrease the grain size of the sintered material with respect to what achievable through conventional sintering.(37,210,211) The most straightforward route to study the grain size effect on radiation damage would then be the synthesis of α -doped UO_2 with various grain sizes applying FAST to the powders already used in section 3.1.

However, at the time of writing, only few FAST devices have been nuclearized all around the world, and none of them are able to process Pu-containing compounds. For this reason, the synthesis of nanograined α -doped sintered materials has never been achieved yet.

The approach used in the present study foresaw the synthesis of non-doped UO_2 samples of uniform composition and density, in which the radiation damage would then be reproduced by successive ion implantation in dedicated ion beam facilities.

In the present chapter, the production of UO_2 samples with grain size down to ~50-100nm is reported. The work described here is the result of the optimisation of previously reported studies.(38,40,41,212)

To limit the grain growth during the UO_2 sintering, several starting powders were tested, and different sintering treatments were applied. The explored powder synthesis routes are described, together with their sintering behaviour, and the design and application of different sintering treatments is also illustrated and discussed. The ion implantations on the samples with the different grain sizes will be instead reported in a dedicated section.

3.2.1 Samples design/elaboration

As introduced in section 1.2.1.3, when trying to limit the grain size of the final sintered product, several precautions can be adopted in different stages of the samples preparation. Coarsening during sintering must be avoided since it has the double negative effect of increasing the final grain size and competing with the densification process. Grain growth takes place predominantly once reached high densities at high temperatures, so the main objective is to limit as much as possible the maximum temperature undergone by the samples but also the time spent at this temperature.

However, during sintering, the achieved density increases as function of the sintering temperature and time. It is crucial then to select accurately the maximum sintering temperature and the dwell time in order to reach high density (95%TD) while limiting the growth of the grains.(45)

The use of Spark Plasma Sintering (introduced in 2.2.1 and 3.2.3), where the powder is subject to uniaxial pressure, electric field and high heating rates, allows lowering significantly both sintering temperatures and times. Furthermore, the applied pressure and the heating rate are two additional factors which can affect the sintering of the powder and eventually lower temperature and shorter dwell-time when properly chosen.

Another significant decrease in the sintering temperature of the UO_2 powders can be achieved by synthesising very sinteractive powders. Fine powders have a much higher sintering potential, as it is proportional to their specific surface, and will then sinter at lower temperature. Nonetheless, the size of the starting powders particles has a larger effect on the incipit of the sintering, while the final part of the densification process is more affected by the agglomerates size and shape.(213) Since most of the grain growth will occur in this last stage, as the temperature is high but most importantly as the material has already reached a relatively high density, the agglomeration of the powders plays a role at least as important as the one of the particle size.

An additional factor influencing the sinterability of the UO_2 powders is their deviation from stoichiometry. The increased disorder of the crystal lattice brought by the excess oxygen atoms enhances the self-diffusion coefficient of both anions and cations of up to three orders of magnitude.(214) Being the sintering process diffusion-driven, this means that oxidised powders will sinter at much lower temperatures than stoichiometric UO_2 powders.

It is worth noting that nanograined sinteractive powders, due to their extremely high specific surface, have also a high tendency to oxidize, even at very low oxygen potentials. The two effects of non-stoichiometry and nanosize of the particles are then usually coupled while sintering such powders.

As mentioned in section 1.2.2.1.2, the SPS graphite environment ensures a complete reduction to stoichiometric $\text{UO}_{2.00}$ when sintering commercial hyperstoichiometric powders.(45) However, the reaction between the carbon of the graphite die and the oxygen present in the sample to form the CO reductive atmosphere starts occurring at temperatures not below 600 °C.(33) In case of sintering around this temperature, especially for short times, the reduction of a very oxidised powder would be incomplete. For this reason, and to avoid further reduction treatments which could lead to grain growth, the deviation from stoichiometry of the starting powder has to be kept within a controlled range.

At the moment of the synthesis of the powders, several methods were employed for the production of nanocrystalline UO_2 powders. Some tests were conducted on powders of different particle size and agglomeration to assess their response to spark plasma sintering. The combination of final grain size and stoichiometry of the resulting disks were taken into account, together with the temperature of sintering, which then limits the maximum temperature of any additional thermal treatment.

Some modifications were then applied to the regular SPS treatment to limit as much as possible the grain growth during sintering, mainly by further lowering the sintering temperature. This was achieved by increasing the applied pressure using the High Pressure (HP – SPS) setup, or by limiting the time spent at high temperature to just few seconds and then completing the densification at lower temperature in a two-step (2S – SPS) sintering process.

3.2.2 Materials and methods

For the preparation of the nanograined UO_2 samples, two precursors already available at the institute were used. Also in this case, despite the relatively limited radioactivity of the compounds involved, all the work was done in shielded gloveboxes at the JRC-KA to cope with the risks of incorporation while handling volatile materials.

With the final goal of controlling the grain growth by limiting the maximum temperature during the sintering, the preparation of the UO_2 powders from these two precursors aimed to achieve highly sinterable powders.

Two different processes were applied to each of the two precursors to obtain four UO_2 powders. The particles and agglomerate sizes were kept as low as possible by lowering the temperature of the conversion of the precipitates into oxides. Their behaviour was then tested in SPS, the resulting disks were characterized (as it will be reported in the dedicated chapter) and one powder was selected based on grain size and final stoichiometry and was used for the sintering in 2S – SPS and HP – SPS.

3.2.2.1 *Uranyl nitrate solution*

The first precursor was the same uranyl nitrate solution mentioned in 4.1.1.2. At the same way as the $(\text{U,Pu})\text{O}_2$ starting powder was produced, UO_2 powder was synthesised through hydrolysis and successive calcination.

However, with this solution also the so called "sol-gel" process was applied, in order to achieve monodispersed spherical particles (beads). As reported in 2.2.2 and 4.1.3, this process was already employed for the synthesis of mixed oxides compound which required a very good homogeneity. Nonetheless, the size of the resulting particles remained also quite small, allowing the use of such obtained powders also for the compaction of sub-micrometric dense UO_2 .(40) For this reason, it was logical and straightforward to start the testing from this well-known synthesis route.

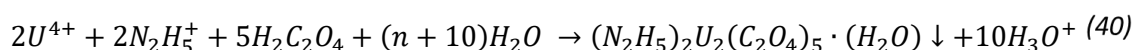
This process differs from the simple hydrolysis precipitation for some additional steps which aim to normalize the final shape and size of the agglomerates. The uranyl nitrate solution is added with complex formers, organic thickeners (to increase the viscosity), and then dropped into an ammonia bath by mean of a rotating cup atomizer, which allows tuning the size of the resulting spherical droplets by changing the rotational speed. The high viscosity of the uranyl nitrate solution helps the droplets keep their shape and integrity. Surfactants are added to the ammonia bath to lower the surface tension, and this allows the droplets to penetrate the surface without losing their round shape.

3.2.2.2 *Uranium oxalate powder*

In order to start from particles of even smaller size, a batch of uranium oxalate powder previously produced was also used. This precursor is known to result into nanocrystalline UO_2 powder after thermal decomposition(215), suitable for the production of nanostructured UO_2 .(41) As reported in previous studies, U oxalate first dehydrates below 250°C and then amorphises and finally fully decomposes at around 450°C . At the same time, UO_2 starts crystallising around 400°C and undergoes grain growth upon rising the temperature of the treatment, although with a very slow kinetic at least for temperatures up to 800°C .(215)

In the oxalate powder production, firstly the starting uranyl nitrate solution has to be electroreduced to U(IV). Oxalic precipitation results in fact ineffective on U(VI), as it is still fairly soluble in these conditions, as opposed to U(IV). The electroreduction is done with the addition of hydrazinium, which takes part in the reaction and stabilizes the final U(IV) oxidation state in the solution.

The precipitation is then achieved by dropping the U(IV) solution in a mixture of oxalic acid, nitric acid and hydrazinium (in excess), following reaction (2), and the resulting precipitates are filtered, washed with water and dried at room temperature in the nitrogen glovebox atmosphere.



The stability of U(IV) in oxalate made possible to obtain near-stoichiometric final UO₂ powders, as opposed to the highly oxidised final product of the hydrolysis-based processes.

As mentioned in 4.2.1, the shape and size of the agglomerates affects the sintering behaviour as efficiently as the particles size. The morphology of the uranium oxalate powders particles is constituted of mostly cuboids of stacked platelets, which are fully preserved as agglomerates while the UO₂ nanocrystals start nucleating and growing during the conversion to oxide. In the sintering step, the beneficial effect of the nanosized crystals is partially hindered by the low sinterability of such squared agglomerates, resulting in a high density only at relatively high temperatures. For this reason, a second conversion route was tried, in order to obtain oxide nanocrystalline powders without the characteristic stacked platelets agglomerates.

The hydrothermal decomposition was recently proved to be a suitable route for the conversion of actinide oxalates to oxides(117,118,216), resulting in completely destructured agglomerates and even smaller crystallite size due to the lower treatment temperature. The addition of hydrazinium is needed to preserve the U(IV) oxidation state after the conversion.

3.2.2.3 Sintering of the powders

Each one of the four produced powders, after being characterized by means of XRD and SEM, was tested in SPS. The response of the different powders to similar sintering conditions was evaluated.

However, by following the parameters that the machine records during the treatment, such as piston displacement and speed, it was possible to stop the treatment as soon as the densification was completed, to limit further grain growth in the dense material. All the samples were then compared having undergone the same sintering conditions except for the maximum sintering temperature, as the different powders reached full densification at different temperatures.

The best performing powder was selected based on the final microstructure and stoichiometry and, to limit further the grain growth, different types of thermal treatments were explored.

The application of a two-step approach to conventional sintering was successful in the realisation of nanograined ceramics(217–220), but was rarely tried in combination with any field assisted sintering technique (FAST).

In the two-step sintering the sample is quickly fired to a temperature (T₁) to reach about 80 % TD, and then sintered for very long time at a lower temperature (T₂) where densification occurs with

limited grain growth. Each one of the two temperatures has to be chosen appropriately, otherwise either the densification or the hindering of the grain growth would not take place.

A second approach that was adopted to limit the grain growth during sintering was to raise the pressure applied to the powder, as this is reported to lower the sintering temperature.(36,221) As mentioned in section 1.2.1.4, the insertion of some SiC components within the graphite die allows to raise the applied pressure from 70-100 MPa to 500 MPa. An additional decrease in the sintering temperature was achieved by testing different heating rates, as this also affects the onset of the sintering.(213)

However, as mentioned in the design section, the lowering of the sintering temperature is detrimental to the reductive capacity of the SPS treatment. For temperatures as low as 600°C and short dwell times, the reduction of the hyperstoichiometric UO_2 powder might be incomplete. In the same way, a short-timed sintering at low temperature in the SiC inner die of the HP – SPS setup also does not guarantee the full reduction of the sample. On the other hand, diffusion coefficients increase abruptly with x in UO_{2+x} (see section 1.2.2.3), meaning that incomplete sample reduction during sintering could have been another factor helping to further lower the sintering temperature.

In order to bring the O/M ratio of the still-oxidised samples, a final calcination treatment under Ar- H_2 was necessary. All of the samples were calcined together, in order to end up with the same lattice parameter in each sample regardless the differences in grain size.

3.2.3 Samples preparation

As introduced in 4.2.2, four main synthesis routes were applied to the two precursors to obtain UO_2 powders. In the following processes description, the heating rate for calcinations were always kept at 300°C/h and the furnace was flushed with the appropriate gas (Ar or Ar- H_2) for 1h before the beginning of each treatment.

3.2.3.1 Hydrolysis

As applied to the Pu-doped powder, also in this case the precipitation of the hydroxides was achieved by pouring the solution into an ammonia bath. Two different batches were then prepared, by washing the resulting precipitates in one case with water and in the other one with acetone and ethanol.

In both cases, the conversion to oxide was obtained by calcining the powders for 4h at 650°C under Ar- H_2 mixture.

3.2.3.2 Sol-gel

In the present work, the additives used were Triton X-100 (Merk) as a surfactant, Methocel (cellulose) as a thickener and THFA as a complex former. After preparation, the solution was pumped into the rotating cup atomizer which was spun with a constant angular velocity. For the integrity of the machine and the good outcome of the process, N_2 was fluxed through the rotating cup downwards to prevent gelation inside the rotating cup due to ammonia vapours.

The precipitates were sucked from the bath and left to rest overnight to achieve complete gelation, and then washed repeatedly with water to remove the residual ammonia and organics.

For the drying of the precipitates, tetrachloroethylene was added to remove all the water by azeotropic distillation. The azeotrope was carefully heated up to a temperature around 180°C and then further to about 220°C to avoid re-condensation in this part of the column. Once all of the water was removed, the initially floating beads precipitated at the bottom, and the leftover tetrachloroethylene was removed after cooling down. Any residual tetrachloroethylene left in the agglomerates was left to evaporate at room temperature. The use of azeotropic drying of the powder yields results in more porous and softer beads, enhancing their sinterability.

Finally, the conversion to oxide was achieved in a calcination treatment for 4h at 600°C under Ar-H₂.

3.2.3.3 Oxalate thermal conversion

For the thermal decomposition, roughly 2g of oxalate powder was placed in a glass crucible and calcined for 2h under Ar at 600°C. This temperature was chosen to achieve sure and full decomposition of the oxalate while limiting the growth of crystallites.

3.2.3.4 Oxalate hydrothermal decomposition

As for the thermal decomposition, also in this case roughly 2g of oxalate powder were used: they were placed in an autoclave in presence of 5mL of water and 0.5mL of hydrazinium, and then heated up to 170°C for 5h. The resulting powder precipitates were then sucked from the autoclave and washed in order with water, ethanol and acetone. Drying was achieved by letting the powder rest over two nights in a dessiccator under low pressure and Ar flux.

3.2.3.5 Overview of the synthesised powders

Table 5 summarizes some characteristics of the different powders produced. The two different washing procedures applied to the hydrolysis derived powders had no significant effect on the particles size and agglomeration, but resulted in two slightly different O/M ratios.

Synthesis route	Crystallite size (with Williamson-Hall approach)	O/M ratio (from cell parameter)	Synthesis T [°C]
Hydrolysis	50	2.05 ^(w) – 2.08 ^(e)	650
Sol-gel	35	2.24	600
Oxalate thermal decomposition	10	2.01	600
Oxalate hydrothermal decomposition	5	2.04	170

Table 5: summary of the powders produced and their key features: crystallite size and deviation from stoichiometry. The shape and size of the agglomerates will be discussed in chapter 4. ^(w) and ^(e) in the hydrolysis powder line indicate the powder washed respectively with water and acetone-ethanol.

It is worth mentioning that the high reactivity of these powders due to their high specific surface resulted in a quick oxidation even with the low oxygen partial pressure present in the N₂ gloveboxes. Despite starting from a near-stoichiometric powder then, due to some practical limitations, most of the tests were conducted on over-stoichiometric powders.

3.2.3.6 Spark plasma sintering

The sintering conditions are summarised in Table 6, and the different sintering curves are shown in Figure 51 A-B. Between the two hydrolysis-derived powders, only the one washed with acetone and ethanol is reported here and will be considered in the following discussion, as it was the one sintering at lower temperatures.

Powder	Hydrolysis	Sol-gel	Ox. Th. Dec.	Ox. Hyd. Dec.
Max T [°C]	900	850	1200	700

Table 6: sintering conditions applied to each powder. 250-300 mg of powder were placed in a 6 mm diameter die and pre-pressed with 0.5 kN (17 MPa). Before the start of the thermal treatment, the force was raised to 2 kN (70 MPa) and held until the end of the cooling. Every treatment was done entirely under vacuum and with a 200 °C/min rate for heating and cooling.

Before going to the microstructural characterization of the final pellets, the sintering curves already highlight some differences among the powders. It is remarkable in particular how differently the two oxalate-derived powders behave. The decrease of the crystallite size thanks to the application of the hydrothermal decomposition lowered the temperature of the incipit of the sintering by about 100 °C. The biggest effect is anyways evident in the final part of the sintering, where the flat elongated shape of the thermally decomposed oxalates agglomerates resulted in a residual slow densification at temperatures as high as 1200°C, which means several hundreds of °C above any other powder, including those formed by significantly larger crystallites.

Considering the sintering behaviour and the final disks microstructural features, all the successive sintering treatments were performed using the powder derived by the hydrothermal decomposition of oxalates. The amounts needed throughout the development of the work were not possible to be converted all at the same time, and for this reason several nominally-identical batches were used. Each one of them was characterized by means of XRD but not as extensively through microscopy as the one used in the pre-tests.

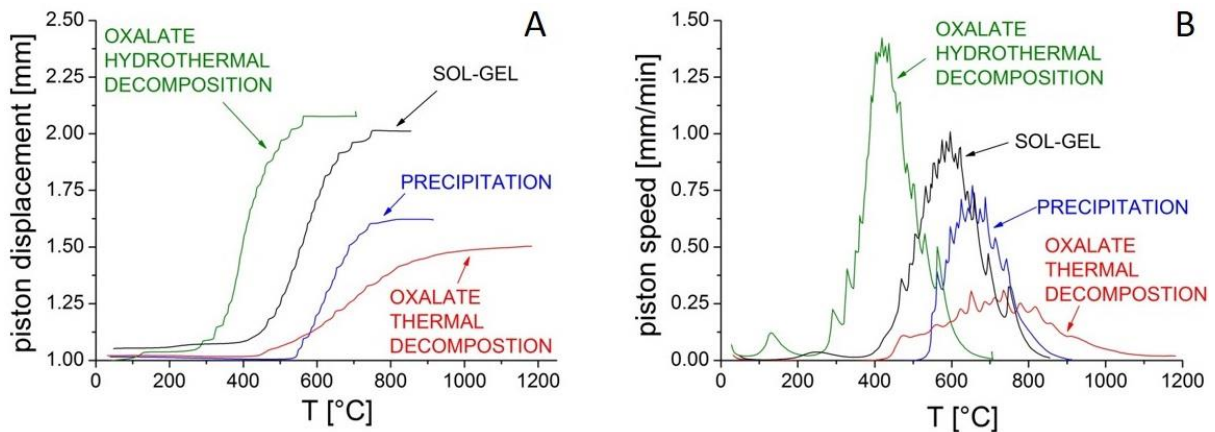


Figure 51: comparison among the sintering behaviour of the four UO_2 powders tested. In Figure 51-A the piston displacement is plotted, but the sintering range might be better identified in Figure 51-B where the speed is plotted.

3.2.3.7 Two-step spark plasma sintering

A range of different T_1 and T_2 were tested (Table 7), and the final samples were analysed by means of SEM and XRD. A further limitation to the choice of T_2 in our case was the reduction of the hyperstoichiometric powders during sintering. Some samples synthesized at extremely low temperatures were presenting a satisfying density and microstructure, but showed incomplete reduction and rather phase separation. In the range resulting in a full reduction of the samples, complete grain growth suppression was not achieved, but the grain size was kept significantly smaller than in regular SPS.

$\downarrow T_1$	$T_2 \rightarrow$	650°C	600°C	550°C	500°C	450°C
700°C						
650°C					O/M>2	
600°C					O/M>2	
550°C					biphasic	biphasic
500°C						$\rho < 95\%TD$

Table 7: 2S – SPS temperatures tested. Each sintering was done under vacuum, in 6 mm diameter dies with an applied pressure of 70 MPa, with a dwell time of 3 s at T_1 and 100 min at T_2 . Heating and cooling were done at 200 °C/min, and the pressure was loaded and unloaded at room temperature.

3.2.3.8 High pressure spark plasma sintering

The adoption of this setup involves some drawbacks, first of all the reduced size of the samples, which affected the accuracy of the geometrical density measurements as well as limiting the possible use of these samples when the geometric requirements could not be matched (for example thermal diffusivity measurements). Also the shape of the disks was much more irregular than for those obtained in regular SPS, since at these high pressures some powder always was pushed between piston and die and sintered there, giving final disks with a marked rim. Finally, the extremely high loads applied, in addition to the already high thermal stresses to which the samples are subject in FAST, resulted often in extremely fragile disks. However, despite these limitations, the treatment successfully produced near-stoichiometric UO_2 dense disks with extremely fine grain size, which were then annealed without alteration of the microstructure.

The sintering conditions used in this work are summarised in Table 8.

Max T [°C]	Rate [°C/min]	Dwell [s]	Success
800	200	10	X
750	200	10	X
750	100	10	X
700	200	10	
700	100	10	X
650	100	10	
650	50	10	X

Table 8: HP – SPS temperatures, heating rates and dwell times tried. Each treatment was performed under vacuum and with an applied pressure of 500 MPa, loaded and unloaded during a 4 min dwell at 250 °C.

3.2.3.9 Calcination

Since all of the samples experienced already for at least few seconds a temperature of 600°C, this was chosen as starting temperature for the reduction treatment to avoid grain growth. Different dwell times were tested, down to 2h, and all resulted in a successful reduction to $UO_{2.00}$ of each one of the still not reduced samples, together with no detectable grain growth or loss of integrity. All of the treatments applied are summarised in Table 9.

Dwell T [°C]	Dwell t [h]	Rate [°C/h]	Reduction [y/n]
600	12	300	y
600	6	300	y
600	2	300	y
570	12	300	y

Table 9: calcination conditions tried on the UO_{2+x} samples resulting from incomplete reduction of the powders during 2S – SPS and HP – SPS treatments.

3.2.4 Summary

In this section, the process that led to the synthesis and production of dense nanograined UO_2 was described. Four different powders were synthesised starting from two precursors, and they were sintered in Spark Plasma Sintering. The best performing powder was then used in two modified SPS setups in order to lower as much as possible the sintering temperature to hinder grain growth during densification.

To obtain a dense disk with grains down to 100 nm, UO_2 powder was synthesised by converting U(IV) oxalate under hydrothermal conditions at 170 °C for 5 h, and it was then sintered under vacuum under an applied pressure of 500 MPa at 700 °C, with a dwell time of few seconds and a 100°C/min heating and cooling rate. The resulting sample was overstoichiometric UO_2 and was then annealed at 600 °C for 2 h under Ar- H_2 .

3.3 Nanograined ThO_2 for grain size effect study on radiation resistance

During the time of the preparation of the nanograined UO_2 samples, intensive research was ongoing at the institute on the synthesis of other actinides highly reactive nanopowders. Given the vicinity of the topics, it was decided to try to apply the same treatment that was successful for UO_2 to the most recently developed ThO_2 sinteractive powders. Given the novelty of the result, the preparation of nanograined ThO_2 disks has been described carefully in a dedicated publication. (222)

3.3.1 Interest in ThO_2

The opportunity of having such interesting material available and ready to be tested paired very well with some of the issues that could be faced during ion implantation on nanograined UO_2 .

One major difference between the UO_2 and the ThO_2 systems is that the latter exists in only one valence state. Due to its electronic configuration indeed, Th only has its 4+ oxidation state. For this reason, a ThO_2 sample could be used as a benchmark in case of experiments in which some oxidation of the UO_2 takes place during ion implantation.

Moreover, due to its perfect stoichiometry, the self-diffusion coefficients of both ions in ThO_2 are relatively low. This is reflected in the much higher sintering temperatures needed for ThO_2 than for UO_2 , but also results into much slower grain growth kinetics. As the ion beam could result in non-negligible sample overheating during irradiation, a ThO_2 sample could be used a very useful benchmark also in case of grain growth in UO_2 during ion implantation.

3.3.2 Materials and methods

The thoria nanopowder used for this work was produced by hydrothermal decomposition of Th hydroxide under hydrothermal conditions.

The $\text{Th}(\text{OH})_4$ starting powder was produced by direct precipitation from a Th nitrate solution by ammonia addition. The conversion to oxide was achieved after 22h at 200-320°C in an autoclave in the presence of 10mL of water under continuous stirring and autogenic pressure. The obtained powder was washed several times with ethanol and acetone to remove the possible water absorbed on the surface and then dried in air. Such as in the case of UO_2 , hydrothermal decomposition

resulted in single-phased powder with extremely small starting crystallites (5 – 10 nm from XRD and TEM characterisation).

3.3.3 Sample preparation

Such as for UO_2 , the powder was first tested in a regular SPS treatment to obtain the characteristic sintering curve (Figure 52). Based on this, a high pressure treatment was applied in order to limit as much as possible the grain growth. Finally, a HP SPS treatment at higher temperatures was applied to sinter a disk with analogue characteristic but micrometric grain size.

3.3.3.1 Spark plasma sintering

The preliminary SPS treatment was done based on those performed on UO_2 : approximately 250 mg of powder were loaded in a 6mm large die and pre-pressed at 0.5 kN (17 MPa), then the force was raised to 2 kN (70 MPa) and the sample heated up to 1600 °C and kept there for 10 minutes, under vacuum and with a heating and cooling rate of 200 °C/min.

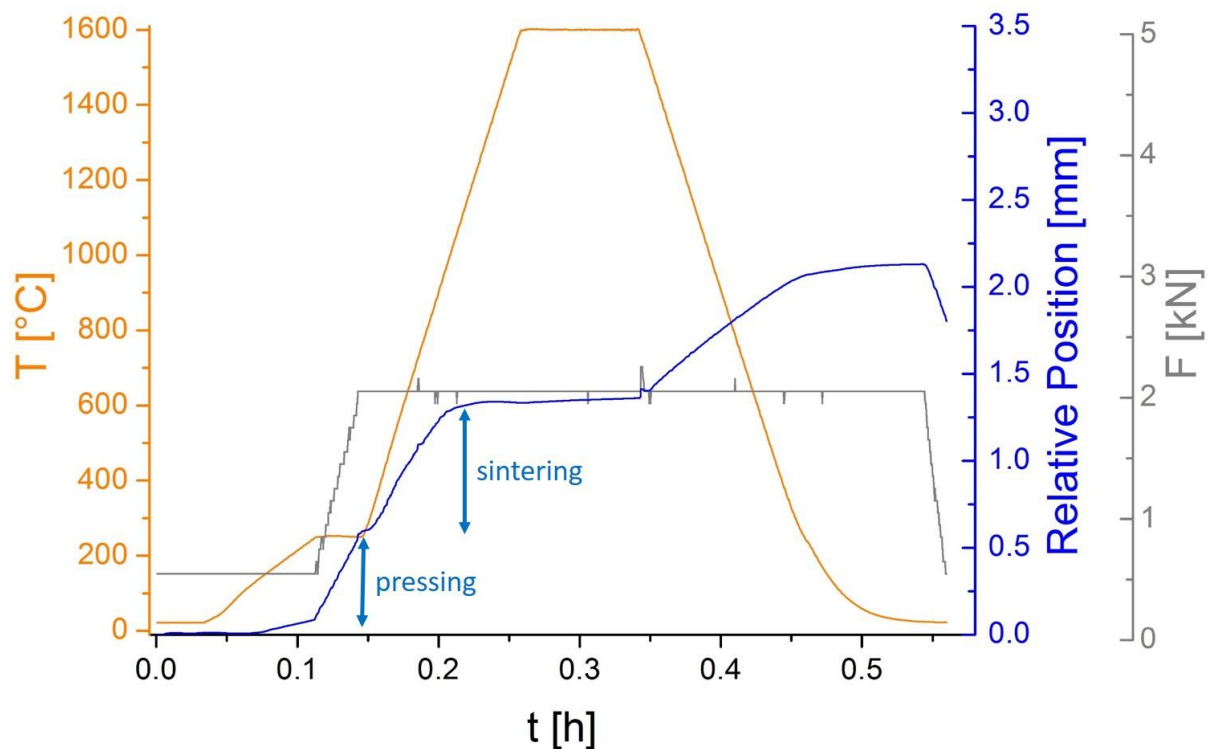


Figure 52: SPS behaviour of the ThO_2 powder. The small displacement ongoing during the dwell time at 1600°C indicates that full densification has not yet been achieved at this temperature.

In agreement with the literature data, the sintering of ThO_2 requires much higher temperatures than UO_2 . Indeed, as it will be confirmed later by the density measurements, the sintering seems to be incomplete and still ongoing during the dwell at the maximum temperature, implying that a complete sintering curve as function of temperature is out of the range of possibility of the available SPS device.

3.3.3.2 High pressure spark plasma sintering

For the HP treatment, the chosen solution was to stop the sintering after the densification derived from the piston displacement had stopped, as shown in Figure 53. The resulting pellet was dense

and nanograined, as it will be shown in chapter 4. Later on, a second pellet was pressed at a higher temperature and with a dwell time, and the conditions of sintering of both are reported in Table 10. In the case of the nanograined sample, some loading and unloading steps were designed before the final heating in order to try to break the agglomerates and achieve a higher green density. The effect was non-negligible and likely helped in the achievement of such a fine microstructure, but was not repeated in the high temperature sintering treatment (Figure 54) as there was no need to lower the sintering temperature in this case. In an attempt to improve the mechanical stability of the disk, in this case the force was released at high temperature (1200°C).

Max T [°C]	Applied p [MPa]	Dwell t [s]	F load/unload [°C]	atmosphere
915	500	3	250/250	vacuum
1600	500	600	250/1200	vacuum

Table 10: sintering conditions of the ThO₂ samples produced in HP – SPS.

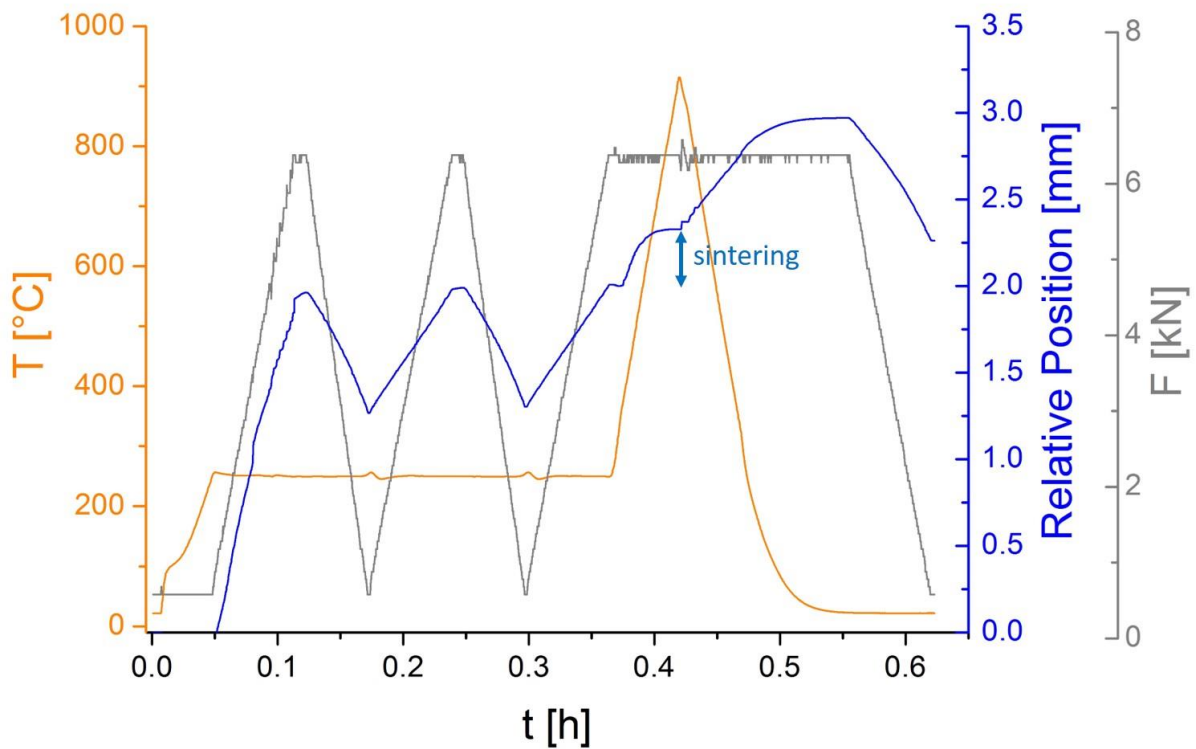


Figure 53: HP – SPS treatment applied to the ThO₂ powders for the realization of the nanograined pellet. The load/unload cycles helped breaking the powder agglomerates. The treatment was stopped as soon as the piston displacement was exhausted at 915°C.

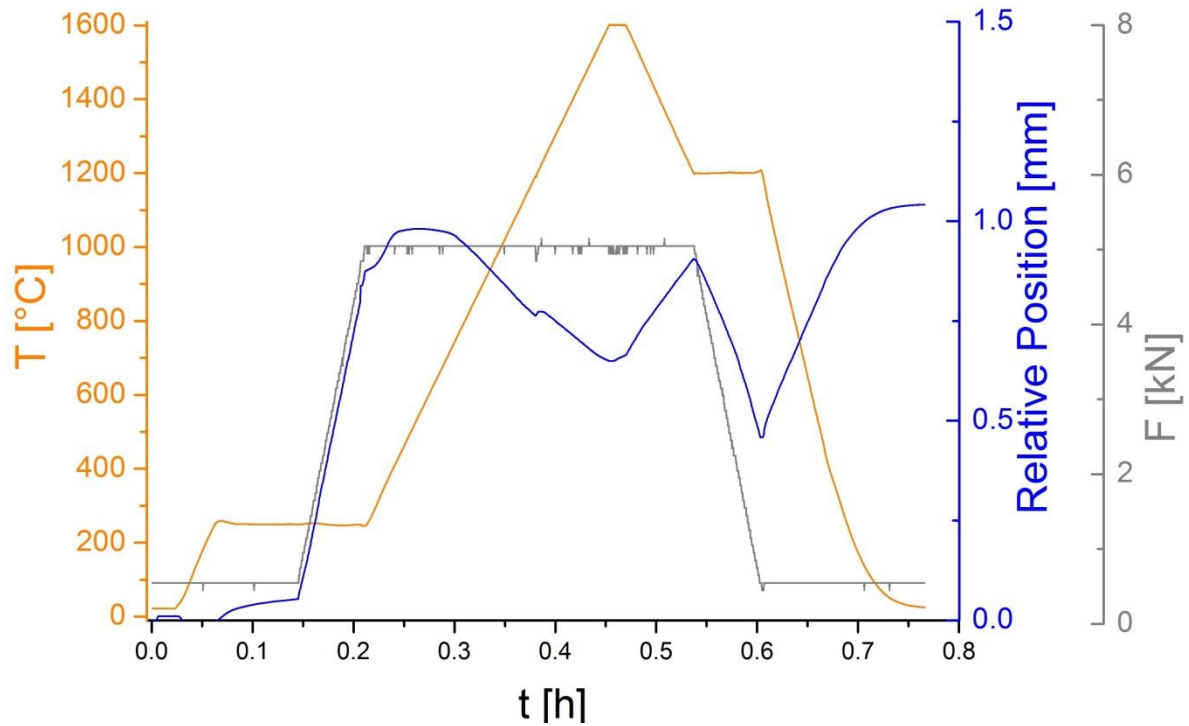


Figure 54: HP – SPS treatment applied to the ThO_2 powders for the realization of the micrograined pellet. In this case, no load/unload cycle was foreseen. On the contrary, more attention was put on the release of the pressure, which was done at 1200°C in an attempt to improve the mechanical stability of the final disk. Notably, the sintering is exhausted around 900°C also in this case, followed by a long part of thermal expansion.

3.3.4 Summary

In this section, the application to ThO_2 of the same procedure used to obtain nanograined dense UO_2 was described. No systematic study on ThO_2 was done. The powder was synthesised by hydrothermal decomposition of Th hydroxide at 200-320°C for 22h, and it was sintered in HP SPS under vacuum with an applied pressure of 500 MPa at a maximum nominal temperature of 915°C with a dwell time of few seconds and 200°C/min rate during heating and cooling.(222)

4 SAMPLES CHARACTERIZATION

In this chapter, the characterization of the samples used in the work is presented. While for the SPS UO_2 samples the characterization was fundamental during the development of the procedure for achieving the different microstructures, in the case of the $(\text{U,Pu})\text{O}_2$ samples the applied production route was more standard, thus most of the effort was put in the characterization of the final products. In the end of the chapter, a separate, smaller section reports the characterization of the ThO_2 samples.

The characterization of the as-produced material has a key role in the study, as the main goal of the work is to assess the successive damage produced by self-irradiation or ion implantation. However, in the case of the α -doped samples, due to the intrinsic difficulties of working with such hazardous substances, any process took additional time and the characterization of the as-produced samples was sometimes troublesome.

For different practical reasons, some hours or days had to pass between the samples production and their characterization and, as mentioned chapter 1 and 3, for some properties the variation in the initial stages of ageing can be very quick. An assessment of the quality of the sintered materials was performed as soon as possible after the samples production and was concluded after maximum two weeks. When possible, the samples were prepared for characterization right after the production, limiting thus the damage accumulation between the sintering and the actual characterization that took place only some days later. In the other cases, a successive dedicated annealing was performed before the characterization to obtain data on the non-damaged samples.

The annealing treatments were performed at 1250°C for 2 h under Ar-H_2 to achieve a full recovery of the cumulated damage. (88,96)

The characterization of the UO_2 nanograined samples was less problematic, but due to the high number of samples produced was more limited in the number of techniques adopted. The production of these samples was indeed a very iterative process between synthesis and characterization, and SEM and XRD were used to quickly assess the effectiveness of the applied treatments towards the goal of minimising the final grain size of the sintered samples.

4.1 Density determination

4.1.1 ^{238}Pu -doped UO_2 samples for accelerated spent nuclear fuel ageing study through α -self-irradiation

The resulting $(\text{U,Pu})\text{O}_2$ disks had very regular shapes and smooth and clean surfaces. Some of the samples were damaged during handling, but the broad majority of the two batches conserved a regular disk shape.

The geometrical density was measured on all the samples which did not exhibit evident damage, and it showed a very low dispersion. A summary of geometrical densities of samples belonging to the different batches is presented in Table 11.

Also, no trend relatable to the different compositions was found.

Pu [%]	m [mg]	ϕ [mm]	h [mm]	ρ [mg/mm ³]	ρ [%TD]
2.5	119	4.483	0.716	10.51	95.7
2.5	128	4.46	0.796	10.28	93.6
2.5	121	4.45	0.735	10.57	96.2
2.5	136	4.459	0.835	10.43	95.0
2.5	122	4.473	0.742	10.45	95.1
2.5	164	4.475	1.014	10.31	93.9
2.5	95	4.496	0.575	10.45	95.2
2.5	97	4.487	0.581	10.61	96.6
10	85	4.474	0.532	10.19	92.5
10	90	4.446	0.549	10.60	96.2
10	85	4.388	0.54	10.44	94.7
10	78	4.45	0.495	10.15	92.1
Average density		94.7 % TD	Standard deviation		0.7

Table 11: examples of geometrical densities of some of the produced samples. Geometrical density was measured on the samples which exhibited a regular geometry. Average = 94.7 ± 0.7 % TD.

Given the high importance of the density in the thermal conductivity measurement with LAF, the sample dedicated to it was measured also with the Archimedes method. As expected, this resulted in a slightly higher density of 97.5 % TD, while the average of the geometrical densities is 94.7 ± 0.7 % TD.

4.1.2 Nanograined UO₂ for grain size effect study on radiation resistance

The measurement of the density of the SPS-produced samples was more complex due to their less regular shapes and their low mechanical stability. Many samples in fact crumbled during the post-production handling.

However, some estimations were always possible based on the overall height and mass of the die and sample assembly, helped by the constant 6 mm diameter, which does not change during the treatment as the shrinkage is purely axial thanks to the applied pressure. Known the height and mass of the empty die and piston assembly, it is straightforward to derive volume and mass of the sample by weighing and measuring the assembly with still the sample inside.

In general, as it will be shown in the next section, the samples full densification was also double checked under the scanning electron microscope.

The large number of samples to be measured, together with the necessity for a quick assessment of the achieved density during the development of the SPS treatments, made it not practical to apply the Archimedes measurement to each one of the produced samples. Only those which satisfied the requirements of geometrical density, stoichiometry and microstructure were eventually measured with the Archimedes method. Throughout the whole work a precise value of the density will not be reported for each sample, but only samples that reached 95 % TD were considered sufficiently dense and hence employed in the successive experiments.

A summary of the conditions to achieve a high degree of densification (≥ 95 % TD) with the smallest grain size achievable in each of the three different SPS treatments applied to the powder obtained by oxalate hydrothermal decomposition is reported in Table 12.

Treatment	Pressure [MPa]	Temperature [°C]	Heating rate [°C/min]	Dwell time
SPS	70	700	200	3 s
2S – SPS	70	650 – 550	200	3 s – 100 min
HP – SPS	500	700	100	3 s

Table 12: sintering conditions for having dense (≥ 95 %TD) UO_2 disks while minimising the grain growth. HP – SPS at 650 °C with 50 °C/min heating rate is also effective but does not reduce further the final grain size. All treatments were performed under vacuum.

4.2 Microstructure – Scanning Electron Microscopy

4.2.1 ^{238}Pu -doped UO_2 samples for accelerated spent nuclear fuel ageing study through α -self-irradiation

Scanning electron microscopy (SEM) inspection was conducted on the fracture surfaces of two disks of the two different compositions. The samples for microscopy were broken immediately after the production, meaning that the observed fracture surfaces did not undergo any bulk self-irradiation phenomenon few hours after the sintering was finished, and thus preserving as much as possible the as-sintered internal microstructure. As it will be shown in the dedicated chapter, the damage accumulation has no effect on the free surfaces of the samples at the SEM-measurable scale and for this range of time (or dpa).

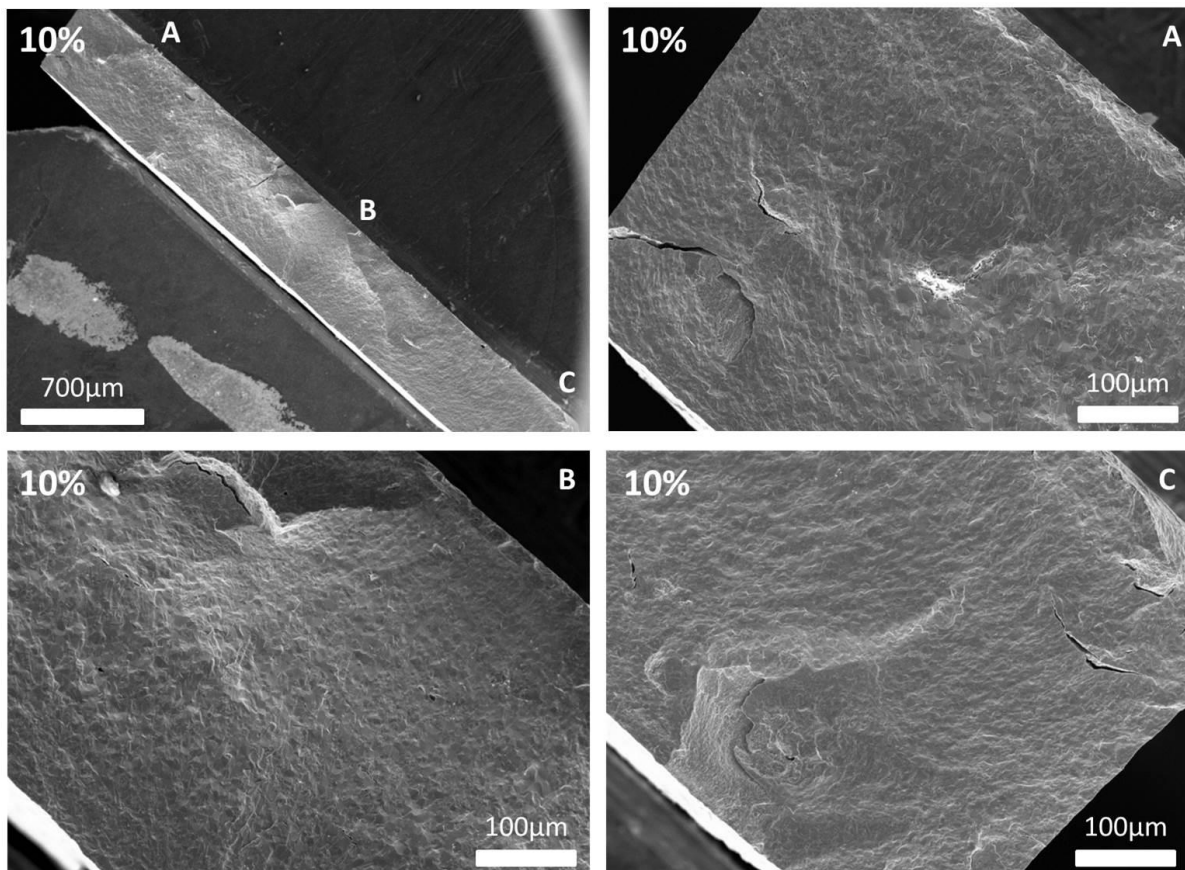


Figure 55: SE overview on the fracture surface of the 10 wt % Pu sample.

Figure 55 and Figure 56 show an overview of the fractured disks of both compositions. In both samples few small cracks are observed, in the 10 % appearing larger in number and dimension. However, this characteristic is present only in a very peripheral region of the disk and the size of the mentioned crack is far from being harmful to the overall disk density or measured bulk properties.

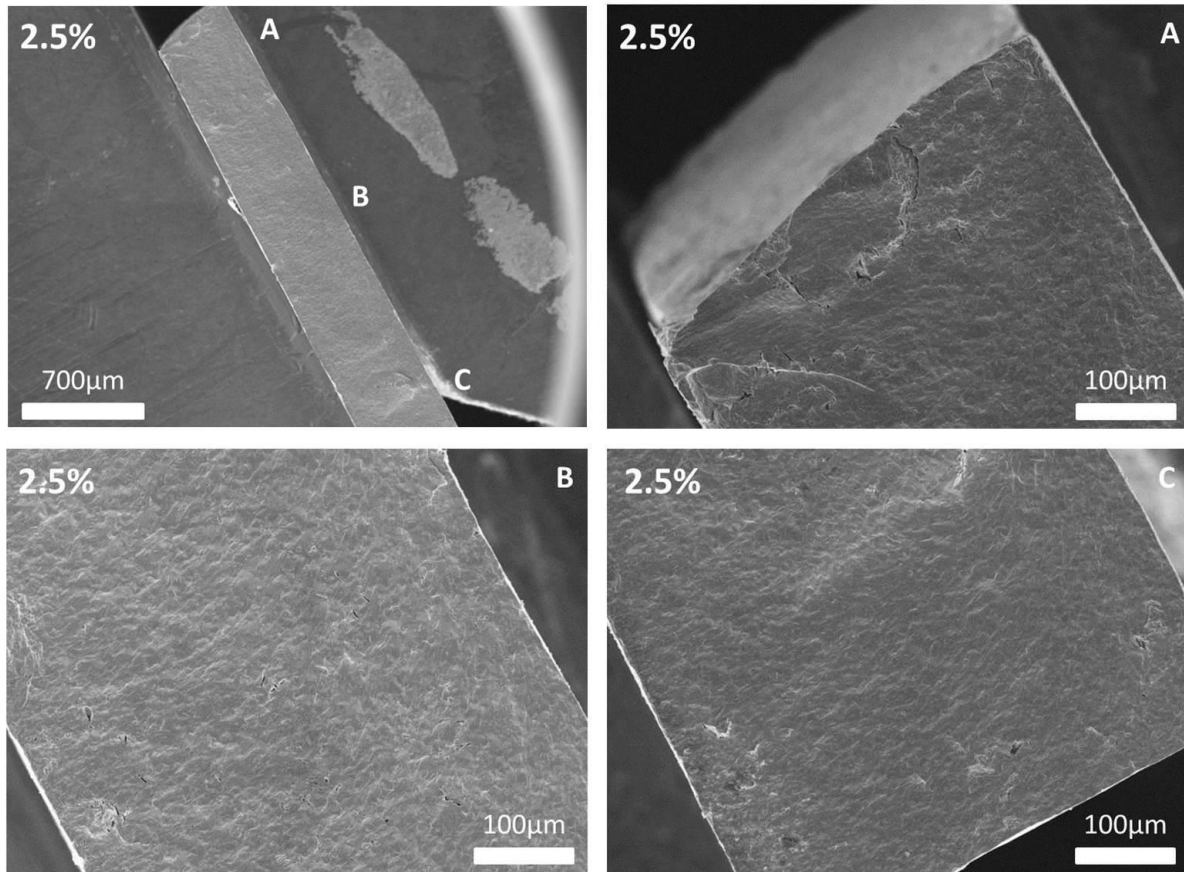


Figure 56: SE overview on the fracture surface of the 2.5 wt % Pu sample

The homogeneity of the samples was probed via EDX with line and spot analysis. Figure 57 shows the position of four different scans with the obtained U and Pu atomic and weight percent on the 10 wt % Pu-doped UO_2 . Each scan was performed at a much higher magnification, such as can be seen

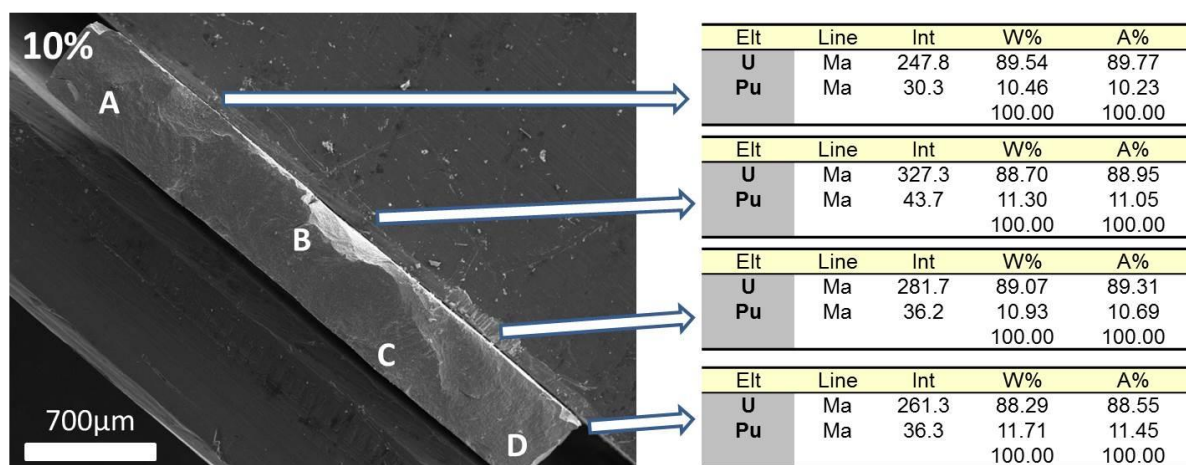


Figure 57: EDX in four different points of the fracture surface of the 10 wt % Pu sample observed at the SEM

in Figure 58, as the non-flat geometry of the fracture surface would have affected significantly the accuracy of the method. The same procedure, although not reported here, was applied to the 2.5 wt % Pu-doped UO_2 and gave similar results.

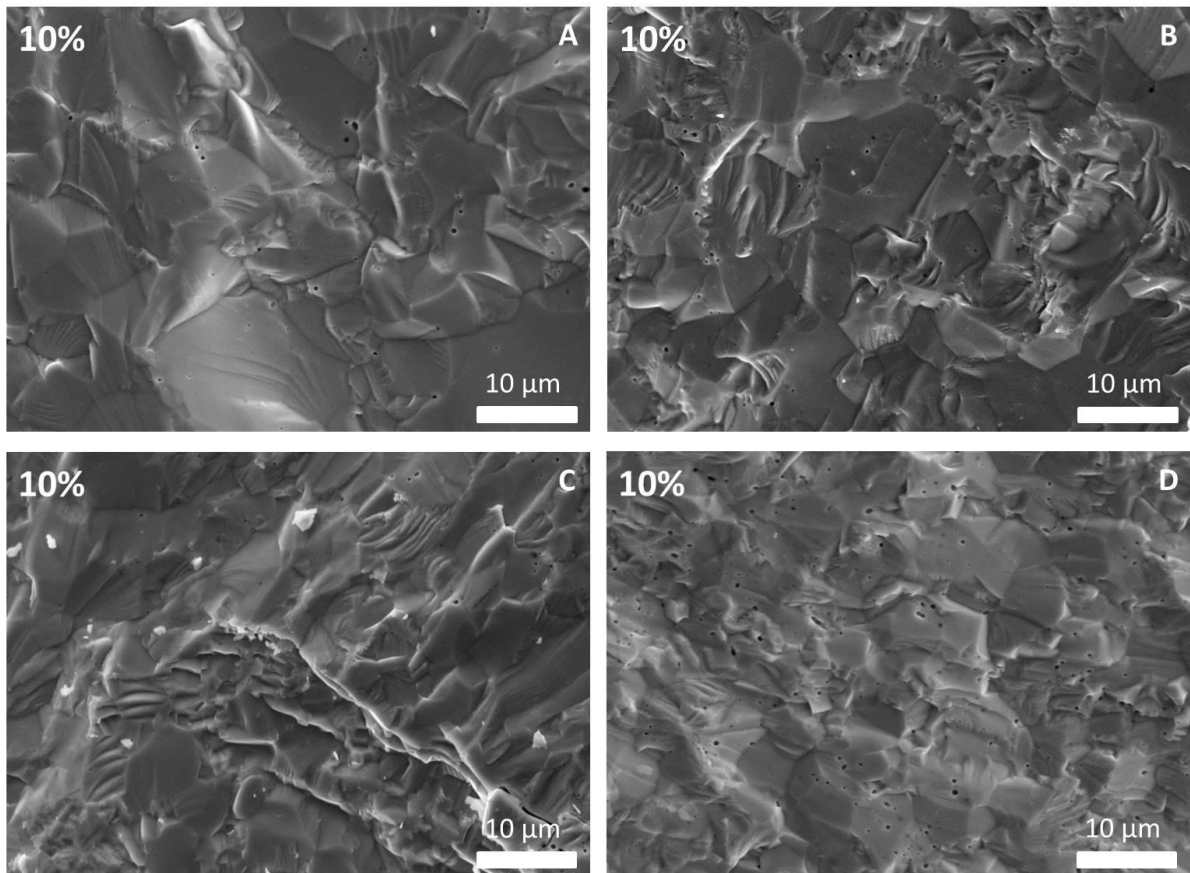


Figure 58: detail of the regions of interest of the EDX scanning in the 10 wt % Pu-doped sample.

Within the uncertainty of the technique, no inhomogeneity was detected, and no trend was seen either in radial or axial direction.

At higher magnification, as shown in Figure 58 and Figure 59, the microstructure appears to be the one typical of a sintered ceramic. The grains are well-faceted and porosity is very limited. The size of the pores ranges from 0.1 to few μm , both for inter and intra granular porosity. As the fracture is not entirely intergranular, an estimation of the grain size cannot be accurately made, but the visible grains measure between 5 and 20 μm . Slight local variations in the pores size and number are present in both samples observed and do not seem to have any dependence on the composition. At this magnification also more un-sintered regions become visible at the periphery of the disk, with

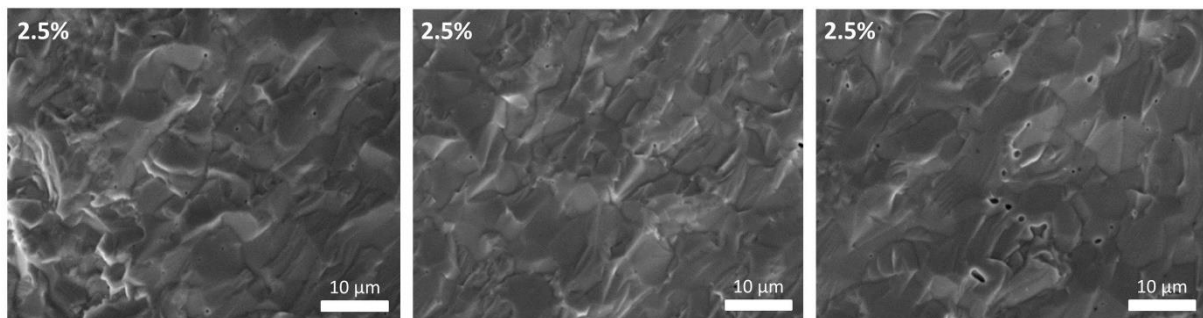


Figure 59: higher magnification images of three different zones of the fracture surface of the 2.5 wt % Pu-doped sample. The different zones are the same as marked A, B and C in Figure 56.

pore channels running along one or more grains. It is important to identify these types of inhomogeneity to be able later to correctly attribute the variation of the thermophysical properties of the material to the damage or the porosity effect.

4.2.2 Nanograined UO_2 for grain size effect study on radiation resistance

As mentioned in the previous section, SEM observations on the fracture surfaces were crucial to qualitatively estimate the density of the samples. Moreover, they constituted the main source of data for grain size evaluations. Finally, the homogeneity of the microstructure was assessed, in terms of densification/porosity, grain size, shape and possible orientation. A very small variation in the temperature, pressure (and hence green density) or chemical composition (due to contaminations) during the thermal treatment can result in an abrupt change in the final grain size. In this section, only some images are shown as examples of the achieved microstructures, but samples were carefully mapped for density and homogeneity evaluations. All the samples shown have been previously proven to be dense and homogeneous.

The four powders used to press the disks were also characterized by means of SEM. Although the powders particles were too small to be observed, the agglomerates size and shape could be analysed and compared.

4.2.2.1 UO_2 nanopowders

As discussed in section 3.2.1, the powders sintering behaviour is dictated by their particle size as well as by their agglomeration. Namely, the size of the primary particles affects more the initial stages of sintering, while the effect of the size of the agglomerates is more evident in the final part of the densification (agglomerates and primary/secondary particles are defined in Figure 60 – last row).(41,213) A summary of the powders produced is given in Figure 60(A-H), and as expected the size of the agglomerates reflects the same trend of the maximum sintering temperatures.

The beneficial effect of the application of the sol-gel process with respect to the simple hydrolisis of the uranyl nitrate solution is evident. The addition of organics results in almost spherical beads, opposed to the very irregular shapes of the precipitates without any additives. Furthermore, thanks to the employ of the rotating cup atomizer, the beads are monodisperse. This regularization of the shape and size of the agglomerates results in better flowability and packing density and an easier sintering among them in the last stages of the process, when densification within the agglomerates has completed already.

It is worth noting that, for the two oxalate-derived powders, the nanocrystalline primary particles cannot be seen in the SEM images. During the oxalate thermal decomposition, UO_2 nanocrystals start growing and ordering inside the original oxalates microcrystals.(215) This morphology (shown in the insert of Figure 60-F) is retained after conversion as polycrystalline primary particles, which are those visible in Figure 60-F. These stacked-platelets structures are destroyed during the hydrothermal decomposition (117), resulting into smaller, round particles (Figure 60-H). Also for this powder, XRD results (which will be presented in section 4.3.2.1) indicate that the visible particles are polycrystalline, resulting in this case from the destructuring of the original oxalate platelets. These primary particles are then grouped to form different types of larger secondary particles, which are

bigger in the case of the hydrothermal decomposition, and in both cases are much smaller than for the hydrolysis-related powders (left column of Figure 60). Bigger agglomerates are also visible.

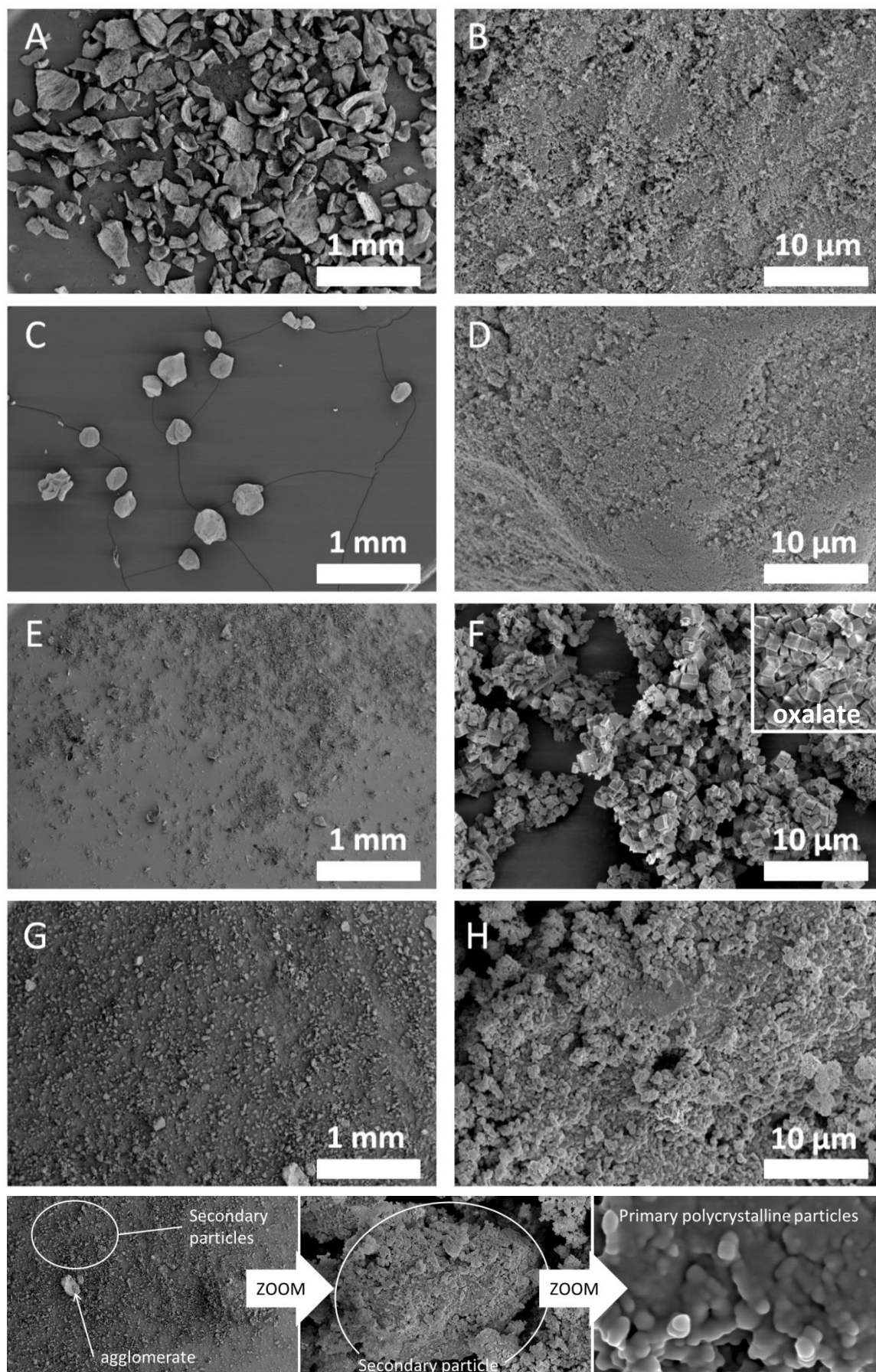


Figure 60: comparison of the four powders tested for the production of nanograined UO_2 pellets. A-B hydrolysis; C-D sol-gel; E-F oxalate thermal conversion; G-H oxalate hydrothermal conversion. The last row of pictures defines what has been labelled as agglomerate and primary/secondary particle in the text.

On the contrary, the particles visible in Figure 60-B and Figure 60-D match with the crystallite size derived from XRD for these two powders.

4.2.2.2 UO_2 SPS disks

As explained in Section 3.2.3, each produced powder was tested in SPS in a standard treatment that was interrupted every time as soon as the densification rate decreased to zero, in an attempt to minimize the grain growth. These conditions are summarised in Table 13, and the final microstructures obtained are presented in Figure 61.

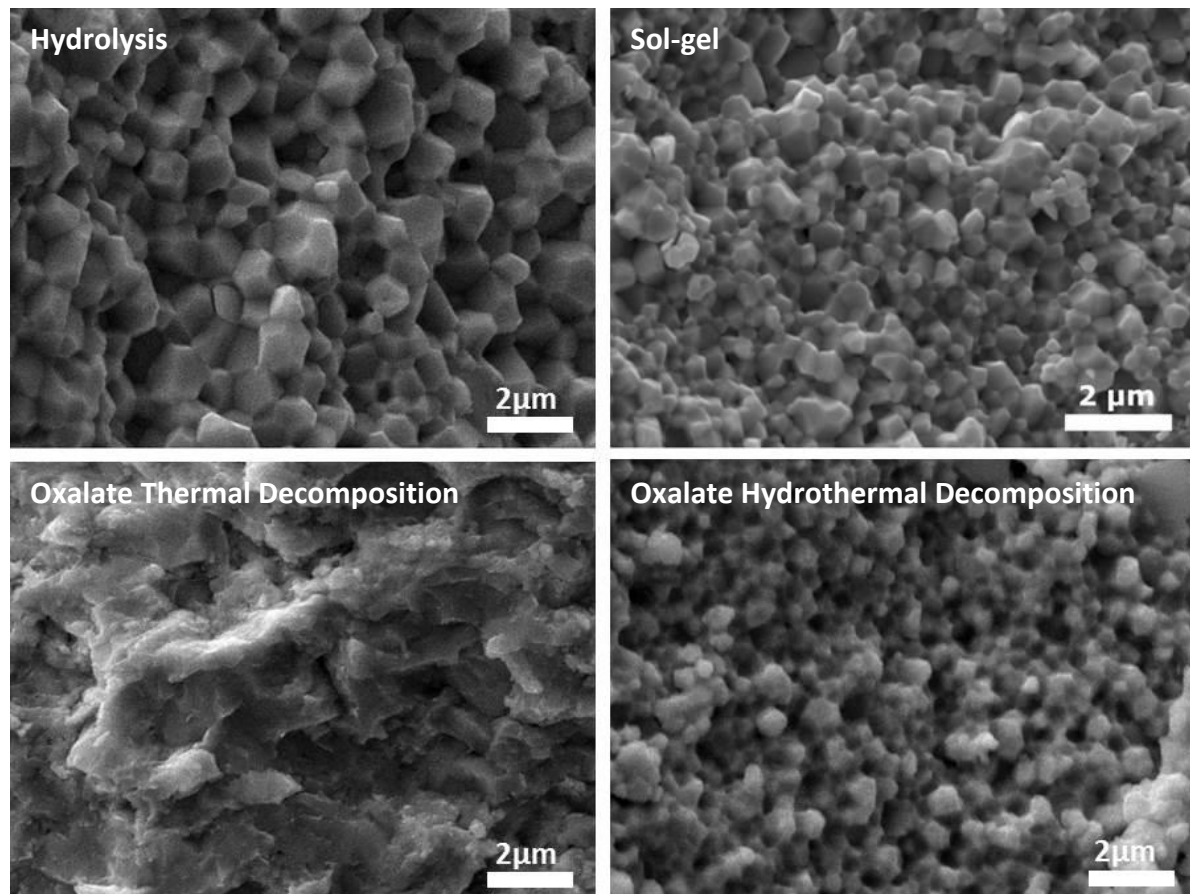


Figure 61: SE images of the fracture surfaces of the four disks obtained by sintering the powders shown in 4.2.2.1 under the same conditions (70 MPa, vacuum, 200°C/min) and interrupting the treatment as soon as densification was achieved.

Synthesis route	Crystallite size [nm]	O/M ratio	Synthesis T [°C]	Sintering T [°C]
Hydrolysis	50	2.08	650	900
Sol-gel	35	2.24	600	850
Oxalate thermal decomposition	10	2.01	600	1200
Oxalate hydrothermal decomposition	5	2.04	170	700

Table 13: main characteristics of the powders tested in SPS. Before sintering the powders were pre-pressed at 17 MPa and thermal treatments were performed in vacuum, with an applied pressure of 70 MPa and heating and cooling rate of 200 °C/min.

As expected, the samples sintered at higher temperatures exhibit a larger grain size. Remarkably, the grain size of the sol gel powder remained quite low with respect to the precipitated powder, despite a minimal difference in the maximum sintering temperatures. A similar microstructure is obtained

with the oxalate hydrothermal decomposition powder, despite being the sintering temperature almost 200 °C lower.

However, as it will be explained more in detail in 5.3.2, joint considerations on the final O/M ratio and microstructure, led to the adoption of the oxalate hydrothermal decomposition synthesis route for the preparation of the powder to be used in the further tests.

4.2.2.3 Nanograined UO₂ disks and successive annealing

The application of 2S – SPS and HP – SPS led to further lowering of the maximum sintering temperature and hence of the final grain size. Figure 62(A-H) shows the response of the powder to 4 different thermal treatments, which are summarized in Table 14.

The integrity of the samples and the regularity of their shape were also affected by the different sintering conditions applied, with the HP – SPS disks crumbling in most of the cases before any direct height or diameter measurement on the disk could take place.

It is worth mentioning that the pores diameter scales with the grain size of the sintered material. For this reason, samples of finer grain size seem to exhibit a higher porosity at high magnifications, despite having the same overall density as their analogue with larger grains. This is due to the fact that, by decreasing the grain size of a factor x , a similar decrease is achieved on the pores diameter, resulting in having approximately x^3 more pores (and x^2 more grain boundaries) for the same fractional porosity.

Treatment	Heating rate [°C/min]	Temperature [°C]	Dwell time	Pressure [MPa]	Grain size
HT – SPS	200	1600	60 s	70	3.08 μ m
LT – SPS	200	700	3 s	70	863 nm
2s – SPS	200	650 – 550	3 s – 100 min	70	467 nm
HP – SPS	100	700	3 s	500	163 nm

Table 14: sintering conditions applied to produce the four microstructures shown in Figure 62. Before sintering the powder was pre-pressed at 17 MPa and every treatment was performed under vacuum. LT – SPS are the same sintering conditions used during the powders

After annealing, a second SEM inspection was performed to make sure that the microstructure was not altered during the thermal treatment. Figure 63 shows the microstructure of the HP – SPS pellet before (A) and after (B) annealing thermal treatment. No grain growth could be detected, as well as any detrimental effect on the porosity and integrity of the sample. The samples with larger grains also did not exhibit any change after annealing, but the micrographs are not reported here for sake of brevity and can be consulted in the annexes.

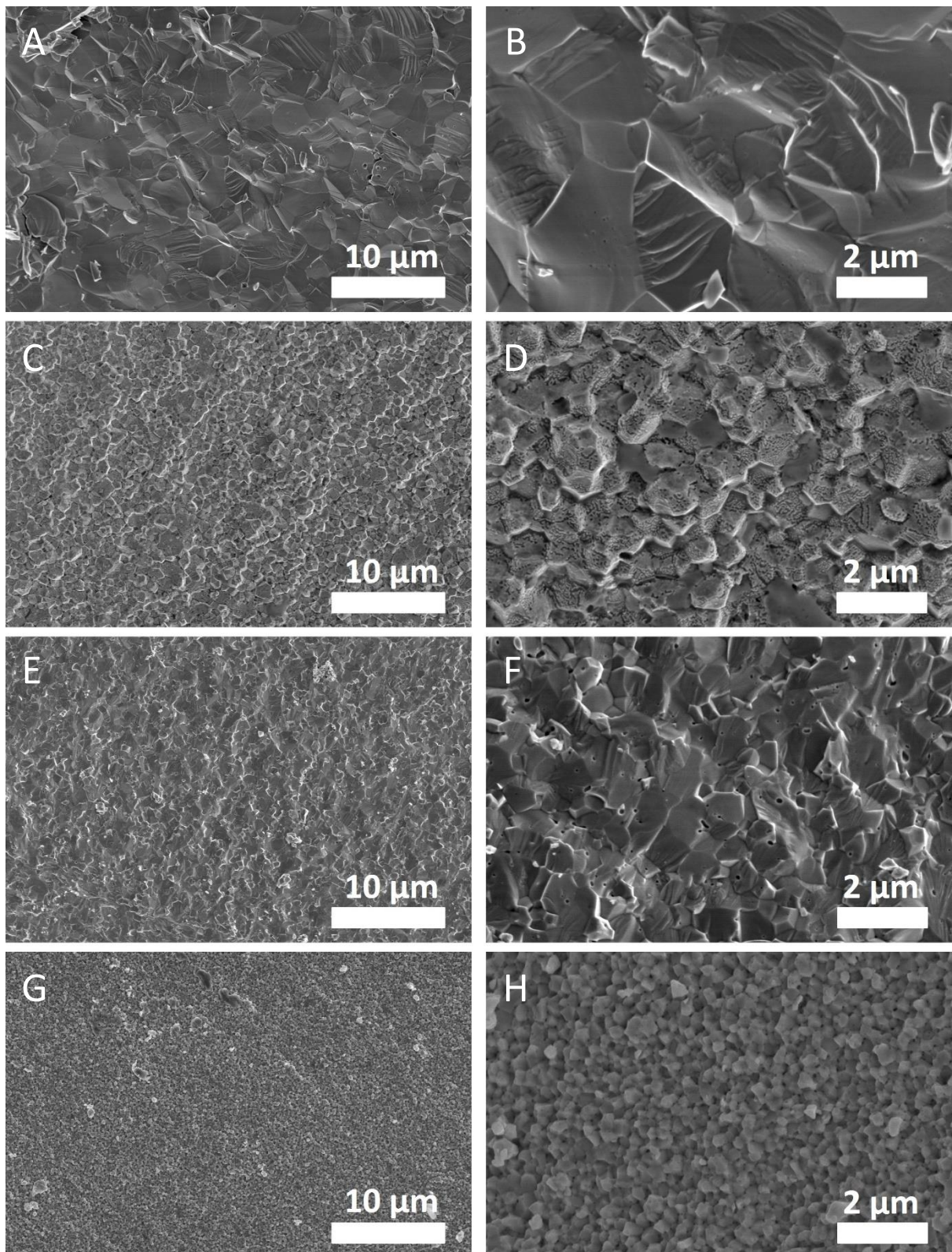


Figure 62: SE images of the fracture surfaces of the UO_2 samples sintered with different SPS treatments. A-B high temperature (70 MPa - 1600°C) SPS, C-D low temperature (70 MPa - 700°C) SPS, E-F two-step (70 MPa - 650-550°C) SPS, G-H high pressure (500 MPa - 700°C) SPS.

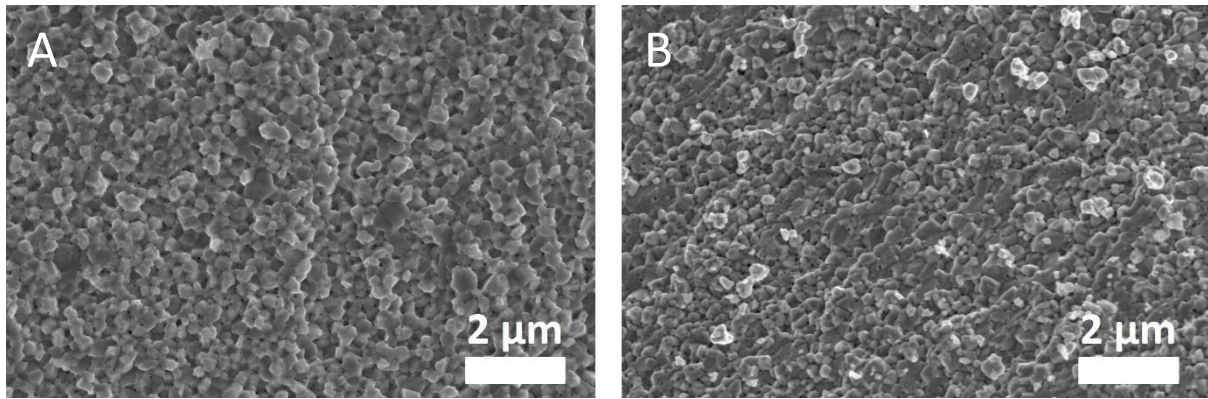


Figure 63: SE images of the fracture surfaces of the HP – SPS sample before (A) and after (B) annealing at 600 °C under Ar-H₂ for 2h.

4.3 Crystal structure – X-ray diffraction

4.3.1 ²³⁸Pu-doped UO₂ samples for accelerated spent nuclear fuel ageing study through α -self-irradiation

XRD analysis of samples belonging to the different batches was performed in the days immediately after the production. However, as it will be shown in the dedicated chapter, few days of damage accumulation with the activity involved can already significantly alter the XRD response of the material. In order to minimize this effect, the samples were ground right after the sintering, and their characterization was then carried on in the shortest possible time in the following days.

For both compositions, as can be seen in Figure 64, the diffraction pattern highlights the presence of a single fluorite structure, meaning that the solid solution of UO₂ and PuO₂ was successfully achieved.

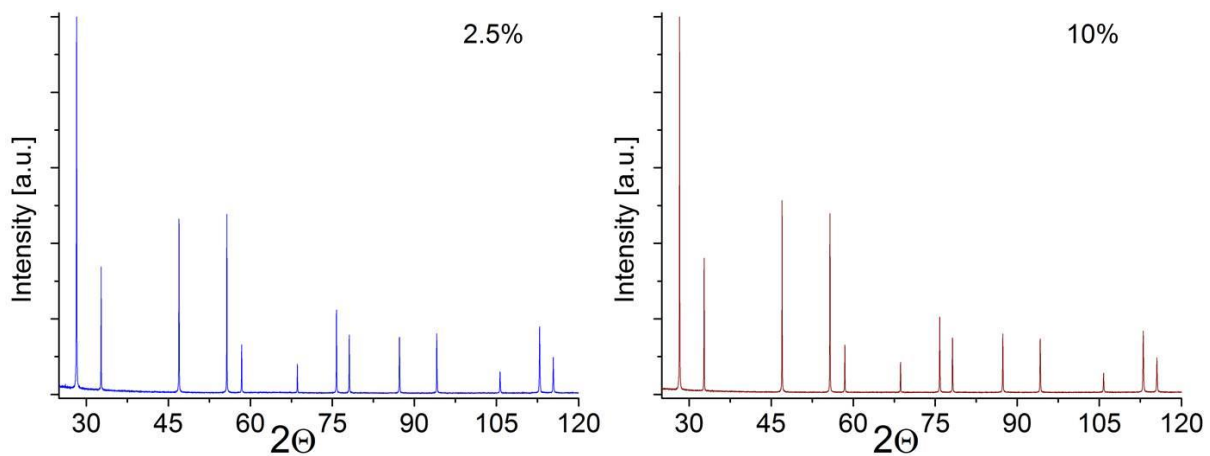


Figure 64: XRD patterns of the 2.5 and 10 wt % Pu samples

The lattice parameters of the resulting solid solutions were calculated with a Rietveld refinement and the obtained values are reported in Table 15. As shown in Figure 65, their values are in good agreement with the Vegard law, considering the initial composition of the dopant powder. Data from Elorrieta et al (223) and Lyon and Bailly (224) are shown for comparison.

Nominal Pu [%]	Refined a [Å]	Vegard law a [Å]	Microstrain [10^{-4}]
2.5	5.468(1)	5.46863	2.5
10	5.463(1)	5.46303	2.7

Table 15: refined lattice parameters, values predicted by the Vegard, and microstrain of the samples.

Values of the microstrain are also reported as calculated with the Williamson-Hall approach (191), and they are quite small for both compositions with a slight increase with the Pu content.

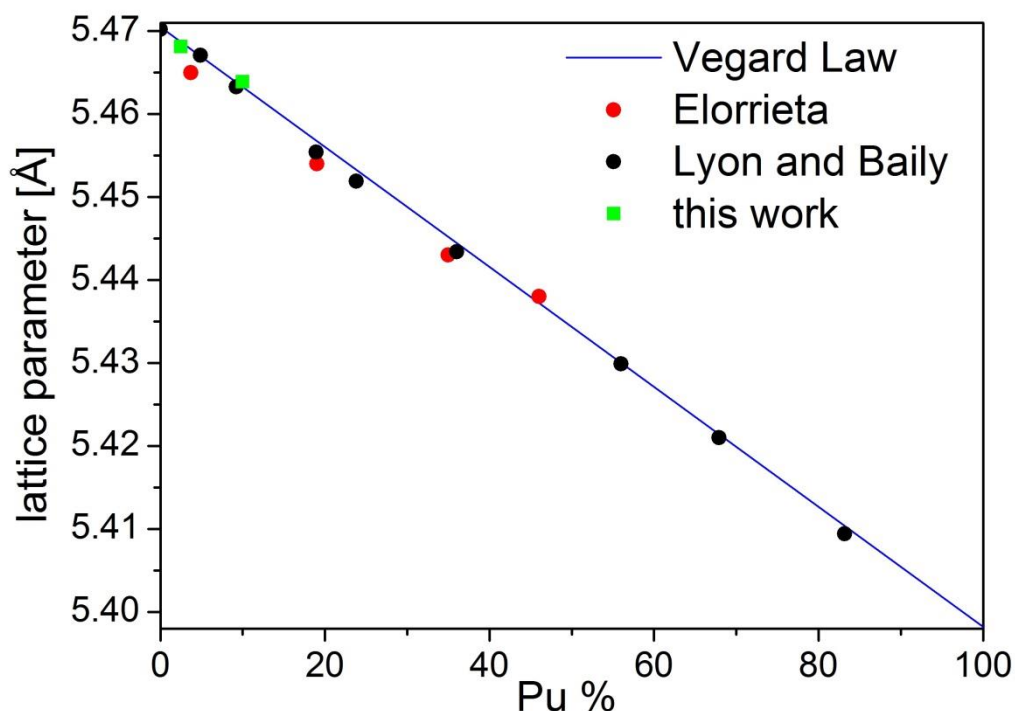


Figure 65: Vegard law for the lattice parameter of solid solutions (such as $\text{UO}_2\text{-PuO}_2$) and experimental points from this work, Elorrieta et al (223) and Lyon and Bailly (224).

4.3.2 Nanograined UO_2 for grain size effect study on radiation resistance

Contrarily to the $(\text{U,Pu})\text{O}_2$ case, here any variation of the lattice parameter from the literature data can be attributed only to the deviation from the stoichiometric O/M ratio equal to 2.00. XRD was systematically used throughout the work to assess the stoichiometry of the compounds in different stages of the nanograined UO_2 pellets preparation.

Furthermore, microstrain and, when possible, crystallite sizes were also determined by XRD with the Williamson-Hall approach. In particular, for the powders the crystallites were too small to be clearly discerned with SEM so their size was determined mainly from XRD refinements. On the contrary, for the sintered material the crystallite size was already too high to be measured with the available XRD equipment. The microstrain was instead of major interest, to assess the homogeneity of the samples and its possible dependency on the crystallite size (as evaluated from SEM micrographs).

4.3.2.1 *UO₂ nanopowders*

Just like it was done with the SEM observations of the powders, where it was possible to correlate the size and shape of the agglomerates with their effect on the sintering behaviour, also XRD results help explaining some features of the sintering curves. The main features of each one of the produced powders were already presented in Section 3.2.3.5. As anticipated in Chapter 3, the nanosized powders obtained by conversion of oxalates were oxidising very quickly even under the gloveboxes N₂ or Ar atmosphere, due to hardly avoidable oxygen or moisture impurities. Analysis performed after one month of storage on leftover nanopowders showed already complete oxidation to U₄O₉, which in such small domains can be detected from the change in intensity ratio of the 002 and 202 reflections (225). This explains why, in the following sections, the O/M ratio of some sintered pellets is higher than the initial value for the starting powder, as these disks were sintered some days after the powder synthesis and hence starting from O/M > 2.04.

4.3.2.2 *UO₂ disks*

When testing the four produced powders in SPS, the time and temperature of the treatment were kept as low as possible to avoid any grain growth. The lattice parameter and O/M ratio of the sintered material is reported in Table 16, together with the initial powder O/M ratio and the treatment temperature.

Powder	Powder O/M	Sintering T [°C]	Sintered O/M
Hydrolysis	2.08	900	2.00
Sol-gel	2.24	850	2.06
Oxalate Thermal Conversion	2.01	1200	2.00
Oxalate Hydrothermal Conversion	2.04	700	2.00

Table 16: O/M of the powders sintered in SPS, sintering temperature and O/M of the resulting final pellet. In every treatment the powder was pre-pressed at 17 MPa and sintered with an applied pressure of 70 MPa, under vacuum. The treatments were all stopped as soon as densification was completed, to avoid grain growth.

As shown in section 4.2.2, the finest grain size was obtained from the powders produced by sol gel and oxalate hydrothermal decomposition. However, the final O/M ratio of the sintered sol gel powder was still considerably higher than the other sintered powders, leading to the choice of the oxalate hydrothermal decomposition as preferred synthesis route.

4.3.2.3 *Nanograined UO₂ disks and successive annealing*

Due to the very low sintering temperatures and dwell times, the HP – SPS treatment was not resulting in complete reduction to O/M = 2.00 of the starting powder. As mentioned in Section 3.2.3.7, 2s –SPS treatments with T₂ below 550 °C also resulted into slightly hyperstoichiometric samples but without bringing any improvement to the final microstructure, and were hence discarded.

As shown in Table 17, the progressive oxidation of the nanopowders in the days immediately after production was reflected in an increasing O/M ratio also in the final HP – SPS disks.

Treatment	Powder O/M	Sintering T [°C]	Sintering t	Disk O/M	Microstrain [10 ⁻⁴]
HT – SPS	2.04	1600	60 s	2.00	3
LT – SPS	2.04	700	3 s	2.00	5
2s – SPS	2.04	650 – 550	3 s – 100 min	2.00	4
HP – SPS	2.04	700	3 s	2.05	18
HP – SPS – 2 weeks old powder	2.16	700	3 s	2.09	29

Table 17: initial O/M of the powders, sintering conditions, and final O/M and microstrain of the sintered material. All the samples were sintered in vacuum. The powders were pre-pressed with 17 MPa and then sintered under 70 MPa in HT, LT and 2s – SPS, and 500 MPa in HP – SPS.

It is worth noting that the temperature and dwell time of sintering of HP – SPS and LT – SPS treatments are the same, but the latter results in full reduction of the samples. The difference in the final O/M of the sintered disks can be attributed to the SiC inserts, which make the environment around the sample more inert and at the same time decrease the accuracy of the temperature measurement.

The higher final oxidation of the HP – SPS samples is accompanied by a larger microstrain. The application of the Williamson-Hall approach shows no dependence of the microstrain on the probed depth (i.e. Bragg angle). In addition to a higher overall oxidation, the HP – SPS samples hence present also lattice parameter (and thus O/M) gradients from boundary to centre of the grains, hinting that reduction was occurring during sintering at the particles surfaces but was not completed in the core. For the other samples, despite having no contribution of the crystallite size, its evaluation was less accurate as the breadth of the peaks is constituted almost entirely by instrumental broadening.

The application of the successive reduction treatment had the effect of homogenising the O/M and microstrain of the samples. Table 18 shows the effect of the same annealing treatment on the different samples.

Sintering treatment	Sintered O/M	Annealing T [°C]	Annealing t [h]	Annealed O/M	Microstrain [10 ⁻⁴]
HT – SPS	2.00	600	2	2.00	4
LT – SPS	2.00	600	2	2.00	3
2S – SPS	2.00	600	2	2.00	2
HP – SPS	2.05	600	2	2.00	8
HP – SPS – 2 weeks old powder	2.09	600	2	2.00	7

Table 18: O/M of the sintered samples, annealing conditions, and final O/M and microstrain of the annealed samples.

As expected, the reduction of the hyperstoichiometric samples to UO_{2.00} resulted also in a decrease of the microstrain, meaning that full reduction occurred uniformly throughout the whole sample depth and from the grains surface to the centre.

Figure 66 shows the comparison of the XRD spectra of HT and HP SPS samples before and after annealing. The thermal treatment had substantially no effect on the already homogeneous samples (HT, LT and 2S – SPS), with little-to-no decrease in the peak breadth (the slight broadening seen in Figure 66-B can be attributed to the lower signal-to-noise ratio of the annealed pattern). On the contrary, on the HP – SPS samples the effect was remarkable, leading to a significant shrinking of the peaks while the grain size was unmodified, as confirmed by SEM micrographs.

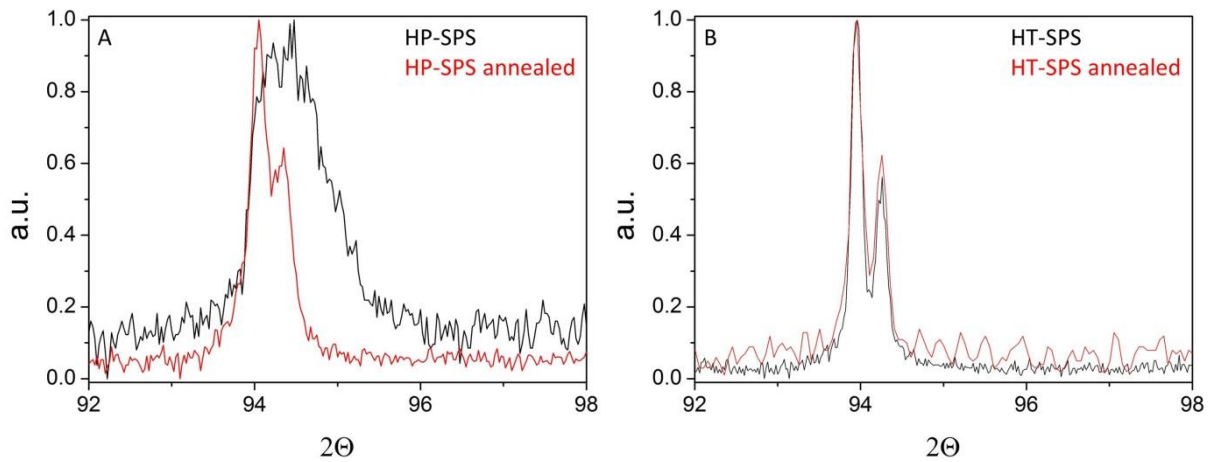


Figure 66: effect of the annealing treatment on the HP – SPS sample (A), and on the HT – SPS sample (B) for comparison. The HP – SPS sample undergoes significant reduction (peak shift) and microstrain relaxation (peak breadth decrease).

4.4 Transmission electron microscopy

4.4.1 ^{238}Pu -doped UO_2 samples for accelerated spent nuclear fuel ageing study through α -self-irradiation

TEM samples preparation of Pu-bearing compounds can take up to some days of time, during which already a significant damage can arise. For this reason the TEM analysis was conducted on a piece of 10%-Pu-doped UO_2 after a dedicated annealing, with careful planning of the activities in order to minimise the time between the treatment and the analysis. In addition to that, the sample was crushed already immediately after the annealing, limiting the possible successive damage accumulation.

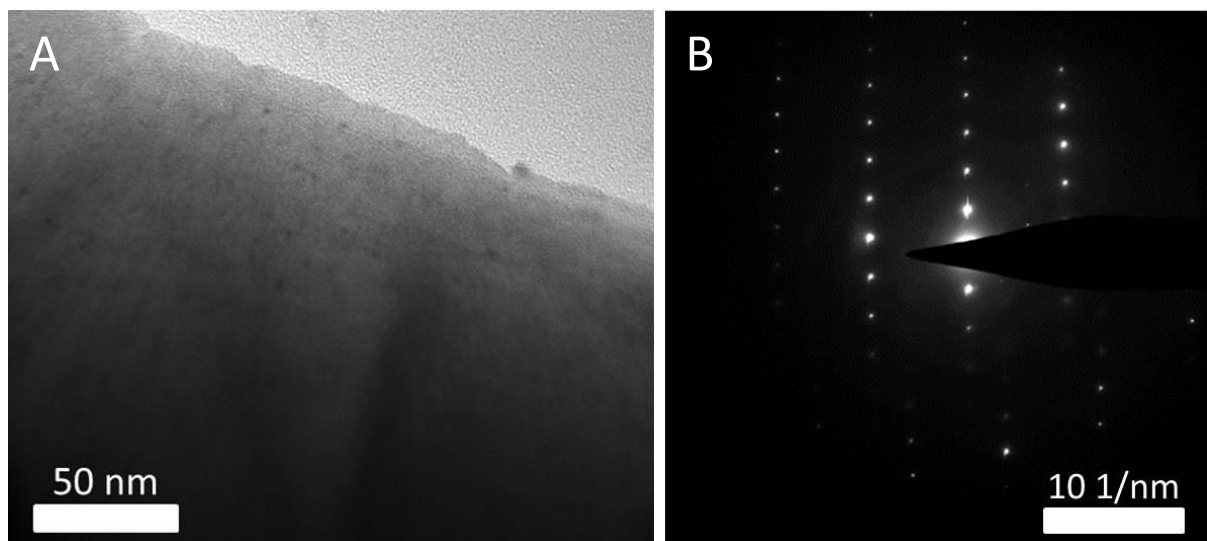


Figure 67: TEM image (A) and diffraction pattern (B) of a freshly annealed 10 wt % Pu-doped UO_2 sample. The annealing of the sample resulted in a damage-free sample.

As can be seen in Figure 67, the precautions taken during the sample preparation made it possible to observe a completely undamaged sample. The diffraction pattern (Figure 67-B) confirms the existence of only one phase, as determined already by XRD, meaning the achievement of a uniform (U,Pu)O₂ solid solution.

4.4.2 Nanograined UO₂ for grain size effect study on radiation resistance

UO₂ samples produced by HP – SPS were also observed by mean of TEM. The preparation was done by cutting and polishing a FIB lamella. Due to the fine and diffused porosity, grain pull-out could not be completely avoided, frustrating the possibility to have good images of the cut surface during the FIB lamella preparation.

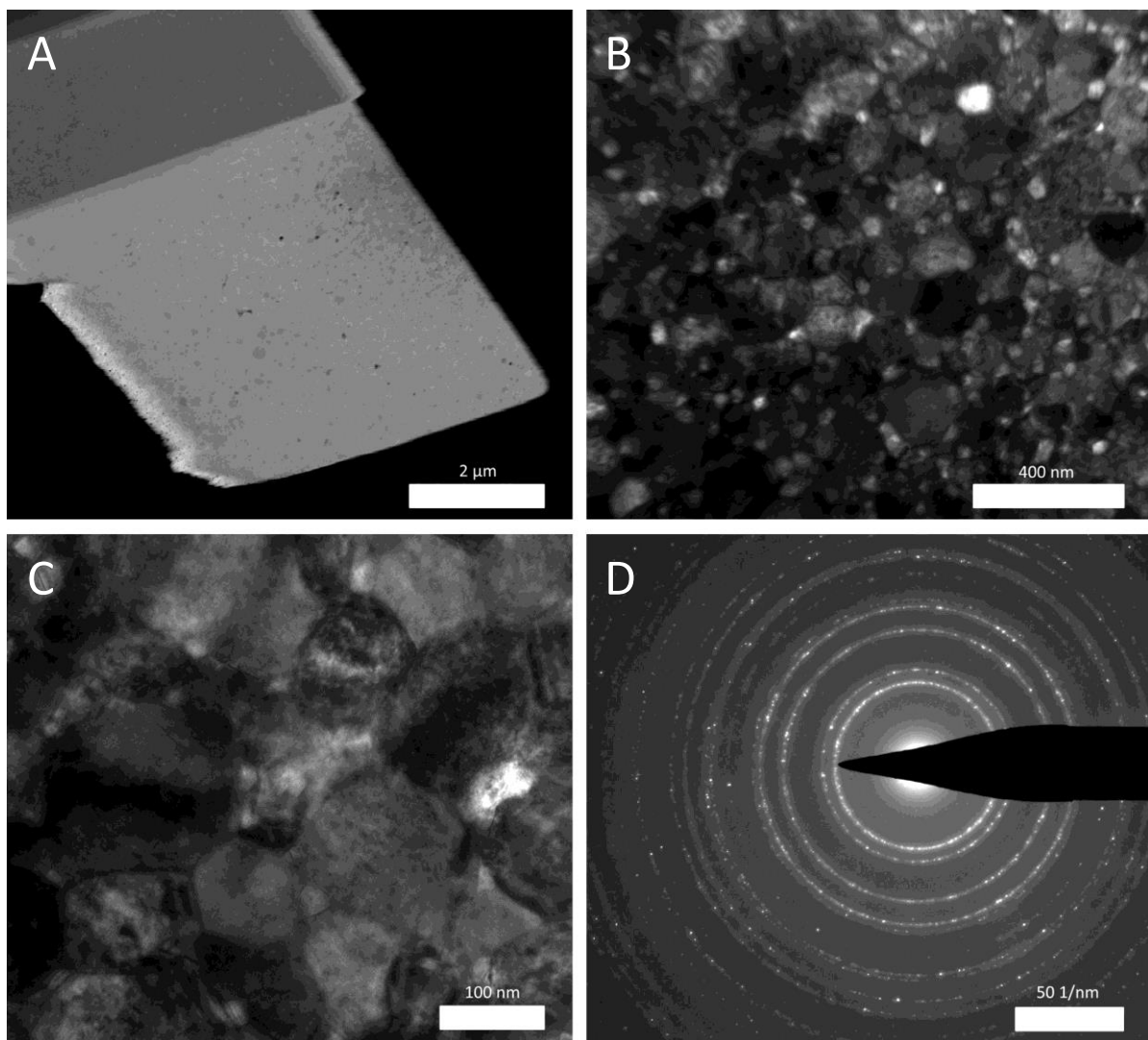


Figure 68: nanograined UO₂ FIB lamella STEM overview (A), microstructure as seen from TEM (B – C) and diffraction pattern (D).

As can be seen in Figure 68, TEM observations confirm what already highlighted from the SEM analysis, with grain size of about 160 nm and pores of few tenths of nm. As for the SEM images, also here it is worth remembering that the apparently high amount of porosity is due to the reduced diameter of the pores, which scales together with the grain size. During coarsening in fact grain

growth is accompanied by pores growth (see Section 1.2.1.2). For this reason, pores appear to be much more numerous, in samples where grain growth was avoided (i.e. the HP – SPS disks), at higher magnifications, while the overall porosity is the same for all samples. Moreover, in TEM this effect is highlighted as the pores present in different layers throughout the thickness of the lamella are all visible at the same time.

4.5 Other fresh MOX properties

Since for the (U,Pu)O₂ the periodical monitoring of the evolution of many thermophysical properties was foreseen, the determination of the initial state of the samples involved more characterization techniques. Moreover, due to the higher complexity of the system, a more exhaustive comparison with literature values was conducted, in order to assess the quality of the produced samples, and back-up the conclusions drawn from EDX and XRD results on the composition of the samples.

4.5.1 Crystal structure - Raman

Due to the complexity of the setup available at the JRC-KA, the Raman measurement could not take place immediately after the samples sintering, since the procedure involves several steps which would delay the other characterizations. However, with a dedicated sample annealing, it was possible to have the measurement done just few hours after the end of the thermal treatment.

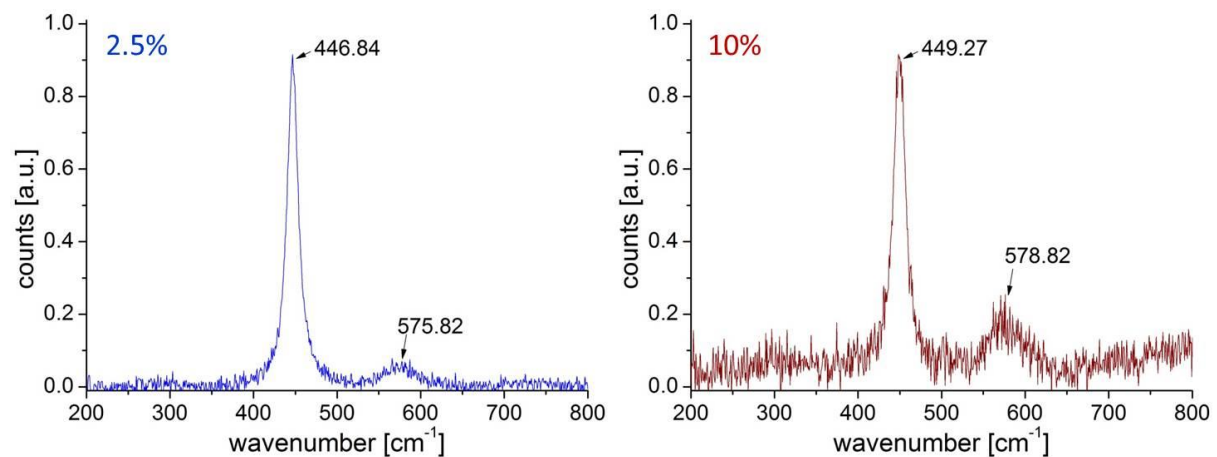


Figure 69: T_{2g} and defect bands of the two different compositions.

The spectra of both samples are presented in Figure 69. As introduced in Section 2.2.3, the peaks with the highest intensities are associated to the T_{2g} vibrational mode. Its position depends on the strength of the anion-cation bond, as this mode is generated by the anti-phase oscillation of the two oxygen sublattices while the cation is at rest. Considering the very simple model of the atom harmonic oscillator, the frequency of the atoms vibrations ω depends on $\sqrt{K/M}$, with M being the mass of the oscillating atom (O in this case) and K the stiffness of the bond. The substitution of U by Pu has the consequence of hardening the M-O bond(226), and as can be seen in Figure 70 this effect is linear with the Pu fraction (at least up to 20 % Pu), providing further evidence for the achievement of a solid solution between UO₂ and PuO₂. Data of Elorrieta et al (223) and Talip et al (227) are used for comparison and they show the same trend up to the considered dopants concentrations.

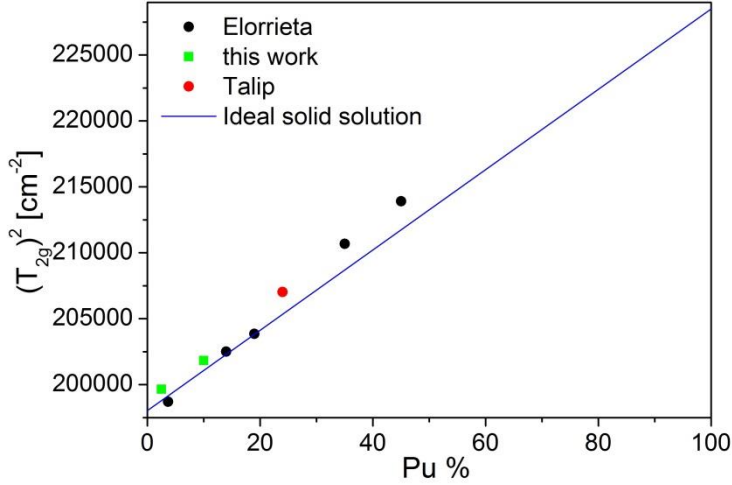


Figure 70: linear dependence of the ω^2 of the T_{2g} mode on the Pu content. Considering the harmonic oscillator approximation, the oxygen oscillation frequency is related to the M-O bond stiffness as $\omega^2 = K/M$. The elastic constant K , i.e. the bond stiffness, increases linearly with the Pu content. Data from Elorrieta et al (223) and Talip et al (227) are shown for comparison.

A second peak is also present at higher wavenumbers, corresponding to the LO component of the triple degenerate ungerade T_{1u} optic mode around 575 cm^{-1} . (228) This mode, originally only infrared-active, becomes also Raman-active due to the loss of selection rules by symmetry breaking, caused by a substitutional atom in the cation sublattice. In fact, its relative intensity increases with the Pu content, although a precise estimation is heavily affected by the higher noise in the 10 % spectrum.

4.5.2 Thermal diffusivity and conductivity – LAser Flash

The thermal diffusivity measurement was also not practically feasible immediately after the samples production. However, the annealing of the concerned sample under inert atmosphere is possible in the machine itself, so it was straightforward to derive a value for the undamaged (U,Pu)O₂. For sake of benchmarking, it is much more convenient to calculate the thermal conductivity and correct it for a 95 % TD dense material, as this is the thermal property that is most commonly reported in literature. Since our measurements took place at 550 K, some further corrections had to be taken into account.

Thermal diffusivity and thermal conductivity are related by the following equation:

$$\alpha = \frac{k}{\rho c_p} \quad (41)$$

Where α is the thermal diffusivity [m^2/s], k is the thermal conductivity [$\text{W}/\text{m}\cdot\text{K}$], ρ is the density [kg/m^3] and c_p is the specific heat capacity [$\text{J}/\text{kg}\cdot\text{K}$].

The c_p values used in our calculation were taken from the work of Duriez et al. (71), while corrections on the density and dilatation of the sample at 550 K were done accordingly to the recommendations of Fink et al. (51) as they do not differ significantly from the values for UO₂.

The measured value, reported in Table 19, is in relatively good agreement with the literature data for low-Pu MOX fuel (71) and is representative also of a fresh UO₂ fuel (200), since for such low Pu content the effect on the thermal properties is negligible(199).

On the contrary, there is some disagreement on the effect of increasing the Pu content on the thermal conductivity. In the range between our two compositions, the models foresee a slight decrease as the Pu content increases (229), in particular at low temperatures, but this is not reported in experimental data (71), suggesting that the variation could be within the uncertainties of the measurement. Nonetheless, in this study no sample with 10 % Pu was dedicated to the thermal conductivity periodic study, since the degradation would have been too abrupt to be followed, and so also the value for the undamaged material was not measured.

T [K]	α [m ² /s]	c_p [J/kg·K]	ρ [kg/m ³]	$k_{95\%TD}$ [W/m·K]
543.78	2.04E-06	287.75	10650	5.83
544.04	2.04E-06	287.78	10650	5.83
544.47	2.03E-06	287.83	10650	5.81
544.87	2.03E-06	287.87	10649	5.79
545.17	2.03E-06	287.91	10649	5.82

Table 19: measured values of the thermal diffusivity α at the reported temperatures and with the calculated values for specific heat capacity, real measured density corrected for 550 K, and thermal conductivity corrected for 5 % porosity.

It is worth mentioning that precision of the measurement of the thermal diffusivity itself is very reliable, yielding an uncertainty below 1 %. However, the accuracy of the measurement is lowered by the uncertainties on the thickness of the samples as well as on the measured temperature (± 5 K). Within these ranges, our data are in excellent agreement with the published literature data.

4.6 Nanograined ThO₂ for grain size effect study on radiation resistance

4.6.1 Microstructure - SEM

In a similar way as it was done for UO₂, each stage of the production of the SPS ThO₂ samples was accompanied by SEM characterization. However, as the process for sintering nanograined dense disks was already designed for the UO₂, and then directly applied to ThO₂, in this case no intermediate grain size samples were produced.

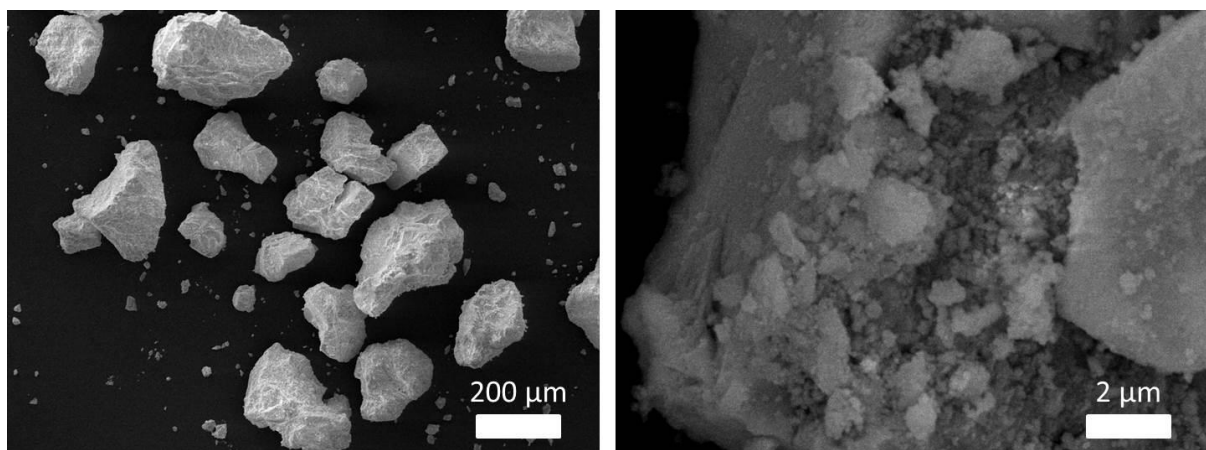


Figure 71: SEM images of the ThO₂ powders derived by hydroxide hydrothermal decomposition.

Figure 71 shows the ThO₂ starting powder. Also in this case, the crystallite size of the powder derived from XRD is much lower than the size of the smallest particles visible by SEM, which appear to be first-order agglomerates.

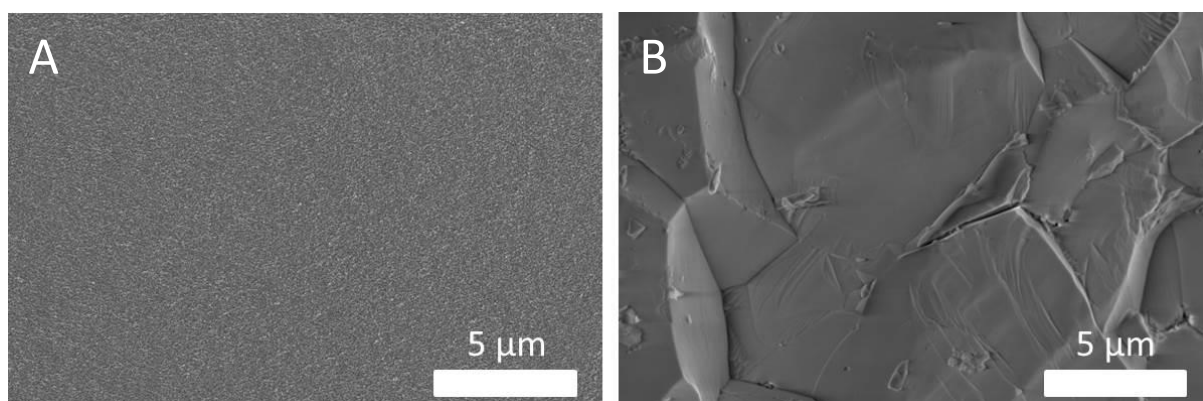


Figure 72: SE images of the fracture surfaces of the two HP – SPS ThO₂ samples produced at 915 °C (A) and 1600 °C (B).

The microstructure of the two samples produced in HP – SPS is shown in Figure 72. The grain size of the sample shown in Figure 72-A is so small that no porosity is visible at this magnification, while for higher magnifications (Figure 73) some small pores start to appear. The increase of the sintering temperature from 915 to 1600 °C in HP – SPS conditions brought the grain size to increase of several orders of magnitude, from roughly 50 nm to more than 5 µm.

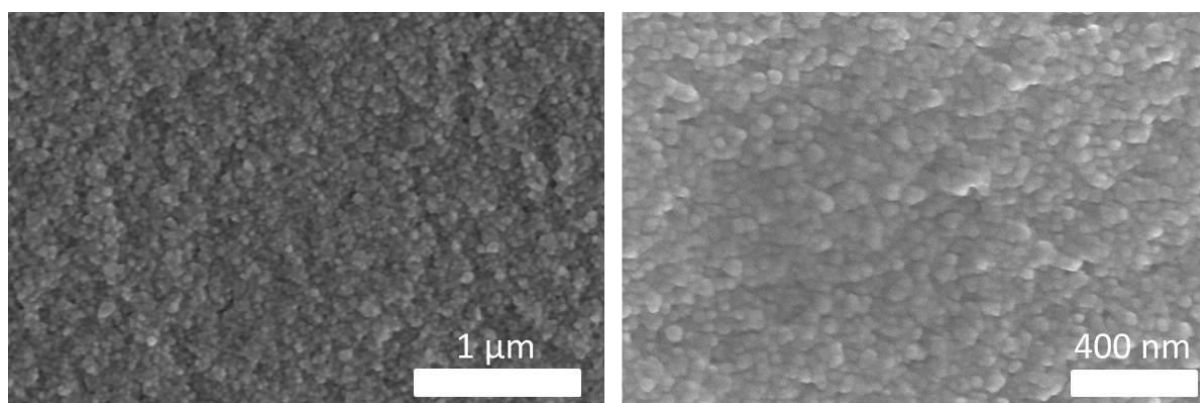


Figure 73: SE higher magnification images of the fracture surface of the ThO₂ HP – SPS samples sintered at 915 °C.

4.6.2 Crystal structure - XRD

In comparison with the UO₂ and (U,Pu)O₂ systems, ThO₂ behaves in a much simpler way, as in this case also no hypo or hyper-stoichiometry effect is present. However, small variations of the lattice parameter were detected, together with increasing values of microstrain as the crystallite size decreases. The summary of the values measured on the disks and powder is reported in Table 20, while a comparison of the pattern of the two disks is shown in Figure 74 A-B.

Sintering temperature [°C]	Dwell time [s]	Lattice parameter [Å]	Microstrain [10^{-4}]	Grain size (intercept method)	Crystallite size (Williamson Hall)
Powder	/	5.6121	42	/	4 nm
915	3	5.5988	6	50 nm	45 nm
1600	600	5.5981	1	8.3 μm	/

Table 20: main sintering parameters of the ThO_2 HP – SPS samples and resulting disks lattice parameter, microstrain and grain size. Powder data are also shown for comparison.

The grain growth was so limited in the sample sintered at 915 °C that the crystallite size was measurable by XRD, and matches quite well the size of the grains evaluated with the intercept method on the SEM of the fracture surfaces.

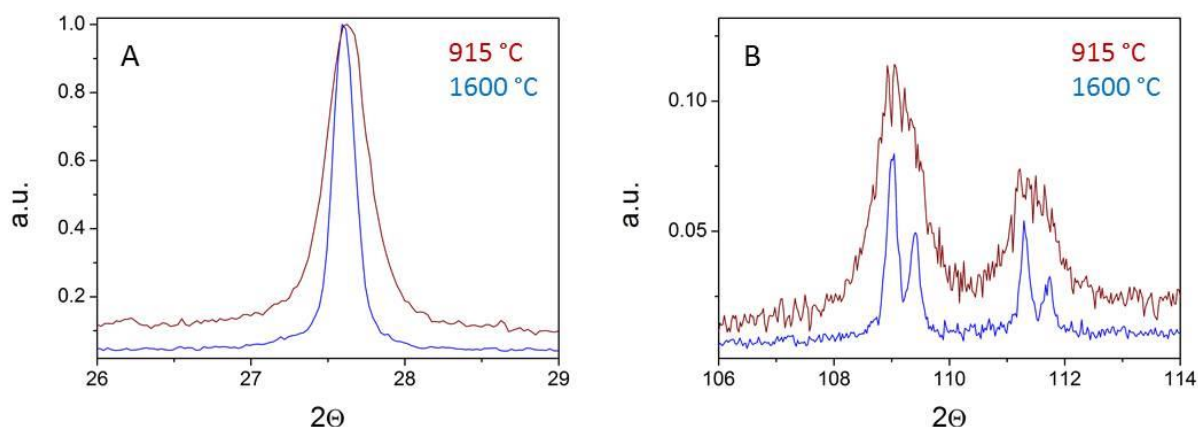


Figure 74: comparison of the XRD patterns of the two HP – SPS ThO_2 samples produced at 915 °C and 1600 °C for low (A) and high (B) angles.

4.6.3 TEM

Contrarily from the UO_2 case, for the ThO_2 samples no FIB lamella preparation was performed. On the other hand, TEM was performed on the ThO_2 nanopowders (Figure 75) as well as on both the HP – SPS samples (Figure 76), for a better comparison.

TEM performed on the nano powders (Figure 75) confirmed the crystallite size derived from the Williamson Hall approach on the XRD data. The grain size visible in Figure 76-B is also in good agreement with what can be observed in the SEM images and also with the calculated crystallite size from XRD data.

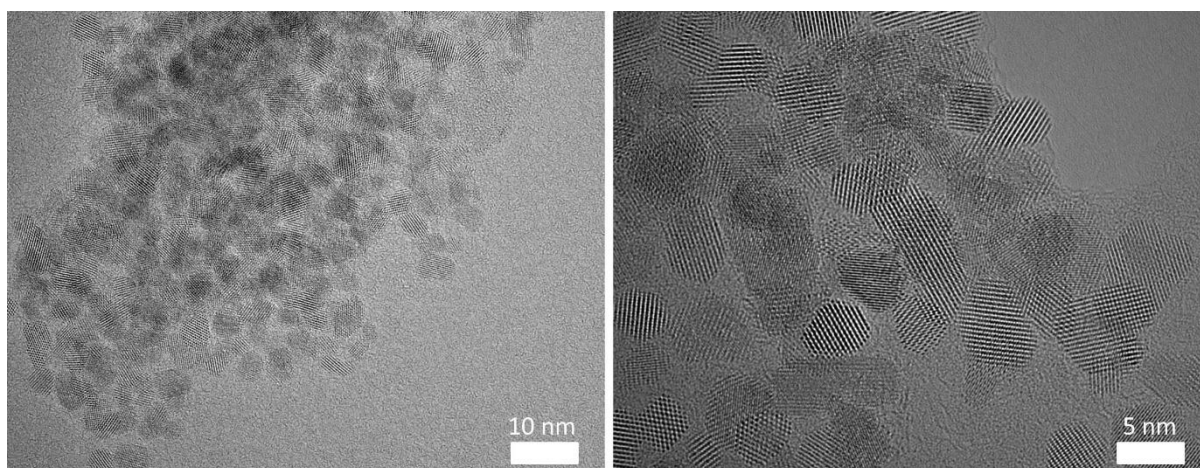


Figure 75: TEM images of the ThO_2 nanopowders produced by hydroxide hydrothermal decomposition

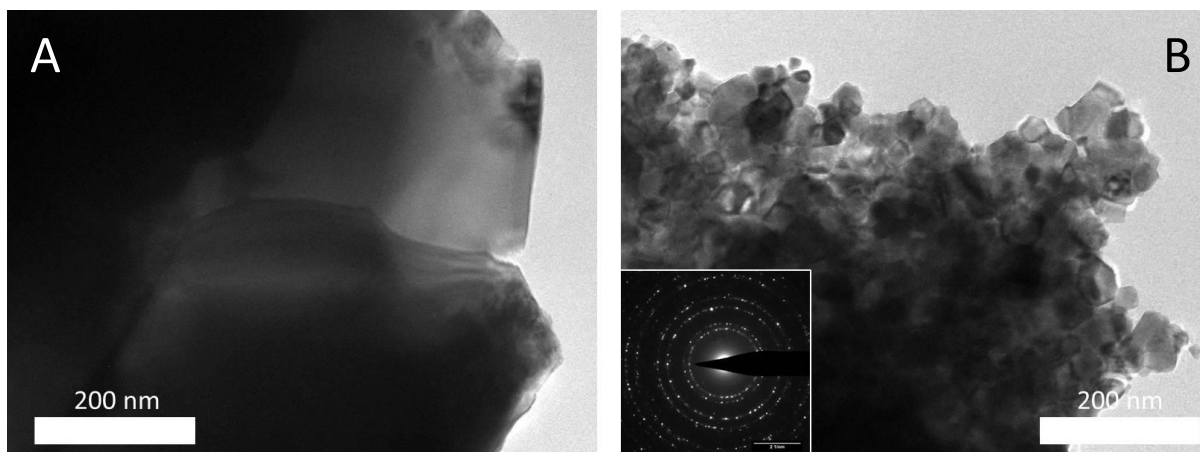


Figure 76: TEM images of the of the two HP – SPS ThO₂ samples produced at 1600 °C (A) and 915 °C (B).

4.6.4 Ion implantation at 600 °C

The characterization of the experiment described in Section 2.1.2.4 is currently ongoing, hence the results presented here should be considered as preliminary and a final interpretation will be provided once all the samples will have been examined.

Due to some logistic aspects, the first beam time was dedicated to ThO₂ samples. The literature about ion implantation in ThO₂ is not as abundant as for UO₂, consisting only in some studies performed to assess the damage induced in electronic stopping regime (230–232), rather than rare gases behaviour, for which this work represents the first systematic investigation. The results were hence benchmarked against UO₂ literature data, given the vicinity of the two systems as well as the final goal of the work, which is the study of UO₂-based SNF.

4.6.4.1 Samples before implantation

Samples were carefully characterised by TEM prior to implantation to be able to discern the implantation-induced features from those arising from FIB preparation. Samples were relatively damage-free, as shown in Figure 77, providing an ideal starting material for gas bubbles identification. Once again, the grain size was confirmed to be orders of magnitude different between the two samples.

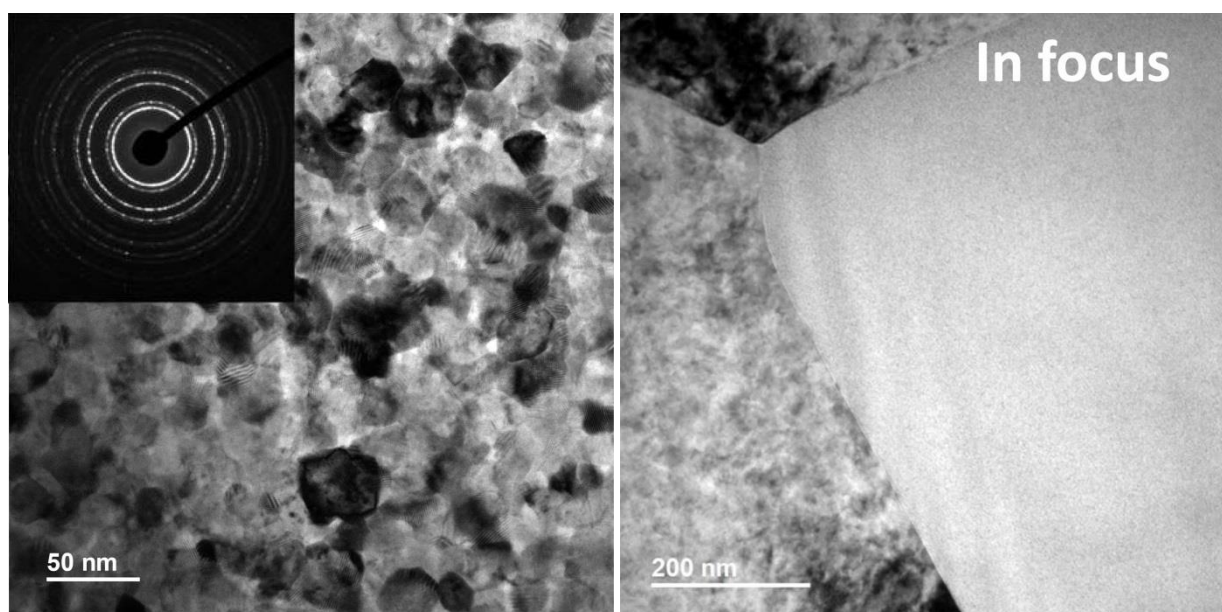


Figure 77: TEM images of lamellas produced from nanogained (left) and micrograined (right) ThO₂ samples.

4.6.4.2 300 keV Xe

Characterization on Xe-implanted samples revealed interactions between nanograined ThO₂ and the Pt holder, whose causes are currently under investigation. The presence of large islands of reacted material prevented any reliable bubble or loops size study.

Micrograined samples instead did not present any alteration imputable to Pt contamination during irradiation. The sequence in Figure 78 shows under and over focused images of the same region

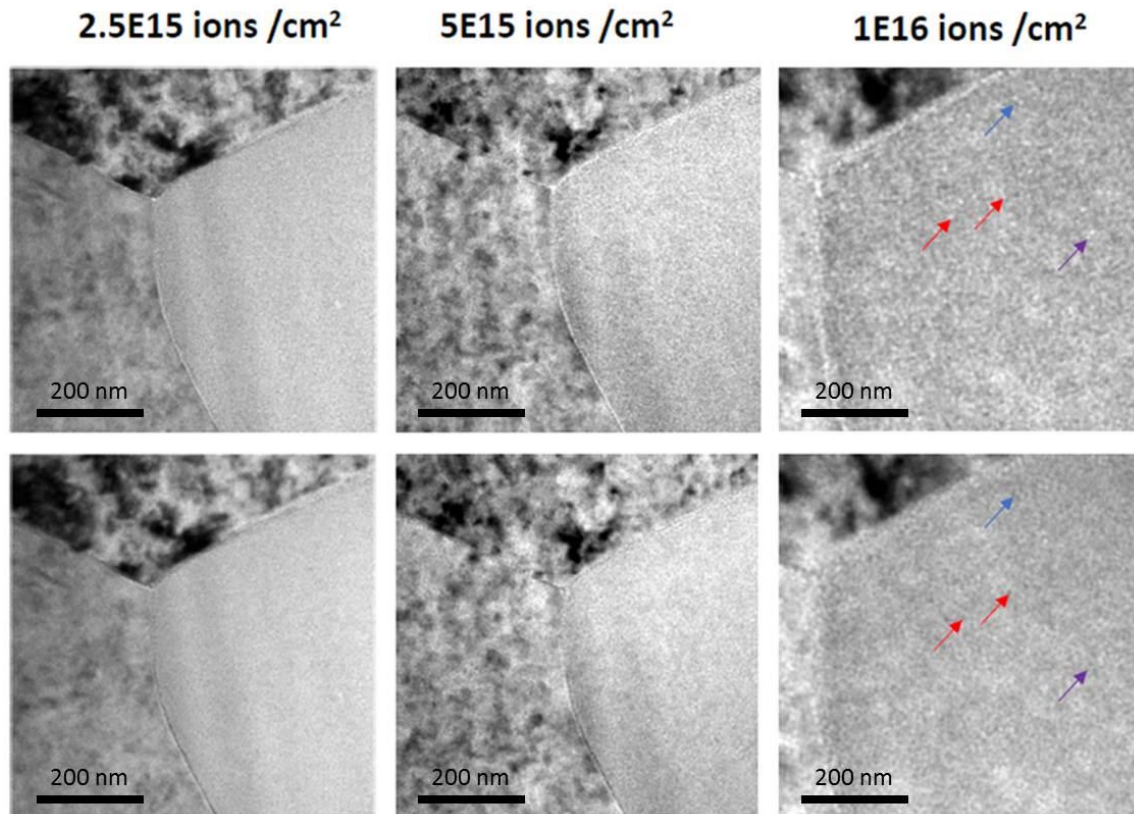


Figure 78: micrograined ThO₂ irradiated at 600 °C with 300 keV Xe ions at increasing fluences. Bubbles start being visible at 10¹⁶ Xe/cm².

pictured in Figure 77 as a function of increasing fluence, where Xe bubbles started being visible for 10¹⁶ at/cm². This result is in quite good agreement with the literature data reported for UO₂, where Xe was reported to form nanosized bubbles at 600 °C for fluencies as low as 8·10¹⁵ at/cm².(181,187)

As mentioned in Section 2.1.2.4, characterization on the response of ThO₂ in the ballistic regime was also foreseen and is currently ongoing.

4.6.4.3 16 keV He

For samples implanted with He at 600 °C, no interaction with sample holders was triggered. A direct comparison of the response of the two microstructures was then possible. Figure 79 shows bubbles formation in both nano and micrograined samples for a fluence of 10¹⁶ at/cm², as expected from what seen in other experiments with UO₂.(186,187)

The grain size had a major effect on the He behaviour within the matrix: bubbles appeared to be smaller and more randomly distributed in the micrograined material, while in the nanograined sample they seemed larger and, partially, lined up (those marked in red in Figure 80). This effect is

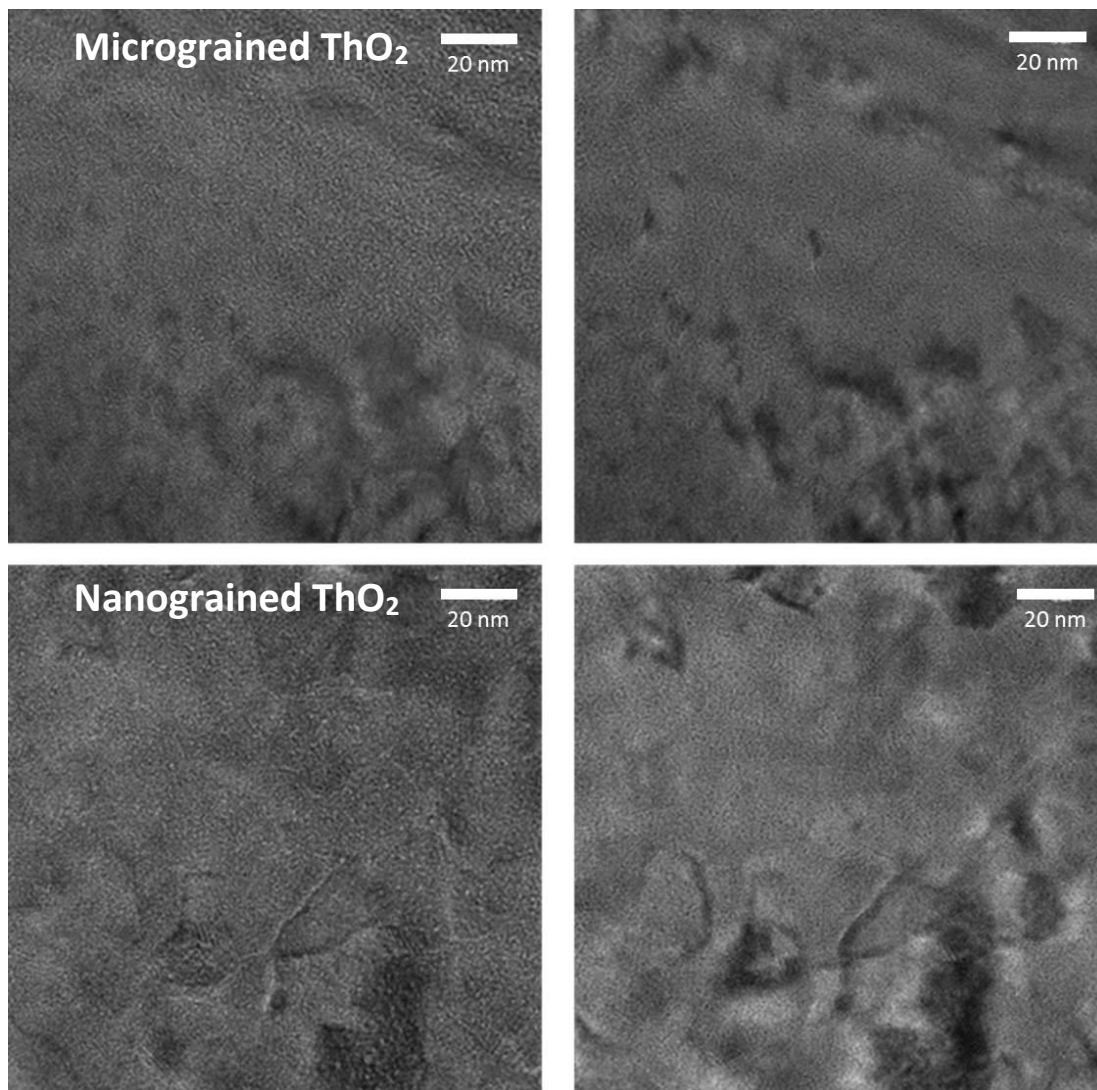


Figure 79: over and under focused TEM images of micrograined (above) and nanograined (below) ThO_2 samples implanted with 16 keV He, 600 °C to the fluence of 10^{16} cm^{-2} .

attributed to the shortening of the diffusion path to sinks (grain boundaries) with decreasing grain size. In this way, in nanograined samples less nucleation sites are available and growth dominates over nucleation of new bubbles.

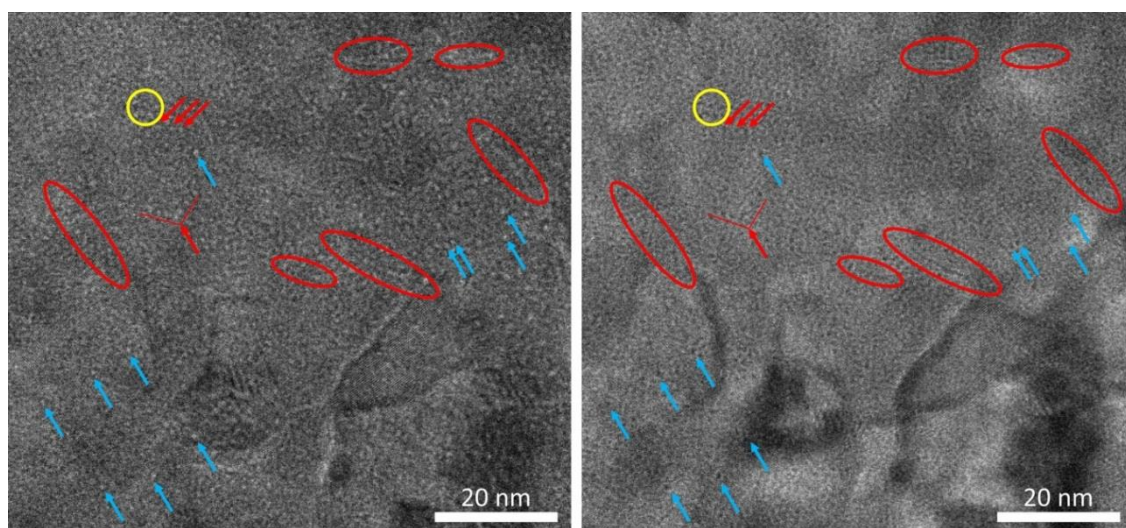


Figure 80: same regions of the He-implanted nanograined ThO_2 sample shown in Figure 79, with part of the lined-up He bubbles highlighted in red, while in blue and yellow some of the more isolated ones.

More accurate statistic on bubbles size and density are currently being performed by the research group which carried on the implantation and characterization. Once more reliable data on bubbles population are available, an estimation of the diffusion coefficient can be attempted.

4.7 Conclusions

In this chapter, the characterization of the samples used in this work, in their initial state, was presented. Due to the very different nature of the samples and of the studies to be performed on them, different techniques and different devices were used for the characterization of the (U,Pu)O₂ and SPS UO₂ and ThO₂ samples.

The α -doped samples were extensively characterised in order to assess their initial state before self-irradiation damage took place. XRD, SEM, EDX, Raman and LAF and did not highlight any microstructural difference imputable to the chemical composition. The values of lattice parameter, thermal conductivity and Raman shift of the T_{2g} band are in good agreement with the available literature data. The obtained compositions of the prepared samples should recreate, in few years, a damage build-up within the matrix representative of a spent nuclear fuel after up to 10.000 years of repository.

SPS UO₂ samples were characterized by XRD and SEM in all the steps of the samples preparation, in order to be able to quickly design modifications of the SPS treatments and setups to further lower the final grain size of the sintered samples. Different SPS treatments applied on UO₂ nanopowders resulted in samples of fixed density and composition (O/M ratio), with grain size down to around 100 nm. A small influence on the grain size on the microstrain of the final samples was also detected. TEM was performed on FIB lamellas of the nanograined UO₂ samples and confirmed what deduced from SEM observations.

Less extensive characterization was performed on the SPS ThO₂ samples, since no process was developed on purpose for their production, limiting the use of XRD, SEM and TEM to the starting powder and the final dense pellets. The application of low temperature HP – SPS to ThO₂ nanopowders lowered the grain size of the dense material down to about 50 nm. Also in this case, the microstrain of the samples seems to increase by decreasing the grain size.

ThO₂ samples were implanted with 300 keV Xe and 16 keV He ions at 600 °C to study the microstructural effect on the gas bubbles formation. This represented the first systematic study of this type on ThO₂. Fluences (10¹⁶ at/cm²) and temperatures for bubbles formation are in excellent agreement with the values reported in literature for UO₂.

Grain size effect could be observed only on the He-implanted sample, since Xe-implanted nanograined ThO₂ reacted with the Pt sample holders, preventing any possible bubble study. He bubbles appeared to be smaller and randomly distributed throughout the micrograined ThO₂ lamella, while in they were bigger and partially lined up in the nanograined one. The higher density of sinks (grain boundaries) with decreasing the grain size favours bubbles growth over nucleation

5 STORAGE – SELF IRRADIATION

In this chapter, the characterization of the effects of α -self-irradiation in our (U,Pu)O₂ samples are described. The ageing of the two batches of 2.5 and 10 wt % Pu-doped UO₂ was followed by means of several techniques through a periodical characterization.

During the production phase, described in Section 3.1, the samples number was optimised taking into consideration all the different techniques to be employed as well as the specific material needs for each of them, in terms of quantity and geometry.

For non-destructive techniques, dedicated samples were produced and then stored directly at the characterization device, monitoring periodically always exactly the same points/areas of the sample (for example, in the case of Raman, LAF and SEM).

In the case of destructive techniques instead, dedicated sets of samples (DSC, indentation), or fragments of samples (TEM, XRD), were prepared in advance and then stored at the characterization device. In this way, despite not analysing periodically always the same exact sample, any effect of different storing conditions could be ruled out.

A second, smaller, batch of samples was dedicated to storage at 200 °C under inert Ar atmosphere. This temperature was chosen as representative of wet storage conditions in order to shed some light on possible annealing effects already at this relatively low temperature, especially for long storage times. Due to practical reasons, the samples stored at 200 °C were analysed only by XRD.

5.1 Room T ageing

5.1.1 Crystal structure – XRD

As seen in Section 4.3.1, samples were constituted of a (U,Pu)O₂ solid solution, and hence their evolution could be accurately monitored by XRD. The lattice parameter swelling was monitored over a time span of more than 550 days, resulting in 0.411 and 0.102 dpa in the 10 and 2.5 wt % samples respectively. The increase of the cell volume results in a shift of the XRD peaks, as shown for the first peak in Figure 81, while Figure 82 displays the calculated relative increase of the lattice constant for both compositions as function of the dpa.

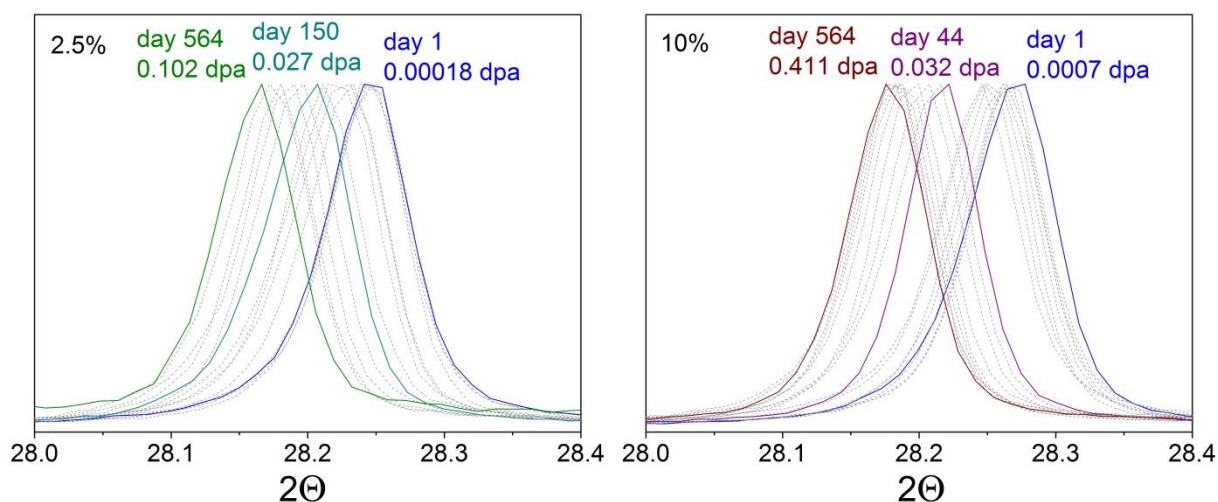


Figure 81: first XRD peak of both compositions. As a consequence of the radiation-induced cell swelling, the peaks shift to lower angles as the damage accumulation proceeds until about 0.4-0.6 dpa.

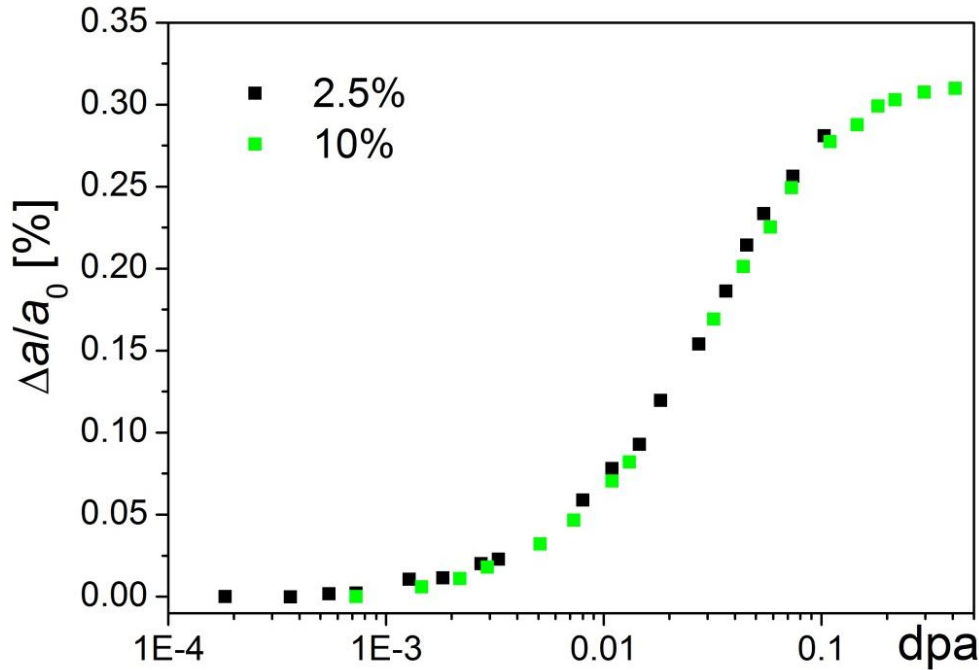


Figure 82: lattice parameter relative increase, as calculated from XRD data, as function of the dpa. The different activities, and hence the radiation damage kinetics, do not seem to have an impact on the lattice parameter swelling, which appears to depend only on the cumulated dose.

Within the uncertainties of the measurement, the two curves in Figure 82 follow the same trend, excluding any dependence of the cell swelling on the samples activity, at least at these dopant concentrations.(144)

Comparing the lattice parameter evolution measured in this work with data coming from Pu-doped UO_2 previously measured at JRC – Karlsruhe (88) (Figure 83), relatively good agreement is found with the reported data up to the current cumulated dose, although the previous data appear more scattered. The dpa level targeted for reaching saturation was 0.6, and the 10 wt % samples in this work appear close to reaching a plateau for 0.411 dpa. On the contrary, the saturation value of the lattice parameter relative increase appears lower than what expected from the previously measured samples, but is in good agreement with the 0.3 % threshold found in literature for self-irradiating $(\text{U,Pu})\text{O}_2$ (233), $^{238}\text{PuO}_2$ (234) or ^{241}Am -doped UO_2 (207).

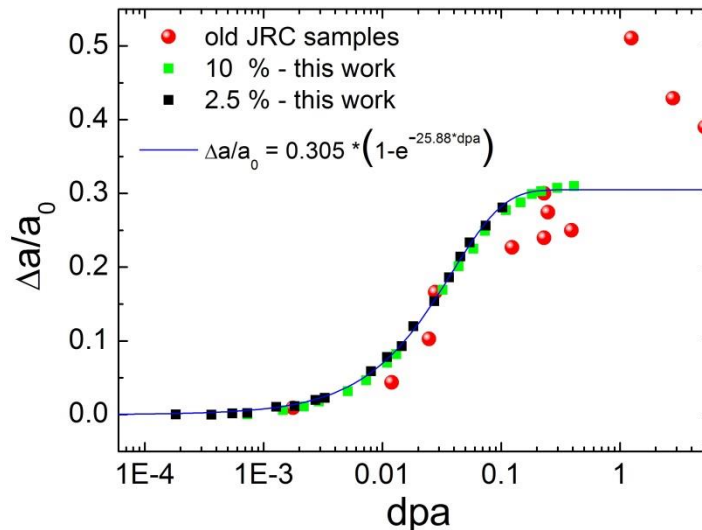


Figure 83: comparison of the data found in the present work with some samples previously measured at the JRC – Karlsruhe (red dots). In blue the fit curve proposed for the data derived in this work, which aims to represent a reassessment of what done in (144).

Microstrain was also periodically evaluated with the Williamson-Hall approach, and its evolution is plotted in Figure 84. The values are in general quite low and scattered, but an overall decrease can be noticed. Remarkably, the decrease seems to be more pronounced in the early stages of self-irradiation, up to about 0.05 dpa, where the lattice parameter increase is not yet pronounced. For 0.1 dpa a plateau could be approached, similarly to what was measured for the lattice constant evolution. No effect of the composition was detected in the starting microstrain nor in its evolution.

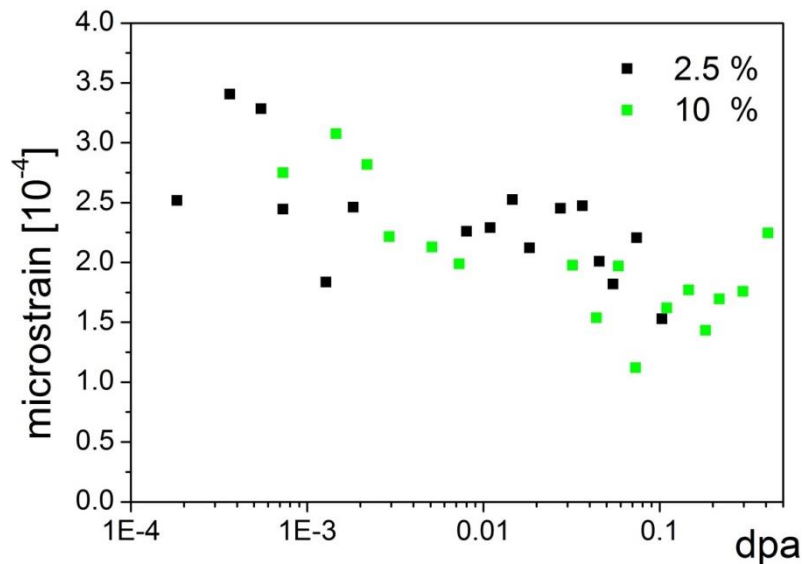


Figure 84: microstrain calculated with the Williamson-Hall approach for the samples of both compositions, plotted as function of the dpa.

5.1.2 Microstructure – SEM

The periodical SEM characterization was conducted on the two samples that were already presented in section 4.2.1, using some microstructural features such as pores or cracks as references to track back every time the same positions. Figure 85 and Figure 86 show the same area of the 10 and 2.5 wt % samples respectively, over a storage time of 550 days, resulting in 0.1 and 0.4 dpa in the two compositions. In none of the two cases any appreciable differences can be noticed, even at higher magnifications (not reported here for sake of brevity). After long storage (550 days – 0.4 dpa) the 10 wt % sample was broken and the new fracture surface was also analysed and compared to the previously observed one. Some images of the "fresh" fracture surface are reported in Figure 87, and they do not exhibit any substantial difference with the as-sintered fracture surfaces shown in section 4.2.1, nor with any of the figures shown in this section.

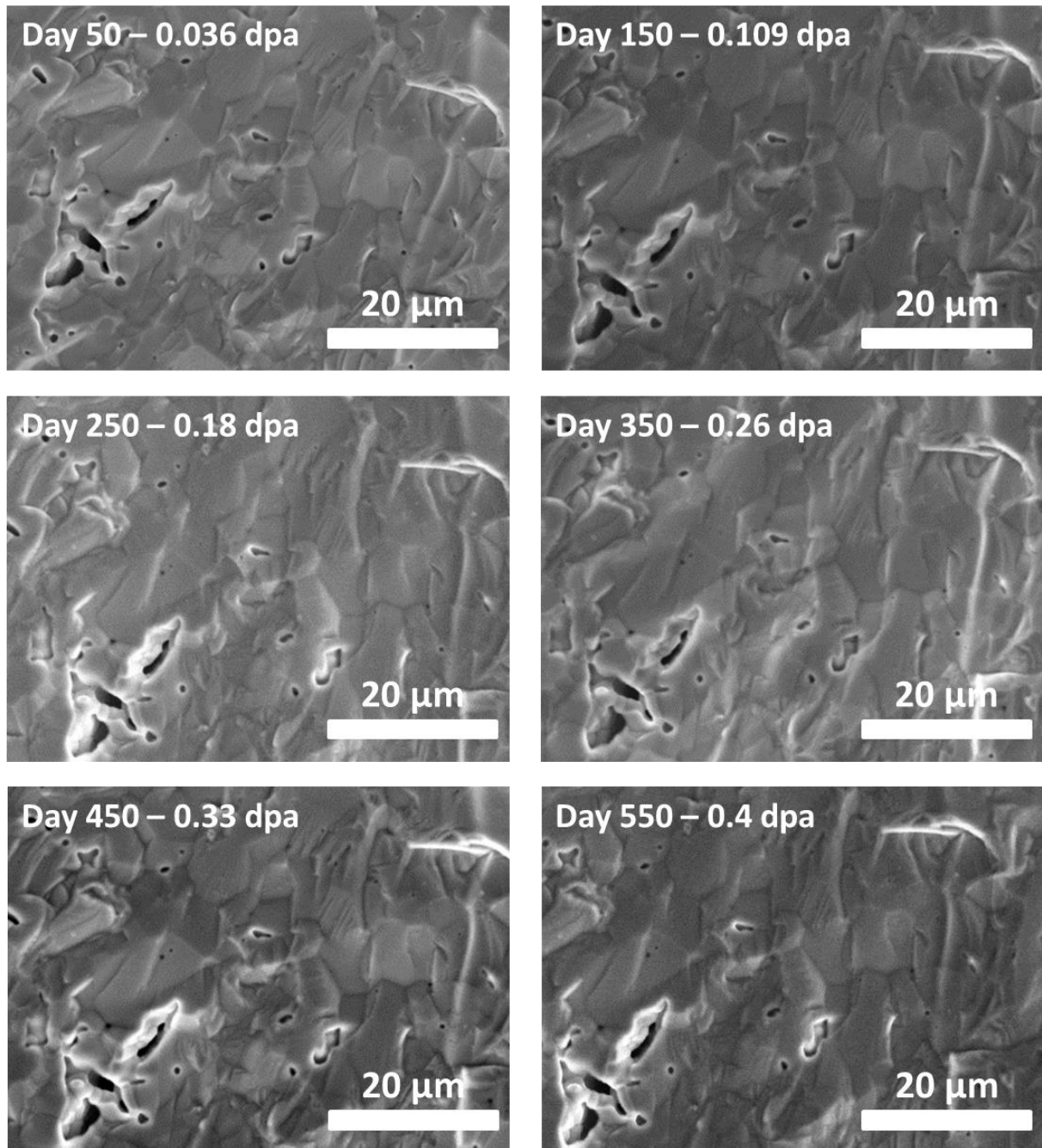


Figure 85: SE images of the same point on the fracture surface of a 10 wt % sample over 550 days of storage, resulting in 0.4 dpa. No significant change in the microstructure can be detected.

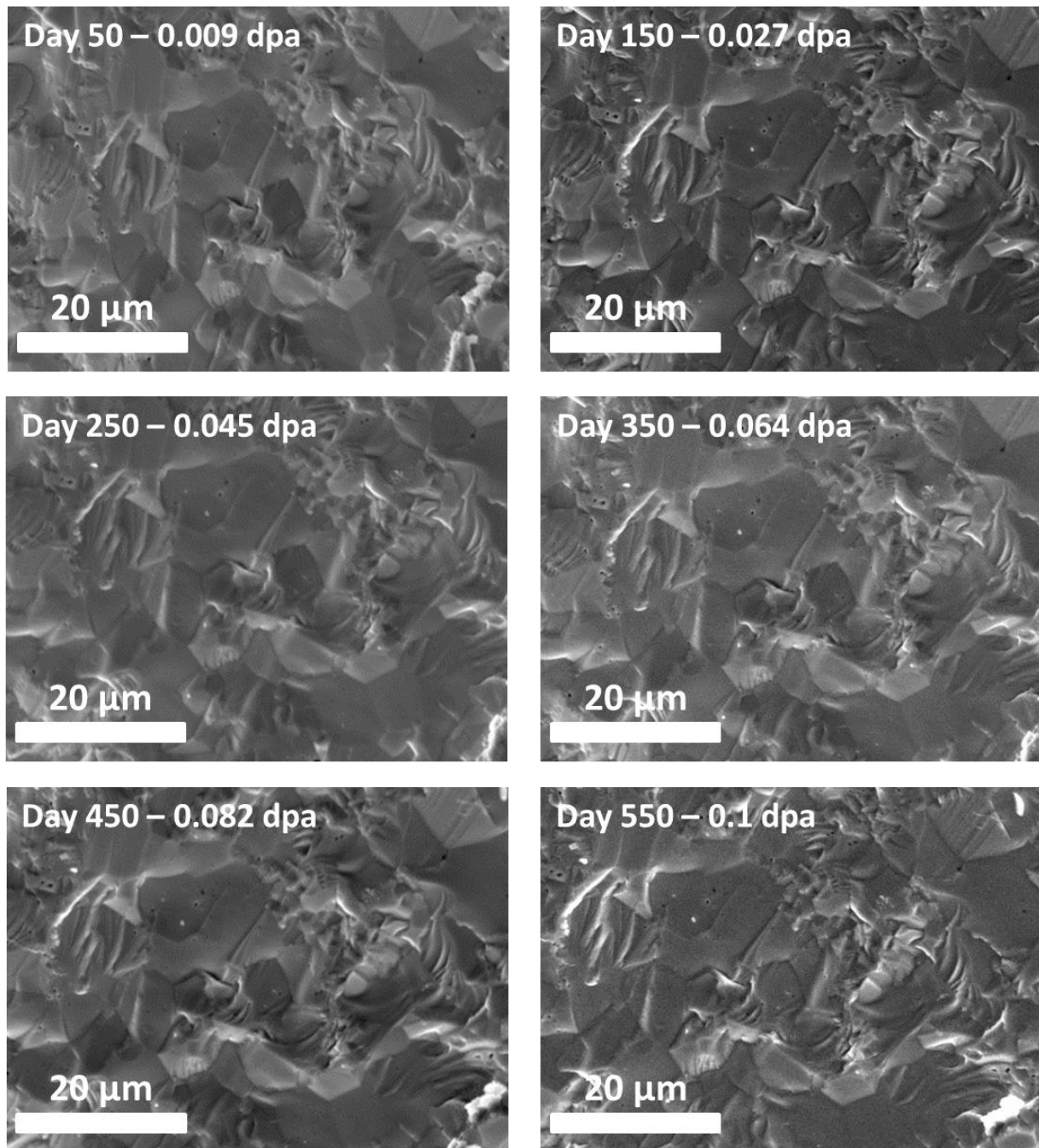


Figure 86: SE images of the same point on the fracture surface of a 2.5 wt % sample over 550 days of storage, resulting in 0.1 dpa. No significant change in the microstructure can be detected.

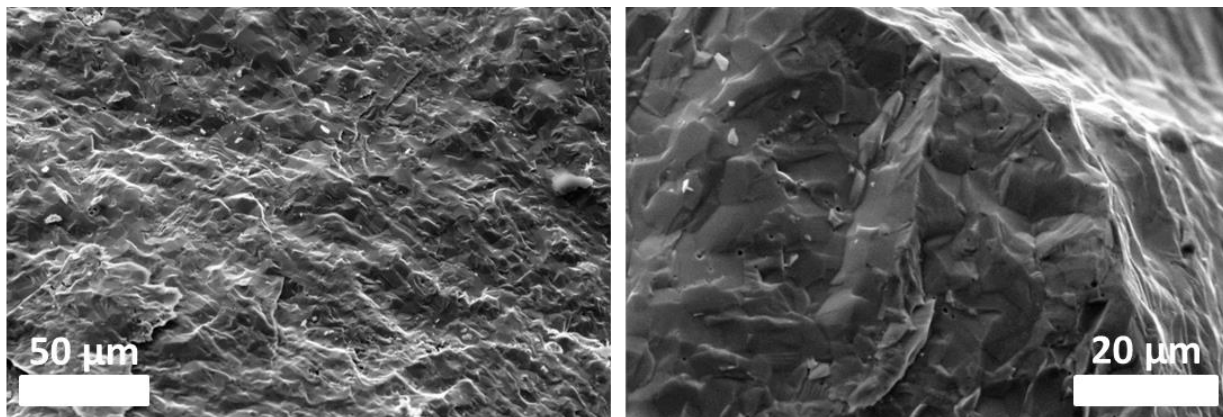


Figure 87: SE images of the "fresh" fracture surface created after 550 days of storage, and 0.4 dpa of accumulated damage, in the 10 wt % samples. No differences with the fracture surface of the as-sintered material can be detected.

5.1.3 Raman

Similarly to what was done for the SEM inspections described in 5.1.2, also the Raman spectra were acquired periodically on exactly the same sample pieces characterized after the synthesis (results were presented in section 4.5.1). Figure 88 shows the evolution of the measured spectra from day 1 up to day 583 of storage (0.106 and 0.425 dpa for 2.5 and 10 wt %). For both compositions, the T_{2g} becomes asymmetric with increasing dpa, while the defects triple band broadens and grows in intensity.

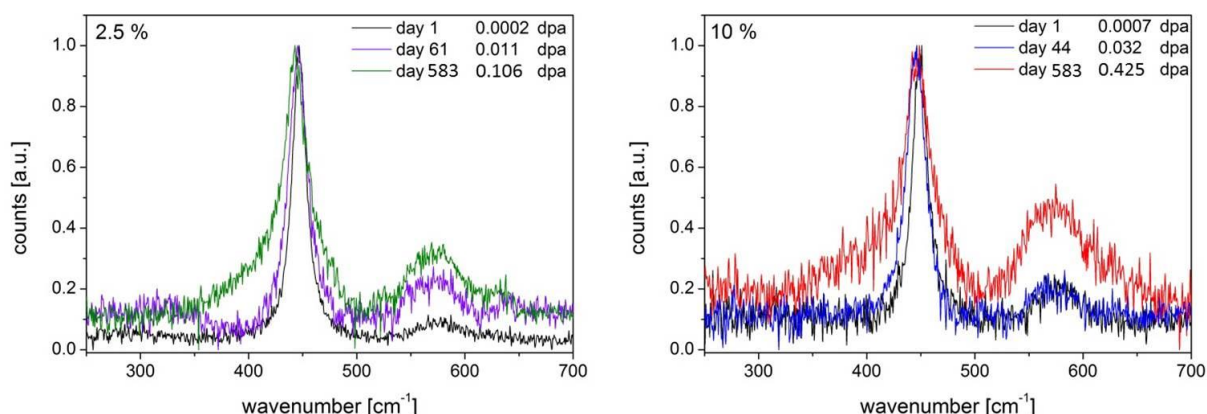


Figure 88: evolution of the Raman spectra for the 2.5 and 10 wt % samples over 583 days of ageing, resulting in 0.077 and 0.307 dpa respectively. As the damage accumulation proceeds, the T_{2g} peak becomes asymmetric and the defects triple band increases in intensity and broadens.

The asymmetric broadening of the T_{2g} peak leads the peak position to slightly shift to lower wavenumbers. In literature, the T_{2g} shift is systematically reported for α - or self-irradiated UO_2 (161). Figure 89-A shows the relative T_{2g} peak shift for both compositions as function of the damage, which seems to evolve independently from the samples activity, like the lattice parameter increase measured by XRD. However, this apparent shift is not due to a change in the T_{2g} frequency given by the swelling of the lattice. The reason is instead to be searched in the gradual loss of order of the lattice, which leads the material not to behave like a perfect crystal anymore and to the subsequent loss of the selection rules.(165) Considering the dispersion curves derived by Dolling et al (228), outside the centre of the first Brillouin zone the T_{2g} mode starts to have disperse components at higher and lower wavenumbers. In parallel to Figure 89-A, Figure 89-B shows the relative increase of the low-wavenumber dispersed T_{2g} mode as a function of dpa.

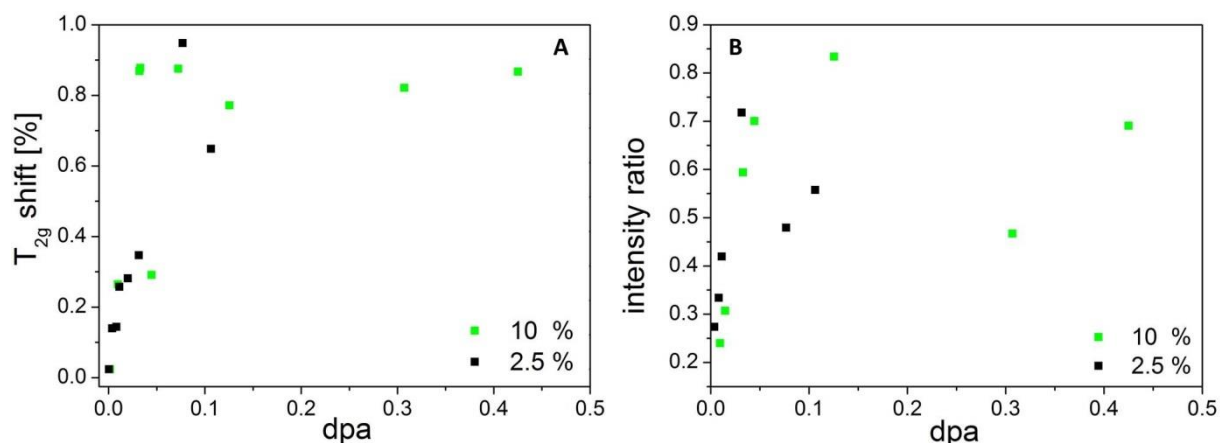


Figure 89: A: T_{2g} apparent relative shift as function of the dpa for both compositions. B: ratio between the intensity of the low-wavenumber dispersed component and T_{2g} . Both trends seem so show dependence on the dpa and not on the activity of the samples.

Figure 90 A-B shows instead the T_{2g} broadening, in terms of integrated area increase, as function of dpa and days respectively. Contrarily to the others effects observed so far, in this case the phenomenon seems to be at least partially kinetically driven. Indeed, the points given by the two different compositions are in much better agreement with each other when plotted against time rather than dpa.

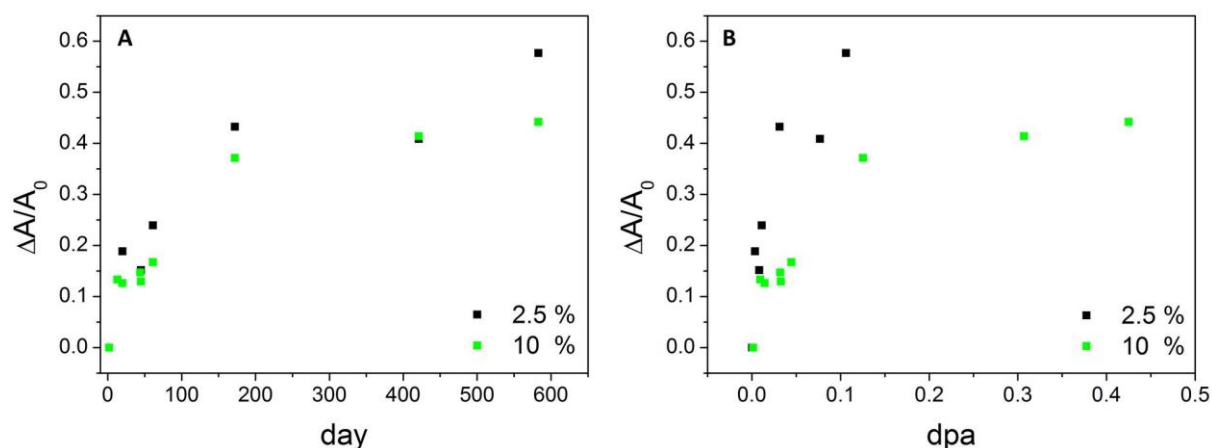


Figure 90: T_{2g} integrated area increase as function of dpa (A) and days (B)

Considering the Raman triplet defects band, the radiation-induced loss of order is reported to produce an overall broadening and intensity increase of the peak located around 570 cm^{-1} . (160,165) This is due to the appearance of the ν_1 (530 cm^{-1}) and ν_3 (630 cm^{-1}) band together with the increase of the already present ν_2 (575 cm^{-1}). In our case a relative intensity increase can clearly be noticed (Figure 88), but it is hard to deconvolute the contribution of the three individual bands. In particular, the presence of ν_1 and ν_3 is hardly detectable for dpa levels below 0.077, and even at this point a quantitative analysis is not easy.

It is worth mentioning in fact that the overall quality of the measurement degraded with the damage accumulation. Fluorescence increased with storage time, decreasing the signal-to-noise ratio of the latest measurements. The α -activity of the sample significantly damaged the carbon glue of the sample holder as well, which also harmed the quality of the data.

It is hence hard to distinguish the individual defects contribution to the triplet defects band up to now, although a general broadening and increase could be detected, consistently with the reported damage-induced loss of order of the structure.

5.1.4 Thermal diffusivity – LAF

Thermal diffusivity was measured only on a 2.5 wt % sample, as its degradation would have been too fast in a sample with higher activity. As expected indeed, the thermal diffusivity decreases of about 40 % already in the first 150 days, which correspond to a cumulated damage of 0.03 dpa, in good agreement with the literature data. (96)

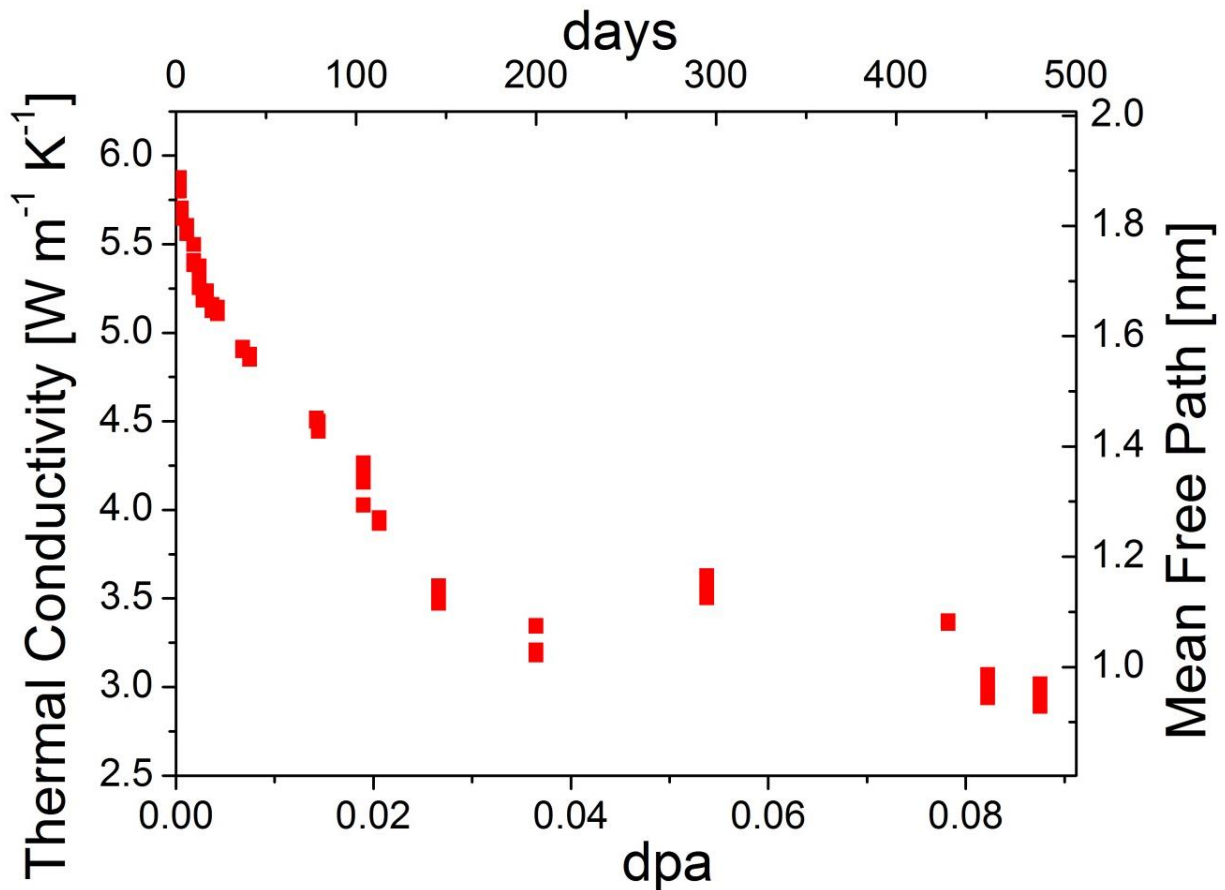


Figure 91: thermal conductivity of the 2.5 wt % Pu-doped UO₂ and phonon mean free path over dpa and time (days). The thermal conductivity was measured at 550 K and corrected for 95 % TD, for sake of consistency with the literature.

Figure 91 shows the relative decrease of the calculated thermal conductivity (measured on the sample at 550 K and corrected for 95 % TD) and the derived phonon mean free path. The mean free path was calculated from the measured data using the formula:

$$k = \frac{1}{3} c_V v l \rightarrow l = \frac{3k}{c_V v} \quad (42)$$

Where k is the thermal conductivity [W m⁻¹ K⁻¹], c_V is the volumetric heat capacity [J K⁻¹ m⁻³], v is the speed of sound in UO₂ [m s⁻¹] and l is the mean free path [m]. The measurements were performed considerably above the Debye temperature for UO₂ (377 K), and hence the heat capacity can be considered independent from T .

In UO_2 , the thermal conductivity is dominated by the phonon heat transport mechanism. Any irregularity in the lattice resulting in a displacement of anions or cations from their original lattice position, such as radiation-induced point defects, acts like a phonon scattering centre. As the samples self-irradiation proceeds, more defects are introduced in the lattice and hence the phonons mean free path between two scattering centres becomes shorter. This directly affects the thermal conductivity of the material.

Extended defects contribute much less to the local strain on the lattice, inducing only very limited additional scattering on the phonons, and hence do not affect the phonon mean free path. For this reason, the decrease of the thermal conductivity occurs at the very initial stages of self-irradiation, when the point defects are generated, and becomes almost insignificant when point defects start clustering to form extended defects.

Taking a closer look at the descending part of the thermal conductivity curve, it appears to proceed following two different stages, with a quite marked slope change around 0.0025 dpa. As shown in Figure 92, this change of slope occurs roughly at the same dose as for the microstrain decrease.

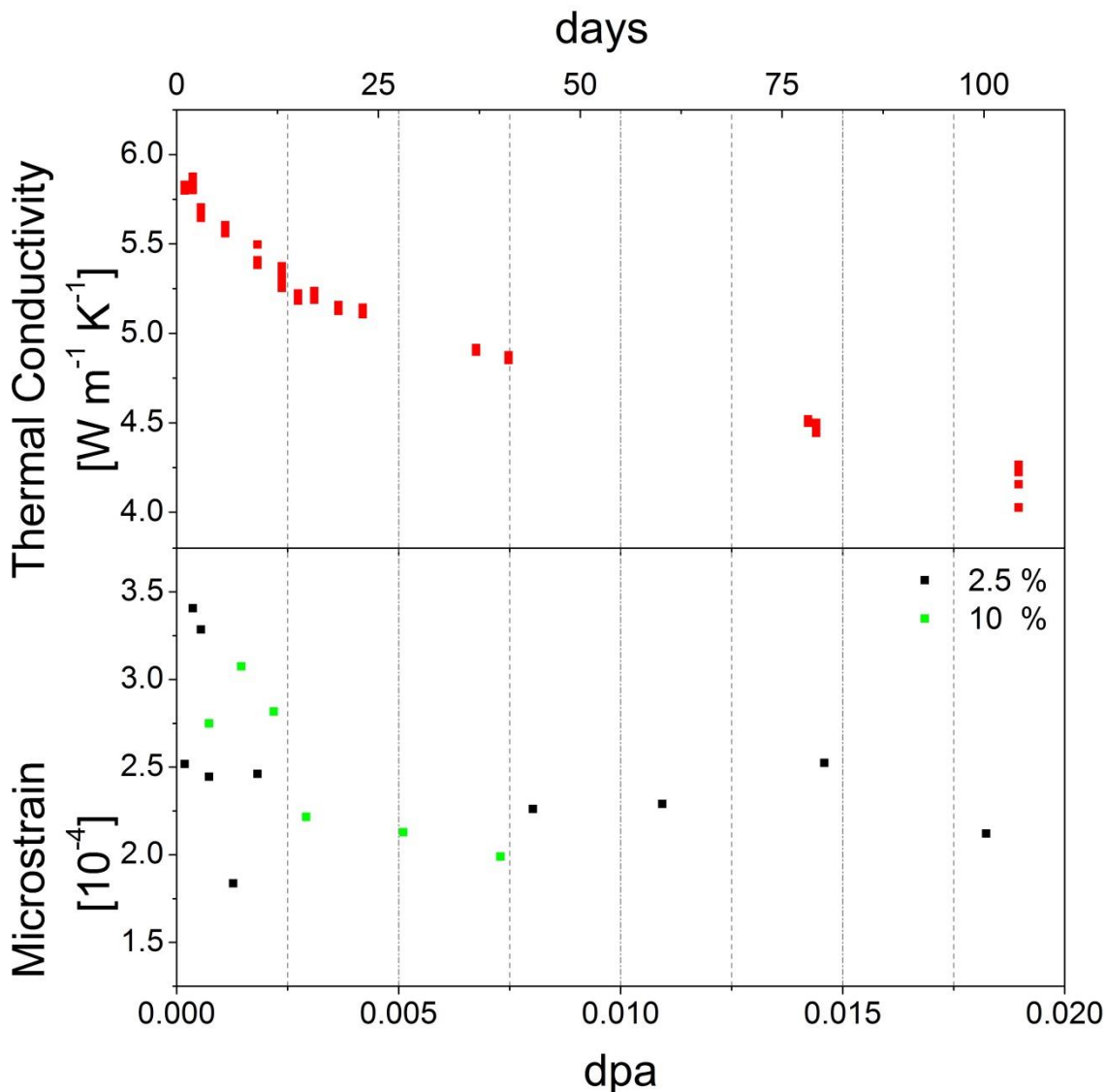


Figure 92: thermal conductivity (at 550 K and corrected for 95 % TD) degradation and microstrain evolution as function of the dose. Both trend decrease more steeply before about 0.0025 dpa, and successively they proceed more slowly towards the final saturation. The days scale reported on the top x axis is referred to the 2.5 % composition.

The relaxation of the microstrain occurring in this early stage, implying a more uniform lattice parameter throughout the structure, hints that at about 0.0025 dpa the structure is already relatively "uniformly damaged". From this point on, the contribution of any additional point defect to the lattice strain and scattering process is lower, up to the value of 0.03 dpa when the thermal conductivity stops decreasing.

5.1.5 TEM

Due to the complexity of the testing of such radioactive material, and the high demand of the device, TEM analysis could not be as systematic as other techniques. Figure 94 shows a 2.5 wt % sample analysed roughly at the same ageing time for which thermal conductivity has completely degraded.

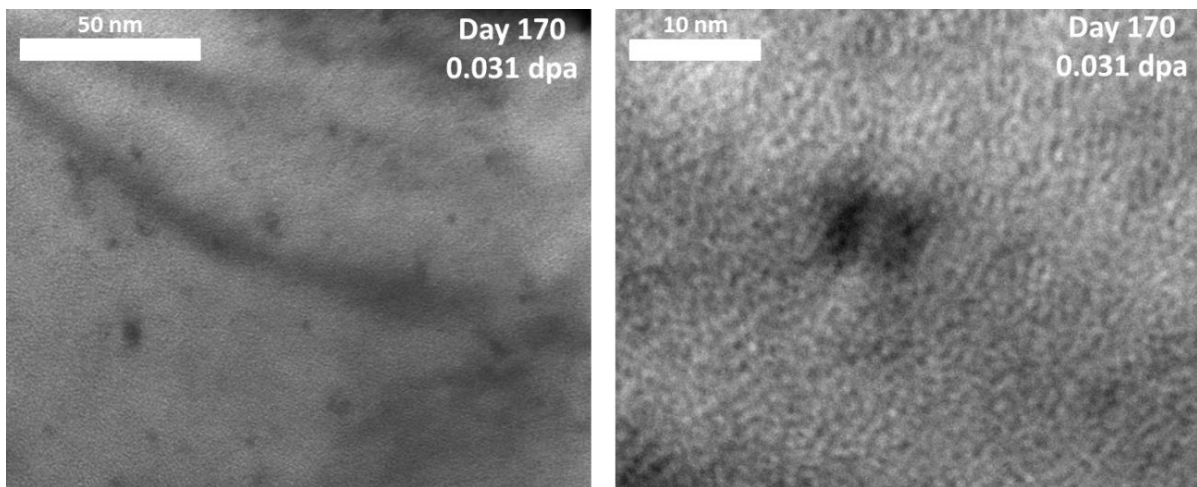


Figure 94: TEM picture of a 2.5 wt % sample aged 170 days (0.031 dpa). This ageing time corresponds roughly to the saturation time for the thermal conductivity decrease.

The sample is substantially free of observable defects with the exception of some black dots that were partially already visible in the as-sintered material (see Figure 67 in section 4.4.1). At higher magnification, the larger ones reveal to be small (< 10 nm) dislocation loops, while the smaller ones remain unclear (defect clusters or very small loops). The point defects which led to the degradation of the thermal conductivity cannot be seen, but, as anticipated in the previous Section (5.1.4), extended defects start to be visible around this dose level.

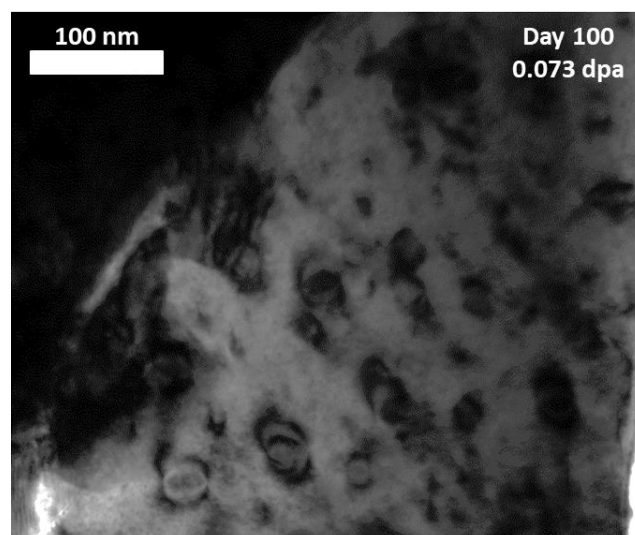


Figure 93: TEM picture of a 10 wt % sample aged 100 days (0.073 dpa).

Timewise, the first characterization campaign was performed after 100 days of ageing, on a 10 wt % sample which would have accumulated 0.073 dpa by the time. As shown in Figure 93, the sample is already populated with dislocation loops of various sizes, up to about 50 nm. Helium bubbles could not be clearly seen at this stage.

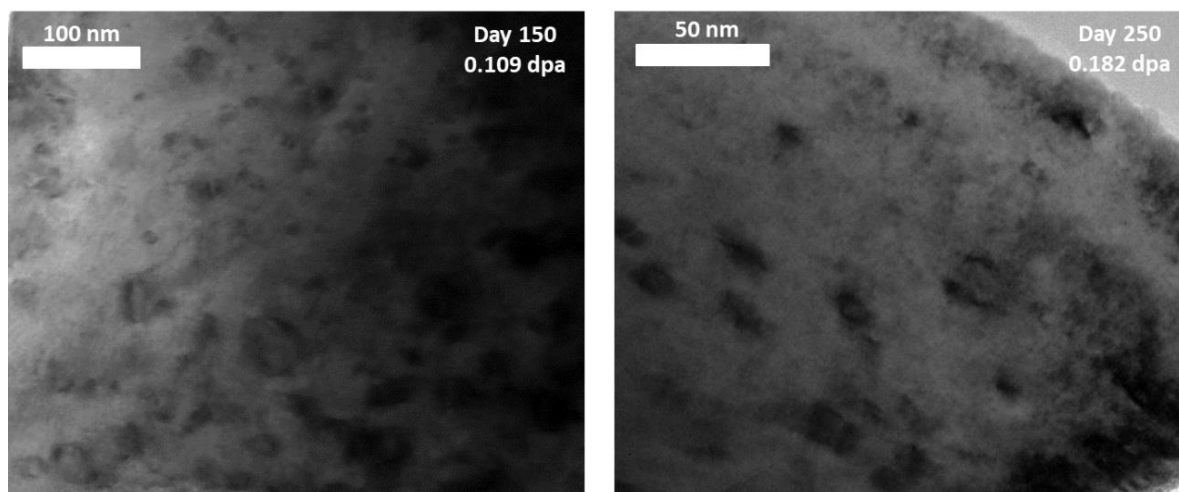


Figure 96: the same sample pictured in Figure 93, observed again after additional 50 and 150 days of storage (150 and 250 days in total), having cumulated a dose of 0.109 and 0.182 dpa.

Due to some technical issues, it was not possible to prepare a sample for successive characterizations over some months, thus the same sample already observed was re-inspected after 50 and 150 days (reaching hence 0.109 and 0.182 dpa). The results are shown in Figure 96.

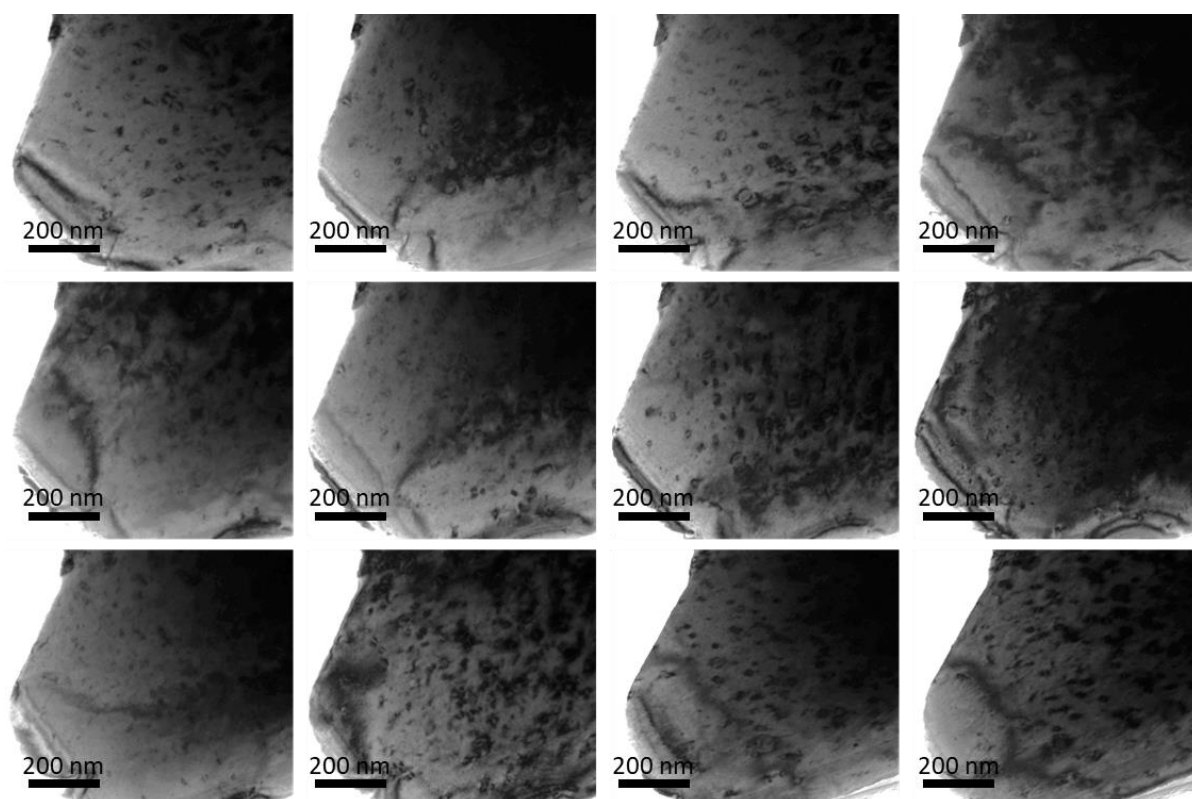


Figure 95: dislocation loops families visible on the 10 wt % doped sample after 100 days (0.73 dpa) for different tilting angles.

In these two further observations, no clear increase of the dislocation loops number or size could be detected. However, dislocation loops nucleate and growth preferentially in some specific crystallographic directions,(183) so this effect could be due to the different tilting of the sample. Figure 95 shows the effect of stage tilting on the apparent density and size of the detectable dislocation loops.

For small loops, annealing to free surfaces can be induced by the electron beam of the TEM, as shown by the micrograph sequence in Figure 97. In the observation interval of a few seconds one can see the glide of a dislocation loop toward the grain surface until fully released.

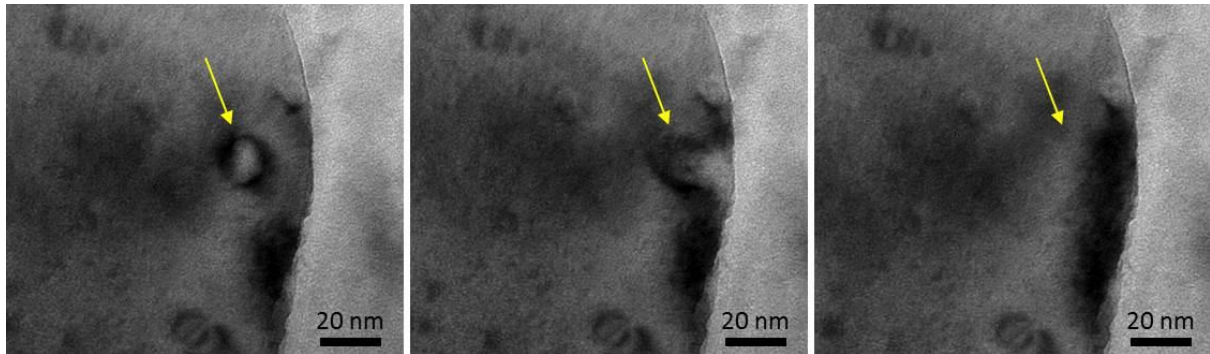


Figure 97: dislocation loop annealing under the TEM beam, observed in a 10 wt % sample aged 100 days (0.073 dpa).

A second bulk sample was crashed after additional 200 days, summing a total of 0.328 dpa (450 days of storage). As shown in Figure 98, this time the concentration of dislocation loops appears to have increased significantly, while the size of the loops also seems slightly larger.

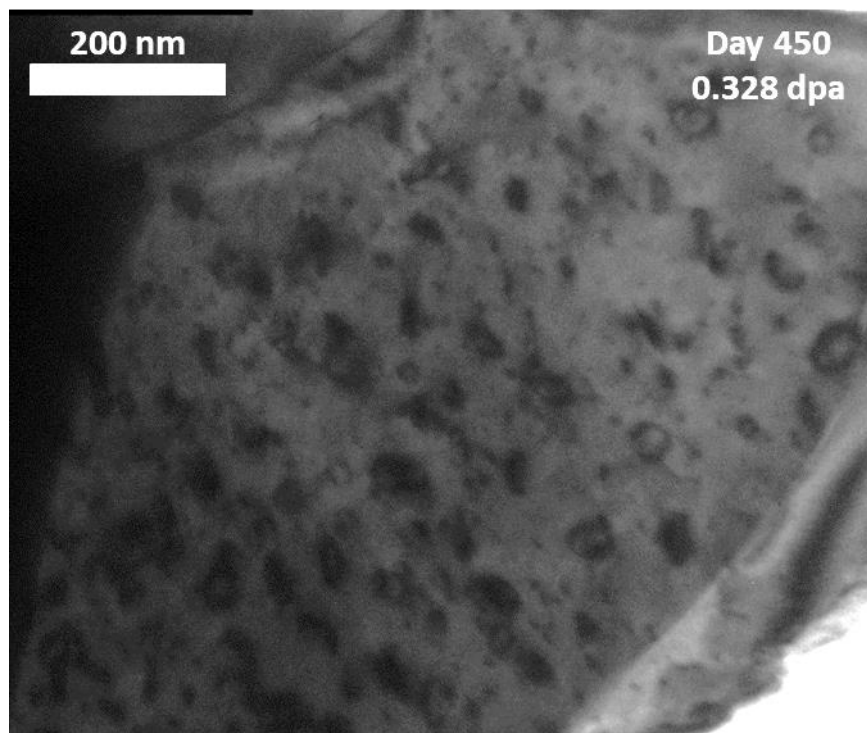


Figure 98: 10 wt % sample crashed after 450 days of ageing, and 0.328 dpa accumulated.

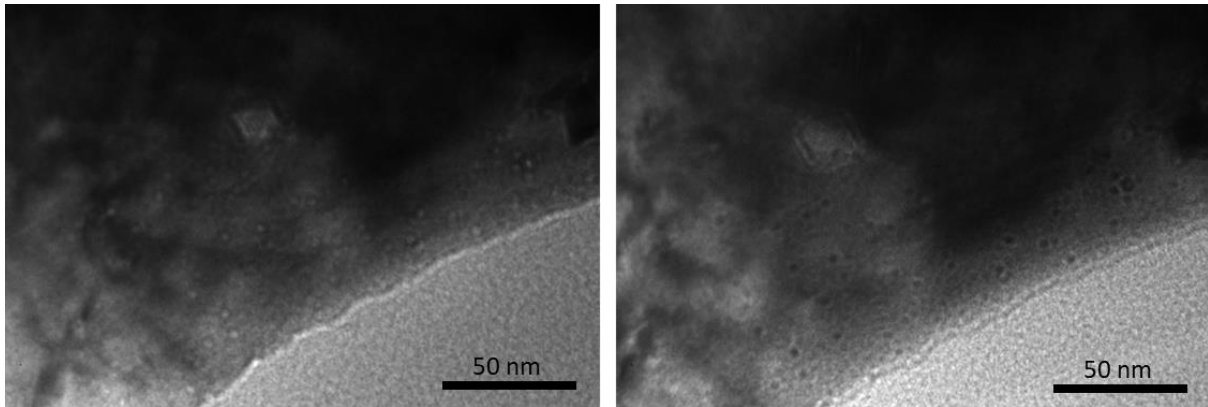


Figure 99: Over and under focused images of the 10 wt % sample stored 450 days (0.328 dpa) showing He bubbles.

At this stage, a significant amount of radiogenic He had been already produced in the lattice, which was quantified based on the starting sample activity to be about $1.2 \cdot 10^{18}$ He/g. Consistently with what reported in the literature (88,150), no grain boundary opening or embrittlement was observed in the SEM for this level of dpa, and the totality of the He can be assumed to be retained in the UO_2 matrix. As evidenced by an overfocused and underfocused image in Figure 99, intragranular He bubbles were now visible in the sample. The size is homogeneous around 2nm.

5.1.6 Helium release – KEMS

As shown in the previous Section (5.1.5), at 0.328 dpa the amount of radiogenic He is enough to form nanometric bubbles within the UO_2 matrix. A thermal desorption study was conducted to assess the amount of He included in the matrix as well as its release kinetics. A 10 wt % sample was heated at the constant rate of 30 K/min up to 2300 K, a temperature which should guarantee full release of the accumulated He in polycrystalline samples.(147,150,235) TEM and SEM analyses were performed after the thermal treatment and the microstructure was compared to the one of damaged samples of comparable dose.

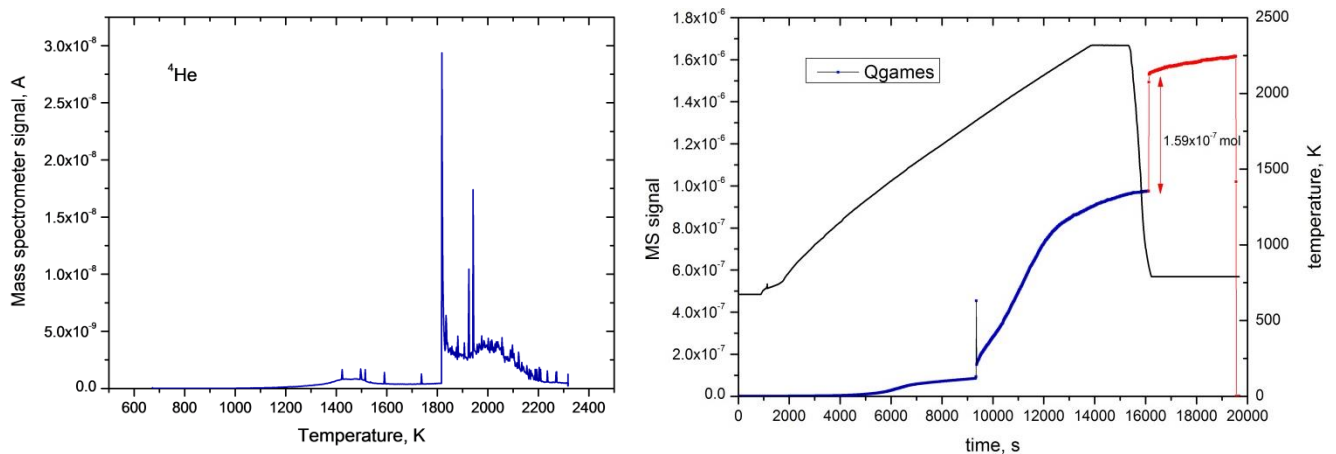


Figure 100: He release while heating a 10 wt % sample up to 2300 K as measured by KEMS (left) and Q-GAMES (right).

Figure 100 shows the KEMS and Q-GAMES measurements, as a function of temperature and time respectively. In the latter, time is used to be able to represent the calibration spike on the same plot with the gas to be quantified. Consistently with what reported in the literature for ^{238}Pu -doped

(147,150) and He-infused polycrystalline (149,235) UO_2 , two stage of He desorption were detected, corresponding to two very different release kinetics and attributed to two separate mechanisms.

The first step, starting around 1100 K, is associated with He atoms diffusion to the grain boundaries, which act as shortcut to the free surface (168,173,236), and simultaneous trapping in bubbles. The two processes are assumed to be controlled by the same diffusion mechanism, but their magnitude is determined by the morphology of the traps (bubbles and pores) in relation with the diffusion length. (147) During this first stage, roughly 10 % of the total He is slowly released. As the temperature increases, bubbles start growing and the trapping effect overtakes the release, so the release rate gradually decreases.

A second step starts abruptly around 1800 K and results in the massive release of the total remaining He, at a rate roughly four times higher than in the first stage. This second step is attributed to the bubbles migration to the grain boundary and then to the surface, possibly with the formation of tunnels. (149,237) In literature, the onset temperatures reported for this stage are more scattered, ranging from 1600 K (150) to above 1800 K (149), but anyways in line with what observed in this work. It is possible that the onset for the release was somehow delayed, resulting in pressure build-up leading to the subsequent abrupt blowout initiating the second stage.

The smaller bursts which can be seen throughout the whole treatment can be considered as a third concurrent stage and are associated with the sporadic release of intergranular bubbles, or groups of bubbles, possibly through interconnection. Evidences are given by the complete absence of these bursts in experiments performed on UO_2 single crystal. (149,235)

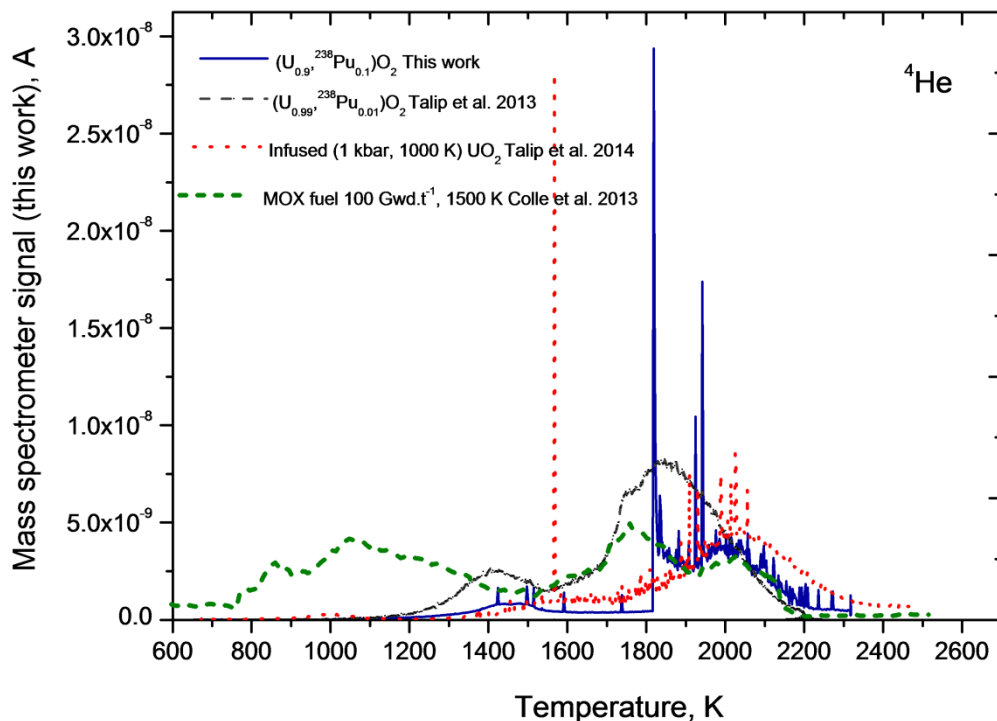


Figure 101: He release obtained in this work compared with the KEMS curves of infused polycrystalline UO_2 (149,235), ^{238}Pu -doped UO_2 (150) and irradiated MOX fuel (238) previously measured at JRC-KA. The MS signal on the y axis is only relative to the present work data, the others had to be rescaled in order to be all presented in the same plot.

The literature data from references (149,150,235) and from a MOX fuel with 100 Gwd/t of burnup (238) are plotted in Figure 101 (left) for comparison. Polycrystalline samples (149,235) were infused for 15 minutes, so He was introduced by diffusion in absence of defects and hence occupied stable lattice sites. In such conditions, He was found to settle in the octahedral sites of the fluorite structure. (172,239) For the ^{238}Pu -doped UO_2 , let aside the different signal intensities, which depend on the samples masses, the release profile compares excellently with the one obtained in the present work.

While the second part of the curve (1900 – 2100 K) is shared by all samples, the onset of the release is more variable. Irradiated MOX already starts releasing He at about 800 K, attributed to desorption from vacancies, thanks also to DSC evaluations.(238) For less defected samples, like the α -doped UO_2 , the onset is around 1100 K, while for the defect-free infused UO_2 it shifts to 1300 K. In damaged samples, He is easily trapped and released by radiation-induced defects; on the contrary, in damage-free samples He occupies stable lattice positions and is then released only at higher temperatures.

As anticipated in Section 5.1.5, the calculated radiogenic He generated in the sample by α -decays amounts to about $1.9 \cdot 10^{-7}$ mol, which is in excellent agreement with what measured by the Q-GAMES by comparison with a $1.59 \cdot 10^{-7}$ mol spike. As reported in literature (147,150), for this low dpa no grain boundary opening is expected, and the totality of the α -He is retained.

Post-treatment microscopy characterization was performed to assess the microstructural modifications correlated with He thermal desorption. As shown in Figure 102, TEM inspection revealed a complete damage-free sample (see Figure 67 in Section 4.4.1) and the absence of residual He bubbles.

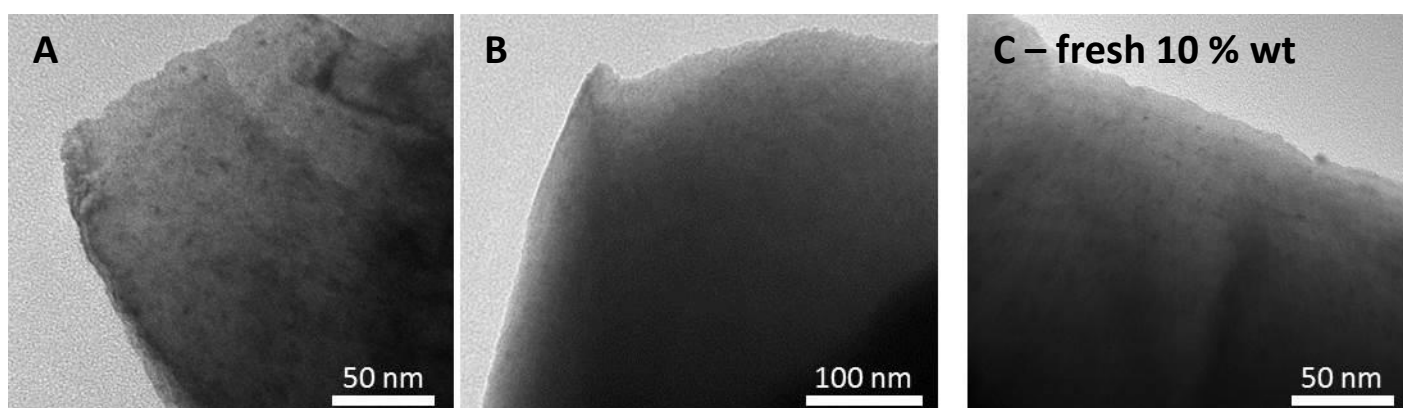


Figure 102: A) and B) post-treatment TEM; C) annealed 10 wt % from Section 4.4.1.

5.1.7 Apparent specific heat – DSC

Contrarily to what was done for the other characterization reported in this chapter, the DSC campaign was not periodic, since the initial stages of self-irradiation would have given a signal too weak to be correctly analysed and interpreted. Initially, several intermediate measurements were foreseen, but then it was decided to preserve the majority of the samples for characterization of the late stages of self-irradiation.

Figure 103 shows the DSC result of the measurement done on samples of both compositions after 450 days of self-irradiation, corresponding to 0.082 and 0.326 dpa respectively. The curve presented

in the picture is the difference between the descending and ascending curve of the treatment that, subtracted the self-heating effect due to ^{238}Pu radioactive decay, have the same slope. The energy released was around 35 J/g for the 2.5 and 43 J/g for the 10 wt % sample.

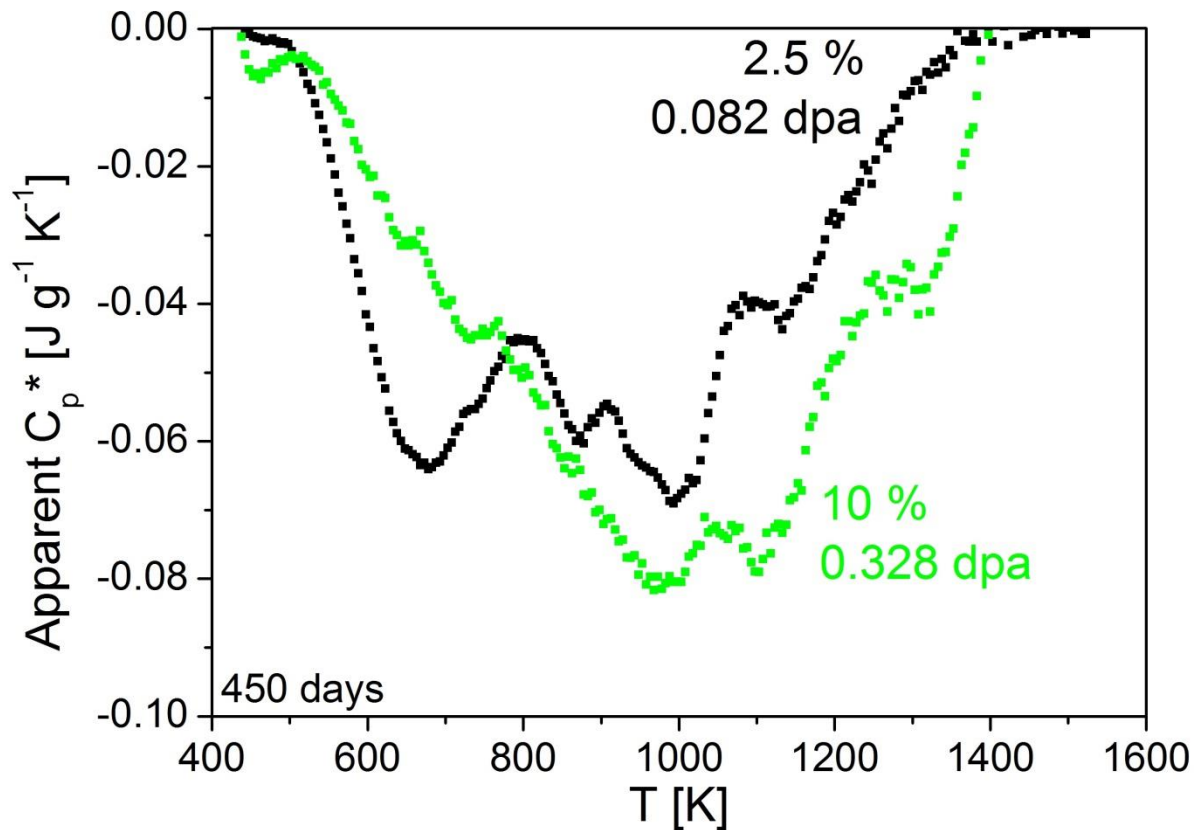


Figure 103: DSC plot of the 2.5 and 10 wt % samples after 450 days of ageing, having cumulated respectively 0.082 and 0.328 dpa. The curve presented is the difference of the descending and ascending curves, obtained at a 15 K/min rate, which (taken into account self-heating of the sample) have the same slope.

Similarly to the work of Staicu et al (96), the peaks characteristic for each defects family can be distinguished. Also in the case of our samples, the annealing of the defects is an exothermic process and the total energy released can be correlated to different types of defects. The temperature range was between 550 and 1350 K for the 2.5 wt % sample, and between 450 and 1400 K for the 10 wt % one. In both plots, the presence of four main peaks could be detected; again referring to the work of Staicu et al, peaks centred around 650, 850, 950 and 1150 K were identified. In addition to this, the 10 wt % sample exhibit two additional features, one small peak at 450 K and a second, more marked peak, around 1350 K that could be attributed to the He release thanks to the KEMS measurement (5.1.6). However, the presence of several shoulders hints towards the existence of possibly more phenomena. Table 21 summarises the defects annealing stages associated with each peak. It is worth remembering that the peak centre is a good feature for peak identification purposes, but the most physically meaningful temperature is the one of the flex, which corresponds to the maximum reaction (for example, defects recombination) rate.

Stage	T [K]	Involved process
I	450	O interstitials/vacancies recombination
II	650	U interstitials/vacancies recombination
III	850	Pu interstitials/vacancies recombination
IV	950	Dislocation loops annealing
V	1150	Voids precipitation
VI	1350	He desorption

Table 21: 6 main peaks were identified on the apparent C_p^* curve and attributed to different defects recombination, based on the interpretation given by Staicu et al. (96)

The relative intensity of the peaks in the two plots shown in Figure 103 is very different between the two samples. This effect can be imputed to the clustering of defects and to the different compositions. Initially, most of the generated point defects remain as individual defects, and the contribution of interstitial/vacancies grows quicker than the one of extended defects. After a certain threshold, reorganisation of defects into loops and voids becomes more and more significant, leading the contribution of extended defects to grow, and the one of point defects to stabilise and eventually decrease. This possibly takes place with different kinetics depending on the composition: in the case of the 10 wt % sample, the self-heating effect largely exceeds the overall defect contribution, while for the 2.5 wt % it is the reverse. It is expectable that the defects mobility in the two systems is quite different, meaning that the samples with higher activity could experience easier and quicker defect recombination, and hence a more marked contribution of extended defects. Also radiogenic helium shown to diffuse starting at 1100 K (but becoming intense around 1300 K – see Section 5.1.6) produces an exothermic effect which supports the hypothesis that He atoms are

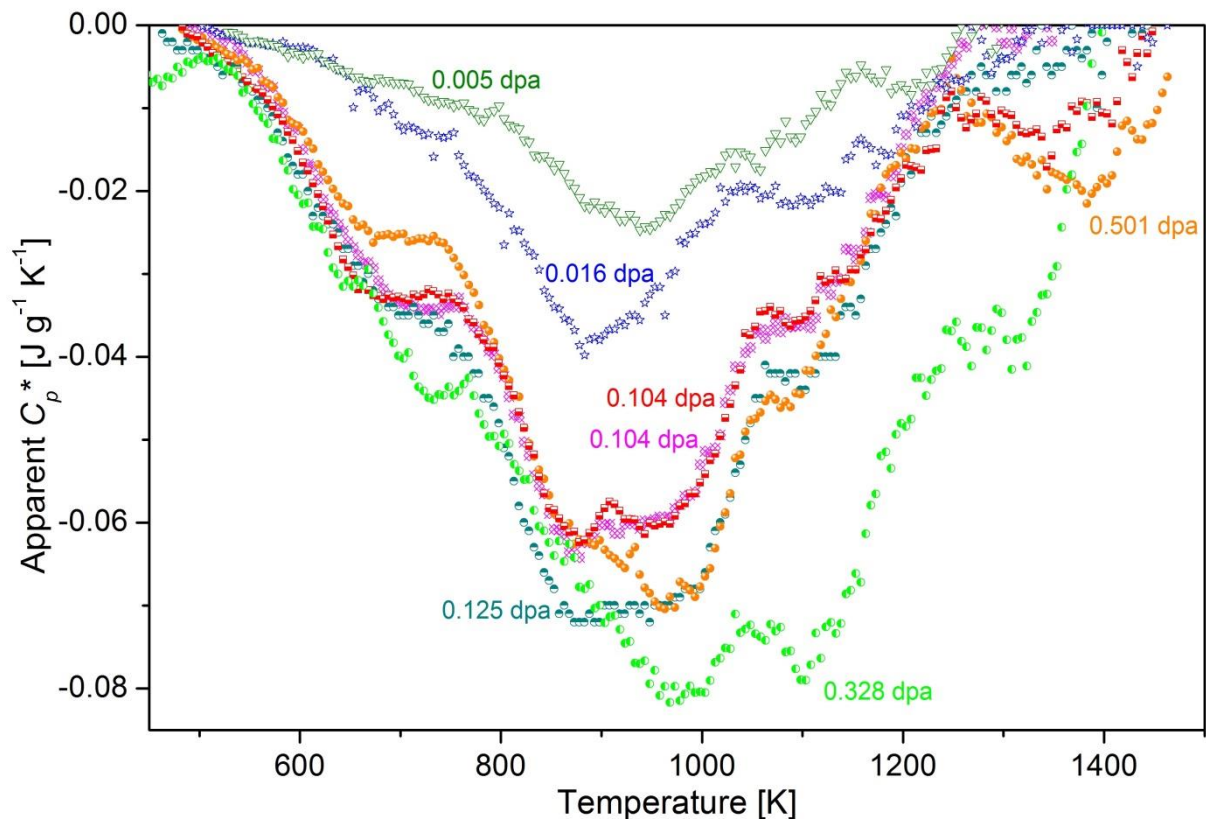


Figure 104: DSC data of the 10 wt % sample used in this work together with the data collected over the years from similar samples at the JRC-Karlsruhe (partially included in (96)).

associated to defects (vacancy type).

Some other ^{238}Pu -doped UO_2 samples of similar composition (around 10 wt %) were analysed at the JRC throughout the years, and they are plotted together with the 10 wt % sample of this work in Figure 104. Remarkably, the sample used in the present study released a significantly higher energy with respect to the others, mostly in the 1000 to 1300 K range. This discrepancy can be due to the subtraction of the self-heating effect, which is performed manually by the operator during the data analysis phase. A small change in the slope of the real C_p (obtained by average of the ascending and descending curves of the annealed, undamaged sample) can result in such an artefact as the one observed in Figure 104. In general, a qualitative trend can be observed, with the point defects effect increasing up to about 0.125 dpa and then saturating, going then to contribute to the extended defects signal.

5.1.8 Summary

Periodic XRD characterization of the self-irradiating samples showed very good scalability for the lattice parameter increase for the two different compositions. The samples reached 0.411 and 0.102 dpa for the 10 and 2.5 wt %, with a relative cell parameter increase of 0.31 and 0.27 %. The lattice swelling does not seem to be a kinetically driven process, depending solely on the dpa and not on the activity of the samples.

Microstrain was found to be decreasing with dpa, but with a different dependence with respect to the lattice constant increase. The microstrain values indeed decrease more steeply in the early stages of self-irradiation, up to 0.05. Consistently with the lattice parameter swelling instead, the microstrain evolution approaches a plateau for dpa values above 0.1.

SEM periodic characterization of the samples evidenced no significant change after 550 days, for a maximum of 0.4 dpa reached in the 10 wt % samples. The inspection of a new fracture surface, created by cracking the sample after the characterization of day 550, also showed no alteration of the original microstructure.

Raman periodic characterization evidenced an apparent broadening and shift of the T_{2g} peak to lower wavenumbers. This is due to the loss of order of the structure, which leads the T_{2g} mode to disperse to lower and, less markedly, higher wavenumbers. These two disperse modes increase in intensity up to 0.1 dpa to remain then fairly constant up to 0.4 dpa. The broadening of the same T_{2g} peak, quantified in terms of integrated area increase, seems to be at least partially kinetically driven, since the two compositions follow the same trend over time rather than over dpa. The broadening and increasing of the intensity of the defects triplet band was also detected, but could not be quantified.

LAF periodic characterization was performed only on a 2.5 wt % sample, as the degradation of the thermal conductivity was expected to be very quick. Indeed, a loss of 40 % of the thermal diffusivity takes place within the first 0.03 dpa, after which the value becomes almost constant. The phonon mean free path was also derived.

Remarkably, the thermal conductivity drops more abruptly in the first 0.0025 dpa, the same dose value for which also the microstrain relaxation seems to become less intense. It was proposed that

around this value the new point defects start interacting with those previously existing, inducing less additional lattice distortion and hence contribute less to the phonon scattering process.

TEM observations were performed less systematically than the SEM inspections due to the higher complexity of the sample preparation and the partial availability of the device.

A 2.5 wt % sample was examined after 170 days, having cumulated 0.031 dpa, and only some black dots were visible, the biggest of those appearing to be very small dislocation loops. This observation seems to confirm what was expected from the LAF results, where it was speculated that around 0.03 dpa point defects (not visible at the TEM) start to cluster into extended defects, resulting into a reduced degradation of the thermal conductivity.

A 10 wt % sample was examined first after 100 days (0.073 dpa), showing numerous and large (about 50 nm) dislocation loops, and then again re-observed at 150 and 250 days (0.109 and 0.182 dpa respectively) showing no significant increase in size or number of the dislocation loops. A second identical sample was examined after 450 days (0.328 dpa) and showed a marked increase in the number and size of the dislocation loops (up to 100 nm) together with the presence of He bubbles.

He release was measured on a 10 wt % sample aged 570 days (0.41 dpa). As seen in Section 5.1.5, already after 450 days (0.33 dpa) the radiogenic He quantity in the sample was enough to form visible bubbles. The amount of α -He in the sample was calculated to be $1.9 \cdot 10^{-7}$ mol, which is in excellent agreement with the released measured quantity. Consistently with what reported for polycrystalline UO_2 and $(\text{U,Pu})\text{O}_2$, grain boundaries acted as shortcut to surface desorption, and three main release mechanisms were detected:

- $T > 1100 \text{ K}$ – He atomic diffusion to grain boundaries and release, with concomitant trapping in bubbles
- $T > 1800 \text{ K}$ – intragranular He bubbles diffusion to grain boundaries and release
- Sporadic intergranular He bubbles release throughout the whole treatment, possibly involving interconnection

Post-treatment TEM inspection revealed undamaged bubble-free microstructure.

DSC characterization was conducted after the samples cumulated a significant dose, so that to have a clear signal during the measurement. Samples of both compositions were analysed after 450 days, corresponding to 0.082 and 0.326 dpa, and released in total 35 and 43 J/g respectively. Characteristic peaks for the recombination of different defects families could be identified for compositions, allowing drawing some qualitative interpretation of the defects evolution and clustering. Development of dislocation loops and voids from point defects was observed by comparing the new data with literature and previously measured samples. A difference between the two compositions was also found and attributed to the self-heating effect enhancing defects mobility in the sample with higher activity.

5.2 Low T C_p measurement

5.2.1 Results

Such as in the LAF case, the quick degradation of a thermophysical property like heat capacity could be accurately studied only on the low concentration samples. A periodic measurement of the sample specific heat in the 5 – 50 K temperature interval was performed. The antiferromagnetic transition at the Neel temperature typical of UO_2 -based compounds was found also in the examined 2.5 wt % sample, influenced by the disorder brought by the substitutional Pu atoms in the U lattice. As expected, excess heat capacity due to the substitutional-induced strain of the lattice was also measured.

Figure 105 shows the measured C_p curves as function of T for different ageing times, together with the curves for the two end members as references.

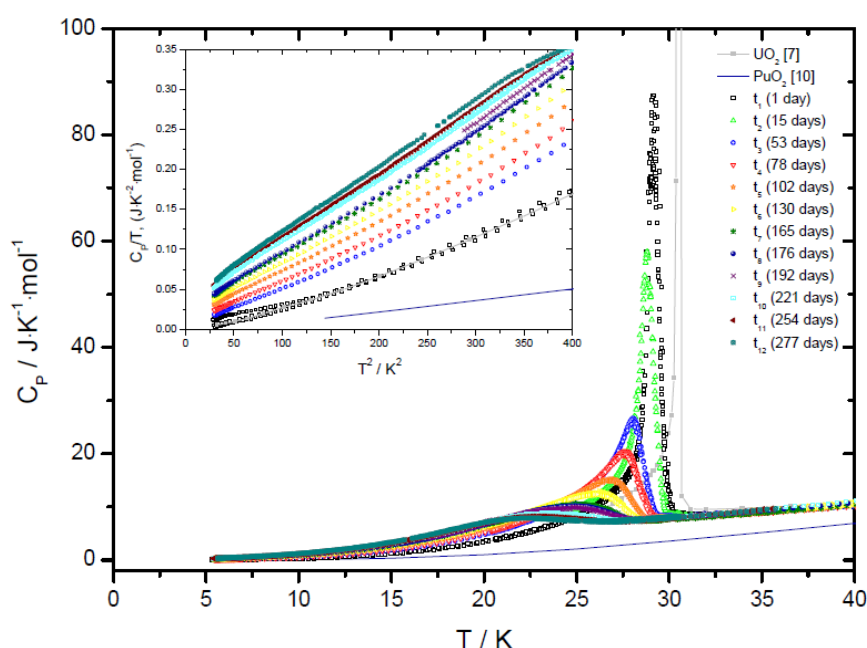


Figure 105: low temperature heat capacity of $(\text{U,Pu})\text{O}_2$ 2.5 wt %, together with the curve for PuO_2 obtained by Flotow *et al.* (242) and UO_2 measured at JRC.

As the disorder in the lattice increased as consequence of α -self-irradiation, the UO_2 magnetic transition peak broadened and decreased its maximum intensity. At the same way, the peak maximum (or the Neel temperature) shifted towards lower temperatures. While the excess entropy at the Neel temperature also decreased with disorder, the overall total excess entropy in the 5 – 50 K temperature range slowly increased. Figure 106 shows an overview on these variations, plotted as function of time and dpa.

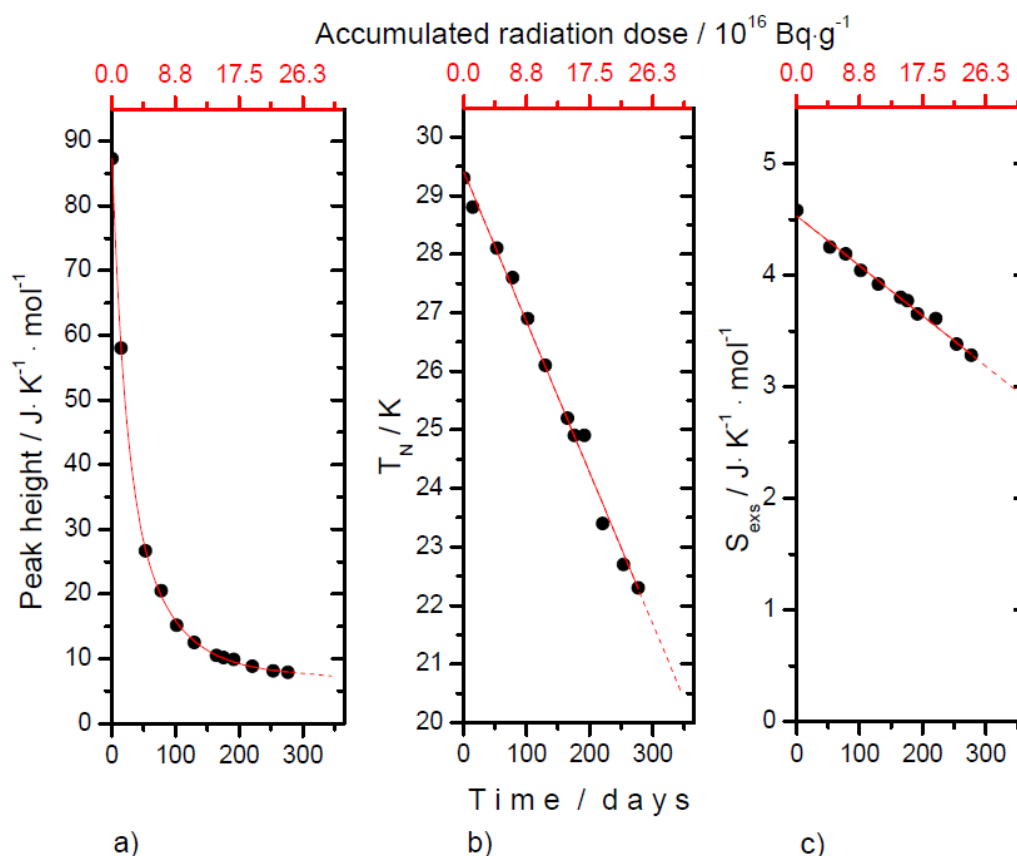


Figure 106: variations of peak height (a), position (hence Neel temperature – b) and excess entropy of the peak (c) as a function of time and accumulated dose.

5.2.2 Summary

The α -self-irradiation induces significant disorder in the cation lattice already from the early stages of damage accumulation. This results in a quick deterioration of the phonon transmission in the matrix, leading to significant decrease of the thermal properties of the material. The effect of the increasing disorder leads also the UO₂ C_p antiferromagnetic sharp transition to become a broader anomaly, with the peak decreasing in intensity, broadening and shifting to lower T, and the excess entropy being then redistributed over the whole T interval. As expected, and as seen for other thermal properties, the impact of self-irradiation is significant already for a moderate cumulated dose. A detailed description of the experiment can be found in the publication by Valu et al.(243)

6 CONCLUSIONS AND OUTLOOK

Interfaces represent one of the most important microstructural elements for determining the properties of nuclear fuels. They serve as sources and sinks of dislocations, recombination sites for vacancies and interstitials, traps for dopants or fission gases, fast diffusion paths, crack initiation sites, and more. Also, they play a very important role in reducing the concentrations of point defects produced by irradiation: vacancies and interstitials migrate to the interfaces, where they recombine. Close to equilibrium conditions, the migration of defects is also responsible for the elementary redistribution of species at the interface, which causes either the enrichment or the depletion of guest species.

During irradiation, the original microstructure of the nuclear fuel is reorganised into the so-called high burnup structure, characterized by grains down to 100 nm in size and therefore a significantly higher density of interfaces. This structure was found to exhibit better properties than initially thought, at the point that it could be taken into consideration as a potential accident tolerant fuel. Moreover, the high burnup structure will represent the spent fuels first interface facing the external environment (water in most cases), meaning that these interfaces-rich regions will play a key role in determining the safety of spent fuel repository solutions. Understanding the phenomena taking place at grain boundaries, and their impact on the material interactions with radiation and/or the external environment, is then fundamental to predict the fuel behaviour in operation and afterwards during the repository. Ideally, this basic knowledge would serve in the future for designing materials with stable structures and microstructures, or even better, able to evolve under irradiation to even more radiation-resistant states.

The control of material process conditions is therefore essential for understanding the response of these systems to structural and chemical modifications: this is an essential step in understanding the global response of the fuels submitted to irradiation, temperature transients, and various environments (oxygen potential of the surrounding atmosphere...). To minimize (and sometimes eliminate) these heterogeneities in doped samples, samples with crystallites of nanometric size can be produced where the interface properties of these crystallites can be measured and sometimes controlled.

In order to address these challenges, this dissertation was developed along two main directions:

- A first axis relying on parametric studies of nuclear ceramics synthesised with different grain sizes. The focus was on the study of the correlations between the characteristics of the particles constituting the pellets and the physical characteristics measured on these samples. The aim is to ultimately deduce the impact of those changes for the technological properties and then mitigate the eventual adverse features, potentially improving the operating and long-term behaviour of those ceramics.
- A second axis addressing self-irradiated materials. This work programme completes and extends a large number of parametric studies on simulated fuels where the key ingredient of self-irradiation was missing. We show that this ingredient has essential consequences and therefore this supports the need of this kind of studies.

In both cases, considerable effort was dedicated to the sample preparation. For self-irradiating samples, the dopant concentrations had to be accurately chosen and then successfully obtained to have some measurable effects within the project timeframe. The number of samples to be produced was also carefully designed, in order to allow monitoring the self-irradiation effect on different facets of the material by means of a broad set of techniques. The process to obtain simulated fuels with different grain sizes instead involved a long optimisation phase, to control the microstructure of the final product. Different features, from the powders synthesis routes to the sintering treatment parameters were adjusted and improved.

For the first time, dense (95 % of the theoretical density) and stoichiometric UO_2 with grain size down to 50-100 nm was successfully produced. Samples were prepared by powder sintering using spark plasma sintering (SPS). Different powders synthesis routes were explored and the final products were carefully characterized, before being tested in SPS, and the influence of the synthesis route on the sintering behaviour of the powders was qualitatively assessed. The best results were obtained using a powder synthesised from U(IV) oxalate by hydrothermal decomposition, resulting in near-stoichiometric highly-sinterable nanoparticles. The adoption of hydrothermal decomposition replacing a thermal process improved the morphology of the powder particles and agglomerates, leading to a sintering enhancement. Different variations of the standard SPS sintering treatments were also explored to improve the control of the final microstructure: a two-step method, exploiting the benefits of fast firing of the powders, and a high pressure setup, to provide extra driving force to the sintering. High-pressure SPS was found to be the optimal solution and its parameters were further optimised to achieve densification with limited grain growth, whereas a final annealing treatment was designed to homogenise the stoichiometry of all the produced samples. Extensive characterization of the final products by XRD, SEM and TEM proved that identical UO_2 samples differing only by the grain size were successfully produced.

Due to the resemblance of the topic and availability of high-quality starting materials, the same strategy was then applied for the preparation of ThO_2 with different microstructures. ThO_2 presents interesting similarities with UO_2 , with the advantage of existing only in a stoichiometric form with a unique oxidation state of Th, representing a simplified system useful for benchmark studies. In this case, the powder was produced by hydrothermal decomposition of Th hydroxide. Sintering conditions for densification with limited grain growth were also optimised for ThO_2 , resulting in samples with grain size smaller than 50 nm. These samples were also characterized by means of XRD, SEM and TEM.

The production route developed in the present work represents a solid basis for grain boundary studies on UO_2 or ThO_2 based systems. Submitting an ensemble of such-produced samples to the same conditions (irradiation, oxidation, dissolution...) will pave the way for a better understanding of the role played by interfaces in the material response.

Sets of ThO_2 and UO_2 lamellas coming from samples of different microstructures were prepared to be implanted with He and Xe ions, to study their response to ballistic damage as well as their gas-retention behaviour. Due to logistic reasons, implantations could be performed only on ThO_2 samples within the timespan of this thesis work. Results for micrograined ThO_2 were in good agreement with the already reported UO_2 behaviour in literature, which was the only comparison because, to our knowledge, this study represents the very first systematic He and Xe irradiation

study on ThO₂. In-situ TEM after irradiation with 16 keV He at 600 °C revealed an extremely different response of the two different microstructures: in micrograined (~10 µm) ThO₂ bubbles were small and randomly distributed, while in nanograined (~50 nm) ThO₂ they were lined up at grain boundaries and larger in size. These differences were attributed to the much shorter diffusion path to reach sinks in nanograined ThO₂, resulting into fewer nucleation sites and consequently a predominance of the bubbles growth mechanism over nucleation. These first results confirm the leading role played by interfaces in gas retention, highlighting the need for further investigation. The materials synthesised in this work resort to be excellent systems for a separate effect study of the influence of interfaces on the behaviour of otherwise identical samples. The production route presented in this dissertation can serve as a paradigm for further experiments, which will help understanding the importance of grain boundaries on rare gases retention and radiation damage resistance.

(U,Pu)O₂ samples were synthesised with desired dopant concentrations to study the full evolution of their microstructural and thermophysical properties during 2 years of accelerated ageing under self-irradiation. The Pu powder used as a dopant consisted of about 53 % of the short-lived α -emitting ²³⁸Pu. Considering the very different kinetics at which properties evolve, two compositions were chosen, allowing accurate measurement of fast transients and, at the same time, ensuring reaching saturation for most of the properties evolution. Moreover, with this approach, the independence on the samples activities of the radiation-induced macroscopic changes could be reassessed, at least in the low dopant concentration range taken into account.

Liquid phase mixing and co-hydrolysis ensured intimate mixing of U and Pu in the starting powder, and conventional sintering was performed to densify homogeneous, stoichiometric (U_{0.975},Pu_{0.025})O₂ and (U_{0.9},Pu_{0.1})O₂ disks. SEM and TEM observations did not show any difference between the two batches of produced samples, while XRD characterization confirmed the achievement of solid solutions for both the desired compositions.

The amount of identical samples to be produced was calculated based on the foreseen characterization techniques, and geometries of certain samples were optimised for technique-specific needs. This constituted an unprecedented set of specimens, ideal for isochronal and isothermal systematic studies of thermophysical and microstructural evolutions of the properties as a function of the cumulated dose.

Periodic measurements were performed up to a cumulated dose of 0.41 dpa, comparable to those of a 40 GWd/t UO₂ spent nuclear fuel after 300 years of storage, or of a 65 GWd/t spent MOX fuel (45 % Pu) after 25 years of storage.

XRD characterization confirmed the lattice swelling behaviour already reported in literature, re-assessing it with improved accuracy and showing for the first time that it is accompanied by a decrease of the microstrain. Consistently with what already reported for α -self-irradiating samples, saturation of the lattice swelling was approached for 0.41 dpa, at a value reaching a 0.3 % increase. Comparison of the data obtained from the two compositions resulted in almost perfect overlapping of the two trends as a function of the dose, confirming the independence of the analysed effect on the initial samples activity, for those different compositions.

The thermal conductivity, as calculated from laser flash method (LAF) data, was also in excellent agreement with previous literature data, and it also constitutes an improved data set for future modelling purposes. Already at 0.03 dpa, the density of radiation-induced point defects reduced the thermal conductivity of 40 %, but no further significant effect when further increasing the dose. XRD microstrain also was found to evolve more slowly after 0.03 dpa.

Taking advantage of the innovative device setup available at the JRC – Karlsruhe, Raman characterization as a function of the dose was also performed for the very first time on (U,Pu)O₂ samples. In agreement with what already reported in literature for α -implanted UO₂, it evidenced the progressive loss of crystalline long-range order of the structure, which also proceeded independently from the initial samples activities.

Periodic SEM and TEM inspection provided an overview on the microstructural evolution of the material at different scales. By SEM, it was possible to trace back and observe always the same positions on the sample fracture surfaces, which exhibited no grain boundary opening or cracking. Freshly-created fracture surfaces at 0.41 dpa did not show any difference compared to those monitored up to that point, ruling out any difference between the bulk and the surface. By TEM it was also possible to follow the ingrowth of dislocation loops and He bubbles throughout the lattice. At 0.03 dpa, when thermal conductivity had already decreased to a plateau, only tiny (≤ 10 nm) dislocation loops could be detected, confirming the negligible adverse effect of extended defects compared with more prominent point defects on the thermal conductivity. Beyond that point, the dislocation loop population increased in size and concentration with increasing dpa, and at 0.33 dpa He bubbles were first detected. Annealing of dislocation loops under the TEM beam was also observed.

In the latest stages of the storage, He release and calorimetry measurements were also performed. As measured by Knudsen effusion mass spectrometry (KEMS), up to 0.41 dpa, the totality of the radiogenic He is retained within the matrix. Post-mortem TEM characterization revealed a complete damage and bubble free microstructure. In agreement with literature data on irradiated fuel and α -doped UO₂, two main release stages were observed and attributed to atomic He migration to free surfaces and concomitant trapping ($T > 1100$ K), or bubbles migration to free surfaces ($T > 1800$ K). Burst releases from intergranular bubbles migration were also observed throughout the whole treatment, similarly to what reported for polycrystalline doped or infused UO₂ samples. Comparison with undamaged He-infused UO₂ highlighted the importance of radiation-induced defects over He mobility.

Differential scanning calorimetry (DSC) annealing treatments allowed distinguishing the contributions of different defects recovery stages on the apparent sample heat capacity. Recombination of point defects was measured for temperatures as low as 450 K, while effects attributed to extended defects arose around 950 K. Comparison of the relative intensities of the signals between the two compositions and with literature data qualitatively revealed point defects clustering and reorganisation into extended defects. Cross-checking with He release data helped identifying the increasing contribution of He migration and precipitation in bubbles for increasing dpa.

Based on this sound and comprehensive data collection, obtained through a quite exhaustive set of techniques, some preliminary estimation on the state of spent fuel after some centuries of storage

was attempted. As mentioned already, the 0.41 dpa reached by the samples involved in the present study are comparable to what cumulated by a 40 GWd/t UO₂ spent nuclear fuel after 300 years of storage. At this stage, as a result of α -self-irradiation:

- The thermal conductivity of spent nuclear fuel will decrease by 40 %, and will not be decreasing significantly further. This of course has implications on the temperature of the spent fuel, as it will generate internal heat throughout the whole disposal time.
- Lattice swelling also will be approaching its saturation at 0.3 %, implying potential interactions and stress generation with the cladding material.
- The totality of the He generated within the spent fuel matrix will still be retained, and will not be released unless the storage temperature raises of several hundred degrees. This will also have to be taken into account as contributing to fuel swelling, but allows ruling out overpressurization of the fuel pin.
- Spent fuel will be completely integer, no crack of grain boundary opening has taken place.

Moreover, at the temperature reached in wet storage conditions (~ 200 °C), defects which do not immediately recombine will not anneal but rather cluster and organise into extended defects.

After this accurate and comprehensive re-assessment of the influence of α -self-irradiation on the fuel evolution, it is evident the need for a complete understanding of the role of interfaces in relation with radiation resistance and rare gases retention of the material. Most of the measured effects, such as defects recombination and He precipitation, and less directly fuel swelling, integrity or even thermal conductivity decrease, are affected by the presence of grain boundaries in the system, and the preliminary results obtained on ThO₂ suggest very different behaviours between nano and micro grained samples. He and Xe implantation experiments on UO₂ which will be performed on the already prepared samples should give further qualitative insight on the responses of microstructures with very different interfaces densities.

However, a more systematic study of grain size effect on spent nuclear fuel ageing (radiation damage resistance and rare gases retention) should foresee ion implantations at increasing fluences and at different temperatures. Ideally, the same situations reproduced in the self-irradiation study could be targeted in terms of dpa and thermal history. In-situ characterizations like the ones available at ANL (TEM), JANNUS-Orsay (TEM) or JANNUS-Saclay (Raman) would simplify the experimental setup and provide quick feedback on analogies/differences with the α -doped systems. Post-mortem annealing studies and characterizations should complete the study, giving insight on the influence of grain boundaries density on defect annealing temperatures. Moreover, grain growth can be triggered in nanograined samples already at moderate temperatures, allowing studying more easily the effects of grain boundaries migration on defects and rare gases.

A more faithful reproduction of α -decay would involve multi-beam implantations, to simulate concomitantly the electronic and nuclear stoppage of the α -particle and recoil nucleus generated in the α -decay.

Finally, once the appropriate devices are installed, the synthesis of nanograined ²³⁸Pu-doped UO₂ would represent the junction point between the two branches of the work. It is worth remembering that no SPS device is available for Pu sintering around the world at the time of writing. Self-irradiating (U,Pu)O₂ of different grain sizes would clarify the role of grain boundaries on radiation-

damage resistance and rare gases accumulation and retention. This should shed light on the potentially beneficial implications of the HBS in SNF during long-term storage.

As a last remark, self-irradiation studies at higher temperatures, namely the one of dry storage conditions, are also advised. The poor sensitivity of some of the devices used in the present work between room temperature and about 400 °C leaves behind a knowledge gap on the effects ongoing in this temperature range. It is possible that, for systems with a high density of grain boundaries which can act as defects sinks, some defects annealing already could already take place at relatively low temperatures.

References

1. COMMISSARIAT À L'ÉNERGIE ATOMIQUE ET AUX ÉNERGIES ALTERNATIVES. Les centrales nucléaires dans le monde, CEA, Gif-sur-Yvette, 2018. <http://www.cea.fr/english/Documents/scientific-and-economic-publications/Elecnucl-2018.pdf>
2. INTERNATIONAL ATOMIC ENERGY AGENCY, IAEA Annual Report for 2017, IAEA, Vienna, 2018. <https://www.iaea.org/opic/annual-report-2017>
3. INTERNATIONAL ATOMIC ENERGY AGENCY, Status and Trends in Spent Fuel and Radioactive Waste Management, Nuclear Energy Series No. NW-T-1.14, IAEA, Vienna, 2018. <https://www.iaea.org/publications/11173/status-and-trends-in-spent-fuel-and-radioactive-waste-management>
4. Pushnov A, Ryabushenko A, Berengarten M. The risks of global warming and cooling efficiency of circulating water in cooling towers of nuclear power plant. In: The 9th International Conference "Environmental Engineering 2014". Vilnius, Lithuania: Vilnius Gediminas Technical University Press "Technika" 2014; 2014. <http://enviro2014.vgtu.lt/Abstracts/1/046.html>
5. UNITED STATES NUCLEAR REGULATORY COMMISSION. U.S. NRC: The Student Corner, <https://www.nrc.gov/reading-rm/basic-ref/students>, accessed on 07/2019
6. NUCLEAR ENERGY AGENCY / INTERNATIONAL ATOMIC ENERGY AGENCY, Uranium 2018: Resources, Production and Demand, OECD Publishing, Paris, 2019. <https://doi.org/10.1787/uranium-2018-en>.
7. Kok KD. Nuclear Engineering Handbook. Kok KD, CRC Press, Boca Raton, 2009. <https://www.taylorfrancis.com/books/9781420053913>
8. Carbol P, Wegen DH, Wiss T, Fors P. Spent Fuel as Waste Material. In: Comprehensive Nuclear Materials. Elsevier; 2012. p. 389–420. <https://linkinghub.elsevier.com/retrieve/pii/B9780080560335001063>
9. INSPYRE, Investigations Supporting MOX Fuel Licensing in ESNII Prototype Reactors, www.eera-jpnm.eu/inspyre
10. H2020, Horizon 2020, <https://ec.europa.eu/programmes/horizon2020/en>
11. Cacuci DG. Handbook of Nuclear Engineering. Cacuci DG, Springer, Boston, MA: Springer US; 2010. 3642 p. <http://link.springer.com/10.1007/978-0-387-98149-9>
12. Kingery WD. Sintering from Prehistoric Times to the Present. Solid State Phenom. 1992 Jan; 25–26:1–10. <https://www.scientific.net/SSP.25-26.1>
13. Rahaman MN. Ceramic Processing. Vol. 111, CRC Press, Boca Raton, 2017. <https://doi.org/10.1201/9781315274126>
14. Coble RL. Diffusion models for hot pressing with surface energy and pressure effects as driving forces. J Appl Phys. 1970;41(12):4798–807. <https://doi.org/10.1063/1.1658543>
15. FRENKEL JJ. Viscous flow of crystalline bodies under the action of surface tension. J Phys. 1945;9:385. <https://ci.nii.ac.jp/naid/10012829642/en/>
16. Ullrich H-J, Cahn RW, Haasen P, Kramer EJ. Materials science and technology A comprehensive treatment. Volume 2B: Characterization of Materials (Part II) Volume Editor: E. Lifshin. VCH Weinheim; New York; Basel; Cambridge; Tokyo 1994, 775 pages, 491 figur. Cryst Res Technol. 1994;29(6):786–786. <http://doi.wiley.com/10.1002/crat.2170290603>
17. Shewmon P. Diffusion in Solids. Cham: Springer International Publishing; 2016. <http://link.springer.com/10.1007/978-3-319-48206-4>
18. Prof. Dr. Helmut Föll. Kiel University Christian-Albrechts-Universität zu Kiel. https://www.tf.uni-kiel.de/matwis/amat/def_en/
19. Materials Science and Engineering. University of California, Berkeley. <http://www.mse.berkeley.edu/groups/morris/MSE200/I-structure.pdf>
20. Sōmiya S, Moriyoshi Y, editors. Sintering Key Papers. Dordrecht: Springer Netherlands; 1990. <http://link.springer.com/10.1007/978-94-009-0741-6>

21. Coble RL. Sintering Crystalline Solids. I. Intermediate and Final State Diffusion Models. *J Appl Phys.* 1961 May;32(5):787–92. <http://aip.scitation.org/doi/10.1063/1.1736107>
22. Kingery WD, Berg M. Study of the Initial Stages of Sintering by Viscous Flow, Evaporation—Condensation, and Self-Diffusion. In: Sômiya S, Moriyoshi Y, editors. *Sintering Key Papers*. Dordrecht: Springer Netherlands; 1990. p. 367–82. https://doi.org/10.1007/978-94-009-0741-6_22
23. Coble RL. Initial Sintering of Alumina and Hematite. *J Am Ceram Soc.* 1958 Feb 1;41(2):55–62. <https://doi.org/10.1111/j.1151-2916.1958.tb13519.x>
24. Johnson DL, Cutler IB. Diffusion Sintering: I, Initial Stage Sintering Models and Their Application to Shrinkage of Powder Compacts. *J Am Ceram Soc.* 1963 Nov 1;46(11):541–5. <https://doi.org/10.1111/j.1151-2916.1963.tb14606.x>
25. Yin Q, Zhu B, Zeng H. *Microstructure, Property and Processing of Functional Ceramics*. Berlin, Heidelberg: Springer Berlin Heidelberg; 2010. <http://link.springer.com/10.1007/978-3-642-01694-3>
26. Greenwood G. The growth of dispersed precipitates in solutions. *Acta Metall.* 1956 May;4(3):243–8. <https://linkinghub.elsevier.com/retrieve/pii/0001616056900608>
27. Wagner C. Theory of the aging of precipitates by dissolution-reprecipitation (Ostwald ripening). *Z Elektrochem.* 1961;65(7):511–81.
28. Lifshitz IM, Slyozov VV. The kinetics of precipitation from supersaturated solid solutions. *J Phys Chem Solids.* 1961 Apr;19(1–2):35–50. <https://linkinghub.elsevier.com/retrieve/pii/0022369761900543>
29. Burke JE, Turnbull D. Recrystallization and grain growth. *Prog Met Phys.* 1952 Jan;3:220–92. <https://linkinghub.elsevier.com/retrieve/pii/0502820552900099>
30. BROOK RJ. Controlled Grain Growth. In *Treatise on Materials Science & Technology*, Elsevier. 1976, p. 331–64. <https://linkinghub.elsevier.com/retrieve/pii/B9780123418098500243>
31. Yan MF. Microstructural control in the processing of electronic ceramics. *Mater Sci Eng.* 1981;48(1):53–72. [https://doi.org/10.1016/0025-5416\(81\)90066-5](https://doi.org/10.1016/0025-5416(81)90066-5)
32. Cavaliere P. *Spark Plasma Sintering of Materials*. Cavaliere P, editor. *Spark Plasma Sintering of Materials*. Cham: Springer International Publishing; 2019. <http://link.springer.com/10.1007/978-3-030-05327-7>
33. Guillon O, Gonzalez-Julian J, Dargatz B, Kessel T, Schiering G, Räthel J, et al. Field-Assisted Sintering Technology/Spark Plasma Sintering: Mechanisms, Materials, and Technology Developments. *Adv Eng Mater.* 2014 Jul;16(7):830–49. <http://doi.wiley.com/10.1002/adem.201300409>
34. Anselmi-Tamburini U, Garay JE, Munir ZA. Fast low-temperature consolidation of bulk nanometric ceramic materials. *Scr Mater.* 2006;54(5):823–8. <https://doi.org/10.1016/j.scriptamat.2005.11.015>
35. Grasso S, Kim BN, Hu C, Maizza G, Sakka Y. Highly transparent pure alumina fabricated by high-pressure spark plasma sintering. *J Am Ceram Soc.* 2010;93(9):2460–2. <https://doi.org/10.1111/j.1551-2916.2010.03811.x>
36. Krsmanović Whiffen RM, Bregiroux D, Viana B. Nanostructured Y₂O₃ ceramics elaborated by Spark Plasma Sintering of nanopowder synthesized by PEG assisted combustion method: The influence of precursor morphological characteristics. *Ceram Int.* 2017; 10.1016/j.ceramint.2017.08.153
37. Chaim R, Shen Z, Nygren M. Transparent nanocrystalline MgO by rapid and low-temperature spark plasma sintering. *J Mater Res.* 2004; 19(9): 2527–2531. doi:10.1557/JMR.2004.0334
38. Yao T, Scott SM, Xin G, Gong B, Lian J. Dense nanocrystalline UO_{2+x} fuel pellets synthesized by high pressure spark plasma sintering. *J Am Ceram Soc.* 2018; 101(3):1105–1115. <https://doi.org/10.1111/jace.15289>
39. Gong B, Frazer D, Yao T, Hosemann P, Tonks M, Lian J. Nano- and micro-indentation testing of sintered UO₂ fuel pellets with controlled microstructure and stoichiometry. *J Nucl Mater.* 2019 Apr;516:169–77. <https://doi.org/10.1016/j.jnucmat.2019.01.021>
40. Cologna M, Tyrpekl V, Ernstberger M, Stohr S, Somers J. Sub-micrometre grained UO₂ pellets consolidated from sol gel beads using spark plasma sintering (SPS). *Ceram Int.* 2016 May;42(6):6619–23. <https://linkinghub.elsevier.com/retrieve/pii/S0272884216000079>

41. Tyrpekl V, Cologna M, Vigier JF, Cambriani A, De Weerd W, Somers J. Preparation of bulk-nanostructured UO_2 pellets using high-pressure spark plasma sintering for LWR fuel safety assessment. *J Am Ceram Soc.* 2017; 100(4): 1269-1274. <https://doi.org/10.1111/jace.14647>
42. Olander DR. Fundamental aspects of nuclear reactor fuel elements. U.S. Department of Energy; 1976 Jan. <http://www.osti.gov/servlets/purl/7343826/>
43. Guéneau C, Chartier A, Van Brutzel L. Thermodynamic and Thermophysical Properties of the Actinide Oxides. In: *Comprehensive Nuclear Materials.* Elsevier; 2012. p. 21–59. <https://linkinghub.elsevier.com/retrieve/pii/B9780080560335000094>
44. Franceschin G, Flores-Martínez N, Victorio GV, Ammar S, Valenzuela R. Sintering and Reactive Sintering by Spark Plasma Sintering (SPS). In: *Sintering of Functional Materials.* InTech; 2018. <http://www.intechopen.com/books/sintering-of-functional-materials/sintering-and-reactive-sintering-by-spark-plasma-sintering-sps->
45. Ge L, Subhash G, Baney RH, Tulenko JS. Influence of processing parameters on thermal conductivity of uranium dioxide pellets prepared by spark plasma sintering. *J Eur Ceram Soc.* 2014; 34(7): 1791-1801. <https://doi.org/10.1016/j.jeurceramsoc.2014.01.018>.
46. Leinders G, Cardinaels T, Binnemans K, Verwerft M. Accurate lattice parameter measurements of stoichiometric uranium dioxide. *J Nucl Mater.* 2015; 459:135-142. <https://doi.org/10.1016/j.jnucmat.2015.01.029>
47. INTERNATIONAL ATOMIC ENERGY AGENCY. Thermophysical Properties Database of Materials for Light Water Reactors and Heavy Water Reactors. TECDOC Series, IAEA, Vienna, 2006.. <https://www.iaea.org/publications/7489/thermophysical-properties-database-of-materials-for-light-water-reactors-and-heavy-water-reactors>
48. Martin DG. The thermal expansion of solid UO_2 and (U,Pu) mixed oxides - a review and recommendations. *J Nucl Mater.* 1988; 152(2-3):94-101. [https://doi.org/10.1016/0022-3115\(88\)90315-7](https://doi.org/10.1016/0022-3115(88)90315-7).
49. Adamson MG, Aitken EA, Caputi RW. Experimental and thermodynamic evaluation of the melting behavior of irradiated oxide fuels. *J Nucl Mater.* 1985 Feb;130(C):349–65. <https://linkinghub.elsevier.com/retrieve/pii/002231158590323X>
50. Carbajo JJ, Yoder GL, Popov SG, Ivanov VK. A review of the thermophysical properties of MOX and UO_2 fuels. *J Nucl Mater.* 2001 Dec;299(3):181–98. www.elsevier.com/locate/jnucmat
51. Fink JK. Thermophysical properties of uranium dioxide. *J Nucl Mater.* 2000 Mar;279(1):1–18. <https://linkinghub.elsevier.com/retrieve/pii/S0022311599002731>
52. Hiernaut JP, Hyland GJ, Ronchi C. Premelting transition in uranium dioxide. *Int J Thermophys.* 1993 May;14(3):609–12. <http://link.springer.com/10.1007/BF00566058>
53. Ronchi C, Sheindlin M, Musella M, Hyland GJ. Thermal conductivity of uranium dioxide up to 2900 K from simultaneous measurement of the heat capacity and thermal diffusivity. *J Appl Phys.* 1999;85(2):776–89. <https://doi.org/10.1063/1.369159>
54. Konings RJM, Beneš O, Kovács A, Manara D, Sedmidubský D, Gorokhov L, et al. The Thermodynamic Properties of the f-Elements and their Compounds. Part 2. The Lanthanide and Actinide Oxides. *J Phys Chem Ref Data.* 2014 Mar;43(1):013101. <http://aip.scitation.org/doi/10.1063/1.4825256>
55. Harding JH, Martin DG. A recommendation for the thermal conductivity of UO_2 . *J Nucl Mater.* 1989;166(3):223–6. [https://doi.org/10.1016/0022-3115\(89\)90218-3](https://doi.org/10.1016/0022-3115(89)90218-3)
56. Higgs JD, Lewis BJ, Thompson WT, He Z. A conceptual model for the fuel oxidation of defective fuel. *J Nucl Mater.* 2007;366(1–2):99–128. <https://doi.org/10.1016/j.jnucmat.2006.12.050>
57. Teske K, Ullmann H, Rettig D. Investigation of the oxygen activity of oxide fuels and fuel-fission product systems by solid electrolyte techniques. Part I: Qualification and limitations of the method. *J Nucl Mater.* 1983 Jun;116(2–3):260–6. <https://linkinghub.elsevier.com/retrieve/pii/0022311583901101>
58. Matzke H. Lattice disorder and metal self-diffusion in non-stoichiometric UO_2 and (U, Pu) O_2 . *Le J Phys Colloq.* 1973 Nov;34(C9):C9-317-C9-325. <http://www.edpsciences.org/10.1051/jphyscol:1973956>

59. Lucuta PG, Matzke H, Hastings JJ. A pragmatic approach to modelling thermal conductivity of irradiated UO₂ fuel: Review and recommendations. *J Nucl Mater.* 1996 Sep;232(2–3):166–80. <https://linkinghub.elsevier.com/retrieve/pii/S0022311596004047>
60. Conradson SD, Begg BD, Clark DL, Den Auwer C, Ding M, Dorhout PK, et al. Charge distribution and local structure and speciation in the UO_{2+x} and PuO_{2+x} binary oxides for x≤0.25. *J Solid State Chem.* 2005;178(2 SPEC. ISS.):521–35. <https://doi.org/10.1016/j.jssc.2004.09.029>
61. Penneman RA, Paffett MT. An alternative structure of Pu₄O₉ (“PuO_{2.25}”) incorporating interstitial hydroxyl rather than oxide. *J Solid State Chem.* 2005;178(2 SPEC. ISS.):563–6. <https://doi.org/10.1016/j.jssc.2004.08.022>
62. Gibson JK, de Jong WA, Dau PD, Gong Y. Heptavalent Actinide Tetroxides NpO₄[−] and PuO₄[−]: Oxidation of Pu(V) to Pu(VII) by Adding an Electron to PuO₄. *J Phys Chem A.* 2017 Nov 30;121(47):9156–62. <http://pubs.acs.org/doi/10.1021/acs.jpca.7b09721>
63. Yamashita T, Nitani N, Tsuji T, Inagaki H. Thermal expansions of NpO₂ and some other actinide dioxides. *J Nucl Mater.* 1997;245(1):72–8. [https://doi.org/10.1016/S0022-3115\(96\)00750-7](https://doi.org/10.1016/S0022-3115(96)00750-7)
64. Tokar M, Nutt AW, Keenan TK. Linear Thermal Expansion of Plutonium Dioxide. *Nucl Technol.* 1973;17(2):147–52. <https://doi.org/10.13182/NT73-A31241>
65. Martin DG. The thermal expansion of solid UO₂ and (U, Pu) mixed oxides - a review and recommendations. *J Nucl Mater.* 1988;152(2–3):94–101. [https://doi.org/10.1016/0022-3115\(88\)90315-7](https://doi.org/10.1016/0022-3115(88)90315-7)
66. Kato M, Morimoto K, Sugata H, Konashi K, Kashimura M, Abe T. Solidus and liquidus temperatures in the UO₂-PuO₂ system. *J Nucl Mater.* 2008; <https://doi.org/10.1016/j.jnucmat.2007.06.002>
67. De Bruycker F, Boboridis K, Pöml P, Eloirdi R, Konings RJM, Manara D. The melting behaviour of plutonium dioxide: A laser-heating study. *J Nucl Mater.* 2011;416(1–2):166–72. <http://dx.doi.org/10.1016/j.jnucmat.2010.11.030>
68. Kruger OL, Savage H. Heat Capacity and Thermodynamic Properties of Plutonium Dioxide. *J Chem Phys.* 1968;49(10):4540–4. <https://doi.org/10.1063/1.1669909>
69. Oetting FL. The chemical thermodynamics of nuclear materials. VII. the high-temperature enthalpy of plutonium dioxide. *J Nucl Mater.* 1982;105(2–3):257–61. [https://doi.org/10.1016/0022-3115\(82\)90382-8](https://doi.org/10.1016/0022-3115(82)90382-8)
70. Flotow HE, Osborne DW, Fried SM, Malm JG. Heat capacity of ²⁴²PuO₂ from 12 to 350°K and of ²⁴⁴PuO₂ from 4 to 25°K. Entropy, enthalpy, and Gibbs energy of formation of PuO₂ at 298.15°K. *J Chem Phys.* 1976;65(3):1124–9. <https://doi.org/10.1063/1.433186>
71. Duriez C, Alessandri J-P, Gervais T, Philipponneau Y. Thermal conductivity of hypostoichiometric low Pu content (U,Pu)O_{2-x} mixed oxide. *J Nucl Mater.* 2000 Feb;277(2–3):143–58. <http://linkinghub.elsevier.com/retrieve/pii/S0022311599002056>
72. Kandan R, Babu R, Nagarajan K, Vasudeva Rao PR. Calorimetric measurements on uranium-plutonium mixed oxides. *J Nucl Mater.* 2004;324(2–3):215–9. <https://doi.org/10.1016/j.jnucmat.2003.10.005>
73. Wiss T. Radiation Effects in UO₂. In: *Comprehensive Nuclear Materials*. Elsevier; 2012. p. 465–80. <https://linkinghub.elsevier.com/retrieve/pii/B9780080560335000392>
74. Soullard J, Alamo EA. Etude du ralentissement des ions dans une cible diatomique. *Radiat Eff.* 1978 Jan;38(3–4):133–9. <http://www.tandfonline.com/doi/abs/10.1080/00337577808233221>
75. Ziegler JF, Ziegler MD, Biersack JP. SRIM – The stopping and range of ions in matter (2010). *Nucl Instruments Methods Phys Res Sect B Beam Interact with Mater Atoms.* 2010 Jun;268(11–12):1818–23. <http://dx.doi.org/10.1016/j.nimb.2010.02.091>
76. Ishikawa N, Sonoda T, Sawabe T, Sugai H, Sataka M. Electronic stopping power dependence of ion-track size in UO₂ irradiated with heavy ions in the energy range of ~1 MeV/u. *Nucl Instruments Methods Phys Res Sect B Beam Interact with Mater Atoms.* 2013 Nov 1 [cited 2019 Sep 7];314:180–4. <https://www.sciencedirect.com/science/article/pii/S0168583X13006022>
77. Seitz F, Koehler J. *Solid State Physics*. 1956. 2: 305.
78. Toulemonde M, Paumier E, Dufour C. Thermal spike model in the electronic stopping power regime. *Radiat Eff*

- Defects Solids. 1993 Mar 19;126(1–4):201–6.
<https://www.tandfonline.com/doi/full/10.1080/10420159308219709>
79. Wiss T, Matzke H, Trautmann C, Toulemonde M, Klaumünzer S. Radiation damage in UO_2 by swift heavy ions. Nucl Instruments Methods Phys Res Sect B Beam Interact with Mater Atoms. 1997 Feb;122(3):583–8. <https://linkinghub.elsevier.com/retrieve/pii/S0168583X96007549>
 80. Ronchi C. The nature of surface fission tracks in UO_2 . J Appl Phys. 1973;44(8):3575–85. <https://doi.org/10.1063/1.1662802>
 81. Matzke H. Radiation enhanced diffusion in UO_2 and $(\text{U}, \text{Pu})\text{O}_2$. Radiat Eff. 1983 Jan;75(1–4):317–25. <http://www.tandfonline.com/doi/abs/10.1080/00337578308224715>
 82. Blank H, Matzke H. The effect of fission spikes on fission gas re-solution. Radiat Eff. 1973;17(1–2):57–64. <https://doi.org/10.1080/00337577308232598>
 83. Thomé L, Debelle A, Garrido F, Trocellier P, Serruys Y, Velisa G, et al. Combined effects of nuclear and electronic energy losses in solids irradiated with a dual-ion beam. Appl Phys Lett. 2013 Apr 8;102(14):141906. <http://aip.scitation.org/doi/10.1063/1.4801518>
 84. Gutierrez G, Gosset D, Bricout M, Onofri C, Debelle A. Effect of coupled electronic and nuclear energy deposition on strain and stress levels in UO_2 . J Nucl Mater. 2019;519:52–6. <https://doi.org/10.1016/j.jnucmat.2019.03.034>
 85. Dayman K, Biegalski S, Haas D. Determination of short-lived fission product yields with gamma spectrometry. J Radioanal Nucl Chem. 2015 Jul 15;305(1):213–23. <http://link.springer.com/10.1007/s10967-015-3993-9>
 86. Sickafus KE, Kotomin EA, Uberuaga BP. Radiation effects in solids. Vol. 235. Springer Science & Business Media; 2007. <https://www.springer.com/gp/book/9781402052941>
 87. ÉLECTRICITÉ DE FRANCE, L'uranium : le combustible nucléaire, EDF. <https://www.edf.fr/groupe-edf/espaces-dedies/l-energie-de-a-a-z/tout-sur-l-energie/produire-de-l-electricite/l-uranium-le-combustible-nucleaire>
 88. Wiss T, Hiernaut J-P, Roudil D, Colle J-Y, Maugeri E, Talip Z, et al. Evolution of spent nuclear fuel in dry storage conditions for millennia and beyond. J Nucl Mater. 2014 Aug;451(1–3):198–206. <https://linkinghub.elsevier.com/retrieve/pii/S0022311514001822>
 89. Roudil D, Jégou C, Deschanel X, Peugeot S, Raepsaet C, Gallien J-P, et al. Effects of alpha self-irradiation on actinide-doped spent fuel surrogate matrix. MRS Proc. 2006 Jan 21;932:66.1. http://journals.cambridge.org/abstract_S1946427400638617
 90. Weber WJ. Ingrowth of lattice defects in alpha irradiated UO_2 single crystals. J Nucl Mater. 1981 May;98(1–2):206–15. <https://linkinghub.elsevier.com/retrieve/pii/0022311581904001>
 91. Olander DR, Van Uffelen P. On the role of grain boundary diffusion in fission gas release. J Nucl Mater. 2001;288(2–3):137–47. [https://doi.org/10.1016/S0022-3115\(00\)00725-X](https://doi.org/10.1016/S0022-3115(00)00725-X)
 92. Matzke HJ. Gas release mechanisms in UO_2 — a critical review. Radiat Eff. 1980;53(3–4):219–42. <https://doi.org/10.1080/00337578008207118>
 93. Cappia F, Pizzocri D, Marchetti M, Schubert A, Van Uffelen P, Luzzi L, et al. Microhardness and Young's modulus of high burn-up UO_2 fuel. J Nucl Mater. 2016;479:447–54. <https://doi.org/10.1016/j.jnucmat.2016.07.015>
 94. Spino J, Cobos-Sabate J, Rousseau F. Room-temperature microindentation behaviour of LWR-fuels, part 1: fuel microhardness. J Nucl Mater. 2003 Nov;322(2–3):204–16. <https://linkinghub.elsevier.com/retrieve/pii/S0022311503003283>
 95. Ronchi C, Sheindlin M, Staicu D, Kinoshita M. Effect of burn-up on the thermal conductivity of uranium dioxide up to 100.000 MWdt⁻¹. J Nucl Mater. 2004;327(1):58–76. <https://doi.org/10.1016/j.jnucmat.2004.01.018>
 96. Staicu D, Wiss T, Rondinella VV, Hiernaut JP, Konings RJM, Ronchi C. Impact of auto-irradiation on the thermophysical properties of oxide nuclear reactor fuels. J Nucl Mater. 2010 Feb;397(1–3):8–18. <https://linkinghub.elsevier.com/retrieve/pii/S0022311509009209>
 97. Klein D, Baer W, Smith GG. Spatial Distribution of U^{238} Resonance Neutron Capture in Uranium Metal Rods. Nucl Sci Eng. 1958 Jun 12;3(6):698–706. <https://www.tandfonline.com/doi/full/10.13182/NSE58-A25505>

98. Noirot J, Desgranges L, Lamontagne J. Detailed characterisations of high burn-up structures in oxide fuels. *J Nucl Mater.* 2008;372(2–3):318–39. <https://doi.org/10.1016/j.jnucmat.2007.04.037>
99. Noirot J, Pontillon Y, Lamontagne J, Zacharie-Aubrun I, Hanifi K, Bienvenu P, et al. High Burn-up Structure in Nuclear Fuel: Impact on Fuel Behavior. *EPJ Web Conf.* 2016;115. https://www.epj-conferences.org/articles/epjconf/abs/2016/10/epjconf_MINOS2015_04005/epjconf_MINOS2015_04005.html
100. KINOSHITA, M. High burnup RIM project : (III) Properties of rim-structured fuel. *Proc 2004 Int Mtg LWR Fuel Performance, Orland, Florida, USA, Sep 19-22, 2004.* 2004 [cited 2019 Sep 3]; <http://ci.nii.ac.jp/naid/10025998267/en/>
101. Sonoda T, Kinoshita M, Ray ILF, Wiss T, Thiele H, Pellottiero D, et al. Transmission electron microscopy observation on irradiation-induced microstructural evolution in high burn-up UO_2 disk fuel. *Nucl Instruments Methods Phys Res Sect B Beam Interact with Mater Atoms.* 2002;191(1–4):622–8. [https://doi.org/10.1016/S0168-583X\(02\)00622-5](https://doi.org/10.1016/S0168-583X(02)00622-5)
102. Hiernaut JP, Wiss T, Colle JY, Thiele H, Walker CT, Goll W, et al. Fission product release and microstructure changes during laboratory annealing of a very high burn-up fuel specimen. *J Nucl Mater.* 2008;377(2):313–24. <https://doi.org/10.1016/j.jnucmat.2008.03.006>
103. Gerczak TJ, Parish CM, Edmondson PD, Baldwin CA, Terrani KA. Restructuring in high burnup UO_2 studied using modern electron microscopy. *J Nucl Mater.* 2018;509:245–59. <https://doi.org/10.1016/j.jnucmat.2018.05.077>
104. Miao Y, Yao T, Lian J, Zhu S, Bhattacharya S, Oaks A, et al. Nano-crystallization induced by high-energy heavy ion irradiation in UO_2 . *Scr Mater.* 2018;155:169–74. <https://doi.org/10.1016/j.scriptamat.2018.04.006>
105. Manzel R, Walker C. EPMA and SEM of fuel samples from PWR rods with an average burn-up of around 100 MWd/kgHM. *J Nucl Mater.* 2002 Mar;301(2–3):170–82. <https://linkinghub.elsevier.com/retrieve/pii/S002231150100753X>
106. Spino J, Santa Cruz H, Jovani-Abril R, Birtcher R, Ferrero C. Bulk-nanocrystalline oxide nuclear fuels - An innovative material option for increasing fission gas retention, plasticity and radiation-tolerance. *J Nucl Mater.* 2012; 402(1-3):27-44. <https://doi.org/10.1016/j.jnucmat.2011.11.056>
107. Rest J, Cooper MWD, Spino J, Turnbull JA, Van Uffelen P, Walker CT. Fission gas release from UO_2 nuclear fuel: A review. *J Nucl Mater.* 2018;513:310–45. <https://doi.org/10.1016/j.jnucmat.2018.08.019>
108. T. Walker C, Bremier S, Portier S, Hasnaoui R, Goll W. SIMS analysis of an UO_2 fuel irradiated at low temperature to 65MWd/kgHM. *J Nucl Mater.* 2009 Sep 1;393:212–23. <https://doi.org/10.1016/j.jnucmat.2009.06.017>
109. Jegou C, Gennisson M, Peugeot S, Desgranges L, Guimbretière G, Magnin M, et al. Raman micro-spectroscopy of UO_2 and MOX spent nuclear fuel characterization and oxidation resistance of the high burn-up structure. *J Nucl Mater.* 2015;458:343–9. <http://dx.doi.org/10.1016/j.jnucmat.2014.12.072>
110. Hayashi K, Kikuchi H, Fukuda K. Radiation damage of UO_2 by high-energy heavy ions. *J Nucl Mater.* 1997 Sep;248:191–5. <https://linkinghub.elsevier.com/retrieve/pii/S0022311597001190>
111. Garrido F, Choffel C, Thomé L, Dran J-C, Nowicki L, Turos A, et al. A channeling investigation of the structural modifications in uranium dioxide submitted to swift-ion irradiation and aqueous corrosion. *Nucl Instruments Methods Phys Res Sect B Beam Interact with Mater Atoms.* 1998 Mar;136–138(97):465–70. <https://linkinghub.elsevier.com/retrieve/pii/S0168583X97007179>
112. Ruello P, Desgranges L, Baldinozzi G, Calvarin G, Hansen T, Petot-Ervas G, et al. Heat capacity anomaly in UO_2 in the vicinity of 1300K: an improved description based on high resolution X-ray and neutron powder diffraction studies. *J Phys Chem Solids.* 2005 May;66(5):823–31. <https://linkinghub.elsevier.com/retrieve/pii/S0022369704003944>
113. Desgranges L, Baldinozzi G, Ruello P, Petot C. Is UO_2 irradiation resistance due to its unusual high temperature behaviour? *J Nucl Mater.* 2012 Jan;420(1–3):334–7. <https://linkinghub.elsevier.com/retrieve/pii/S0022311511008889>
114. Desgranges L, Baldinozzi G, Ruello P, Petot C. How polarons can enhance UO_2 irradiation resistance? *Nucl Instruments Methods Phys Res Sect B Beam Interact with Mater Atoms.* 2012 Apr;277:109–11. <http://dx.doi.org/10.1016/j.nimb.2011.12.046>

115. Baldinozzi G, Desgranges L, Petot C. A statistical approach of the thermodynamic properties of UO_2 at high temperature. *Nucl Instruments Methods Phys Res Sect B Beam Interact with Mater Atoms*. 2014 May;327(1):68–73. <http://dx.doi.org/10.1016/j.nimb.2013.10.096>
116. Usov IO, Dickerson RM, Dickerson PO, Byler DD, McClellan KJ. Uranium dioxide films with xenon filled bubbles for fission gas behavior studies. *J Nucl Mater*. 2014;452(1–3):173–7. <http://dx.doi.org/10.1016/j.jnucmat.2014.04.050>
117. Walter O, Popa K, Blanco OD. Hydrothermal decomposition of actinide(IV) oxalates: A new aqueous route towards reactive actinide oxide nanocrystals. *Open Chem*. 2016; 14(1), <https://doi.org/10.1515/chem-2016-0018>
118. Popa K, Walter O, Blanco OD, Guiot A, Bouëxière D, Colle JY, et al. A low-temperature synthesis method for AnO_2 nanocrystals (An = Th, U, Np, and Pu) and associate solid solutions. *CrystEngComm*. 2018; 20:4616–4622. <https://doi.org/10.1039/C8CE00446C>
119. Tyrpekl V, Holzhäuser M, Hein H, Vigier JF, Somers J, Svora P. Synthesis of dense yttrium-stabilised hafnia pellets for nuclear applications by spark plasma sintering. *J Nucl Mater*. 2014; 454(1–3):398–404. <https://doi.org/10.1016/j.jnucmat.2014.08.029>
120. Yao T, Mo K, Yun D, Nanda S, Yacout AM, Lian J. Grain growth and pore coarsening in dense nano-crystalline UO_{2+x} fuel pellets. *J Am Ceram Soc*. 2017; 100(6): 2651–2658. <https://doi.org/10.1111/jace.14780>
121. Lucuta PG, Verrall RA, Matzke H, Palmer BJ. Microstructural features of SIMFUEL - Simulated high-burnup UO_2 -based nuclear fuel. *J Nucl Mater*. 1991;178(1):48–60. [https://doi.org/10.1016/0022-3115\(91\)90455-G](https://doi.org/10.1016/0022-3115(91)90455-G)
122. Geiger E, Bès R, Martin P, Pontillon Y, Ducros G, Solari PL. Insights on fission products behaviour in nuclear severe accident conditions by X-ray absorption spectroscopy. *J Nucl Mater*. 2016;471:25–33. <https://doi.org/10.1016/j.jnucmat.2015.12.032>
123. Lucuta PG, Matzke H, Verrall RA, Tasman HA. Thermal conductivity of SIMFUEL. *J Nucl Mater*. 1992;188(C):198–204. [https://doi.org/10.1016/0022-3115\(92\)90471-V](https://doi.org/10.1016/0022-3115(92)90471-V)
124. Matzke H, Lucuta PG, Verrall RA, Henderson J. Specific heat of UO_2 -based SIMFUEL. *J Nucl Mater*. 1997;247:121–6. [https://doi.org/10.1016/S0022-3115\(97\)00069-X](https://doi.org/10.1016/S0022-3115(97)00069-X)
125. Verrall RA, Lucuta PG. Specific heat measurements of UO_2 and SIMFUEL. *J Nucl Mater*. 1996;228(2):251–3. [https://doi.org/10.1016/S0022-3115\(95\)00238-3](https://doi.org/10.1016/S0022-3115(95)00238-3)
126. Lucuta PG, Verrall RA, Hastings IJ, Matzke H. Thermal conductivity and gas release from SIMFUEL. International Atomic Energy Agency (IAEA); 1993. http://inis.iaea.org/search/search.aspx?orig_q=RN:24050857
127. Sengupta AKK, Bhagat RKK, Jarvis T, Banerjee J, Kutty TRGRG, Ravi K, et al. Some important properties of simulated UO_2 fuel. 1999 [cited 2019 Sep 3]. https://inis.iaea.org/search/search.aspx?orig_q=RN:31003194
128. Pujol MC, Idiri M, Havela L, Heathman S, Spino J. Bulk and Young's modulus of doped UO_2 by synchrotron diffraction under high pressure and Knoop indentation. *J Nucl Mater*. 2004;324(2–3):189–97. <https://doi.org/10.1016/j.jnucmat.2003.10.002>
129. Quiñones J, Garcia-Serrano J, Serrano JA, Díaz-Arocas P, Almazan JLR. SIMFUEL and UO_2 Solubility and Leaching Behavior Under Anoxic Conditions. *MRS Proc*. 1997 Feb 10;506:247. https://www.cambridge.org/core/product/identifier/S1946427400248732/type/journal_article
130. Ollila K. SIMFUEL dissolution studies in granitic groundwater. *J Nucl Mater*. 1992;190(C):70–7. [https://doi.org/10.1016/0022-3115\(92\)90077-X](https://doi.org/10.1016/0022-3115(92)90077-X)
131. Sundin S, Dahlgren B, Roth O, Jonsson M. H_2O_2 and radiation induced dissolution of UO_2 and SIMFUEL in HCO_3^- Deficient aqueous solution. *J Nucl Mater*. 2013;443(1–3):291–7. <http://dx.doi.org/10.1016/j.jnucmat.2013.07.025>
132. Serrano JA, Quinones J, Cobos J, Diaz Arocas P, Rondinella V V, Glatz J-P, et al. Leaching study of the behaviour of spent fuel and simfuel under simulated granitic repository conditions. *Proc Int Conf Radioact Waste Manag Environ Remediat ICEM*. 2001 Jan 1;2:1081–5.
133. Oversby VMM. Uranium dioxide, SIMFUEL, and spent fuel dissolution rates - a review of published data. Sweden; 1999. http://inis.iaea.org/search/search.aspx?orig_q=RN:31008584

134. Shoesmith DW. Used fuel and uranium dioxide dissolution studies—A review. Rep NWMO TR-2007-03, Nucl Waste Manag Organ Toronto,. 2007;(July).
135. Eriksen TE, Shoesmith DW, Jonsson M. Radiation induced dissolution of UO₂ based nuclear fuel - A critical review of predictive modelling approaches. J Nucl Mater. 2012;420(1–3):409–23. <http://dx.doi.org/10.1016/j.jnucmat.2011.10.027>
136. Di Lemma FG, Colle JY, Rasmussen G, Konings RJM. Fission product partitioning in aerosol release from simulated spent nuclear fuel. J Nucl Mater. 2015;465:127–34. <http://dx.doi.org/10.1016/j.jnucmat.2015.06.002>
137. Wangle T, Tyrpekl V, Cologna M, Somers J. Simulated UO₂ fuel containing CsI by spark plasma sintering. J Nucl Mater. 2015; <https://doi.org/10.1016/j.jnucmat.2015.07.030>
138. Le Gall C. Contribution to the study of fission products release from nuclear fuels in severe accident conditions: effect of the pO₂ on Cs, Mo and Ba speciation. 2018. PhD Thesis
139. Santa Cruz H, Spino J, Grathwohl G. Nanocrystalline ZrO₂ ceramics with idealized macropores. J Eur Ceram Soc. 2008;28(9):1783–91. <https://doi.org/10.1016/j.jeurceramsoc.2007.12.028>
140. Baranov VG, Lunev A V., Reutov VF, Tenishev A V., Isaenkova MG, Khlunov A V. An attempt to reproduce high burn-up structure by ion irradiation of SIMFUEL. J Nucl Mater. 2014;452(1–3):147–57. <http://dx.doi.org/10.1016/j.jnucmat.2014.04.002>
141. Ollila K, Myllykylä E, Tanhua-Tyrkkö M, Lavonen T. Dissolution rate of alpha-doped UO₂ in natural groundwater. J Nucl Mater. 2013;442(1–3):320–5. <http://dx.doi.org/10.1016/j.jnucmat.2013.09.019>
142. Fernández A, Haas D, Konings RJM, Somers J. Transmutation of Actinides. J Am Ceram Soc. 2004 Dec 20;85(3):694–6. <http://doi.wiley.com/10.1111/j.1151-2916.2002.tb00152.x>
143. Rondinella V V, Wiss T, Hiernaut J, Cobos J. Studies on Spent Fuel Alterations During Storage and Radiolysis Effects on Corrosion Behaviour Using Alpha-Doped UO₂. In: 9th ASME International Conference on Radioactive Waste Management and Environmental Remediation: Volumes 1, 2, and 3. ASME; 2003. p. 265–72. <https://doi.org/10.1115/ICEM2003-4593>
144. Rondinella V V, Wiss T, Hiernaut J-P, Staicu D. Dose Rate Effects on the Accumulation of Radiation Damage. In: 11th International Conference on Environmental Remediation and Radioactive Waste Management, Parts A and B. ASME; 2007. p. 1071–6. <https://doi.org/10.1115/ICEM2007-7322>
145. Jonnet J, Van Uffelen P, Wiss T, Staicu D, Rémy B, Rest J. Growth mechanisms of interstitial loops in α -doped UO₂ samples. Nucl Instruments Methods Phys Res Sect B Beam Interact with Mater Atoms. 2008;266(12–13):3008–12. <https://doi.org/10.1016/j.nimb.2008.03.154>
146. Roudil D, Barthe MF, Jégou C, Gavazzi A, Vella F. Investigation of defects in actinide-doped UO₂ by positron annihilation spectroscopy. J Nucl Mater. 2012; 420(1-3): 63-68. <https://doi.org/10.1016/j.jnucmat.2011.08.011>
147. Ronchi C, Hiernaut JP. Helium diffusion in uranium and plutonium oxides. J Nucl Mater. 2004; 325(1): 1-12. <https://doi.org/10.1016/j.jnucmat.2003.10.006>
148. Nakajima K, Serizawa H, Shirasu N, Haga Y, Arai Y. The solubility and diffusion coefficient of helium in uranium dioxide. J Nucl Mater. 2011;419(1–3):272–80. <http://dx.doi.org/10.1016/j.jnucmat.2011.08.045>
149. Maugeri E, Wiss T, Hiernaut JP, Desai K, Thiriet C, Rondinella V V., et al. Helium solubility and behaviour in uranium dioxide. J Nucl Mater. 2009; 385(2): 461-466. <https://doi.org/10.1016/j.jnucmat.2008.12.033>
150. Talip Z, Wiss T, Di Marcello V, Janssen A, Colle JY, Van Uffelen P, et al. Thermal diffusion of helium in ²³⁸Pu-doped UO₂. J Nucl Mater. 2014; 445(1-3): 117-127. <https://doi.org/10.1016/j.jnucmat.2013.10.066>
151. Ferry C, Poinssot C, Cappelaere C, Desgranges L, Jegou C, Miserque F, et al. Specific outcomes of the research on the spent fuel long-term evolution in interim dry storage and deep geological disposal. J Nucl Mater. 2006; 352(1-3):246-253. <https://doi.org/10.1016/j.jnucmat.2006.02.061>
152. Rondinella VV, Matzke H, Cobos CJ, Wiss T. Leaching behaviour of UO₂ containing α -emitting actinides. Radiochim Acta. 2000 Jan 1;88(9–11). <http://www.degruyter.com/view/j/ract.2000.88.issue-9-11/ract.2000.88.9-11.527/ract.2000.88.9-11.527.xml>

153. Rondinella V V, Matzke H, Cobos J, Wiss T. α -Radiolysis and α -Radiation Damage Effects on UO_2 Dissolution Under Spent Fuel Storage Conditions. MRS Proc. 1999 Feb 10;556:447. https://www.cambridge.org/core/product/identifier/S1946427400177942/type/journal_article
154. Rondinella V V., Cobos J, Wiss T. Leaching behaviour of low - Activity alpha-doped UO_2 . Mater Res Soc Symp Proc. 2004;824:167–73. <https://doi.org/10.1557/PROC-824-CC9.8>
155. Muzeau B, Jégou C, Delaunay F, Broudic V, Brevet A, Catalette H, et al. Radiolytic oxidation of UO_2 pellets doped with alpha-emitters (^{238}Pu). J Alloys Compd. 2009; 467(1-2):578-589. <https://doi.org/10.1016/j.jallcom.2007.12.054>
156. Mohun R, Desgranges L, Canizarès A, Raimboux N, Duval F, Omnee R, et al. Investigating the role of irradiation defects during UO_2 oxidative dissolution. J Nucl Mater. 2018 Oct;509:305–12. <https://linkinghub.elsevier.com/retrieve/pii/S0022311518304124>
157. Weber WJ. Thermal recovery of lattice defects in alpha-irradiated UO_2 crystals. J Nucl Mater. 1983; 114(2-3):213-221. [https://doi.org/10.1016/0022-3115\(83\)90259-3](https://doi.org/10.1016/0022-3115(83)90259-3)
158. Weber WJ. Alpha-irradiation damage in CeO_2 , UO_2 and PuO_2 . Radiat Eff. 1984 Jan 13;83(1–2):145–56. <http://www.tandfonline.com/doi/abs/10.1080/00337578408215798>
159. Palancher H, Kachnaoui R, Martin G, Richard A, Richaud JC, Onofri C, et al. Strain relaxation in He implanted UO_2 polycrystals under thermal treatment: An in situ XRD study. J Nucl Mater. 2016; 476: 63-76. <https://doi.org/10.1016/j.jnucmat.2016.04.023>
160. Guimbretière G, Desgranges L, Canizarès A, Caraballo R, Duval F, Raimboux N, et al. In situ Raman monitoring of He^{2+} irradiation induced damage in a UO_2 ceramic. Appl Phys Lett. 2013;103(4). <https://doi.org/10.1063/1.4816285>
161. Guimbretière G, Desgranges L, Canizarès A, Carlot G, Caraballo R, Jégou C, et al. Determination of in-depth damaged profile by Raman line scan in a pre-cut He^{2+} irradiated UO_2 . Appl Phys Lett. 2012 Jun 18;100(25):251914. <http://aip.scitation.org/doi/10.1063/1.4729588>
162. Desgranges L, Guimbretière G, Simon P, Jegou C, Caraballo R. A possible new mechanism for defect formation in irradiated UO_2 . Nucl Instruments Methods Phys Res Sect B Beam Interact with Mater Atoms. 2013; 315: 169-172. <https://doi.org/10.1016/j.nimb.2013.05.081>
163. Mohun R, Desgranges L, Léchelle J, Simon P, Guimbretière G, Canizarès A, et al. Charged defects during alpha-irradiation of actinide oxides as revealed by Raman and luminescence spectroscopy. Nucl Instruments Methods Phys Res Sect B Beam Interact with Mater Atoms. 2016 May;374:67–70. <https://linkinghub.elsevier.com/retrieve/pii/S0168583X15007284>
164. Desgranges L, Guimbretière G, Simon P, Duval F, Canizares A, Omnee R, et al. Annealing of the defects observed by Raman spectroscopy in UO_2 irradiated by 25 MeV He^{2+} ions. Nucl Instruments Methods Phys Res Sect B Beam Interact with Mater Atoms. 2014 May;327(1):74–7. <https://linkinghub.elsevier.com/retrieve/pii/S0168583X14001463>
165. Desgranges L, Simon P, Martin P, Guimbretiere G, Baldinozzi G. What Can We Learn From Raman Spectroscopy on Irradiation-Induced Defects in UO_2 ? JOM. 2014; 66, 2546–2552. <https://doi.org/10.1007/s11837-014-1174-x>
166. Pakarinen J, Khafizov M, He L, Wetteland C, Gan J, Nelson AT, et al. Microstructure changes and thermal conductivity reduction in UO_2 following 3.9 MeV He^{2+} ion irradiation. J Nucl Mater. 2014;454(1–3):283–9. <http://dx.doi.org/10.1016/j.jnucmat.2014.07.053>
167. Martin G, Carlot G, Desgardin P, Vayer M, Ramboz C, Sauvage T, et al. Surface Blistering and Flaking of Sintered Uranium Dioxide Samples under High Dose Gas Implantation and Annealing. Defect Diffus Forum. 2012 Apr;323–325:185–90. www.scientific.net/DDF.323-325.185
168. Martin G, Garcia P, Sabathier C, Carlot G, Sauvage T, Desgardin P, et al. Helium release in uranium dioxide in relation to grain boundaries and free surfaces. Nucl Instruments Methods Phys Res Sect B Beam Interact with Mater Atoms. 2010; 268(11-12): 2133-2137. <https://doi.org/10.1016/j.nimb.2010.02.064>
169. Martin G, Desgardin P, Garcia P, Sauvage T, Carlot G, Barthe M-F. Helium Migration Mechanisms in Polycrystalline Uranium Dioxide. MRS Proc. 2006 Oct 19;985:0985-NN05-02.

170. Guilbert S, Sauvage T, Garcia P, Carlot G, Barthe MF, Desgardin P, et al. He migration in implanted UO_2 sintered disks. *J Nucl Mater.* 2004; 327(2-3): 88-69. <https://doi.org/10.1016/j.jnucmat.2004.01.024>
171. Guilbert S, Sauvage T, Erramli H, Barthe MF, Desgardin P, Blondiaux G, et al. Helium behavior in UO_2 polycrystalline disks. *J Nucl Mater.* 2003; 321(2-3): 121-128. [https://doi.org/10.1016/S0022-3115\(03\)00212-5](https://doi.org/10.1016/S0022-3115(03)00212-5)
172. Garrido F, Nowicki L, Sattonnay G, Sauvage T, Thomé L. Lattice location of helium in uranium dioxide single crystals. *Nucl Instruments Methods Phys Res Sect B Beam Interact with Mater Atoms.* 2004;219–220(1–4):196–9. <https://doi.org/10.1016/j.nimb.2004.01.053>
173. Sauvage T, Desgardin P, Martin G, Garcia P, Carlot G, Labrim H, et al. Microstructure effects on He diffusion in sintered UO_2 by μNRA . In: *Nuclear Instruments and Methods in Physics Research, Section B: Beam Interactions with Materials and Atoms.* 2005. 240(1-2):271-276. <https://doi.org/10.1016/j.nimb.2005.06.128>
174. Martin G, Sabathier C, Carlot G, Desgardin P, Raepsaet C, Sauvage T, et al. Irradiation damage effects on helium migration in sintered uranium dioxide. In: *Nuclear Instruments and Methods in Physics Research, Section B: Beam Interactions with Materials and Atoms.* 2012. 273: 122-126. <https://doi.org/10.1016/j.nimb.2011.07.055>
175. Martin G, Desgardin P, Sauvage T, Garcia P, Carlot G, Khodja H, et al. A quantitative μNRA study of helium intergranular and volume diffusion in sintered UO_2 . *Nucl Instruments Methods Phys Res Sect B Beam Interact with Mater Atoms.* 2006; 249(1-2); 509-512. <https://doi.org/10.1016/j.nimb.2006.03.042>
176. He LF, Valderrama B, Hassan AR, Yu J, Gupta M, Pakarinen J, et al. Bubble formation and Kr distribution in Kr-irradiated UO_2 . *J Nucl Mater.* 2015;456:125–32. <https://doi.org/10.1016/j.jnucmat.2014.09.026>
177. Onofri C, Sabathier C, Palancher H, Carlot G, Miro S, Serruys Y, et al. Evolution of extended defects in polycrystalline UO_2 under heavy ion irradiation: Combined TEM, XRD and Raman study. *Nucl Instruments Methods Phys Res Sect B Beam Interact with Mater Atoms.* 2016; 374; 51-57. <https://doi.org/10.1016/j.nimb.2015.08.091>
178. Djourelou N, Marchand B, Marinov H, Moncoffre N, Pipon Y, Bérerd N, et al. Study of temperature and radiation induced microstructural changes in Xe-implanted UO_2 by TEM, STEM, SIMS and positron spectroscopy. *J Nucl Mater.* 2013;443(1–3):562–9. <http://dx.doi.org/10.1016/j.jnucmat.2013.07.066>
179. Djourelou N, Marchand B, Marinov H, Moncoffre N, Pipon Y, Nédélec P, et al. Variable energy positron beam study of Xe-implanted uranium oxide. *J Nucl Mater.* 2013;432(1–3):287–93. <http://dx.doi.org/10.1016/j.jnucmat.2012.07.035>
180. Marchand B, Moncoffre N, Pipon Y, Garnier C, Bérerd N, Delafoy C, et al. Xenon migration in UO_2 : A SIMS study. *Prog Nucl Energy.* 2012;57:145–9. <http://dx.doi.org/10.1016/j.pnucene.2011.10.009>
181. Michel A, Sabathier C, Carlot G, Kaïtasov O, Bouffard S, Garcia P, et al. An in situ TEM study of the evolution of Xe bubble populations in UO_2 . In: *Nuclear Instruments and Methods in Physics Research, Section B: Beam Interactions with Materials and Atoms.* 2012. 272; 218-221. <https://doi.org/10.1016/j.nimb.2011.01.069>
182. Marchand B, Moncoffre N, Pipon Y, Bérerd N, Garnier C, Raimbault L, et al. Xenon migration in UO_2 under irradiation studied by SIMS profilometry. *J Nucl Mater.* 2013;440(1–3):562–7. <http://dx.doi.org/10.1016/j.jnucmat.2013.04.005>
183. Onofri C, Legros M, Léchelle J, Palancher H, Baumier C, Bachelet C, et al. Full characterization of dislocations in ion-irradiated polycrystalline UO_2 . *J Nucl Mater.* 2017; 494: 252-259. <https://doi.org/10.1016/j.jnucmat.2017.07.043>
184. Onofri C, Sabathier C, Baumier C, Bachelet C, Palancher H, Warot-Fonrose B, et al. Influence of exogenous xenon atoms on the evolution kinetics of extended defects in polycrystalline UO_2 using in situ TEM. *J Nucl Mater.* 2018;512:297–306. <https://doi.org/10.1016/j.jnucmat.2018.10.025>
185. Onofri C, Sabathier C, Baumier C, Bachelet C, Palancher H, Legros M. Evolution of extended defects in polycrystalline Au-irradiated UO_2 using in situ TEM: Temperature and fluence effects. *J Nucl Mater.* 2016; 482; 105-113. <https://doi.org/10.1016/j.jnucmat.2016.10.011>
186. Garrido F, Vincent L, Nowicki L, Sattonnay G, Thomé L. Radiation stability of fluorite-type nuclear oxides. *Nucl Instruments Methods Phys Res Sect B Beam Interact with Mater Atoms.* 2008;266(12–13):2842–7. <https://doi.org/10.1016/j.nimb.2008.03.128>

187. Sattonnay G, Vincent L, Garrido F, Thomé L. Xenon versus helium behavior in UO_2 single crystals: A TEM investigation. *J Nucl Mater.* 2006;355(1–3):131–5. <https://doi.org/10.1016/j.jnucmat.2006.04.013>
188. Sabathier C, Martin G, Michel A, Carlot G, Maillard S, Bachelet C, et al. In-situ TEM observation of nano-void formation in UO_2 under irradiation. *Nucl Instruments Methods Phys Res Sect B Beam Interact with Mater Atoms.* 2014;326:247–50. <http://dx.doi.org/10.1016/j.nimb.2013.10.055>
189. Gutierrez G, Onofri C, Miro S, Bricout M, Leprêtre F. Effect of ballistic damage in UO_2 samples under ion beam irradiations studied by in situ Raman spectroscopy. *Nucl Instruments Methods Phys Res Sect B Beam Interact with Mater Atoms.* 2018;434(August):45–50. <https://doi.org/10.1016/j.nimb.2018.08.010>
190. Rietveld HM. A profile refinement method for nuclear and magnetic structures. *J Appl Crystallogr.* 1969 Jun 2;2(2):65–71. <http://scripts.iucr.org/cgi-bin/paper?S0021889869006558>
191. Williamson G., Hall W. X-ray line broadening from fcc aluminium and wolfram. *Acta Metall.* 1953 Jan;1(1):22–31. <https://linkinghub.elsevier.com/retrieve/pii/0001616053900066>
192. Petříček V, Dušek M, Palatinus L. Crystallographic Computing System JANA2006: General features. *Zeitschrift für Krist - Cryst Mater.* 2014 Jan 1;229(5):345. <https://www.degruyter.com/view/j/zkri.2014.229.issue-5/zkri-2014-1737/zkri-2014-1737.xml>
193. TESCAN. TESCAN-VEGA working principles, <https://www.tescan.com/product/sem-for-materials-science-tescan-vega/>
194. E112-12. Standard Test Methods for Determining Average Grain Size. *ASTM Int.* 2012;E112-12:1–27. <https://www.astm.org/Standards/E112.htm>
195. Tyrpekl V, Berkman C, Holzhäuser M, Köpp F, Cologna M, Wangle T, et al. Implementation of a spark plasma sintering facility in a hermetic glovebox for compaction of toxic, radiotoxic, and air sensitive materials. *Rev Sci Instrum.* 2015; 86(2): 023904. <https://doi.org/10.1063/1.4913529>
196. Naji M, Colle JY, Beneš O, Sierig M, Rautio J, Lajarge P, et al. An original approach for Raman spectroscopy analysis of radioactive materials and its application to americium-containing samples. *J Raman Spectrosc.* 2015; 49(9): 750-756. <https://doi.org/10.1002/jrs.4716>
197. Parker WJ, Jenkins RJ, Butler CP, Abbott GL. Flash Method of Determining Thermal Diffusivity, Heat Capacity, and Thermal Conductivity. *J Appl Phys.* 1961 Sep;32(9):1679–84. <http://aip.scitation.org/doi/10.1063/1.1728417>
198. Sheindlin M, Halton D, Musella M, Ronchi C. Advances in the use of laser-flash techniques for thermal diffusivity measurement. *Rev Sci Instrum.* 1998 Mar;69(3):1426–36. <http://aip.scitation.org/doi/10.1063/1.1148776>
199. Staicu D, Barker M. Thermal conductivity of heterogeneous LWR MOX fuels. *J Nucl Mater.* 2013 Nov;442(1–3):46–52. <http://dx.doi.org/10.1016/j.jnucmat.2013.08.024>
200. Vlahovic L, Staicu D, Küst A, Konings RJM. Thermal diffusivity of UO_2 up to the melting point. *J Nucl Mater.* 2018; 499: 504-511. <https://doi.org/10.1016/j.jnucmat.2017.11.050>
201. Drowart J, Chatillon C, Hastie J, Bonnell D. High-temperature mass spectrometry: Instrumental techniques, ionization cross-sections, pressure measurements, and thermodynamic data (IUPAC technical report). *Pure Appl Chem.* 2005;77(4):683–737. <https://doi.org/10.1351/pac200577040683>
202. Hiernaut JP, Colle JY, Pflieger-Cuvellier R, Jonnet J, Somers J, Ronchi C. A Knudsen cell-mass spectrometer facility to investigate oxidation and vaporisation processes in nuclear fuel. *J Nucl Mater.* 2005;344(1–3):246–53. <https://doi.org/10.1016/j.jnucmat.2005.04.050>
203. Colle J-Y, Freis D, Beneš O, Konings RJM. Knudsen Effusion Mass Spectrometry of Nuclear Materials: Applications and Developments. *ECS Trans.* 2013;46(1):23–38. <http://ecst.ecsdl.org/content/46/1/23.short>
204. Colle JY, Maugeri EA, Thiriet C, Talip Z, Capone F, Hiernaut JP, et al. A mass spectrometry method for quantitative and kinetic analysis of gas release from nuclear materials and its application to helium desorption from UO_2 and fission gas release from irradiated fuel. *J Nucl Sci Technol.* 2014; 51(5):700-711. <https://doi.org/10.1080/00223131.2014.889583>
205. Javorský P, Wastin F, Colineau E, Rebizant J, Boulet P, Stewart G. Low-temperature heat capacity measurements on encapsulated transuranium samples. *J Nucl Mater.* 2005;344(1–3):50–5.

<https://doi.org/10.1016/j.jnucmat.2005.04.015>

206. Javorský P, Rebizant J, Boulet P, Stewart G, Wastin F. Specific heat measurements on transuranium systems at ITU Karlsruhe. 2003. <https://jda-conf.org/2003/javorsky.pdf>
207. Horlait D, Lebreton F, Roussel P, Delahaye T. XRD Monitoring of α Self-Irradiation in Uranium–Americium Mixed Oxides. *Inorg Chem*. 2013 Dec 16;52(24):14196–204. <http://pubs.acs.org/doi/10.1021/ic402124s>
208. Lebreton F, Martin PM, Horlait D, Bès R, Scheinost AC, Rossberg A, et al. New insight into self-irradiation effects on local and long-range structure of uranium-amerium mixed oxides (through XAS and XRD). *Inorg Chem*. 2014; 53, 18, 9531–9540. <https://pubs.acs.org/doi/abs/10.1021/ic500681k>
209. Prieur D, Jankowiak A, Leorier C, Herlet N, Donnet L, Dehaut P, et al. Influence of the Microstructure on the $U_{1-y}Am_yO_{2-x}$ ($y = 0.1; 0.15$) Pellet Macroscopic Swelling. *Adv Sci Technol*. 2010 Oct;73:104–8. <https://www.scientific.net/AST.73.104>
210. Amorín H, Jiménez R, Ricote J, Hungría T, Castro A, Algueró M. Apparent vanishing of ferroelectricity in nanostructured $BiScO_3$ – $PbTiO_3$. *J Phys D Appl Phys*. 2010 Jul 21;43(28):285401. <http://stacks.iop.org/0022-3727/43/i=28/a=285401?key=crossref.5b395cb70e99f8365cbda907d38615d7>
211. Maglia F, Tredici IG, Anselmi-Tamburini U. Densification and properties of bulk nanocrystalline functional ceramics with grain size below 50nm. *J Eur Ceram Soc*. 2013 Jun;33(6):1045–66. <http://dx.doi.org/10.1016/j.jeurceramsoc.2012.12.004>
212. Miao Y, Yao T, Lian J, Park JS, Almer J, Bhattacharya S, et al. In situ synchrotron investigation of grain growth behavior of nano-grained UO_2 . *Scr Mater*. 2017; 131; 29–32. <https://doi.org/10.1016/j.scriptamat.2016.12.025>
213. Tyrpekl V, Cologna M, Robba D, Somers J. Sintering behaviour of nanocrystalline ThO_2 powder using spark plasma sintering. *J Eur Ceram Soc*. 2016; 36(3); 767–772. <https://doi.org/10.1016/j.jeurceramsoc.2015.11.006>
214. Matzke H. On uranium self-diffusion in UO_2 and UO_{2+x} . *J Nucl Mater*. 1969 Apr;30(1–2):26–35. <https://linkinghub.elsevier.com/retrieve/pii/0022311569901652>
215. Tyrpekl V, Vigier JF, Manara D, Wiss T, Dieste Blanco O, Somers J. Low temperature decomposition of U(IV) and Th(IV) oxalates to nanograined oxide powders. *J Nucl Mater*. 2015; 460; 200–208. <https://doi.org/10.1016/j.jnucmat.2015.02.027>
216. Balice L, Bouëxière D, Cologna M, Cambriani A, Vigier J-F, De Bona E, et al. Nano and micro $U_{1-x}Th_xO_2$ solid solutions: From powders to pellets. *J Nucl Mater*. 2018 Jan;498:307–13. <https://linkinghub.elsevier.com/retrieve/pii/S002231151731334X>
217. Razavi Hesabi Z, Haghighatzadeh M, Mazaheri M, Galusek D, Sadrnezhaad SK. Suppression of grain growth in sub-micrometer alumina via two-step sintering method. *J Eur Ceram Soc*. 2009; 29(8);1371–1377. <https://doi.org/10.1016/j.jeurceramsoc.2008.08.027>
218. Razavi Hesabi Z, Mazaheri M, Ebadzadeh T. Enhanced electrical conductivity of ultrafine-grained $8Y_2O_3$ stabilized ZrO_2 produced by two-step sintering technique. *J Alloys Compd*. 2010; 494(1–2);362–365. <https://doi.org/10.1016/j.jallcom.2010.01.046>
219. Maca K, Pouchly V, Zalud P. Two-Step Sintering of oxide ceramics with various crystal structures. *J Eur Ceram Soc*. 2010; 30(2); 583–589. <https://doi.org/10.1016/j.jeurceramsoc.2009.06.008>
220. Wang XH, Chen PL, Chen IW. Two-step sintering of ceramics with constant grain-size, I. Y_2O_3 . *J Am Ceram Soc*. 2006;89(2):431–7. <https://doi.org/10.1111/j.1551-2916.2005.00763.x>
221. Munir ZA, Anselmi-Tamburini U, Ohyanagi M. The effect of electric field and pressure on the synthesis and consolidation of materials: A review of the spark plasma sintering method. *J Mater Sci* 41, 763–777 (2006). <https://doi.org/10.1007/s10853-006-6555-2>
222. De Bona E, Walter O, Störmer H, Wiss T, Baldinozzi G, Cologna M, et al. Synthesis of nanostructured ThO_2 pellets. *J Am Ceram Soc*. 2019 Jul 25;102(7):3814–8. <http://doi.wiley.com/10.1111/jace.16375>
223. Elorrieta JM, Manara D, Bonales LJ, Vigier JF, Dieste O, Naji M, et al. Raman study of the oxidation in $(U, Pu)O_2$ as a function of Pu content. *J Nucl Mater*. 2017; 495;484–491. <https://doi.org/10.1016/j.jnucmat.2017.08.043>

224. Lyon WL, Baily WE. The solid-liquid phase diagram for the $\text{UO}_2\text{-PuO}_2$ system. *J Nucl Mater.* 1967 Jun;22(3):332–9. <https://linkinghub.elsevier.com/retrieve/pii/0022311567900517>
225. Belbeoch B, Boivineau JC, Perio P. Changements de structure de l'oxyde U_4O_9 . *J Phys Chem Solids.* 1967 Jul;28(7):1267–75. <https://linkinghub.elsevier.com/retrieve/pii/0022369767900704>
226. Jégou C, Caraballo R, Peugeot S, Roudil D, Desgranges L, Magnin M. Raman spectroscopy characterization of actinide oxides ($\text{U}_{1-y}\text{Pu}_y$) O_2 : Resistance to oxidation by the laser beam and examination of defects. *J Nucl Mater.* 2010 Oct;405(3):235–43. <https://linkinghub.elsevier.com/retrieve/pii/S0022311510003739>
227. Talip Z, Peugeot S, Magnin M, Berardo L, Valot C, Vauchy R, et al. Raman microspectroscopic studies of unirradiated homogeneous ($\text{U}_{0.76}\text{Pu}_{0.24}$) O_{2+x} : the effects of Pu content, non-stoichiometry, self-radiation damage and secondary phases. *J Raman Spectrosc.* 2017;48(5):765–72. <https://doi.org/10.1002/jrs.5092>
228. Dolling G, Cowley RA, Woods ADB. The Crystal Dynamics of Uranium Dioxide. *Can J Phys.* 1965 Aug;43(8):1397–413. <http://www.nrcresearchpress.com/doi/10.1139/p65-135>
229. Nichenko S, Staicu D. Molecular Dynamics study of the mixed oxide fuel thermal conductivity. *J Nucl Mater.* 2013 Aug;439(1–3):93–8. <http://dx.doi.org/10.1016/j.jnucmat.2013.03.075>
230. Cureton WF, Palomares RI, Walters J, Tracy CL, Chen C-H, Ewing RC, et al. Grain size effects on irradiated CeO_2 , ThO_2 , and UO_2 . *Acta Mater.* 2018 Nov;160:47–56. <https://linkinghub.elsevier.com/retrieve/pii/S1359645418306773>
231. Cureton WF, Palomares RI, Tracy CL, O'Quinn EC, Walters J, Zdorovets M, et al. Effects of irradiation temperature on the response of CeO_2 , ThO_2 , and UO_2 to highly ionizing radiation. *J Nucl Mater.* 2019;525:83–91. <https://doi.org/10.1016/j.jnucmat.2019.07.029>
232. CLINARD FW, DOUGLASS DL, LAND CC. Strain Effects and Spalling in Alpha-Bombarded ThO_2 . *J Am Ceram Soc.* 1971;54(4):177–9. <https://doi.org/10.1111/j.1151-2916.1971.tb12257.x>
233. Kato M, Komeno A, Uno H, Sugata H, Nakae N, Konashi K, et al. Self-radiation damage in plutonium and uranium mixed dioxide. *J Nucl Mater.* 2009; 393(1);134–140. <https://doi.org/10.1016/j.jnucmat.2009.05.020>
234. Chikalla TD, Turcotte RP. Self-radiation damage ingrowth in $^{238}\text{PuO}_2$. *Radiat Eff.* 1973 Jan 12;19(2):93–8. <http://www.tandfonline.com/loi/grad19http://dx.doi.org/10.1080/00337577308232225>
235. Talip Z, Wiss T, Maugeri EA, Colle JY, Raison PE, Gilibert E, et al. Helium behaviour in stoichiometric and hyperstoichiometric UO_2 . *J Eur Ceram Soc.* 2014; 34(5):1265–1277. <https://doi.org/10.1016/j.jeurceramsoc.2013.11.032>
236. Garcia P, Martin G, Desgardin P, Carlot G, Sauvage T, Sabathier C, et al. A study of helium mobility in polycrystalline uranium dioxide. *J Nucl Mater.* 2012;430(1–3):156–65. <http://dx.doi.org/10.1016/j.jnucmat.2012.06.001>
237. El-Genk MS, Tournier JM. Estimates of helium gas release in $^{238}\text{PuO}_2$ fuel particles for radioisotope heat sources and heater units. *J Nucl Mater.* 2000;280(1):1–17. [https://doi.org/10.1016/S0022-3115\(00\)00036-2](https://doi.org/10.1016/S0022-3115(00)00036-2)
238. Colle JY, Hiernaut JP, Wiss T, Beneš O, Thiele H, Papaioannou D, et al. Fission product release and microstructure changes of irradiated MOX fuel at high temperatures. *J Nucl Mater.* 2013;442(1–3):330–40. <http://dx.doi.org/10.1016/j.jnucmat.2013.09.022>
239. Govers K, Lemehov S, Hou M, Verwerft M. Molecular dynamics simulation of helium and oxygen diffusion in UO_{2+x} . *J Nucl Mater.* 2009 Dec;395(1–3):131–9. <https://linkinghub.elsevier.com/retrieve/pii/S0022311509008514>
240. Fucke K, Steed JW. X-ray and Neutron Diffraction in the Study of Organic Crystalline Hydrates. *Water.* 2010 Jul 9;2(3):333–50. <http://www.mdpi.com/2073-4441/2/3/333>
241. Mamigonian Bessa L. Synthesis and characterization of hydroxyapatite modified with (9r)-9-hydroxystearic acid. Master thesis. <http://amslaurea.unibo.it/7320/>
242. Flotow HE, Osborne DW, Fried SM, Malm JG. Heat capacity of $^{242}\text{PuO}_2$ from 12 to 350°K and of $^{244}\text{PuO}_2$ from 4 to 25°K. Entropy, enthalpy, and Gibbs energy of formation of PuO_2 at 298.15°K. *J Chem Phys.* 1976 Aug;65(3):1124–9. <http://aip.scitation.org/doi/10.1063/1.433186>
243. Vălu S, De Bona E, Popa K, Grivau JC, Colineau E, Konings RJM. The effect of lattice disorder on the low-

temperature heat capacity of $(\text{U}_{1-y}\text{Th}_y)\text{O}_2$ and ^{238}Pu -doped UO_2 . Sci Rep. 2019; 9, 15082.
<https://doi.org/10.1038/s41598-019-51476-3>

Titre : Effet de la microstructure sur le comportement de l'hélium radiogénique dans le combustible nucléaire UO_2

Mots clés : oxydes d'uranium, microstructures, gaz de fission, frittage, actinides, endommagement

Résumé : Dû à l'environnement extrême dans lequel il est exploité, le combustible nucléaire présente des modifications des propriétés thermophysiques ainsi que microstructurales. En particulier se forme en périphérie de l'élément de combustible une structure appelée Structure Haut Burnup (HBS) caractérisée par la subdivision des grains originaux en grains d'environ 100 nm. Dans ce travail, la synthèse d'échantillons denses de UO_2 et ThO_2 avec des grains d'environ 100 nm a été réalisée. De tels matériaux permettront de faire des études à effets séparés sur l'impact de la HBS sur le comportement du combustible en conditions normales et accidentelles.

UO_2 dopé avec ^{238}Pu a également été synthétisé et ce dans le but d'étudier en accéléré l'impact de l'activité alpha sur l'évolution de la microstructure et des propriétés thermophysiques du combustible tel qu'en situation de stockage où ce type de décroissance prédomine pendant des millénaires.

L' UO_2 auto-irradié jusqu'à 0.41 dpa, correspondant à un combustible usagé standard de 300 ans, a été caractérisé périodiquement par un ensemble de techniques. La DRX a mis en évidence une saturation du paramètre de maille à 0.3% tandis que la désorption thermique d'hélium a montré une rétention complète du gaz. Le MEB a montré que l'intégrité de la structure est préservée ; en MET la formation de boucles de dislocations et de bulles d'hélium a été mise en évidence. La conductivité thermique mesurée par flash laser décroît de 40% dès 0.03 dpa et aucune restauration de défauts n'a été observée par calorimétrie différentielle aux températures caractéristiques de l'entreposage. Des spectres RAMAN ont été obtenus pour la première fois sur $(\text{U}, \text{Pu})\text{O}_2$ en fonction de la dose d'auto-irradiation. Cette étude a permis d'évaluer certains aspects du comportement du combustible usagé en conditions d'entreposage pendant 300 ans.

Title : Grain size effects on radiogenic helium gas in the nuclear fuel UO_2

Keywords : uranium oxides, microstructures, fission gases, sintering, actinides, damage

Abstract: Due to the extreme environment in which it is operated, nuclear fuel shows changes of its microstructure and thermophysical properties. In particular it develops a rim structure also named high burnup structure characterized by the subdivision of the original micrometer sized grains into 100 nm grains.

In this work, the synthesis of dense UO_2 and ThO_2 with grains size down to 100 nm was designed. Such material would allow studying through single effect studies the impact of the high burnup structure on the fuel behavior in and out of normal operation.

UO_2 doped with ^{238}Pu was also synthesised to study the accelerated effect of alpha-decays on fuel microstructure and thermophysical properties since alpha activity will be dominating in spent nuclear fuels for millenaires.

Self-irradiated UO_2 cumulating up to 0.41 dpa, the

same reached by a LWR spent fuel after few centuries, was characterized periodically with a broad set of techniques. XRD showed a saturation of the lattice parameter increase around 0.3 %, while thermal desorption spectroscopy proved that the totality of the radiogenic He is still retained. SEM observations highlighted the integrity of the fuel is preserved, while TEM evidenced the ingrowth of dislocation loops and He bubbles within the matrix. Thermal conductivity as measured by laser flash had already decreased by 40 % at 0.03 dpa, and no defects annealing was detected by differential scanning calorimetry at the temperatures foreseen for spent fuel storage. Raman spectra were acquired for the first time on $(\text{U}, \text{Pu})\text{O}_2$ as a function of the self-irradiation dose.

This study allowed assessing some aspects of the behaviour of LWR spent nuclear fuel during the first 300 years of storage time.